IMPERIAL COLLEGE LONDON

UNIVERSITY OF LONDON

Investigation of Ice Removal From Cooled Metal Surfaces

by

Richard Andrew Seppings

A thesis submitted to the University of London for the degree of

Doctor of Philosophy

Imperial College London

Mechanical Engineering Department

Exhibition Road

London SW7 2AZ

October 2005

Abstract

This thesis describes the problem of material build-up on metallic surfaces, with particular reference to ice and frozen sucrose build-up on small diameter pipes. The thesis aims to determine the mechanisms behind ice removal when transverse vibrations act upon the system over a range of frequencies. Additionally, factors such as the noise output from the system and fatigue stresses acting on the system should be minimised. The thesis will outline a system where a practical compromise between ice removal, fatigue life and noise reduction might be achieved, based upon understanding of the failure criteria.

To understand the mechanisms of failure the dynamics of the system with and without the presence of ice have been characterised over a range of frequencies. Ice comprises a complex crystalline structure and a brief outline of its mechanical properties is described within the thesis. Special attention is paid to the relationship between ice and frozen sucrose solution.

A simple experimental system has been developed as a generic example application and results from this rig have been investigated. The same system has been modelled using a finite element program. Data derived from the finite element simulation and experimental results have been compared with data for both cohesive and adhesive failure criteria.

Data on strain rates in excess of those previously reported is presented, showing an apparent decrease in the yield/fracture strength of frozen sucrose after the critical strain rate.

Good agreement has been achieved between the derived results and results from the literature, over a range of frequencies. Hence, an understanding of the mechanisms behind ice failure has been built up. To be fully removed from the pipe the ice must fail in at least three planes: axially, circumferentially and also at the interface. Results derived from experimentation and modelling indicate the order of failure and the magnitude of the last or critical failure stress.

Acknowledgements

Contents

List of Figures

List of Tables

Chapter 1

Introduction

1.1 Motivation for Investigation

Many practical engineering environments involve the build-up of unwanted material inside or outside of pipes. The severity of these problems varies greatly from blockages in gasoline vents in aeroplanes [1], to the common and longstanding problem of burst central heating piping [2], to minor reductions of efficiency in ice slurry production in air-conditioning systems [3], or indeed serious cooling failures in deep mines which can use piped ice slurry as a coolant [4]. Even small build-ups can cause significant costs in terms of efficiency and therefore have both important ecological and economic ramifications. For example in a typical 25 mm heat exchanger tube, 5 mm of scale can lead to a 8-10% increase in fuel consumption [5] due to increased pumping loads. Xie et al. indicate that circa $4billion (US) might be lost to the US electricity industry yearly due to ash deposition on heat exchanger pipes at the burner side of power plants [6].

Other serious problems might occur due to the build-up of material on moving parts. For example in the aircraft industry build-up of ice on aileron and airfoil surfaces can be detrimental to both the aerodynamic properties of the wing and could also impede the normal movement of the affected surface [7, 8]. Some research has been carried out by NASA at the John Glenn research centre into removing unwanted ice deposits using ultrasonic actuation [9]. However, little evidence is presented as to the effectiveness of this method, or indeed even the precise manner of ultrasonic

actuation.

Other work on ice removal undertaken by Petrenko [10, 11] describes the effects of electrical potentials applied to ice/metal interfaces. An outline of how such electrical effects might be used to alter the adhesion of ice to cooled metallic surfaces is described. Here, ice is removed by using variable electronic fields at the interface between the ice and the system under investigation. The adhesive properties of the ice are directly altered resulting in removal because the adhesion is significantly reduced. In these works and via his company web page [12], uses in aerospace, windshield de-icing and domestic refrigeration devices are illustrated. Using this method of ice removal, the ice appears to be melted rather than mechanically removed. In certain applications, where the nature of the crystals is important, melting the interfacial ice layers may be a significant drawback to this otherwise very effective method.

A problem of material build-up on pipes familiar to many people is that of limescale deposition from water based systems. Several methods can be used to remove the limescale from the internal surface of the pipe; one method is chemical treatment of the water to remove the limescale and another is to place the pipe directly into a magnetic field, but the processes in this method, as described by Szkatula et al. [13, 14], do not appear to be well understood. However, the effect is repeatable and a soft easily removable sludge is formed at the pipe interface, rather than the normal hard limescale deposit. Similar effects have been reported by the Russian company UtInlab [15], where ultrasonic waves are passed into a liquid medium where limescale deposits would normally occur. This effect has also been reported for boiler scale prevention [16], but the process details are not described.

The main thrust of this project is to investigate the use of structural vibrations in food processing applications. The main focus of the project is to investigate the potential for:

Prevention of unwanted ice build-up . In the systems to be investigated within
this thesis it is desirable for ice formation to be allowed. However, the use of

structural vibrations has been investigated as a means to stop or at least regulate the agglomeration of ice layers on metal surfaces cooled below the freezing point of ice. The aim is to allow ice formation within the liquid in the system, but to systematically remove the ice from the cooled metal surface. This approach could lead to the development of a continuously operating system, based on structural vibration of a cooled metal surface such as a pipe. This would allow the production of ice slurries for refrigeration systems i.e. ice cream in food processing, or ice storage air-conditioning systems. Such a method might reduce or even remove the need for moving mechanical scrapers which are required on traditional cooling heat-exchangers.

Removal of existing ice build-up . Using the same systems that are mentioned above, ice layers will be allowed to form on the system. Structural vibrations will only be applied once the ice layer has formed. Once the ice has been removed the structural vibrations will no longer be required. If this sort of system could be properly harnessed, a rig based on short pulses of excitation could be used to free ice from a cooling heat-exchanger when "choking" is detected within the system. Such a system might lead to reductions in power consumption and an increase in fatigue life over a continuously operating system.

To achieve these aims and investigate the possible advantages mentioned below, an experimental rig capable of achieving continuous and/or pulsed removal of ice must be developed. Using data produced from this rig and combining this data with suitable modelling of the system, the mechanisms responsible for ice removal can be identified. Attempts to optimise systems for ice removal depend upon a sound understanding of the mechanisms responsible.

A specific example where this type of technology could, after some development, be employed is ice cream manufacturing and processing. However, other applications of the technology are anticipated.

In ice cream production, a typical scrape-surface heat exchanger (as described by

Schwartzberg [17]) uses $\sim 3.8\,\mathrm{kW/m^2}$. A large power supply is required to cool the ice cream mixture and to introduce air into it. More detail of the production method is shown in Section 1.2.

Several advantages over this traditional method might be obtained by the use of structural vibrations to remove the ice layer from the heat exchanger rather than having to rely on the blade of a scrape-surface heat exchanger. If vibrations at ultrasonic frequencies are used then the following advantages over existing production methods might be achieved:

"No moving parts" . In the traditional methods a large scraper is required to clean ice crystals from the heat exchanger once they have formed. Using ultrasonic vibrations the need for the scraper could be removed by using very small amplitudes of vibration ($\ll 0.1\,\mathrm{mm}$) to generate stress fields in the pipe.

Possible efficiency gains compared to scrape-surface heat exchangers . As mentioned above, traditional methods require $\sim 3.8\mathrm{kW/m^2}$ [17] for operation. The pipe system described in Chapter 4 requires $2.4 - 3.6\mathrm{kW/m^2}$ to remove 20% frozen sucrose solution from the pipe. Although this is not significantly lower than the other method the system is not yet optimised and further improvements should be achieved.

Low mechanical heating . This would prevent ice cream quality from being affected by surface melting. Some possible methods of ice removal are due to surface melting at the interface between the ice and cooled metal surface [10, 11]. As ultrasonic vibrations remove the ice mechanically from the cooled metal surface there is no need for degradation of the crystal structure. Keeping the metal surface clear from ice layers would increase the heat transfer properties of the pipe. Due to this, the dwell time or time the ice cream is in the system might even be reduced. This may lead to an improvement in the control over the ice cream quality. Some suggestions have been presented that irradiating a liquid with ultrasound might lead to enhanced nucleation properties [18].

"Silent running" . Traditional scrape-surface heat exchangers generate a signi-

ficant amount of noise, which makes for an unpleasant and possibly damaging working environment, whereas ultrasonic actuation is inaudible. A number of researchers have indicated [19, 20] that repeated exposure to high frequency noise in the range of $8 - 20\,\text{kHz}$ will also lead to a deterioration in the human audible range, especially in the upper audible range of $8 - 16\,\text{kHz}$ [21]. By using frequencies of $30\,\text{kHz}$ or greater the amount of damaging noise affecting workers in factories might be reduced.

The direct motivation for this project was work in a similar area carried out by Unilever Research Group at Colworth [22]. In this work the formation of ice slurries was investigated. A titanium tube of $\sim 1''$ diameter and $\sim 9''$ in length was centrally excited by a PZT stack transducer at $\sim 20 - 22\,\text{kHz}$, exciting some form of vibration in the tube. The thin walled tube was cooled externally using a CO_2 aerosol spray. Water was then passed through the pipe, which was held at a very small angle, with ice slurry passing out through the other side of the tube after a few seconds. It appeared from video evidence that ice build-up on the inside of the pipe could be inhibited for some time. However, attempts to reproduce this experiment from similar equipment has proven somewhat difficult. Therefore this project was initiated to further investigate the precise mechanisms behind ice removal in similar systems.

1.2 Background of Investigation

This section will describe the background of processes in the area of ice cream manufacture. A brief history of the development of the current ice cream production process will be outlined, along with the important factors that determine the success of this process.

Additionally, other processes or studies involving the removal of ice from cooled metal surfaces which are relevant to this investigation will be briefly presented. The aim is to show the range of processes for ice removal which are currently available or under development .
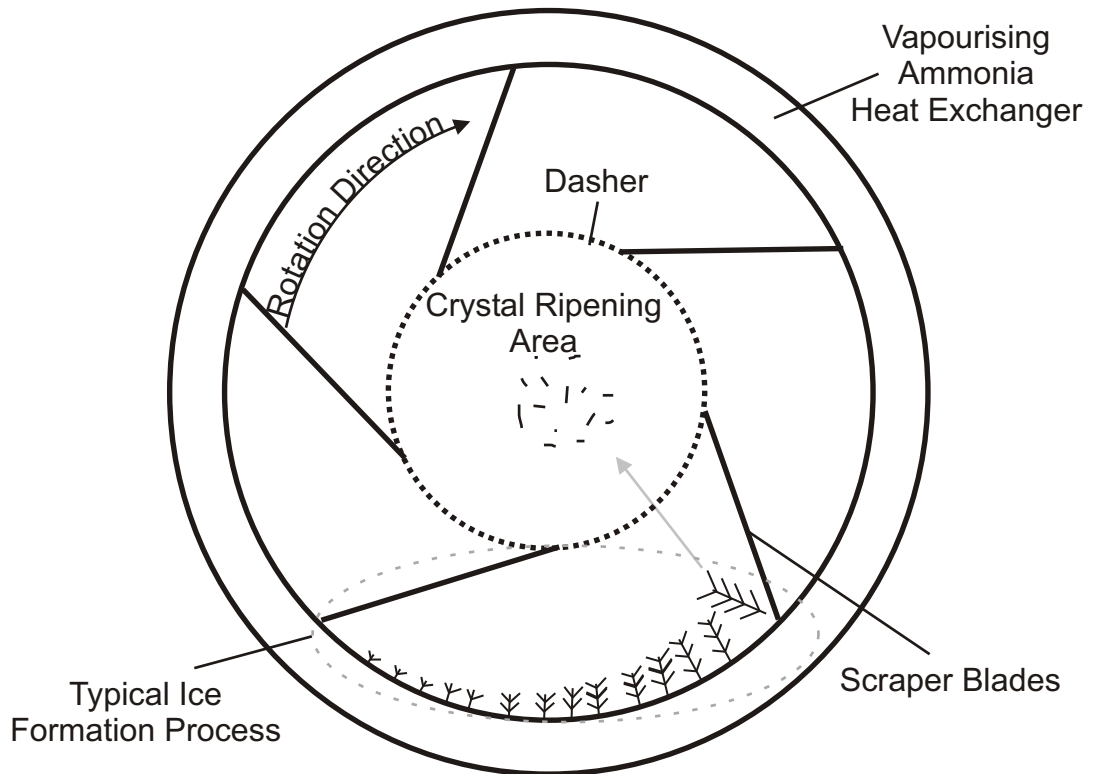
Figure 1.1: Cross-section layout of a typical Scrape-Surface Heat Exchanger

1.2.1   Ice Cream Production

Ice cream manufacture is an old process with early Chinese records referring to the existence of ice cream as a foodstuff [23], having developed as a cottage industry, where cream would be churned and frozen by hand. Control over the product would generally be dependent on the expertise of the individual and freezing methods employed. As demand for ice cream production has increased, the need for improved technologies has arisen. Control over the properties of the ice cream produced while maintaining high volumes of production is essential. Commercial production of ice cream began in 1851 under Mr. Joseph Fussell of Baltimore, USA. This commercial process became possible because of the invention of an industrial freezer [24].

The current ice cream production method involves the use of a "scrape-surface" heat exchanger [25]. This apparatus is illustrated in Figure 1.1. The setup of the equip-

ment is a barrel, cooled externally by an ammonia evaporation process. Ice crystals are formed on the internal surface of the barrel. The crystals take a dendritic form, similar to that exhibited in snowflakes [26]. The crystals continue to grow for a time and are ultimately removed by a blade attached to a "dasher" that is continuously rotating within the barrel. The dasher rotates around the inner surface of the scrape-surface heat exchanger, removing the crystals that have nucleated on the surface and grown since the previous pass of the blade. The motion of the dasher causes the crystals to move from the surface of the barrel to the centre of the barrel, where the crystals "ripen". The dwell period or time the crystals remain in this central region is crucial to the properties of the ice cream produced. Shorter times give smaller crystals and longer times larger crystals.

The optimum size for the ice crystals that are formed is $55 - 60\,\mu$m in diameter [18, 27]. Above this size the ice cream is found to be too coarse and have a "crunchy" texture. The dwell time is controlled by the through flow rate of the ice cream mixture, which is driven by a helical screw drive forcing the mixture axially through the barrel of the scrape-surface heat exchanger. A significant amount of energy is required to drive this system, with the scrape-surface heat exchanger requiring $\sim 3.8\,\mathrm{kW/m^2}$ for normal operation [17]. Ice cream is often produced in batches using this method and the system must be taken off line for regular cleaning.

Even with this automated process there is a demand for improved technology to regulate ice cream properties further, increase the speed of production and increase the efficiency of production methods. As such, several technologies have been developed or are being developed to improve ice cream production techniques for a variety of different products. A brief outline of the techniques employed within ice cream manufacture (or in other industrial processes with a similar basis for removal of unwanted deposits from metal surfaces) is included in the following paragraphs.

1.2.2 Related Procedures

Several patents have been issued to inventors who have provided novel systems to remove ice from cooled metal surfaces using a variety of means. These include the use of applied voltages to modify the adhesion properties of the ice at the interface [28] - hence reducing adhesion between the substrates. In other cases the physical properties of ice have been utilised to allow ice removal. Miller et al. [29] show that at temperatures between $-70°$ C and $-80°$ C there is little adhesion force between the ice and metal mould. Therefore, the ice can be removed in each case with little effort. This method has been employed in the manufacture of 3D ice lollies [30].

Each of these methods is effective in the correct environment, though both suffer from some disadvantages. The method of applied voltages requires some specialised electrode to be added between the surface where the ice is formed and the ice itself. This could be problematic in a food processing environment, where stringent food safety standards must be met. Additionally, the release may be due to melting at the ice-electrode interface (rather than mechanical separation), which would have an adverse effect on the properties of the foodstuff under production. Also the cryogenic approach has some limitations in processing applications against the sort of batch processes that it is designed for. The cryogenic process requires more cooling energy than that of traditional scrape surface heat exchangers as temperatures of -70 to $-80°$C [29] must be generated in large moulds rather than say -20 to $-30°$C that are generated in scrape-surface heat exchangers [25].

A mechanical method [31] has also been patented for aircraft anti-icing. This method involves a pneumatic strip type actuator acting along the leading edge of the airfoil. The strip is strategically located under areas where the formation of ice would be detrimental to the aerodynamic performance of the airfoil. Ice is removed by pressurised air inflating the pneumatic strip, causing large strains to be induced in the ice layer and leading to the fracture of ice. In this method the ice is broken into small pieces and is subsequently removed by the flow of air over the airfoil. A potential disadvantage of this system is that the ideal aerodynamic and structural shape cannot be implemented as the ice removal device must be incorporated within

the structure of the wing. Also the deviation of the devices must be significant $\sim \frac{1}{20}''$ to cause the strain necessary to remove the ice. A similar method is available from Innovative Dynamics Ltd., where eddy-current transducers are attached to the leading edge of the wing and are energised when a large build-up of ice has occurred. This method appears to be based on a rigid body motion inducing inertial forces in the ice layer. [32]. Similar methods using eddy current transducers to induce flexure in the leading edge of an aircraft wing to remove ice build-up have also been proposed [33].

Another method for ice removal has been shown by Yamada et al. [34]. This utilises angular displacements in rigid bodies, using a copper tube to form ice in a water/ethanol-glycol solution. The same tube is then oscillated to produce angular acceleration, causing shear forces in the ice crystals. The ice crystals are removed or broken off, forming a "slurry". It is shown that ice slurry can be removed at varying angular accelerations, however, there is a threshold where small angular accelerations do not produce enough force on the ice crystals to overcome the shear adhesion force of the ice on cooled copper. With a wall temperature of $-10°$C and angular acceleration of $12,000 \frac{\text{deg}}{\text{s}^2}$, separation occurs 30 seconds after excitation begins. At higher accelerations shorter separation times are recorded, i.e. $18,000 \frac{\text{deg}}{\text{s}^2}$ gives a separation time of five seconds. The authors note that even during slurry production some ice remains on the wall of the cooled tube. It is not clear therefore, whether the ice is being removed by cohesive failure due to internal stresses within the ice or by adhesive failure between the ice and copper.

1.3 Objectives of Investigation

The main objective of this thesis is to determine the mechanisms behind ice removal when structural vibrations are excited in a system comprising ice on a cooled metal surface. To achieve this, an experimental rig, capable of producing repeatable and reliable data, is required. Therefore, a secondary objective is to develop a suitable experimental rig which meets these requirements. Further to this, forces acting on

the system, and the stress field generated by the structural vibrations must be identified and then quantified. A suitable model of the system describing the dynamics of the system with and without the ice build-up should be developed in conjunction with the experimental rig. By comparing and combining the output from the model and the experiment an improved understanding of the mechanisms behind the ice removal will be achieved.

The forces that are expected to act on the system will be detailed in the following section. The forces will be described for the built-in slender pipe of Chapter 4, as most of the work of this investigation was centered on this system. However, similar forces would act on the other systems described in Chapter 3.

1.3.1   Nature of Forces

To understand properly the mechanisms behind the removal of ice from the systems studied in this investigation, the differing factors acting on the system undergoing structural vibrations must be identified for each case. Once the factors have been identified, the effect that each variable will have on the system should be understood as far as can be determined. When suitable understanding of the forces acting on the system and the stresses produced is obtained, then the mechanisms behind the removal of ice from the cooled surfaces can be deduced.

Three flexural modes of vibration, denoted modes 1, 3 and 5, will be studied in this investigation of the pipe systems described in Chapters 4 and 5. Only the odd flexural modes were expected, as the T-connector was attached at the centre of the pipe, only allowing symmetrical modes. The first mode of vibration has a displacement maximum at the mid-length of the pipe, with the pipe built-in at each end; the third mode has displacement maxima at ~ 0.25 and 0.75 of the pipe length, with a smaller displacement peak at the mid-length of the pipe, with the pipe ends fixed; the fifth mode has displacement maxima at 0.14, 0.35, 0.65, and 0.86 of the pipe length, with a smaller displacement peak at the mid-length of the pipe, again the pipe ends are fixed.
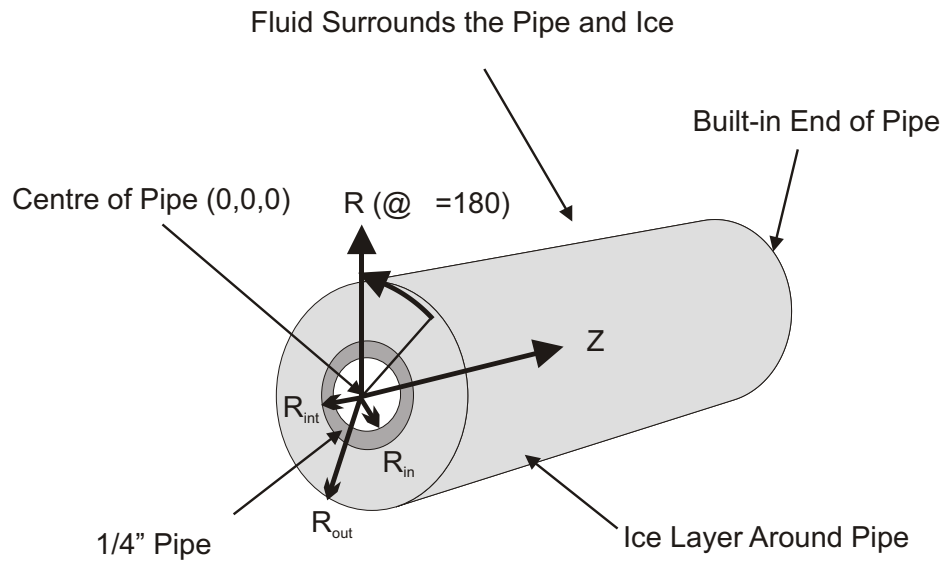
Figure 1.2: Cylindrical co-ordinate system of the built-in pipe described in Chp. 4.

The co-ordinate system for the built-in pipe system described in Chapter 4 is shown in Figure 1.2. The directions described in the following sections refer to the co-ordinate system illustrated in this figure and the forces discussed relate directly to this system.

Bending Forces

Axial forces will be caused both in the pipe and in the ice due to the bending of the pipe. These forces will act in the pipe and also in the ice layer and will be predominantly in the Z-direction. As the pipe is slender it is expected that these forces will be large compared with the other forces acting on the system.

Shear Forces

The flexural modes excited in the pipe will also cause shear forces to be generated in the pipe and ice layer. However, as the pipe is long and slender the shear forces should be small compared with the axial forces caused by the bending. This does not mean, however, that the shear forces can be neglected. Shear forces will be described by the forces acting at the interface between the pipe wall and the ice in the rθ, rZ and θZ planes.
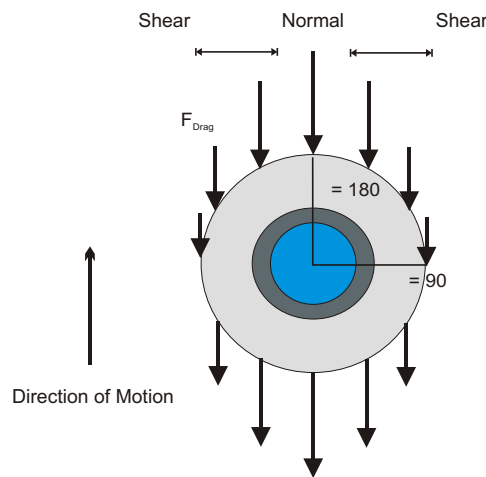
Drag Forces

Figure 1.3: Illustration of how and where drag forces will act.

As the pipe and ice system will be submerged in a liquid, there will be drag forces acting in the opposite direction to the fluid motion, retarding the motion of the pipe. These forces will largely act in the direction of R at $\theta = 180$, when the pipe is moving in the direction of R at $\theta = 0$ as shown in Figure 1.3. The drag forces will vary with the velocity profile as it varies in the Z-direction, which will depend on the mode shape of the vibration. The drag forces act parallel to the R-direction at $\theta = 180$ & 0 over the length of the pipe and ice, wherever the pipe is moving in that direction. These forces can produce normal and shear forces on the system. For example normal forces will be created at the centre of the pipe, but shear forces will act at R_{out} at $\theta = \pm 90°$ due to the viscous drag from the pipe moving in the

surrounding liquid. This variation between normal and shear forces is illustrated in Figure 1.3.

Inertial Forces
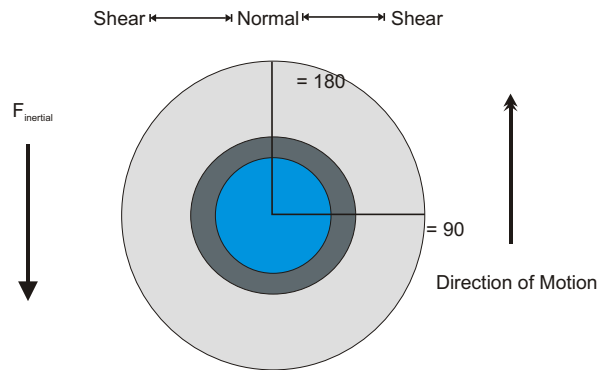
Figure 1.4: Illustration of how and where inertial forces will act, resisting the motion of the system.

The acceleration of the pipe as it vibrates will induce inertial forces normal to the axis of the pipe as shown in Figure 1.4. The inertial forces will cause a shear stress at the interface between the pipe wall and the ice at $\theta = \pm 90°$. A normal stress will also be caused at the interface at $\theta = 0$ and 180°. In the positions between these stresses a combination of shear and normal forces will be caused. Again the mode shape of the pipe will affect the accelerations in the pipe, and the inertial forces acting on the ice will vary with position in the Z-direction. Also the relative magnitude of the inertial forces compared to other forces acting on the pipe may change with each mode.

1.3.2   Stresses Generated

The forces mentioned in the above paragraphs will cause a stress field to be created in both the ice and the pipe. The stresses of most interest in this investigation are

the shear stresses at the interface between the pipe and the ice ($\sigma_{R\theta}$, $\sigma_{\theta Z}$ and σ_{rZ}) and the cohesive stresses (σ_{ZZ} and $\sigma_{\theta\theta}$) generated in the ice. Figure 1.5 shows the expected locations of the stresses in the system. For a full prediction of the stress field see section 5.3.5 of Chapter 5. Typical stress mode shapes are shown in Figures 5.13, 5.14 and 5.15 for the three flexural modes under investigation.
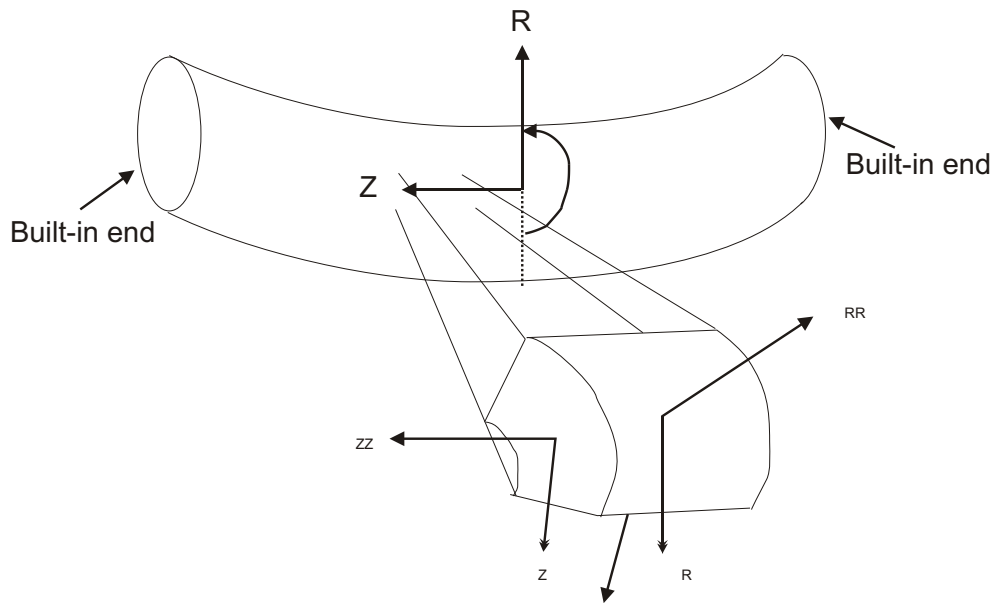
Figure 1.5: Components of the stress field expected within the system

Shear Stresses ($\sigma_{r\theta}$, σ_{rZ} and $\sigma_{\theta Z}$): Shear stresses at the ice metal interface will be caused by a combination of the forces acting on the pipe and ice due to the vibrations. Shear stresses will arise from the forces acting due to drag, inertial forces and the shear stresses generated by the flexure of the pipe. If the shear stresses are greater than the shear adhesive strength then the ice may be freed from the surface of the pipe. Shear stresses will also act in the body of the ice and may cause cohesive failure away from the interface.

Normal Stresses at Interface (σ_{rr}): The normal forces acting at the top and bottom of the pipe due to drag and inertia cause normal stresses at these

locations. If the stresses generated at these locations are greater than the normal adhesive strength of the bond between the metal and the ice then bond will fail and the ice will come free from the metal surface.

Tensile Stresses in Ice Layer (σ_{ZZ}, $\sigma_{\theta\theta}$ and σ_{rr}): Due to the bending of the pipe, there will be an axial stress created in the Z-direction. The magnitude of this stress will vary in the Z-direction with nodes and anti-nodes along the top and bottom surfaces of the pipe. Additionally there will be a variation in the θ-direction, with an absolute maximum at $\theta = 0$ and $180°$ and a minimum at $\theta = \pm 90°$. The uncoupled axial stress in the pipe cannot directly remove the ice from the pipe. Instead the ice may be broken into collars that will remain on the pipe. The stress in the R-direction could cause layers of ice to come off by cohesive failure, but the main consideration is described in the above paragraph on shear stresses.

Stress Limits

Cohesive Strength: If the resultant stress, given by the sum of the forces acting in the body of the ice is greater than the cohesive strength of the ice, then the ice itself will fail.

Adhesive Strength: If the resultant stress, given by the sum of the forces acting at the interface between the ice and the pipe is greater than the strength of the adhesive bond, then the ice may be removed from the surface of the pipe. For the ice to be removed from the pipe, a number of other conditions must be met, e.g. cohesive failure must also occur in at least two directions.

1.3.3 Failure Mechanisms

The failure mechanisms behind the ice removal must be investigated, based upon the stresses that are described in the above paragraphs.

Method and Order of Failure

For the ice to be removed cleanly from the pipe several events must occur. The ice must fail in the hoop (θ) *and* axial (Z) directions. For example *both* conditions:

$\sigma_{\theta\theta} > \sigma_{Critical}^{cohesive}$ and $\sigma_{ZZ} > \sigma_{Critical}^{cohesive}$ must be achieved. In addition to this the interfacial shear ($\sigma_{r\theta}$, σ_{rZ} or $\sigma_{\theta Z}$) or normal σ_{rr} stress must overcome the shear or normal adhesive strength of the bond between the ice and metal at the interface (see figure 1.5).

The net effect of this is to say that the ice must be removed in "chunks". Of course ice could be removed without all of the above conditions being met. For example the ice could fail cohesively in three directions Z, θ and R or Z, θ and a shear failure in the body of the ice. However, such a failure mechanism would not represent success in this investigation, as the aim is to prevent ice build-up on the pipe surface.

To be able to predict when ice will be removed cleanly it is paramount to determine the adhesive and cohesive properties of the ice and sucrose solutions under investigation under the conditions experienced during the experiments. The yield and tensile strengths of both ice and sucrose have shown temperature and strain rate sensitivities [35, 36, 37]. To accurately predict the likely response of a system, a map of these failure criteria i.e ductile-brittle failure transition, must be constructed. An attempt to create this information is shown in section 6.2 of Chapter 5.

By careful comparison of the stress data (generated using a combination of experimental results and finite element modelling) with the failure stresses predicted in the literature the hypothesis of the failure mechanism above can be tested.

1.3.4 Other Factors

Variation of Frequency

The experiments will be conducted over a range of frequencies from $\sim 50 - 2500\,\mathrm{Hz}$. The system could only remove ice up to circa $2500\,\mathrm{Hz}$ due to the amplitude constraints of the shaker compared to the amplitudes required to remove ice from the pipe. The frequency range will encompass the first three flexural modes of vibration of the pipe. Therefore the importance of the differing forces may vary with each

of the modes, i.e. the inertial forces may increase with the increase in frequency if the amplitudes of displacement are in the same order of magnitude for each of the modes for ice removal. Also as the curvature of the pipe increases with increasing mode number then the axial stress may be greater for the higher modes.

Variation of Strain Rate

The strain rate at which the system operates will also have an impact on the yield and tensile strength of the ice. At a low strain rate of less than $10^{-3}\frac{1}{s}$ the ice would exhibit ductile deformation behaviour and at greater strain rates the ice would undergo brittle fracture. Similar trends can be seen in the sucrose-ice matrix that was also investigated.

The nature of the experimental rigs used to investigate the removal of ice from the pipe is such that only brittle fracture will be observed during the failure of ice. The typical strain rates observed from the experiments were around an order of magnitude, or more, larger than those at the transition between the ductile and brittle regimes.

Variation of Temperature

The tensile strength of the ice exhibits a slight temperature dependence. However, the variation is less than 25% over the temperature range $((-1.6) - (-20)°)$ [38] that will be examined during the experiments of this investigation.

Material to be Frozen

A generic system involving a cooled metal surface was developed for this project, where ice could be formed in a repeatable manner. The characteristics of the system were charted through experiments and modelling, both with and without ice present. For the purposes of this investigation both tap water and sucrose solution

(at 10% and 20% concentration by mass) were used as base liquids for ice production.

At this stage, ice cream itself was not considered for the experiments, as ice cream is a complex compound with many differing constituents, i.e. fats, long chain polymers (e.g. guar gum), milk solids and an ice/sucrose matrix. Each of these additives can have a significant effect on the formation of the ice cream in question. For example, increased fat content, stabiliser content or milk solids in ice cream can tend to a decrease in the average crystal size of the ice cream, however emulsifiers are found to have only a secondary effect on the ice crystals in ice cream [39, 40, 41, 42].

Sucrose solution was considered sufficient for preliminary investigations as work by Faydi [43] and communication with Unilever Research Group [22] indicated that at the interface between the ice and cooled metal surface the adhesion properties could be approximated well by an ice sucrose matrix of $\sim 20\%$ concentration.

1.4 Thesis Chapters

The thesis is divided into six further chapters as follows.

1.4.1 Chapter 2: Ice and Frozen Sucrose

The chapter on Ice and Sucrose will present a brief introduction to the physical properties of ice and frozen sucrose that are relevant to the thesis. The elastic properties of ice phase Ih and frozen sucrose solution will be outlined, along with other mechanical properties, such as the strain rate and temperature sensitivities of the yield stress and failure stress of ice and frozen sucrose.

Phase diagrams of water and sucrose solution are presented. The solids produced on cooling of the liquids will be identified and factors that affect the mechanical properties will be investigated. For example the cooling rate and maturation period of the solid can influence the crystal size of the material and hence the Yield Strength,

Young's Modulus and stress at which cracks will propagate, among other things.

1.4.2 Chapter 3: Initial Experiments

This chapter outlines the initial experimental steps taken to try to confirm that ice or frozen sucrose solution could be successfully removed from a cooled metal surface. Different experimental approaches were shown and their potential was evaluated.

The experiments described in this Chapter were based on small, thin, cooled metal plates. Various transducers were used to excite flexural modes of vibration in these systems in the Ultrasonic frequency range. Although ice could be successfully removed in some of these experiments, many questions regarding the failure mechanisms of the ice were left unanswered. Therefore in an attempt to increase the tunability of the experiments and increase fatigue life of the experimental equipment, sonic rigs described in Chapter 4 were developed.

1.4.3 Chapter 4: Rig Development and Experimental Methods

Once the concept of ice removal had been proven, a suitable method had to be developed to clearly demonstrate the mechanisms behind the removal of ice or frozen sucrose. This chapter aims to detail the design process that led from the initial experiments outlined in Chapter 3, to the final experiment that gave the results presented in Chapter 6.

The sonic pipe based rigs that resulted are described and the advantages of such systems for obtaining good data are shown.

1.4.4 Chapter 5: Modelling Process

To understand fully the dynamics of the system under investigation a model of the system was developed, based upon a finite element representation. This chapter

outlines the development and verification of this model. Discussion and justification of the forces which have been modelled and those which have been ignored during this project are also presented.

1.4.5 Chapter 6: Results

Results generated from a combination of the raw experimental data and finite element modelling will be shown in this chapter. Data for the first three flexural modes of vibration encountered in the system (Modes 1, 3 and 5) are presented. Comparisons between the data obtained and predictions from other sources are shown.

1.4.6 Chapter 7: Discussion and Application Optimisation

Based upon the findings from Chapter 6 and some understanding of the mechanical behaviour of frozen sucrose solution an attempt to show an "optimised" operating condition will be presented. This chapter will attempt to show something of the need to obtain certain levels of stress to remove the ice, but also to consider the fatigue life of the permanent components of the system and the noise emission of the system as a whole.

1.4.7 Chapter 8: Conclusions

Conclusions built on the results shown in Chapter 6 will be detailed in this chapter. The mechanisms that underpin the removal of ice from the system examined in the thesis will be shown and explained, where possible.

Chapter 2

Ice and Frozen Sucrose Solutions

2.1 Introduction

Chapter 1 indicated that a study on the removal of ice build-ups from cooled metal surfaces would be conducted. It was further noted that investigation of the potential for processing of frozen desserts, e.g. ice cream or Water Ices, would be considered. (Hereafter, the term "Water Ices" refers to a type of frozen dessert such as a sorbet, the main constituent of which is sucrose solution.)

Therefore, a review of the literature regarding the properties of the substances under investigation was required. Ice cream is a complex mixture of different constituent components, each of which can alter the structure and physical behaviour of the ice cream produced. In some cases, substances such as stabilisers, which can account for only a fraction of a percent of the total mass of the mixture can have a disproportionately large effect on the behaviour of the final product.

The main interest was to investigate the mechanisms responsible for ice removal from cooled metal surfaces. As ice cream presents a difficult modelling problem in its own right it was decided to use 20% sucrose solution (by mass) as the basis for the investigation. Sucrose solution was chosen because, when frozen under the correct conditions and composition, it behaves in a similar way to the way ice cream behaves at its interface with scrape surface heat exchangers.

An additional benefit is that the material is more readily available and easier to produce for experimentation. As sucrose solution is a colourless liquid at the concentrations ($10 - 20\%$ by mass) under investigation, whereas ice cream formula is an opaque liquid; using ice cream formula would render most experimental observations near impossible.

In this chapter a brief outline of the properties and existing models of ice cream will be presented. However, the main focus of this chapter is the structure and behaviour of both frozen sucrose solutions and ice. The latter of the two is considered as it is an important component of frozen sucrose solution and strongly influences its mechanical properties.

A brief description of the ice crystal will be presented. This will consider: how it forms, what states can be assumed, the mechanical properties which are of importance to this investigation, and the structure(s) which is/are likely to form during the course of the experiments conducted during this investigation. The properties will be described with reference to relevant literature on each subject.

Similarly, a brief review of the limited literature available referring to the mechanical properties of sucrose will be presented. The type of structure likely to form on freezing of the sucrose solutions under investigation will also be discussed along with the implications of this structure.

2.2   Models and Behaviour of Ice Cream

A significant amount of effort has been invested in the study of ice cream. Most of this effort has been in the areas of texture and rheological properties [43, 42, 44, 45] of ice cream, and also in the heat transfer properties of ice cream [40, 44, 46]. This research has been driven by the perception of consumers in terms of the end product, i.e. is the product smooth, crunchy, refreshing etc.. Also the post-production behaviour of ice cream, i.e. aging and recrystallisation under different storage condi-

tions [17] has been studied.

It is only relatively recently that the studies into the mechanical properties of ice cream during formation have begun in earnest. Even some of the main constituents (e.g. frozen sucrose solution Section 2.4) are not yet fully characterised or their behaviour understood.

2.3 Structure and Behaviour of Ice

Ice is a commonly occurring material in both natural and artificial environments. Ice can form from a number of physical states (e.g. water or water vapour) and can take many different forms. There are twelve known phases of ice. Some of these phases and their formation conditions are illustrated in Figure 2.1 [47]. The phase that is of most interest to this investigation is ice phase Ih, as this will be the phase of ice formed during the experiments to be conducted.

In this thesis a number of different experiments will be conducted, but the principal mechanism of ice formation will be the same in each experiment. A cooled metal surface (either a plate or a pipe) will be in contact with or immersed in a liquid (either water or sucrose solution). For this section only water will be considered. The metal surface will be sub-cooled to below the freezing point of water, typically down to $-20°$C. All of the experiments will be conducted at atmospheric pressure.

Bearing this in mind, the region of interest shown in Figure 2.1 is near the left axis of the graph in the temperature range of $-5 - -20°$C, as indicated by the black arrow. In this region water changes phase from a liquid to the solid phase ice Ih. Other phases of ice are not considered during this investigation, as they are very unlikely to form.
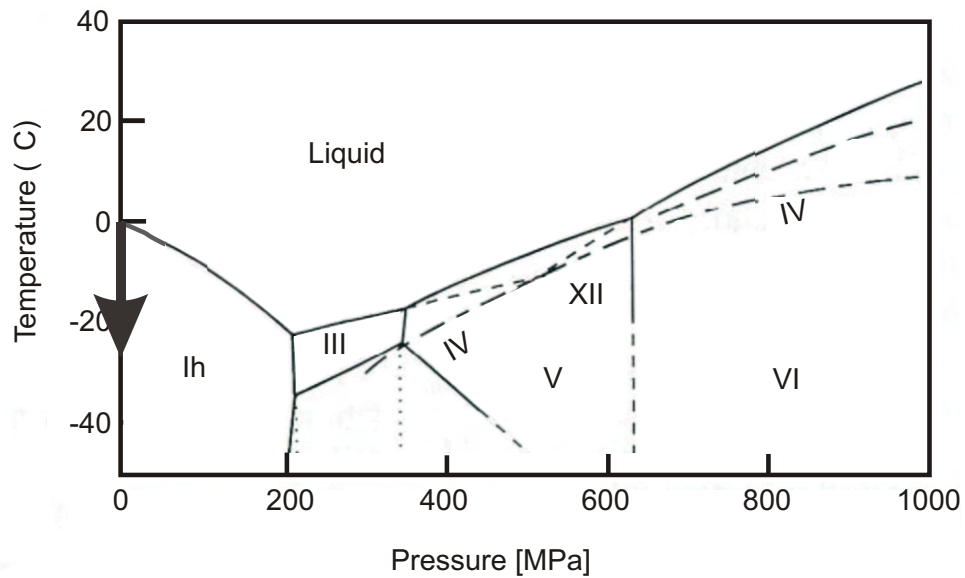
Figure 2.1: Phase Diagram for Water & Ice (Adapted from Fletcher [47])

2.3.1 Structure

Within ice phase Ih a number of different structures of ice can form, depending upon the conditions that the ice is formed under, e.g. type of nucleation, initial conditions etc. These different forms are described as follows.

Ice Single Crystals

Ice is a hexagonal crystal with an axis (c) normal to the hexagonal face. A single crystal of ice will retain this structure, and grows preferentially in the c-direction. Thus, a long relatively slender crystal in the form of a hexagonal prism will form. Single crystals of ice can grow to the order of metres in length; such a crystal may have a width of $\sim 50\,\text{mm}$. These single crystals are the foundation of the other forms of ice discussed in this sub-section.

Under the correct conditions a single crystal of ice may be grown. This would usually be due to a small single crystal taken from another source and placed (or seeded) into a liquid with a low level of undercooling. If the conditions of crystallisation

are controlled carefully the single crystal will continue to grow and very few other crystals will be nucleated in the bulk of the liquid. Single crystals are often grown to study the properties of ice and many results have been reported. Due to large grain sizes and few or no grain boundary interactions, single crystals tend to exhibit enhanced mechanical properties compared to the other ice structures which may form.

Polycrystalline (or Granular) Ice

This is a granular form of ice, where the crystals are randomly oriented. The material may exhibit weakly anisotropic properties if there are slightly elongated crystals in a given direction. The virgin material is statistically isotropic, the anisotropic behaviour is caused by recrystallisation along a preferential c-direction [48]. Schwartzberg and Rao state that densely packed polycrystalline ice forms when pure water is cooled on chilled metal surfaces [17]. This type of structure is expected in the experiments of this Thesis when water is used as the substance to be tested.

Columnar Ice

Columnar ice is as its name suggests a collection of long column like crystals, growing parallel to each other along their c axes. This is a commonly occurring form of ice in nature and is also the study of a number of experimental studies [49]. This ice structure can form from a number of seeded crystals on the surface of a body of water, where a directional temperature gradient exists. An example of this is where snow flakes fall onto the surface of a lake, where the surface temperature is somewhat lower than the than the bulk temperature of the lake. This form of ice Ih is strongly directional and thus exhibits significant anisotropy.

Dendritic Ice

As the name suggests dendritic ice takes a finger-like form. There is a main crystal from which many dendrites can branch off. The effect is shown quite clearly by the

shadow plates taken by Arakawa [50] shown in Figure 2.2. Dendritic ice exhibits weakly anisotropic behaviour, which is caused by the elongated main branch crystals. However, this effect is not as large as may be expected as the dendrites often break off from the main branch after a short period of aging and hence the alignment of the ice crystals is not strongly regimented.

This sort of structure is observed when water with a small amount of impurity is frozen on a chilled metal surface [51].

The general conditions of ice formation experienced during the experiments described in this thesis were: a liquid whose temperature was greater than the freezing point of the liquid is placed in contact with a metal surface whose temperature is less than the freezing point of the liquid. The heat from the liquid is rejected by the cooling circuit, of which the cooled metal surface is part, and hence the temperature of the liquid is reduced.

The following sections outline the possible methods by which ice can form, also explaining which method is most likely to occur. The method of formation will of course affect the structure and properties of ice that will be formed. By determining the method of formation which is likely to occur some information on the location and type of ice which will form can be obtained.

2.3.2 Formation of Ice Crystals

Several mechanisms exist for the formation of ice from the liquid phase. These mechanisms are Primary (or Bulk) nucleation and Secondary (or Contact) nucleation. A brief description of each mechanism and the likelihood of each mechanism taking place during ice formation in the experiments of this investigation will be included in the following subsections.
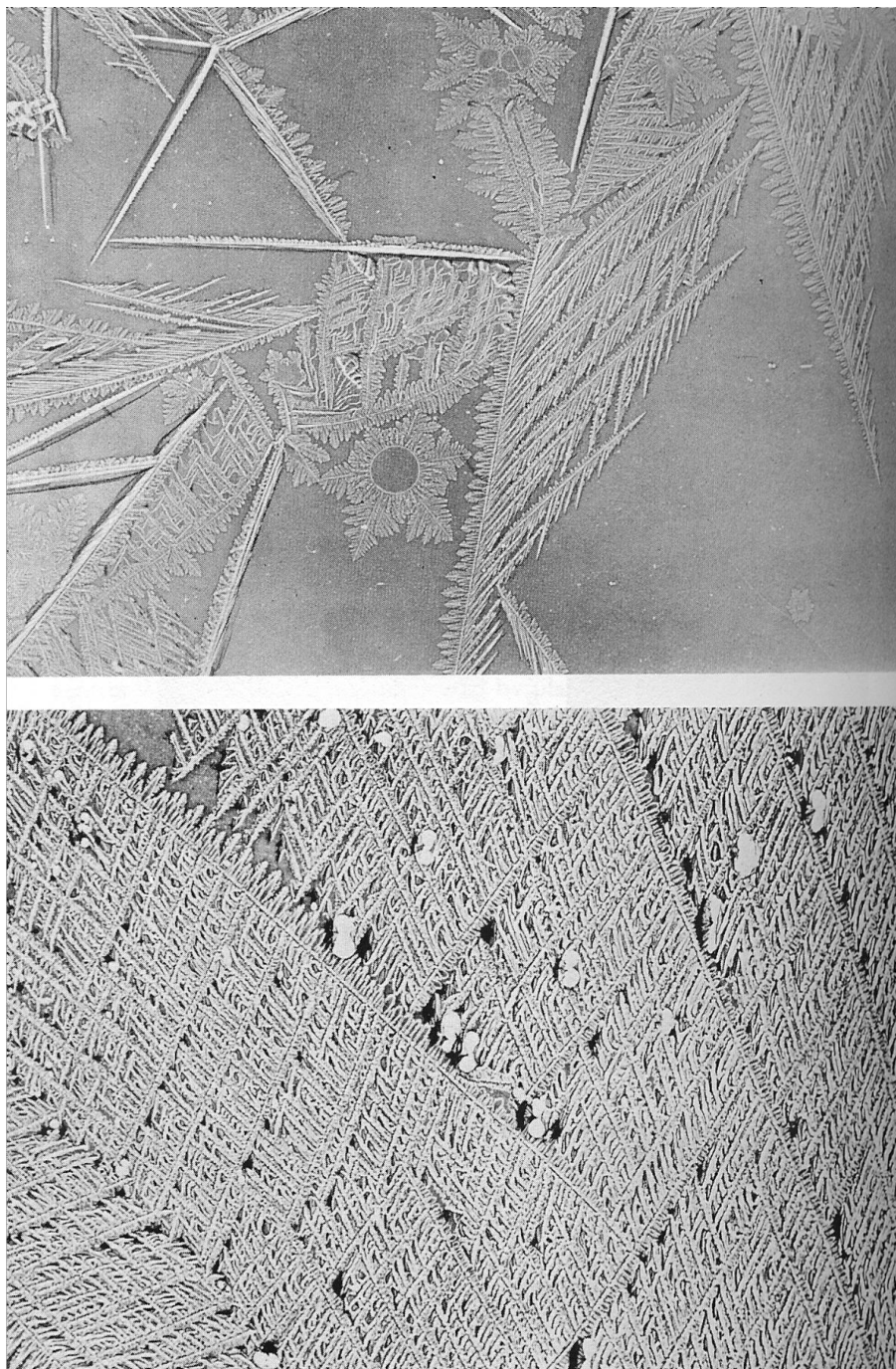
Figure 2.2: Photograph Showing the Dendritic Structure of Ice Taken From Arakawa [50]. Reprinted from the Journal of Glaciology with permission of the International Glaciological Society.

Primary (or Bulk) Nucleation

Primary nucleation is described as homogeneous nucleation, caused by collision and subsequent conglomeration of water molecules in the bulk liquid [17]. This method is less likely to cause crystallisation to occur than Secondary/Contact nucleation. This is because many small embryonic crystals must form in the liquid, each of which has a large surface area/volume ratio, and hence a positive free energy associated with the interface between the crystal and the liquid. Thus, an energy barrier must be overcome prior to the nucleation of the embryonic crystals in the liquid. This could lead to typical values of supercooling of $10 - 30°C$ before ice crystals are actually formed, the spread would depend upon the levels of impurities in the water [47].

Secondary (or Contact) Nucleation

Secondary nucleation is a heterogeneous mechanism where some body foreign to the liquid undergoing nucleation acts to increase the likelihood of nucleation occurring. This mechanism is likely to be the mechanism in operation in the experiments to be conducted, at least during initial stages of the experiments when the levels of supercooling are low. This is because the surface of the metal plate or pipe has a surface roughness which allows ice crystals to become attached at a reduced free energy. Therefore fewer molecules are required to collide and conglomerate for an embryonic crystal to form.

Enhanced Nucleation Due to Ultrasound

Some information has been presented as to enhanced nucleation properties in metals with a dendritic structures on the application of a sonic/ultrasonic field to the molten alloy [52]. Similarly, evidence has been found in other crystalline substances dissolved in water to suggest that crystallisation can be effected by the use of an ultrasonic field applied directly to the solution [53, 54, 55].

Enomoto *et al.* [54] indicated that at higher frequencies, i.e. 1740 kHz (compared with 550 kHz and 200 kHz) the largest crystal sizes were left after filtration of the

solution after a characteristic time. This implies that crystals were formed at a higher temperature than would be expected without the action of the ultrasound. Thus it appears that the frequency of vibration is a factor in determining how much the nucleation effects will be enhanced. In these experiments the intensity of the ultrasound also increased from $1.1 \frac{W}{cm^2}$ at $200\,\text{kHz}$, through $2.2 \frac{W}{cm^2}$ at $550\,\text{kHz}$ to $9.2 \frac{W}{cm^2}$ at $1740\,\text{kHz}$. As both variables increase simultaneously, it is difficult to separate what may be two different effects, i.e. change in nucleation levels with either frequency or intensity or both. A further note on this subject is made in section 2.4.3.

There has also been some work on enhancing crystallisation of ice crystals directly using sonocrystallisation [56, 18]. Using this method to control the crystallisation of the ice has several possible advantages for food processing applications. A low level of super-cooling is required, i.e. the source of cooling only has to be at a slightly lower temperature than that of the liquid/substance to be cooled. It appears that although the effect is well documented, the mechanism responsible for the enhanced nucleation is not well understood. If the effect could be suitably harnessed there is potential for increased efficiency as either dwell time might be reduced, or as implied above the cooling energy for a given process could be reduced.

2.3.3   Mechanical Properties

Pure ice has many distinctive qualities, of which several are particularly important to this investigation. As with many crystalline structures the Tensile Strength (TS) of ice is an order of magnitude less than the maximum strength predicted by force-separation calculations [57].

The elastic modulii of single crystals of ice were found by Gammon *et al.* [58] to be:

$$C_{11} = 139.29 \pm 0.41$$

$$C_{12} = 70.82 \pm 0.39$$

$$C_{13} = 57.65 \pm 0.23$$

$$C_{33} = 150.10 \pm 0.46$$

$$C_{44} = 30.14 \pm 0.11.$$

The units of the stiffness are $10^9 \, \text{dyne cm}^{-2}$. The stiffness matrix is drawn out as follows:

$$
\begin{bmatrix}
C_{11} & C_{12} & C_{13} & 0 & 0 & 0 \\
 & C_{11} & C_{13} & 0 & 0 & 0 \\
 & & C_{33} & 0 & 0 & 0 \\
 & & & C_{44} & 0 & 0 \\
 & & & & C_{44} & 0 \\
 & & & & & \frac{1}{2}\left(C_{11} - C_{12}\right)
\end{bmatrix}
$$

The matrix defines the stiffness of an hexagonal structure, with the assumption that $C_{ij} = C_{ji}$.

The variation of each of the elastic constants may be described by:

$$X(T) = X(T_m)\frac{[1 - aT]}{[1 - aT_m]}; \tag{2.1}$$

where X is an arbitrary elastic parameter (stiffness or compliance), T denotes the temperature in °C, T_m is a temperature for which a measured value of the parameter exists and $a = 1.422 \times 10^{-3}\,°\text{C}^{-1}$

For single crystals of ice the anisotropy varies between $10 - 30\%$ [47]. However, for very fine grained 'granular' ice the results can be statistically isotropic [48]. Therefore, it was assumed that as the level of anisotropy will fall between $0 - 10\%$ and cannot be accurately characterised for the experiments conducted during the

investigation an isotropic material was used. It is expected that some anisotropy will exist, as crystals were seen to grow in the axial direction (or Z-direction as shown in Chapter 4). This implies that the crystals have a preferentially aligned c-direction, corresponding to the Z-axis as shown in Figure 1.2.

The value of E for polycrystalline ice is approximately given by the equation: $E = 5.69 - 0.0648\,T\,(\text{GPa})$, and only varies by around 17 percent in the temperature range $-5 - (-20)°\text{C}$. The poisson's ratio (ν) of polycrystalline ice varies only slightly with temperature in the same range and a value of 0.35 is assumed for this investigation [59].

Cohesive Properties of Ice

In quasi-static tests ice has been found to have a compressive strength of the order of $200 - 400\,\text{kPa}$ [60]. Jellinek [61] finds shear and tensile cohesive strengths to be of similar magnitude and reports the shear cohesive strength to vary between $1.67\,\text{MPa}$ at $-13°\text{C}$ and $1.57\,\text{MPa}$ at $-40°\text{C}$. The variation in cohesive strength with temperature in this range is broadly linear. These experiments were performed at a strain rate of $\dot{\varepsilon} \sim 6 \times 10^{-6}\,\frac{1}{\text{s}}$.

Various authors have studied the cohesive properties of ice [62, 35, 63, 64, 65, 37]. The main findings are summarised below.

Xu [37, 66] shows the yield stress increasing as the strain rate increases from values of $\sim 5\,\text{MPa}$ at $-20\,°\text{C}$ and $\dot{\varepsilon} \simeq 1.0 \times 10^{-4}\frac{1}{\text{s}}$ to a peak at 12–13 MPa at $-20\,°\text{c}$ and $\dot{\varepsilon} \sim 8 \times 10^{-3}\frac{1}{\text{s}}$. At higher strain rates the Yield Strength decreases rapidly and brittle failure occurs. At $\dot{\varepsilon} \sim 8 \times 10^{-3}\frac{1}{\text{s}}$ there is a ductile to brittle transition. This is probably due to the rapid build-up of cracks at elevated strain rates. At these strain rates, stress relaxation effects become secondary [37]. There is some variation in the critical strain rate, depending on the temperature of the ice. For example, the critial strain rate is $1.3 \times 10^{-2}\,\frac{1}{\text{s}}$ for $-20°\text{C}$, falling to $1.0 \times 10^{-2}\,\frac{1}{\text{s}}$ at $-25°\text{C}$ and $0.8 \times 10^{-2}\,\frac{1}{\text{s}}$ at $-40°\text{C}$ [66].

Also the Yield Strength of the ice is seen to increase with decreasing temperature. The Yield Strength appears to decrease almost linearly with increasing temperature from $\sim 20\,\mathrm{MPa}$ at $-45°C$ to $\sim 12\,\mathrm{MPa}$ at $-15°C$, each at the respective critical strain rate.

Rist [63] has found the shear cohesive properties of polycrystalline ice. Rist finds the yield stress maximum of $15\,\mathrm{MPa}$ for ice at $-20\,°C$ and $30\,\mathrm{MPa}$ for ice at $-40\,°C$, at a critical strain rate of $\dot{\varepsilon}_c = 10^{-2}\frac{1}{\mathrm{s}}$. Below this strain rate Rist notes that ductile yielding occurs and above $\dot{\varepsilon}_c$ brittle failure occurs.

Jones [35] has conducted work on fracture of ice at strain rates above $10^{-2}\frac{1}{\mathrm{s}}$. Jones finds that the brittle failure strength either remains the same or continues to rise after this critical strain rate. However, the data presented shows scatter from $4\,\mathrm{MPa}$ to $16\,\mathrm{MPa}$ at $\dot{\varepsilon} = 10^{0}\frac{1}{\mathrm{s}}$, where $4\,\mathrm{MPa}$ is consistent with the decrease in Tensile Strength with increasing strain rate found by the previous researchers. Also, other work by Dutta [65] shows the Tensile Strength to fall with strain rate in Hopkinson's bar tests. Schulson [64] also finds that the Tensile Strength of ice continues to fall at high strain rates of the order 5^{-1}. It is still therefore unclear what effect very high strain rates have upon the Tensile Strength of ice.

Schulson [36] indicates that the grain size of the ice may have an effect on the transitional strain rate, $\dot{\varepsilon}_c$, however this seems only to be important at large grain sizes of 10–100 mm. Grain sizes of 1mm or less are expected during the experiments to be conducted during this investigation, and so this effect was ignored.

Strain Rate Sensitivity

At low applied stresses and low strain rates ice exhibits ductile behaviour [26]. However at increased applied stress or strain rates ice exhibits brittle behaviour. The loading conditions can have a marked effect on the mechanical behaviour of ice. During the experiments it is therefore critical to monitor the applied stress [63], strain rate [37, 35, 36] and temperature of the ice during experimentation [67], as

each variable can have a significant effect on the behaviour of ice under investigation.

During the experiments conducted for this investigation the layers of ice formed on the vibrating pipes and plates will be experiencing high strain rates compared with most of the experimental work conducted on ice. Most of this research has been in the range of $\dot{\varepsilon} = 10^{-8} - 10^{-1} \frac{1}{s}$ [68]. This range has been investigated because the majority of the interest in ice investigations has been concerned with glaciers, ice in lakes and other large scale relatively slow moving objects. At the very lowest strain rates creep is almost certainly the controlling factor in the deformation of ice [69, 70].

During this investigation the majority of the measured strain rates during experiments were in the region of $1 \times 10^{-1} - 2 \times 10^{0} \frac{1}{s}$. It is expected, based on this evidence that the ice will behave in a brittle manner during the experimentation of this investigation. The transitional strain rate has been found to vary between $10^{-2} - 10^{-1} \frac{1}{s}$ [37, 71]. The actual value varies slightly with the temperature of the ice.

Adhesive Properties of Ice

Adhesion in ice is can be controlled by several mechanisms: (i) a covalent or chemical bonding mechanism, (ii) via van der Waals forces between the adherand and the substrate, and (iii) electrostatic forces between the ice and the substrate. Recent research has shown that electrostatic forces play an important role in ice adhesion [72].

The subject of ice adhesion has been investigated in numerous experimental studies. There is a decent body of information on the friction and shear adhesion of ice to a variety of substrates, i.e. metals and plastics [73, 74, 61, 75, 72, 59, 76, 70, 77, 78, 79, 80, 81, 82, 62]. However the normal adhesive strength of ice is more difficult to obtain than the shear adhesive strength. This is because a uniform normal stress is required to predict the adhesive strength of the ice-substrate bond correctly. A uniform force is very difficult to apply [73]. This difficulty is mainly caused by unwanted bending, shearing and peeling effects during tensile tests that make useful

interpretation of the data very difficult. Care should be taken with tensile adhesive strengths as many experiments in this area show cohesive failures, rather than adhesive failures [61] (see Chapter 1 for further explanation).

Nelson *et al.* [81] have studied the effect of ice adhesion to stainless steel 316, which is one of the cooled metals investigated during this project. They find values of 0.91 MPa at -19°C and 0.17 MPa at -6°C. These values are well below those quoted by other workers, as shown in Figure 2.3. This does not imply that the findings are incorrect, but instead highlights the potential pitfalls of trying to interpret ice adhesion data. Values obtained from what is effectively the same experiment can vary significantly, depending on the surface roughness of the substrate, the temperature of adhesion and on the micro-structure of the ice formed. Having stated this, Figure 2.3 shows the "general" variation in adhesive strengths against temperature for ice on a stainless steel substrate (which was obtained by various researchers).

An additional point to mention is that the cleanliness of the substrates can have some effect on the adhesion properties between ice and stainless steel [22]. To minimise any ill effects the rigs used for experimentation were cleaned with a weak detergent and thoroughly rinsed with water prior to experimentation.

The researchers do not generally indicate the strain rates or shear rates at adhesive failure. When the rates are reported the strain rate is generally low: Jellinek [61] reports strain rates of the order of $10^{-6} \frac{1}{\text{s}}$. Therefore, no direct estimation of the effect of strain rate on the adhesive strength of ice on stainless steel can be observed from the literature. One interesting point that should be mentioned is the effect of fracture that has been observed in experimental work. Jellinek [61] notes that the data associated with adhesive failure is consistent with cascade rupture. That is, once the fracture strength has been surpassed, then a crack of a certain length is formed between the substrate and the ice, and following that a cascade of further cracks are formed and the ice/substrate bond is "unzipped".

The shear adhesive strengths of bonds to other metals used during this investiga-
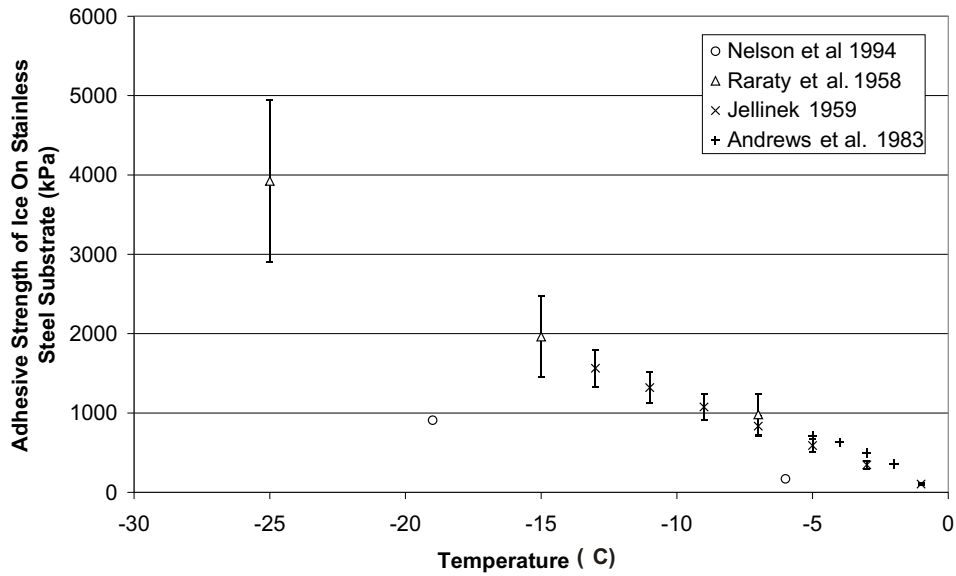
Figure 2.3: Variation of ice shear adhesion to Stainless Steel with temperature. × = Jellinek [61], + = Andrews *et al.* [59], ○ = Nelson *et al.*[81], △ = Raraty *et al.* [73]

tion are of a similar magnitude to those seen in stainless steel/ice bonds: aluminium = 0.77 MPa at−50°C to 0.61 MPa at −6°C [77]; copper ≃ 0.65 MPa [72].

In common with many of the works on the adhesive strength of ice, most of the above methods use some sort of push or pull plunger attached directly to the body of the ice. This is not ideal as the method of actuating the experimental forces is directly affecting the ice, and introducing unexpected stresses in the ice. This tends to add to the already significant scatter in the data associated with the mechanical properties of ice; variance of up to 50% has been calculated for adhesive strengths in ice [26, 83, 73]. Only recently have methods where indirect actuation of the ice substrate interface become available for determining the adhesive strength of ice [82]. Even in this study the variance of the data from the standard deviation is 26%, which was considered reasonable due to the expected scatter when measuring the mechanical properties of ice. This scatter is due to a wide variation in the parameters, e.g. the variance in the pre-testing crack density, the statistical effect of which has been investigated by Gold [84].

Several studies have also shown that as the surface roughness of the material under investigation increases so does the ice adhesion [85, 86]. Highly polished surfaces can have peaks and troughs spaced such that the mean spacing is small compared to the size of a nascent ice crystal. Thus there are few points where a durable adhesion can occur between the ice and the metal surface. As the mean spacing increases to a size comparable with that of the nascent ice crystal then the number of points of attachment increases significantly. Hence the forces required to remove the ice should increase.

There has also been a considerable movement to find suitable treatments and substrates that can be employed to reduce the adhesion strength of ice [87, 88, 89, 90, 91, 92, 93]. Saito *et al.* [91] go on to show that on normal stainless steel surfaces (SUS304), the greater the surface roughness the greater the adhesion, with the converse being true for water repellent surface coatings. Aluminium seems to have similar properties to that of steel [92]. The use of the various polymers and other solid lubricants has the effect of reducing the ice adhesion by up to a factor of 6. Although this approach is suitable for many applications, such as ice removal from mechanical structures, it may not be suitable for large scale food processing applications where food safety is a major concern.

It is important to note that as the level of surface roughness can cause the level of adhesion to change a consistent level of surface roughness should be maintained during experiments where direct comparisons are required. Care was duly taken during this investigation to ensure that each metal was treated with the same surface preparation, in an attempt to produce a similar surface roughness in each case.

2.4 Structure and Behaviour of Frozen Sucrose

2.4.1 Structure

The structure of the ice-sucrose matrix will be that of dendritic ice crystals forming a lattice which trap a sucrose gel matrix [71].

2.4.2 Colligative Effects of Sucrose

Sucrose solution is a mixture of sucrose and water molecules, which tends towards freezing at the freezing point of water. As the concentration of sucrose increases in the aqueous sucrose solution so the freezing point of the solution is depressed. This property is utilised in ice cream manufacture as sucrose concentration is used to control the levels of ice crystals in the ice cream. The depression of the freezing point of sucrose solution can be estimated using the following formula [94]:

$$\Delta T = K_f . m$$

Where:

m = Solution Molarity

K_f = Molal freezing point depression constant

$K_f^{H_2 0}$ = $1.86°C/m$

Sucrose is a saccharide $C_{12}H_{11}O_{11}$ with a molecular weight of 342.3 grams/mole. Using this information with the concentration of sucrose in the solution the depression of the freezing point of sucrose can be estimated for a range of sucrose concentrations. The general effect of the depression point of the freezing point of sucrose compared with pure water can be seen in the sucrose phase diagram Figure 2.4 and Table 2.1.

The sucrose phase diagram shown in Figure 2.4 illustrates the expected freezing path of the sucrose solutions that were investigated during this study. The black lines show the paths for 10% sucrose and 20% sucrose solutions. When the sucrose is cooled below its freezing point, (the roughly horizontal line) the water part of the

Concentration [%, bymass]	Freezing Point [°C]
10.0	-0.604
12.5	-0.776
15.0	-0.959
17.5	-1.153
20.0	-1.358

Table 2.1: Variation of freezing point depression with sucrose concentration

mixture will tend to freeze. There is some evidence that the ice crystals will preferentially form at the sucrose grain boundaries [95]. This leads to the formation of an ice sucrose matrix, where the frozen ice traps a sucrose gel matrix in a lattice-like structure. Much of the mechanical behaviour of the material is dominated by the ice phase of the material, as shall be seen later.
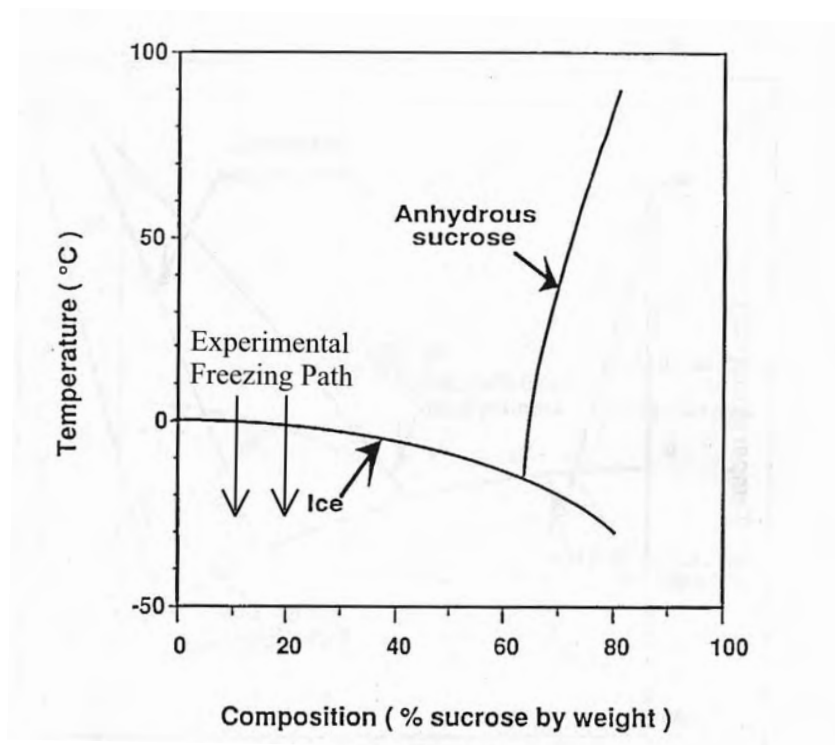
Figure 2.4: Phase Diagram of Sucrose Solution Adapted from Hartel and Shastry [96] to show the freezing path expected during the experiments of this investigation.

Figure 2.5 shows the practical phase diagram of water-sucrose solutions. Little information appears to be available as to the behaviour of sucrose at a given concentration with the pressure it is subjected to. It should be noted that a glassy transition at circa -36 to $-40°$C has been observed in both frozen sucrose solutions and ice creams [42].
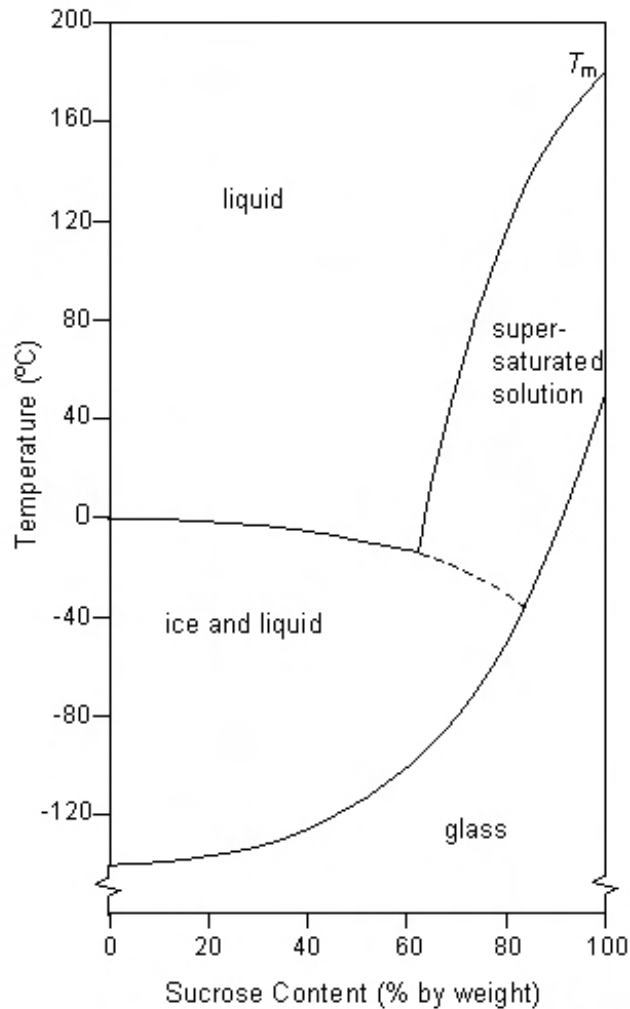
Figure 2.5: Expanded Sucrose Phase Diagram adapted from Department of Materials, Cambridge [97].

Ice-Sucrose Matrix

The composition and structure of the ice-sucrose matrix should theoretically vary with distance away from the nucleation point. This is due to the difference in the

diffusion rate of sucrose molecules and the freezing front growth rate of the ice lattice. Therefore, a greater proportion of the sucrose molecules will be trapped in the ice lattice near to the nucleation point(s). It follows that the overall concentration of the sucrose solution left in the unfrozen solution will decrease as the portion of frozen sucrose-ice matrix increases [98].

2.4.3 Formation of Frozen Sucrose-Ice Matrix

Primary Nucleation

As described in Section 2.3.2, Primary (or Bulk) nucleation is a homogeneous mechanism where crystals form in the body of the solution. Primary nucleation is unlikely in the sucrose phase of the solution as high levels of supersaturation (e.g. ~ 1.6) are typically required for primary nucleation in sucrose solutions [99]. As only solutions of up to 20% mass are to be used in this investigation it is unlikely that primary nucleation will occur. The low levels of subcooling in the experiments described also make primary nucleation in the water phase unlikely.

Secondary (or Contact) Nucleation

As mentioned in Section 2.3.2, Contact nucleation is the most likely mechanism through which ice crystals will form during the experiments conducted for this investigation. This supposition is supported by research conducted by various authors, who demonstrate that contact nucleation is an important mechanism in crystallisation of sucrose solutions onto cooled surfaces [96, 42, 100]

Enhanced Nucleation in Sucrose Solutions

Just as work has been carried out for various aqueous solutions regarding sonocrystallisation, recent work has been carried out into the effects of ultrasonic fields on the nucleation of sucrose solutions [101]. The results are similar to those displayed for other solutions. The onset of nucleation occurs at raised temperatures when the ultrasonic field is "on". The mechanisms that were not previously clear from

the works described in section 2.3.2 are revealed more fully as follows. Chow *et al.* [101] show that at a single frequency the temperature rise for nucleation appears to increase with increasing intensity of the ultrasonic field. Care should be taken when considering the effects of ultrasound in crystallisation, both Chow *et al.* and Miles *et al.* have found that above certain intensities ultrasound can also cause the thawing of ice [102].

The work also shows that there tends to be a cavitation effect associated with the enhanced nucleation effect. It is not expected that there will be a direct cavitation effect due to the actuation methods used during the sonic experiments used in this investigation (see Chapter 4 for details of the sonic rig), however, the probes used in Chapter 3 are similar in nature to those used in the experiments on sonocrystallisation. Even in this case it was not expected that cavitation would occur, as the probes were driving significant masses and the peak amplitudes observed were significantly lower than the maximum obtainable amplitudes of the probes used. No bubbles were observed during the experiments on ice in Chapter 3, but it should be noted that bubbles may have formed and not been observed.

2.4.4   Mechanical Properties

There appears to be very little literature regarding the mechanical properties of sucrose. Much of the work that has been done in this area appears during the mid-nineteen-nineties. The initial work was done by Martin and Jeronomidis [103, 104] looking at sucrose and ice cream fracture toughness, and most subsequent work has been done in the main by Xu *et al.* [71, 66]. Most of the results in this investigation relating to sucrose will be based on this work, with some additional reference to unpublished sucrose adhesion data obtained experimentally by Unilever Research Group [22].

Work on the structure and properties of Water Ice by Daniel et al. [105] has shown that Water Ices are composite materials made from a lattice of ice crystals embedded in a sucrose gel matrix. The composition of this ice/sucrose matrix has a strong

bearing on the mechanical behaviour of the Water Ices. The Water Ices investigated by Daniel are very similar in composition to the sucrose solution to be studied during this thesis. Daniel found that the fracture strength and the hardness of the Water Ice increased linearly with an increasing phase volume.

Using this linear variation the fracture strength of the Water Ices can be developed, resulting in the following relationship:

$$\sigma_f = 1.01\Phi_i - 0.39 \tag{2.2}$$

The fracture strength (σ_f) has units of MPa and Φ_i is the volume fraction of ice.

$$C = \frac{E}{\Phi_i E_i} \tag{2.3}$$

C is the "connectivity" or the area of solid ice grain contact as a fraction of the total interfacial area of the two phases, i.e. ice crystals and sucrose gel. Daniel et al. [105] found the relationship between connectivity of the ice crystals and the volume fraction of the matrix to be:

$$C = \frac{k}{\Phi_m} = k\left[1 + \frac{\Phi_i}{\Phi_m}\right]; \text{ where } k \text{ is the structure factor.} \tag{2.4}$$

The structure factor was determined experimentally to be 0.0084 ± 0.0008. An expression for the Young's modulus of Water Ice could then be found as:

$$E = k\Phi_i E_i \left[1 + \frac{\Phi_i}{\Phi_m}\right] \tag{2.5}$$

In conjunction with the following relationships for the volume fractions (Φ_i & Φ_m) and the mass fractions (ψ_i & ψ_m) an estimate of the Young's Modulus of the 20% (by mass) frozen sucrose to be investigated in this thesis can be estimated.

$$\Phi_i = \frac{\rho_m \psi_i}{\rho_i \psi_m + \rho_m \psi_i} \quad \& \quad \Phi_m = \frac{\rho_i \psi_m}{\rho_i \psi_m + \rho_m \psi_i} \tag{2.6}$$

To calculate the density of the matrix the equation developed by Reiser [106] is used as follows:

$$\begin{aligned}
\rho_m = \rho_w &+ \left(a_1 C + a_2 C^2 + a_3 C^3\right) + \left(b_1 C + b_2 C^2 + b_3 C^3\right)(T - 20) \\
&+ \left(c_1 C + c_2 C^2 + c_3 C^3\right)(T - 20)^2 + \left(d_1 C + d_2 C^2\right)(T - 20)^3 \\
&+ (e_1 C)(T - 20)^4 ; \tag{2.7}
\end{aligned}$$

where ρ_w is the density of supercooled water,

$$\begin{aligned}
\rho_w = (999.83952 &+ 16.952577\,T - 7.9905127 \times 10^{-3}\,T^2 \\
&- 46.241757 \times 10^{-6}\,T^3 + 105.84601 \times 10^{-9}\,T^4 \\
&- 281.03006 \times 10^{-12}\,T^5)/(1 + 16.887236 \times 10^{-3}\,T).
\end{aligned}$$
(2.8)

The coefficients of equation 2.7 are:

$$
\begin{pmatrix}
a1 = 385.85074 & a_2 = -13.03435 & a_3 = -3.6663 \\
b1 = -0.459244 & b_2 = 7.5699 \times 10^{-2} & b_3 = 6.2667 \times 10^{-2} \\
c1 = 6.0198 \times 10^{-3} & c_2 = -1.3008 \times 10^{-3} & c_3 = -4.907 \times 10^{-4} \\
d1 = -5.110 \times 10^{-5} & d_2 = 1.580 \times 10^{-5} & e_1 = 1.986 \times 10^{-7}
\end{pmatrix}
$$

ρ_m is the density of the unfrozen matrix, T is the temperature in °C and C is the concentration of unfrozen matric at temperature T. The concentration (C) of unfrozen matrix is determined from the phase diagram of Roos and Karel [107].

As 20% sucrose was to be used for the experimentation the following values could be substituted into equations 2.5 and 2.6: $E_i = 9.23e9\,\text{Pa}$, $psi_i = 0.2$, $\psi_m = 0.8$, $\rho_i = 960\,\frac{\text{kg}}{\text{m}^3}$, $\rho_m = 1.15\,\frac{\text{kg}}{\text{m}^3}$ at $-10°$ C and $k = 0.0084$. The resulting estimation of the Young's Modulus (E) of 20% (by mass) frozen sucrose solution is $0.50 \pm 0.04\,\text{GPa}$.

Cohesive Properties of Sucrose

Little research appears to have been conducted into determining the mechanical properties of the ice/sucrose matrix. Most of the work conducted has been by Xu, Jeronomidis and Atkins [108, 66, 71]. These studies are primarily on the properties of 7% and 19% (by mass) sucrose solutions, in particular to find the Young's Modulus, Yield Strength and creep constants of the sucrose solutions.

The above mentioned works also present a limited amount of work on the Yield Strength of frozen sucrose solutions at just greater than the ductile-brittle transition strain rate of the sucrose solution under investigation. This strain rate is found to

be approximately $1.0 - 1.3 \times 10^{-2} \frac{1}{s}$ [71, 66] for 7% and 19% sucrose solutions. As the sucrose acts as a brittle material above this strain rate it is fair to assume that the Yield Strength $\simeq$ the Tensile Strength of the sucrose at strain rates greater than the transitional strain rate $\dot{\varepsilon}_c$.

The data above the transitional strain rate fell outside of the main area of research for Xu et al. However, this data has been particularly useful in this study as a direct comparison of the Yield/Failure strength of 20% sucrose at the highest strain rates examined by Xu and the lowest strain rates experienced during this study on the failure of ice.

The cohesive strength of frozen 20% sucrose solutions is shown in more detail in Section 6.2.1.

Adhesive Properties of Sucrose

No published data on the adhesive strength of frozen sucrose solutions was found in the literature. Some unpublished data were available for the shear adhesive strength of sucrose solutions of varying concentrations [22]. The part of this data which is relevant to this study is shown in Chapter 6, section 6.2.2. It should be noted that the variation of sucrose adhesion with temperature is quite different to that of poly-crystalline ice.

Where the variation of ice adhesion strength appears to vary in a broadly linear manner, the adhesion of sucrose appears to build to a peak at $\sim -35°$C as the temperature decreases to $-35°$C and then the adhesion strength falls as the temperature decreases further, until the adhesion appears to be negligible at $\sim -60°$C.

2.5   Summary

A brief description of ice and frozen sucrose solution has been presented. For each substance an outline of the mechanical properties that are relevant to this investigation has been presented.

Predictions have been made of the structures of ice and frozen sucrose solution most likely to form during the experiments of this investigation. These are based on the most relevant literature available. For ice, a polycrystalline structure is predicted, and a dendritic crystalline structure is expected for frozen sucrose solution.

Chapter 3

Initial Experiments

3.1   Introduction

The first step in this investigation was to prove the concept that ice could be removed from cooled metal surfaces using structural vibrations. As one of the aims of the project was to produce a low noise rig, ultrasonic actuation was chosen as the excitation method. This Chapter describes the initial attempts at ice removal from cooled metal surfaces, detailing the experiments that first prompted the investigation, and the following experiments that showed the feasibility of ice removal by ultrasound. Findings from the experiments are described in each section and the actions arising from each experiment are shown.

3.2   Titanium Tube

The initial concept of using ultrasound to remove ice from a cooled metal surface was formed from an experiment conducted by the Unilever Research Group at Colworth [22]. The experiment involved a titanium tube of approximately $1''$ in diameter. The tube was cooled using carbon dioxide spray on the outer surface. Cooled water was passed through the tube, whilst the tube was vibrated at $\sim 20\,\mathrm{kHz}$ using a piezo-electric transducer. When the water passed out from the tube it appeared to contain ice crystals forming a 'slush'. The tube was cooled by the use of a carbon dioxide aerosol.

Although the rig appeared to remove ice from the surface of the titanium, (or at least prevent build-up of ice), as the surface was clean when the flow of water was stopped, the mechanisms behind the ice removal were not understood. For some time the rig was dismantled and when the experiment was revisited the same results were not reproducible, because some of the equipment had been replaced with new apparatus of different specifications, for example the signal generator.

3.3 Failed Attempts at Ice Removal

The first experiments conducted were primarily tests to determine what sort of amplitudes of vibration could be achieved with basic piezo-electric transducers on readily available metal plates. Additionally, some preliminary experiments with ice layers of $< 1\,$mm formed on the plate were conducted. The thin layer was formed by adding single drops of water to the plate using a pipette. The aim was to investigate whether the amplitudes of vibration generated were sufficient to remove the ice from the plate.

3.3.1 First Rig

The expertise of the lab where this research was conducted is Non Destructive Testing. Therefore, relatively low amplitude transducers are in everyday use. The first attempts at ice removal made use of these types of transducer. The basic rigs (see Figure 3.1) were made using a piezo-electric disc (PZT-5A). The disc was glued to an aluminium plate of 1.2 mm thickness using a thin layer of superglue. The initial ultrasonic transducers were constructed in accordance with the guidelines described in the Non Destructive Testing Handbook. The excitation was produced using a Wavemaker-Duet [109] frequency generator and amplifier suitable for use with PZT. The dimensions of the plate were 100 mm squared. These dimensions were initially chosen to correspond to the dimensions of a cooling system available at Unilever Research Colworth.
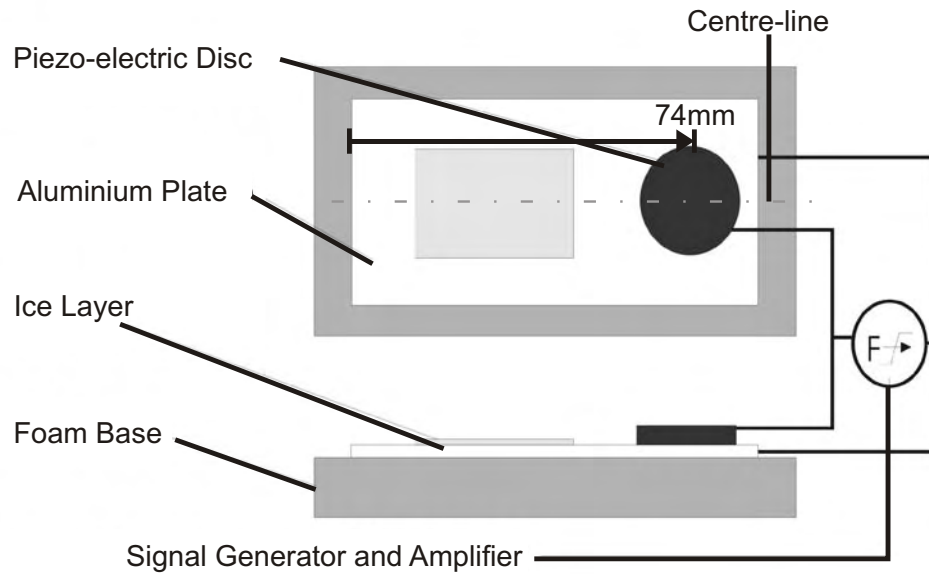
Figure 3.1: First Piezo-Electric Transducer Mounted on Aluminium Plate; Top and Side View

The PZT disc was 10 mm in diameter, and had a thickness of 10 mm (two 5 mm discs bonded together). Assuming that, at resonance, half a wavelength is set up in the thickness of the PZT, the centre frequency of the transducer could be calculated as 215 kHz. It would be desirable to find a flexural mode of vibration within the 50% bandwidth of the transducer, where the transducer could be placed near one edge of the plate, leaving the remainder of the plate for ice formation.

Using a Finite Element model (details will be described in Section 5.2.3) an Eigenvalue solution for the plate was performed in the frequency range 107.5 kHz to 322.5 kHz. A flexural mode was predicted at 147.2 kHz which had a displacement anti-node at 74 mm from one edge of the plate on the centre line of the plate, as shown in Figure 3.1. The mode was confirmed by noting expected node and anti-node locations and checking them experimentally, using the laser vibrometer. This mode also appeared to give several displacement nodes and anti-nodes over the area where ice was to be formed, providing a good opportunity to observe whether ice

could be removed. The PZT disc was duely placed with the centre of the disc at the location described above. The response of the system was measured using the equipment and method mentioned below.

The amplitude of response of the system was measured by scanning a Polytec [110] laser vibrometer along the centre line of the plate, including the location of the piezo-electric disc. The laser comprised a OFV-3001 controller and and OFV-511 sensor head. The laser was capable of both velocity and displacement measurements for out of plane measurements and velocity measurement for in-plane motions. For the purposes of this experiment, out of plane measurements were taken using the displacement function. The amplitudes of vibration were very small. The system was scanned over a range of frequencies in the range of 140 kHz to 160 kHz. The maximum peak to peak amplitudes that were detected were recorded and a maximum of 48 nm was recorded at a frequency of 149 kHz. The comparison between the model and experimental data will be shown in Section 5.2.3.

Ice was formed onto the plate using an aerosol can of liquid CO_2 to freeze the plate and then thin layers of refrigerated water were added using a syringe. Using this method there was some difficulty in producing even layers of ice as water was added drop by drop. However, when ice was formed on the plate the vibrations produced were unable to remove even the thinnest layer of ice at < 0.5 mm.

3.3.2 Improved Rig

In order to produce more motion in the area of the plate where the ice was being formed, the design of the transducer was changed to give a narrower bandwidth. This change was achieved by using a mass backing rigidly attached to the piezo-electric disc. The aim was to choose a frequency of operation and then to design the dimensions of the transducer to give half of a wavelength within the body of the transducer. The relationship $\lambda = \frac{c}{f}$ was used to calculate the wavelength for a given frequency in the backing material.
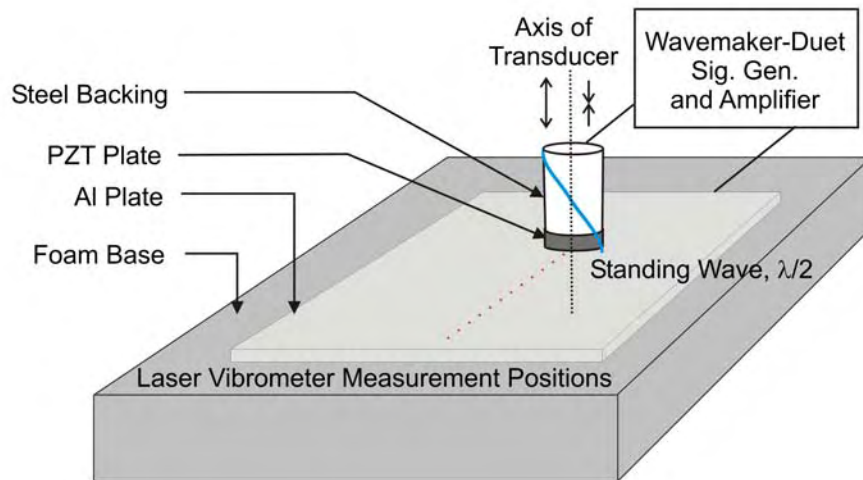
Figure 3.2: Schematic of Improved Rig Using Mass Backing to Create a Narrow Bandwidth Transuducer

A new PZT disc of diameter 10 mm and thickness 1 mm was glued to a steel cylinder of 10 mm diameter using a thin layer of superglue. Using a plate of the same dimensions as the previous rig a flexural mode could be found at 95.8 kHz, (from the same finite element model as described in Section 5.2.4), where a displacement anti-node was found at approximately the same location as with the previous rig.

Assuming that a standing wave of half a wavelength could be produced in the backing and transducer, a suitable length for the mass backing was ~ 30 mm. This length was then altered slightly in conjunction with experiments to try and match the frequency of the transducer to the expected flexural resonant frequency (from modelling) of the plate at around 95.8 kHz. The basic setup of this transducer is shown in Figure 3.2. In practice the mode produced may differ from the predicted mode as the PZT layer was thin compared to the steel mass backing layer. Therefore, the first longitudinal mode of the whole transducer and the first longitudinal mode of the mass backing are likely to be closely spaced in the frequency domain. Care was required when experimenting to avoid destructive interference between the two modes.

By scanning the system a resonance was discovered at 95.1 kHz, agreeing well with the predicted resonance of both the plate and the transducer. Using this setup (and frequency) a significant increase in the amplitudes of the transducer and plate were achieved. At 95.1 kHz peak to peak amplitudes of 110 nm in the body of the plate and 120 nm at the center of the transducer were measured. This represents an increase of a factor of two compared with the values obtained using the initial experiments with an unbacked transducer. Velocities were measured using a laser vibrometer, taking out of plane readings at various points along the centre line of the aluminium plate from the edge of the transducer as shown in Figure 3.2.

However, even with these increases in amplitude the rig was still unable to remove ice from the cooled surface. With this in mind it was necessary to find a method of transduction that was capable of producing greatly enhanced amplitudes of vibration. Various other modes of the system were identified over a range of frequencies, however, none proved to be effective in ice removal. Lesser amplitudes of vibration were found with these other resonances.

3.4   Branson Probe on Small Plate

The experiments outlined in Section 3.3 had failed to remove ice from the plates which were tested. As bending stresses were expected to be important in removing the ice from the plate, attention was focused on maximising the amplitude of out of plane vibration. To try to produce greater amplitudes of vibration, and therefore greater stress levels in the plate and ice, several steps were taken:

1. A commercial high-power resonant device, operating at dedicated frequency, was used to actuate the system (as described below).

2. Plates of 0.5 to 0.8 mm were used, rather than the plates of 1.2 mm that had been used in the experiments of Section 3.3.

The Branson probe [111] is an ultrasonic device used to degas liquids in chemical processing. The transducer design is a stack of thin piezo-electric discs held in compression by a 20 UNF bolt running through the centre of the stack. The amplitude of the transducer is enhanced by an ultrasonic horn attached to the 20 UNF bolt at one end of the transducer. The design is similar to that of an ultrasonic welder, but the tip is substituted by a replaceable, flat titanium tip of $\frac{1}{2}''$ diameter, suitable for causing cavitation in liquid media.

The unit can be purchased off the shelf, and it produces high amplitudes in the range of $40 - 120\,\mu$m (with a free tip) , over a narrow frequency range of $19.5 - 20.5\,$kHz [111]. The use of the Branson Probe as the actuation device represented an increase in expected amplitudes of $3 - 4$ orders of magnitude when compared to the previous experiments that had been conducted.

3.4.1   Description of Experiment

Figures 3.3 and 3.4(b) show the layout of the Branson Probe experiments. An aluminium cooling plate linked to a Haakë DC10 [112] cooling bath by lagged silicon rubber tubing was the cooling method used to produce ice for these experiments. The minimum temperature achievable using this setup was -30°C at the aluminium cooling plate. A thin steel plate $\sim 0.8\,$mm thick was the vehicle for ice formation. The plate had dimensions of $84\,$mm by $44\,$mm. This size was chosen in order to be used in conjunction with a cooling plate fabricated by Unilever, (to replicate an existing design used by themselves), while still giving a flexural mode in the correct frequency range to use with the Branson Probe and the integrated amplifier. A description of the finite element model, which was used to identify these optimum dimensions, can be seen in Section 5.2.5.

The steel plate had four holes drilled in it, corresponding to the corners of the aluminium cooling plate, which had an M2 stud glued at each corner. The locations of the holes are detailed in Section 5.2.5. Vaseline was smeared around the edges of the aluminium cooling plate to a height of $\sim 1.5 - 2.0$mm and the resulting
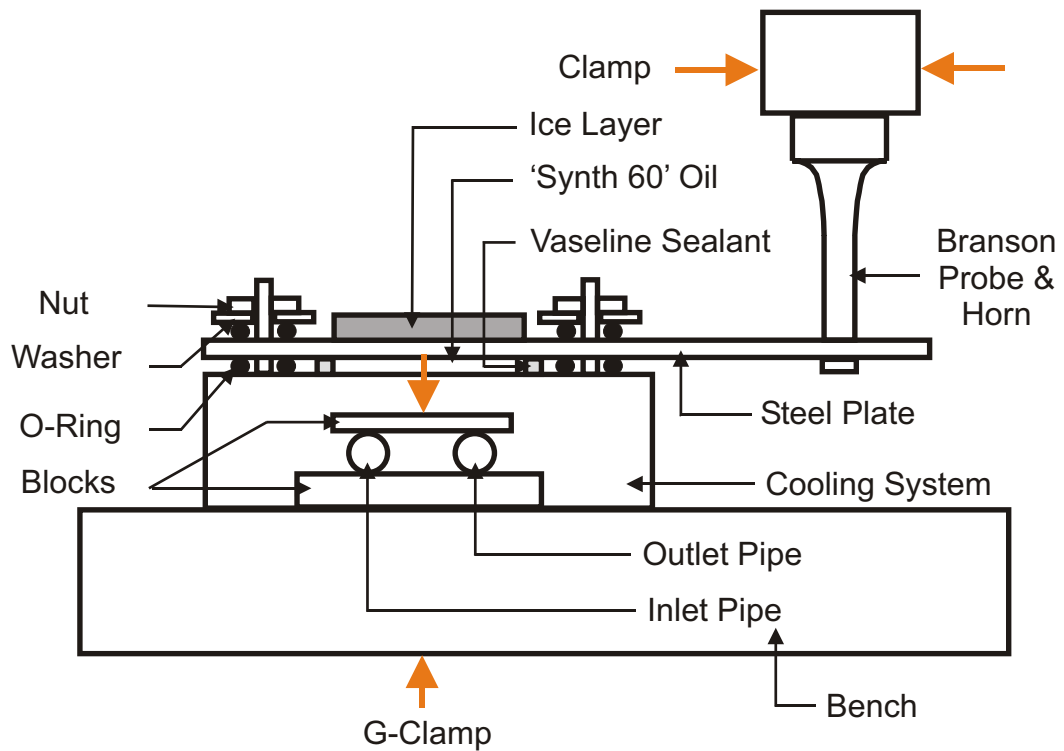
Figure 3.3: Schematic Layout of the Branson Probe Experiments.

reservoir was filled with synthetic silicon oil 'Synth-60' [113] which retains similar heat transfer properties between $-50°C$ and $54°C$. The steel plate was separated from the aluminium cooling plate by a $1.6\,mm$ thick $3.0\,mm$ diameter rubber O-ring over each stud. The plate was located by loosely fitting M2 nuts on top of further o-rings, placed on the steel plate. The attachments were more to position rather than to constrain the plate, as such the nuts were only fastened to finger tightness. The experimental setup can be seen in Figure 3.4, (it should be noted that the probe is shown uncoupled in these photographs).

A fifth hole was drilled at the rear of the steel plate, which protruded from the end of the aluminium cooling plate. The titanium tip was removed by unscrewing it from the end of the horn of the Branson Probe. The tip was then reattached, sandwiching the steel plate between the tip and the horn. Thus, the Branson Probe was attached normal to the steel plate. Both the aluminium cooling plate and the Branson Probe were supported using clamps to maintain the correct alignment during excitation.
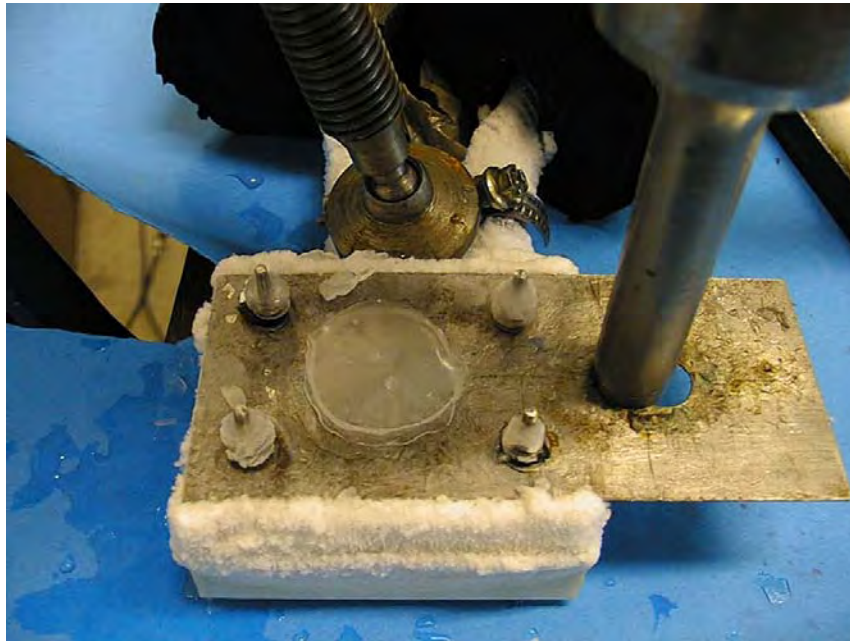
(a) Ice Layer Formed On Steel Plate Before Branson Probe Switched On.
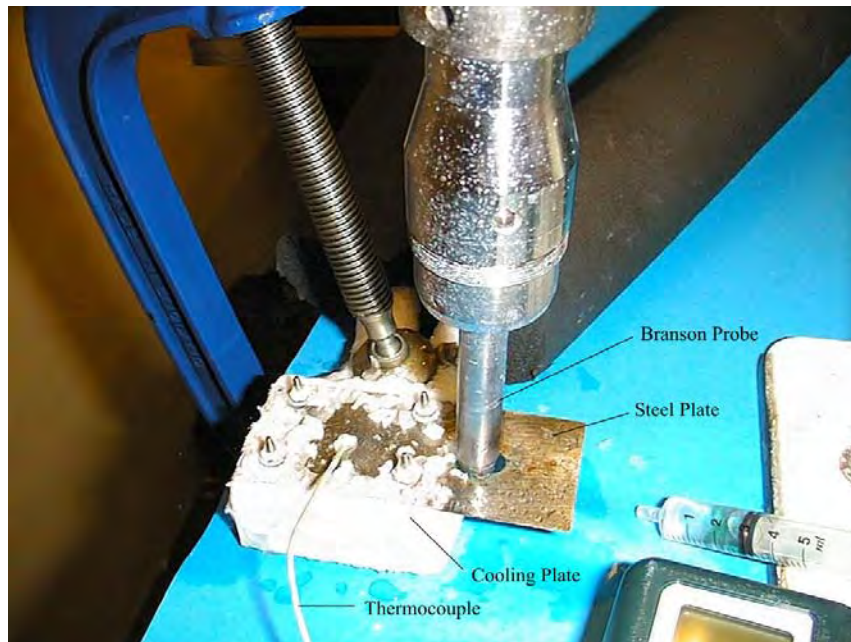
(b) After Branson Probe Switched on only Broken Ice Remains on the Steel Plate.

Figure 3.4: Photographs showing the effects of Ultrasound on an Ice Layer formed on a Cooled Metal Surface. (Before and after shots not from same experiment).

After some experiments were conducted it was found that the arrangement caused considerable heat build-up in the steel plate. During these experiments the ice tended to melt so it was unclear whether the Branson Probe was removing the ice or melting was occurring. By uncoupling the tip of the transducer from the plate this effect was significantly, (but not totally), reduced. The tip was unscrewed from the steel plate and was rested on the top surface of the plate. A small amount of downwards pressure was applied by adjusting the clamp that was supporting the Branson probe, which seemed to largely maintain contact between the tip of the probe and the plate. Some undesirable ringing at $4\,\mathrm{kHz}$ was observed (probably due to a rocking motion between the free tip and the plate), but the flexural mode shape in the plate was not affected significantly.

The temperature at the interface between the ice and the steel plate was measured using a thermocouple, which was glued into place on the steel plate. It has already been seen in Chapter 2 that the adhesive and cohesive properties of ice vary with the temperature of the ice. Therefore, it seemed that recording the temperature during the experiments might yield some information enabling more to be discovered about the mechanisms behind ice removal.

The ice was formed on to the plate as follows. A small blu-tack ring was located on the steel plate. Water or sucrose was then added slowly to the plate using a syringe. Once the ice appeared to have frozen, the blu-tack ring was carefully peeled away, leaving the ice on the plate. Care was taken to ensure the ice was fully frozen before the blu-tack was removed. The temperature of the ice was then monitored. When the desired temperature was reached, say $-6°\mathrm{C}$ or $-12°\mathrm{C}$, the Branson Probe was switched on. The same method was used in each experiment to try to achieve a similar ice structure in each occasion.

3.4.2   Findings From Experiment

Ice Water

The Branson Probe has a range of power settings, i.e. 10%, 20%, 30% $\cdots$ 100%, controlled digitally by the integrated amplifier. There is also a range of duty cycles similarly arranged in terms of percentages. The experiments involved cooling the ice until certain temperatures were reached, for example -6°C, -12°C and -18°C. The adhesion strength of ice varies over these temperatures and it was hoped that some indication of this would become obvious by the power level required to remove the ice layer from the cooled metal surface. In ice the shear adhesion strength varies from $\sim$ 700 to 580 kPa over the same temperature range, however, there is significant scatter relating to this data of typically ±150 kPa [22, 73]. The tensile strength of water ice also varies with temperature as shown by several authors, but tends to be around a factor of two greater than the values displayed for shear adhesion [35, 36, 37].

Ice layers from $1-5$ mm thick were produced and tested at each temperature. However, at each thickness and temperature combination the ice was removed at the lowest power setting, and also the choice of duty cycle appeared to have no effect on the ice removal. In each case the ice was violently removed from the plate. In some cases the broken ice was thrown a considerable distance from the experiment. The ice was fractured too quickly for any discernable detailed effects to be observed by eye.

Sucrose Ice

Rather than using water to freeze on the plate, sucrose solution was applied to the plate in the same manner as the water ice experiments. Sucrose of varying concentrations between 10% and 20% (by mass) was investigated. Once frozen the sucrose formed an opaque white solid. The sucrose was formed in blu-tack rings as before; some care had to be taken when removing the sucrose rings to maintain the integrity of the sample at the higher temperatures and higher sucrose concentrations. At

temperatures within $0.5 - 1.0$°C of the freezing point of the sucrose (see Table 2.1) the sucrose appeared to be like a gel, whereas the ice had almost immediately become solid on passing the freezing point (i.e. < 0°C).

During the experiments the sucrose of each concentration was formed with varying thicknesses of $1 - 5$ mm. The sucrose ice was removed in all conditions that were tested. Unlike the water ice experiments the sucrose was not thrown far from the experiment, but instead, the sucrose ice apparently remained as one body on the plate, but slowly moved from the original location following any small slope on the plate. No residue appeared to remain after the sucrose ice was removed, but ice formed within fractions of a second from the atmosphere so close inspection was rendered very difficult. Additionally, such residue might consist of only a single layer of crystals which would be difficult to view by eye.

3.4.3 Estimated Axial Stresses

From these experiments it was possible to qualitatively determine that the ice had been removed from the cooled metal surface. In the water ice experiments it could be seen that the ice failed cohesively, and then appeared to fail in adhesion at the ice metal interface, i.e. cracks were first seen normal to the plane of the plate and the ice initially remained on the plate, after a short time the ice was removed from the plate in "chunks". In the sucrose ice experiments it appeared that the adhesive strength was overcome.

Observations from Water Ice Experiments

The ice is removed from the plate violently. Small chunks of ice are seen after the experiment, implying that the cohesive strength of the ice had been overcome. Additionally little or no residue appears to be left on the plate after the experiments, which suggests that the adhesive strength of the bond between the ice and steel had also been overcome.

As the ice is removed so quickly, the order of failure, i.e. cohesive then adhesive or vice versa, is not discernable from the experiment as it stands. However, the basic

Finite Element model, described in Section 5.2.5 will allow a rough estimate of the maximum axial stress experienced in the ice.

Observations from Sucrose Ice Experiments

As mentioned above in Section 3.4.2, the removal of frozen sucrose from the plate was not as clear cut as that of water ice. Therefore, it is harder to draw conclusions about the mechanisms behind ice removal in these experiments. It appears that the adhesion in between the sucrose and the plate is overcome, as the sucrose moves along the surface of the plate while the ultrasound is applied to the plate. However, the sucrose appears to move as one body and no cracks could be observed in the sucrose, probably due to the opaque nature of the solid. It was not possible to determine whether the cohesive strength of the ice had been overcome from the results of these experiments.

Finite Element Scaling Process

A laser vibrometer is used to measure the out of plane vibrations at various points on the steel plate, particularly in the region where the ice is formed: as this is where the stresses of most interest in determining the ice removal mechanisms occur. Using the Finite Element model mentioned above, relative values for the stresses in the system and also relative displacements at various positions can be extracted by producing an Eigenvalue solution. As the Eigenvalue solution only produces the shape of a mode and not "expected" amplitudes of vibration, the Eigenvalue shapes must be scaled to actual amplitudes.

One wishes to know something about the stress levels where the ice is attached to the plate. However, the only known value is the physical displacement in the Z-direction (see Figure 3.5(a)) from the results of the laser vibrometer scan along the Y-axis. By comparing the experimental displacements with the relative displacements from the Finite Element model, a suitable scaling parameter can be chosen if the two sets of results agree with each other, i.e. if the scaled Eigenvalue mode

shape corresponds well with the measured mode shape.

Figure 3.5(b) shows that a good agreement can be reached. The scaling factor obtained can then be used to scale the relative stresses from the Eigenvalue solution from the Finite Element model. The axial stress (σ_{YY}) obtained from this method is illustrated in Figure 3.6. Confidence in these values of stress was obtained by the good agreement between the experimental Z-displacements and the Z-displacements of the scaled Finite Element model .

Estimates of Axial Stress: σ_{YY}

An estimate of the axial stresses (defined in Figure 3.5(a)) produced within the steel plate can be obtained from the Eigenvalue solution to the model of the steel plate (see section 5.2.5). The amplitude of vibration of the Branson probe was measured to be $18.6\,\mu\mathrm{m}$ at the lowest setting (10%). (This value was determined by focusing the laser on the probe tip while it was attached to the plate with no ice layer present, at the minimum). It should be noted that $120\,\mathrm{nm}$ had been recorded as the maximum displacement for the PZT transducer arrangement, i.e. the amplitude has increased by around two orders of magnitude.

From the Finite Element model, a listing of "out of plane" displacement and stresses in various directions can be extracted. Figure 3.5(b) shows the comparison between the relative amplitudes from the Finite Element model and the "out of plane" amplitudes determined experimentally, using the laser vibrometer. As this shows good agreement, the value of $18.6\,\mu\mathrm{m}$, at the probe tip, can be used to scale the stresses obtained from the finite element model. This method indicates the maximum stress generated within the steel plate is $263\,\mathrm{MPa}$. It should be noted that this stress level was experienced in the steel part of the system and not the ice layer - or a change in the phase of ice may have been expected; due to elevated pressure levels.

The amplitudes from the experimental setup are shown in figure 3.5(b), compared with the scaled values taken from the Eigenvalue solution shown in section 5.2.5.
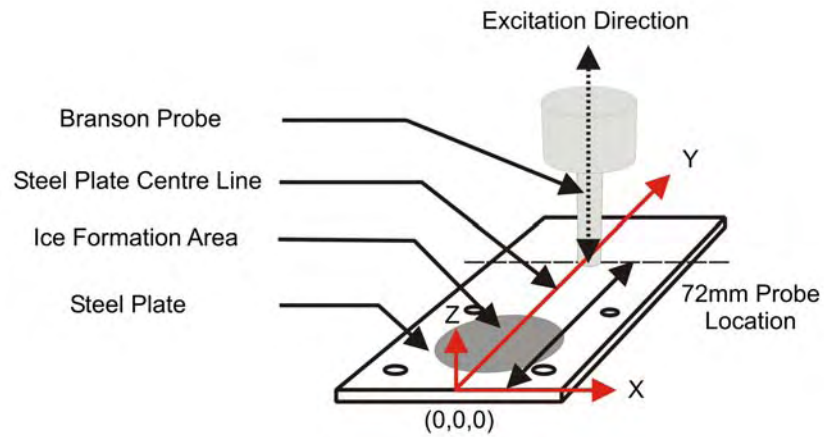
(a) Layout of Branson Probe experiment on small steel plate, showing placement of axes.
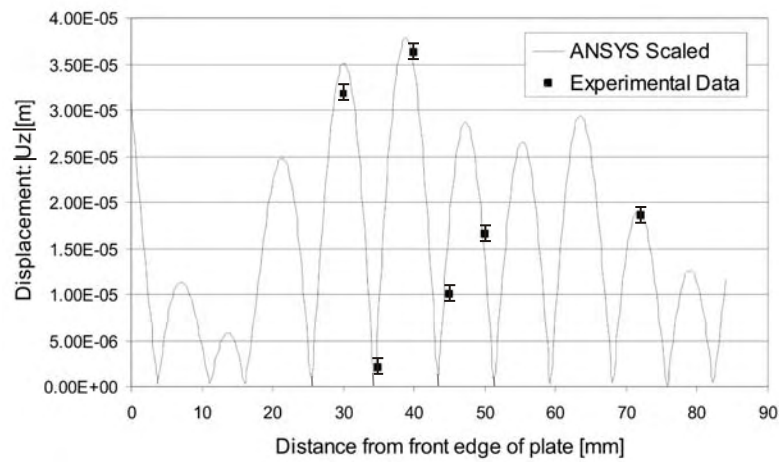
(b) Comparison between the predicted mode shape (from Finite Element model) and the measured mode shape: absolute values in Z-direction, positions taken along Y-axis of the plate.

Figure 3.5: Location of axes and comparison of Finite Element model to experimentally determined amplitudes of vibration.

The experiment was conducted with no ice present on the plate, so as to obtain good readings from the laser vibrometer.

When a thin ice layer (say $\sim 1\,\text{mm}$) was formed on the plate and the power input was set to 10%, i.e. the minimum setting, then the ice appeared to be removed immediately. Therefore, no lower limit for the stress required to remove the ice from the plate could be determined directly from these experiments. However, if we assume that the ice remained attached until just before these stresses were reached (as predicted from the clear plate - $263\,\text{MPa}$), and that the amplitudes of vibration were not greatly affected by the presence of the thin layer of ice, we can estimate the maximum possible bending stresses experienced by the ice layer.

This would give a stress level of $12.2\,\text{MPa}$ at the interface, in the ice layer. This value is, as expected, much greater than the stress levels required for ice to be fractured, see Section 6.2. The variation of the stress experienced by the plate is shown in Figure 3.6, and values in the ice are estimated by comparison of the Young's modulus of each of the two materials.

These results give a rough estimate of the stresses in the system, as the physical effects of the ice on frequency and damping have not been considered. However, the main reason for these estimates is to determine by how much the stresses in the ice might be greater than those required to fracture the ice. As such the stresses generated within this system appear to greatly exceed those required for fracture of frozen sucrose solution and also exceed those required to fracture water ice.

3.4.4 Problems with the Branson Probe Method

Although the Branson Probe experiments show ice removal at ultrasonic frequencies is possible, they are not ideal to use as a basis for determining the mechanisms behind ice removal. Several problems associated with the experiments are discussed below:

  – Excessive heating from the transducer. The Branson Probe is designed for
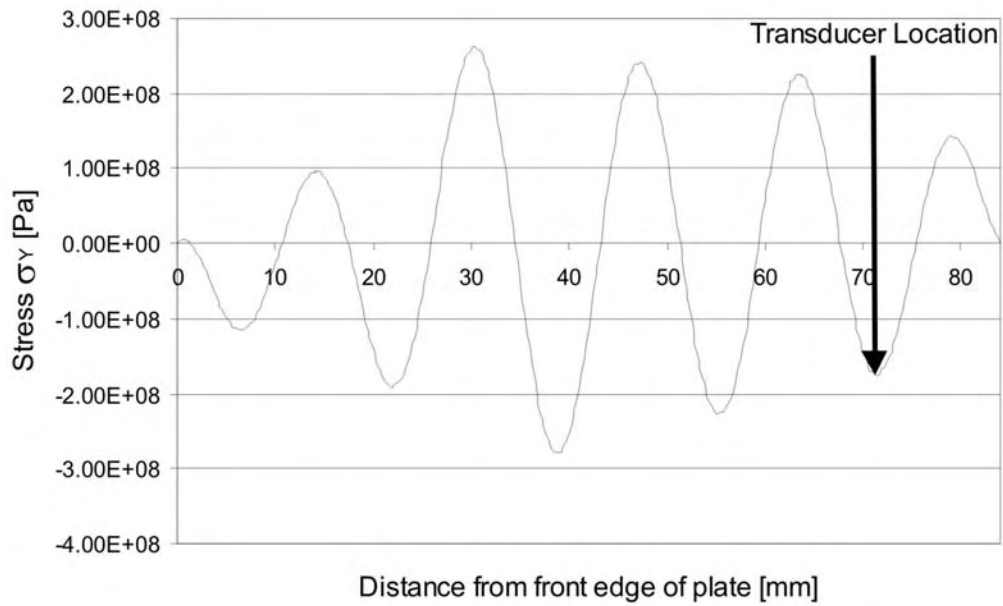
Figure 3.6: Estimation of longitudinal stress variation along the Y-axis of the plate (see Figure 3.5(a)): based on scaled Eigenvalue solutions for the Branson probe setup.

processing of flowing liquids. When used in air in contact with a metal plate it appears that friction occurs between the tip of the probe and the plate. Temperatures of $50 - 60°$C were observed near the tip of the probe during extended periods of operation. This could lead to melting of the ice in extreme cases or in adverse temperature variations in the investigation area in "normal" experiments. Additionally hysteretic heating in the horn of the transducer itself could cause a problem via conduction from the transducer to the plate.

— Low tunability of the Branson Probe amplifier. Limits of ice removal could not be detected due to the high minimum amplitudes exhibited by the transducer even at minimum power settings.

— Non-silent system due to the ringing at $4\,$kHz between the horn, tip and steel plate. The experiment proved to be very noisy and ear defenders had to be worn to protect the ears of the experimenter.

— Complicated redesign of the experimental rig might be required due to the low bandwidth of the digital amplifier. If the resonant frequency of the total system falls outside the frequency range $19.5 - 20.5$kHz then the amplifier does

not drive the transducer at all. This could be caused by either:

- – Altering the dimensions of the system slightly could cause the overall natural frequency to change sufficiently to move from the range 19.5 − 20.5kHz.

- – If the mass of the experimental system was too great, then the behaviour of the horn could be altered adversely and the amplifier would not be powerful enough to drive the system.

- Fatigue in the steel plate caused by the attachment of the horn to the steel plate. The plates tended to fail within fifteen to twenty minutes of continuous operation. Cracks formed at the hole drilled to accommodate the tip and horn of the Branson Probe.

- The rubber o-rings used to locate the steel plate on the aluminium cooling plate also fatigue over time. This is soon seen as nibbling occurs in the o-rings, shortly followed by failure of the o-rings. The rig therefore has to be frequently repaired to allow continued experimentation.

- Fully representative modelling of the system might prove to be complicated due to the interaction between the o-rings, silicon oil and the steel plate.

- Measurement of the parameters of the system with ice attached cannot be achieved using the current laser vibrometer setup.

3.5   Etrema Probe on Small Plate

From the experiments using the Branson Probe it was seen that the amplitudes of vibration were too large to determine a limit of ice removal, even at the lowest settings of the amplifier. To achieve a similar system design but with improved controllability a different transducer and amplifier setup was employed. The type of transducer used was an Etrema AU − 008G300 magnetostrictive device [114]. This transducer could operate over a significant range of frequencies. The limit of displacement for the transducer is $\sim 21\,\mu$m peak to peak, with an applied DC voltage,

7.5 Amps gives $\sim 10.5\,\mu$m and -7.5 Amps gives $\sim -10.5\,\mu$m displacement [114].

The Etrema Probe in air had a peak to peak tip displacement of $1.32 \pm 0.05\,\mu$m at 20 kHz; this displacement was measured using a laser vibrometer focused on the tip of the transducer normal to the direction of motion. A maximum displacement of $\sim 21\,\mu$m (peak-peak) is claimed for this transducer type. However, this requires a burst input of 1 kW and only a continuous input source of ~ 200 W was available. The signal was generated using a Solartron 4431 signal generator and was amplified using an ENI 240L amplifier and also a T&C Power Conversions Inc. AG1021 amplifier. Section 5.2.5 shows the predicted mode shape for the plate at a frequency of 20.3 kHz.

3.5.1 In-line Layout

As the Branson probe had a large amplitude of vibration, a small misalignment to the vertical might have led to a significant longitudinal excitation. For example a 3° angle to the vertical might produce to a $1.1\,\mu$m peak to peak vibration in the horizontal plane - based on an $18.6\,\mu$m vertical vibration peak to peak amplitude.

This amplitude of vibration was significant compared with the amplitude of vibration of the Etrema Probe. Therefore, to determine whether the "in plane" vibrations might be responsible for the ice removal, the Etrema Probe was attached to the plate as shown in Figure 3.7. However, it appeared that this was not the case as these experiments were found to be ineffective at ice removal at the maximum amplitude which could be achieved using the Etrema Probe.

3.5.2 Transverse Layout

In the transverse arrangement of the system, the transducer was aligned perpendicular to the small plate in the same manner as the Branson probe experiments. The location of the transducer was at 70 mm from the end of the plate and on the
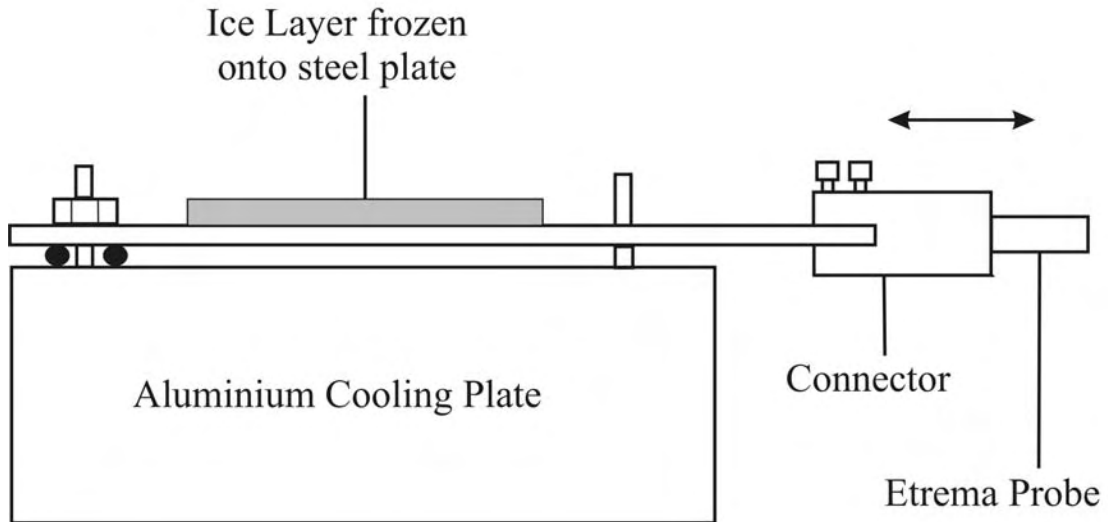
Figure 3.7: Schematic Diagram of the Etrema Probe Longitudinally Exciting a Cooled Steel Plate.

lengthwise centre line of the small plate. This was to coincide with the position of maximum displacement in the out of plane direction of the plate. The maximum tip displacement for the transducer was $0.58 \pm 0.01 \, \mu$m when the system was loaded as shown in Figure 3.8. The amplitudes of vibration in the transducer and plate are shown in terms of the absolute values in Figure 3.9(b).

The experiments were conducted in the same fashion as those for the similar Branson probe experiments. Experiments were conducted over the same temperature range and the amplitude of vibration was also varied. The operational frequency of the system was 20.2 kHz to give the same mode of vibration as that displayed by the Branson probe experiments. This frequency was partially dictated by the amplifier and transducer. The first resonance of the transducer is at 15 kHz and hence the ideal operating frequency would be at 15 kHz. However, the second appears at around 20 kHz and as the ENI amplifier has a lower limiting frequency of approximately 19 kHz this is the first resonance that can be excited with any success.

In most cases the experiments appeared to be ineffective. However, in some of the experiments small cracks appeared in the ice, they were aligned parallel to the short edge of the plate. Even in these cases the ice was not fully removed from the surface

of the plate. This was particularly the case in the sucrose ice experiments, where the tensile strengths and shear adhesion strengths are generally lower than those for water ice in the same temperature range $((-1) - (-20)°\text{C})$. However, the experiments show that the Etrema probe might produce amplitudes that are on the limit of removing the ice. A calculation was performed, which showed the experimental amplitudes did not induce stresses at a high enough level to remove the ice from the plate - see following sections.

3.5.3   Estimating the Axial Stresses: σ_{YY}

The axial stresses produced in the steel plate as modelled in section 5.2.5 indicate that the stresses due to bending in the steel are $8.2\,\text{MPa}$ at the maximum amplitudes of the transducer (i.e. $\sigma_{YY}^{\text{In Plate}} = 8.2\,\text{MPa}$, see Figure 3.9(a) for a definition of the axes used for modelling purposes). Although the model does not directly include the ice layer, an estimate of the order of magnitude of the stresses in the ice can be obtained (see Chapter 5). The scaling process used to obtain these stress levels is outlined in section 3.4.3.

Discussion of Stress Levels

We know that the ice remains attached to the plate during the experiments in most cases during the Etrema Probe experiments. Therefore, if we assume that a thin layer of ice has little effect on the amplitudes of motion of the system under ultrasonic excitation, an estimate of the stress in the ice at the interface can be made.

If the ice remains attached it will take the same shape as the steel plate. Hence, the in-plane strain experienced by a thin layer of ice would be the same as that experienced by the steel plate on the other side of the interface. To make a simple estimate of the strain we can use the expression, $\sigma = \varepsilon\text{E}$ (this simplification can be used as the axial stress is significantly greater than the stress in other directions), where σ is the stress, ε is the strain and E is the Young's modulus of the material in question. As σ_{YY}^{Steel} is known and the strain is comparable for both the steel plate
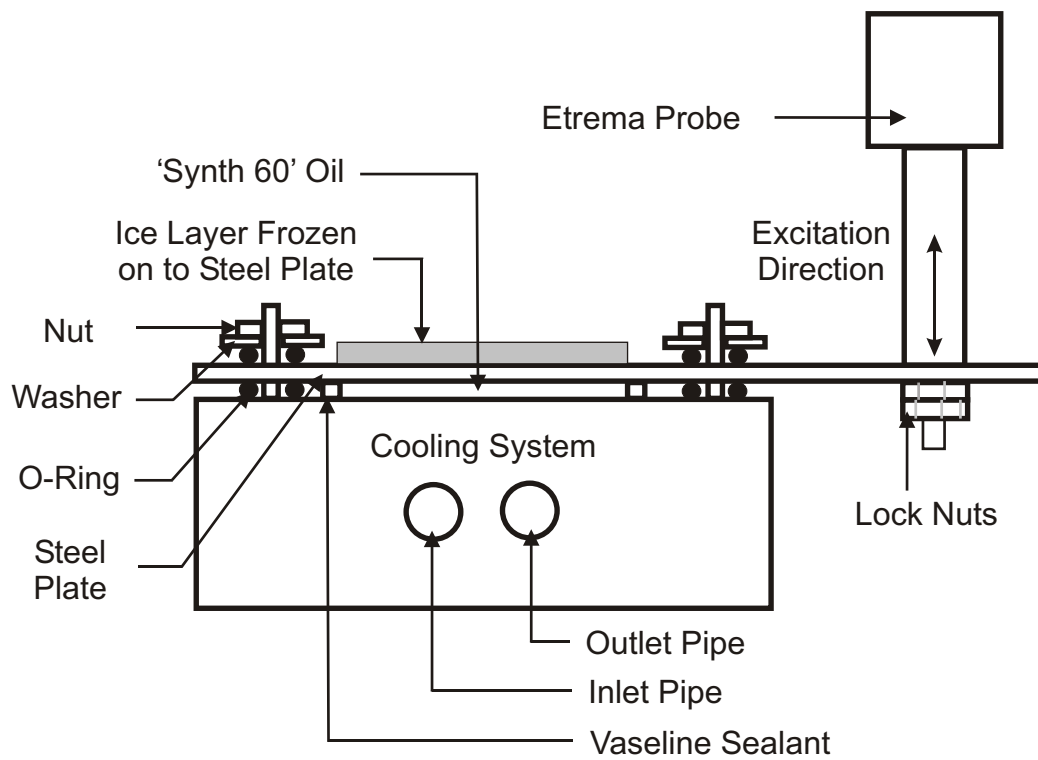
Figure 3.8: Schematic diagram of the Etrema probe exciting a cooled steel plate, with excitation perpendicular to the plane of the plate.
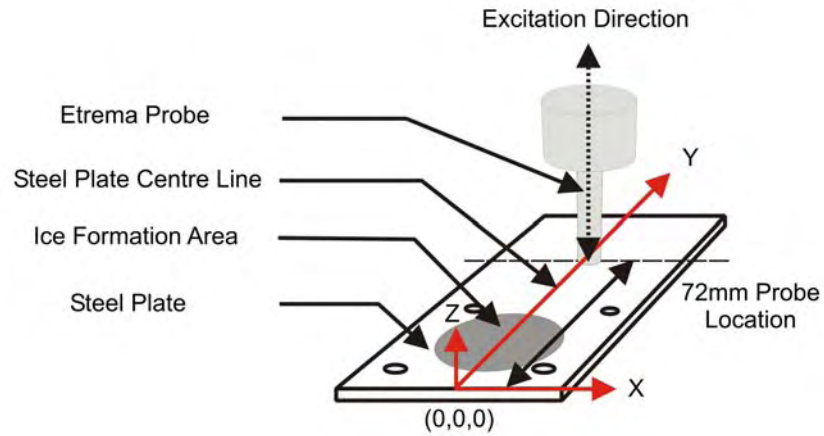
(a) Layout of Etrema Probe flexural experiment on small steel plate, showing placement of axes.
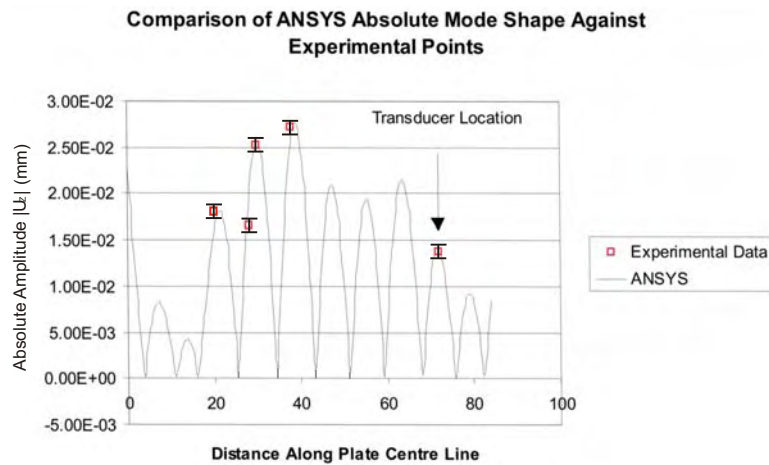
(b) Comparison between the predicted mode shape (from Finite Element model) and the measured mode shape: absolute values in Z-direction. Positions taken along Y-axis of the plate (see Figure 3.9(a)).

Figure 3.9: Location of axes and comparison of Finite Element model output to experimentally determined amplitudes from Etrema Probe experiments.
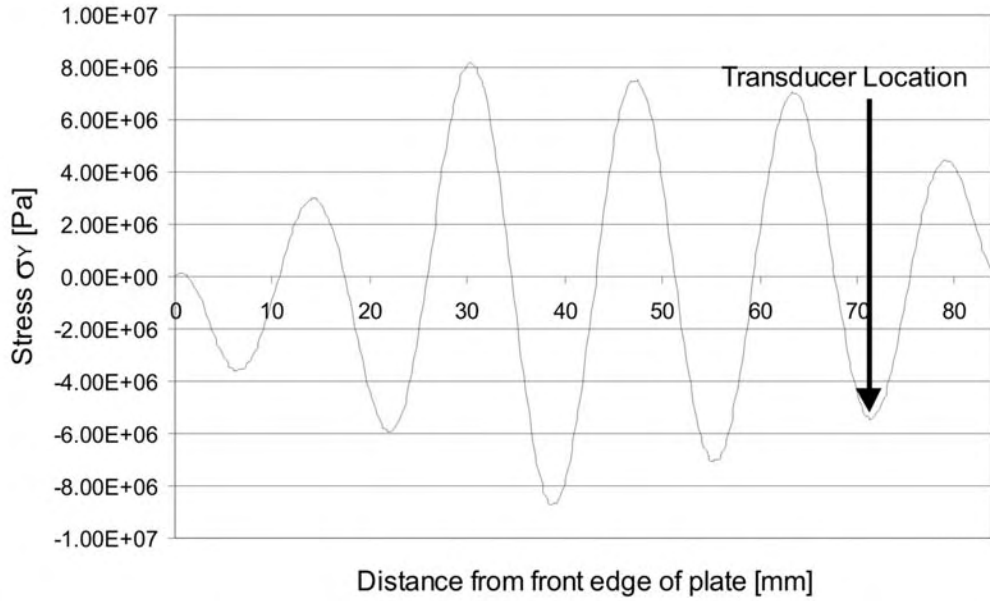
Figure 3.10: Estimation of longitudinal stress variation based on scaled Eigenvalue solutions for the Etrema probe setup. The probe is positioned on Y-axis (see Figure 3.9(a)).

and the ice layer (assumed), an estimate of σ_{YY}^{Ice} can be made using the relationship:

$$\sigma_{YY}^{Ice} = \sigma_{YY}^{Steel} \frac{E_{Ice}}{E_{Steel}} \tag{3.1}$$

By comparing the Young's moduli of the water ice or sucrose/ice and the steel, a rough estimate of the stresses experienced in the ice can be obtained. Gold [115] predicts that crack nucleation will occur at stresses of ~ 0.48 MPa in water ice in the temperature range and ice crystal sizes considered by these experiments.

The estimate of the peak axial stress (σ_{YY}) is 0.38 MPa, obtained from the finite element model, although due to modelling imperfections and variations in the mechanical properties of the ice, significant error might be associated with this value. (Based on E_{steel}, ~ 200 GPa [116] and E_{ice}, ~ 93.2 GPa [26], this ratio will vary slightly with the ice temperature, but should be good enough for a rough estimate.)

The values obtained by Gold and from the experiment are close enough together to suggest that the rig is producing stress levels of the correct magnitude to cause cracks to nucleate in the ice layer. In some experiments cracks were observed in the ice layer, but this was not repeatable and ice was not removed from the steel plate

in any of the experiments.

Ice Inhibition

As the method seemed to be on the limit of fracturing the ice it appeared to be worth conducting some additional experiments. It had been shown so far that the ice could not be removed from the plate. Instead, an experiment, using the same setup, was devised to see if ultrasound could be used to keep the steel plate free of ice buildup.

To achieve this some liquid was to be added to the plate with the ultrasound "turned on". The temperature of the plate was then monitored as time increased, the temperature was decreasing with time. At the point when ice could be observed forming on the plate the temperature displayed by the thermocouple meter was recorded. In order to avoid the liquid running off the plate, and to enhance the visibility of ice forming on the plate, only a very small sample of water, (i.e. a few drops), was used.

The temperature for freezing to occur in solutions with differing levels of sucrose content can be estimated using the formula [94]:

$$\Delta T = k_f.m \qquad\qquad (3.2)$$

Where:

m $=$ molarity of solution

k$_f$ $=$ molal freezing point depression point for solvent.

As seen in section 2.4.2 the value of k_f for water as the solvent is taken as 1.86[°/mole] and obviously the molarity of the solution varies with the concentration by mass of the sucrose in solution.

As a control for the experiment the predicted values can be compared to experimental results where the ice is formed on the plate without the ultrasound being applied to the plate. The results for these experiments can be seen in Table 3.1.

There is some variation in the temperatures observed in the control and the predicted values, however, this could be attributed to slight variations in the concentrations of the sucrose solution and also due to the positioning of the thermocouple, slightly removed from the surface of the steel plate to avoid additional thermocouple effects arising from an interaction between the steel plate and the tip of the thermocouple. The error bars shown are for the data-logger, errors of similar magnitude but slightly lower were observed over the five experiments per point. More experiments would be require to obtain a proper calculation of the standard deviation.

Conc. [%, by mass]	Analytical F. P. [°C]	(i). Control F.P. [°C]	(ii). US on FP [°C]
0.0	0.0	-0.10 ± 0.05	-0.35 ± 0.05
10.0	-0.604	-0.65 ± 0.05	-0.80 ± 0.05
12.5	-0.776	-0.79 ± 0.05	-0.89 ± 0.05
20.0	-1.358	-1.40 ± 0.05	-1.60 ± 0.05

Table 3.1: Variation of freezing point depression with sucrose concentration, analytical and experimental comparison, [(i).control: with ultrasound not applied & (ii). with ultrasound applied].

It can be seen from these results that the formation of ice appears to be retarded using ultrasound. In the presence of ultrasound the temperature where ice is observed to form is lower than in the control case where ice is observed to form close to the predicted value. This may be of interest in frozen food production, where the texture of the ice is very important. Being able to inhibit the formation of ice crystals may enable smaller ice crystals to be formed for the same processing conditions. It should be noted that when the ice did form on the plate, it could not then be removed by the ultrasound.

3.5.4 Problems with Etrema Probe Method

Although ice could occasionally be cracked it could not be fully removed from the steel plate. This was in part due to the amplifier used to excite the system. The

maximum power input to the transducer was 200 Watts but the maximum the transducer can tolerate is 325 Watts under continuous operation. If the amplitude could have been increased, ice may have been removed by this method as the stresses would also have increased.

Additionally the transducer became heated under continuous excitation. After some time the transducer would become hot to the touch, reaching similar temperatures to the Branson probe. This is probably due to hysteresis losses in the Terfenol-D core of the transducer [117].

As with the Branson probe experiments the behaviour of the system with ice attached was difficult to map using the laser vibrometer. This was due to the build-up of ice on the plate obscuring the locations where readings were required.

3.6   Summary

A range of experiments have been devised and conducted at ultrasonic frequencies with varying levels of success. The concept that ice can be removed from cooled metal surfaces using ultrasonic vibrations has been demonstrated.

The Branson Probe experiments described in section 3.4 show that ice can be removed from a steel plate over a temperature range of $-6°C$ to $-18°C$. At the minimum setting of the instrument the tip amplitude was $18.6\,\mu$m and the peak possible axial stress generated was $12.2\,$MPa in the ice. No limits of ice removal could be determined from this experiment due to low controllability of the probe, as the ice was easily removed at these minimum settings.

Experiments using the Etrema probe with a tip amplitude an order of magnitude lower were unable to repeatably remove ice from the same system. In some cases the ice could be cracked but the ice layer was not removed. Also the formation of ice could be delayed until temperatures fell below the expected freezing point of the

ice or sucrose - but could not be prevented at temperatures more than a fraction of a degree Celsius below the expected freezing point. These phenomena imply that the method is producing stresses at the limit of fracturing the ice but the required stresses are not reached or can only just be reached but not overcome.

As the experiments stood, the limits of ice removability could not be determined accurately from either method and hence the mechanisms behind ice removal could not be investigated satisfactorily. Further investigation into experiments that can produce high quality data was needed to determine the limits of ice removal. The improved experiments are outlined in Chapter 4.

Chapter 4

Rig Development & Experimental Procedure

4.1 Introduction

The aim of the thesis is to examine the mechanisms behind the removal of ice from a cooled metal surface. This Chapter aims to describe the process of design and construction of a rig for a thorough experimental study. Chapter 3 showed that the concept of ice removal at ultrasonic frequencies was feasible. However, the systems developed were not well suited to gaining useful information for determining the mechanical properties of the ice and ice/sucrose matrix.

Improved flexibility and data collection are shown as part of an iterative design process. A reliable and repeatable experimental rig has been developed to produce data on the failure of ice. In conjunction with suitable modelling shown in Chapter 5, this data can be developed to help determine the mechanisms behind ice removal from cooled metal surfaces.

A rig was chosen, the basis of which was a $\frac{1}{4}''$ metal pipe with perpendicular excitation at its mid-length. Cooling fluid was passed through the centre of the pipe to provide cooling to a surrounding liquid. Ice would be allowed to form in varying

thicknesses on the outer surface of the pipe. By exciting the pipe near a flexural resonance of the system the ice would be removed.

In this Chapter the rigs which were developed operate in the sonic regime. By modelling the behaviour of each system developed, as shown in Chapter 5, the strengths and weaknesses of each experiment were investigated. Therefore, using an iterative approach to experimental design and modelling, a rig was produced that was suitable to enable repeatable and reliable data to be measured, showing where and when ice was removed from a cooled metal surface using structural vibrations. The various experimental steps will be outlined in the following sections. Data collected from the final rig will be used in conjunction with appropriate modelling, which will be discussed in Section 5.3.5.

4.2   Development of Rigs

This section will briefly describe the development of the final experimental rig. A brief description of the intermediate rigs will be presented and the effectiveness of each rig will be described.

4.2.1   Initial Sonic System: $\frac{1}{4}''$ Copper Pipe, Ends Free-Free

4.2.2   Description of Rig

Figure 4.1 shows the basic setup of the first rig developed for sonic experiments. The initial setup comprised a length of copper pipe soldered to a brass T-connector at the mid-length of the pipe. The T-connector was made of M6 brass studding, cut to about 70 mm in length. The copper pipe was the source of cooling to the system. Initially a Haakë cooling bath capable of temperatures down to $-20°$ C was used. This was later changed for a Grant LTC Series cooling bath which had a minimum temperature of $-30°$ C and a larger reservoir. The cooling bath was connected to the copper pipe using silicon rubber tubing, which had high flexibility and excellent

low temperature resistance.

The system was actuated by a Ling Dynamics Systems $V201$ shaker [118]. The shaker was attached directly to the free end of the brass T-connector via a force gauge [119], by screwing the T-connector into the force gauge. The shaker was held in position using a specially constructed clamp, which could be screwed directly to the base of the shaker, using 3 2BA screws to give a firm hold. The entire assembly was positioned with the shaker aligned directly above the centre of the pipe. The clamp of the shaker was attached to a retort stand, which was clamped to the lab-bench to provide as much rigidity as possible.

A rectangular perspex tank was constructed to hold a volume of liquid sucrose. The tank was longer than the copper pipe, to allow the silicon tubes to bend outwards from the tank without affecting the copper tube. The tank had two separate lids, hinged at the rear of the tank. The lids were separated to allow the brass T-connector to enter and exit the tank unhindered. Each lid also had a notch cut at one end to allow the silicon tube to exit from the tank. The copper pipe was positioned within the tank, so that the tank lids could be closed. The shaker and electrical connections could thus be isolated from the liquid, which tended to splash out of the tank at high amplitudes of vibration. The vibration was measured by miniature accelerometers [119], and by laser vibrometer on the top surface of the pipe. Ice could be formed and removed from the pipe under several experimental conditions. However, the results had a poor repeatability, explained as follows.

4.2.3   System Performance

Although partially successful this rig also produced some significant problems that had to be rectified before useful results could be obtained. The problems with the rig are detailed below.

- Transverse forces added at T-connection. The T-connector rod at the mid-length of the pipe was moving linearly, causing flexural modes of vibration that could be observed clearly by eye at the higher amplitudes of vibration.
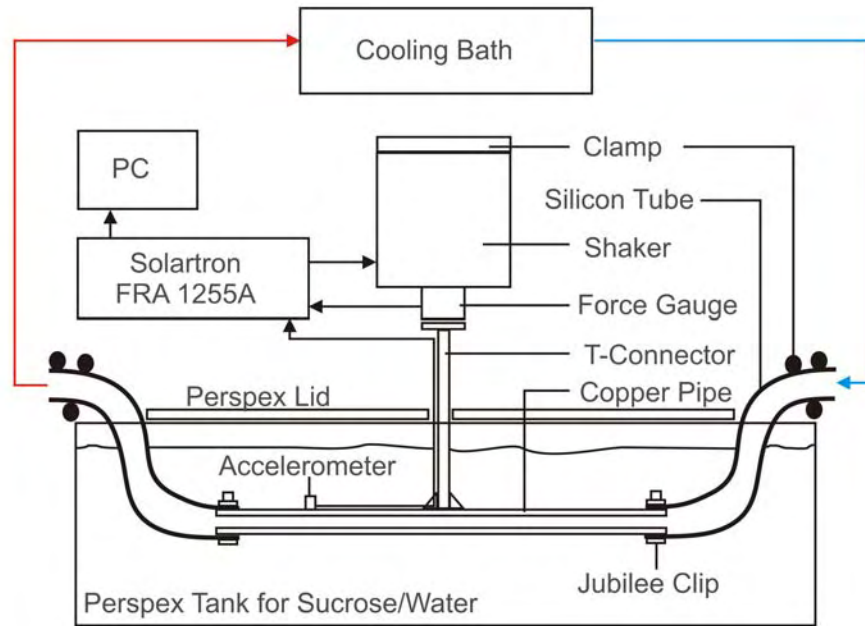
Figure 4.1: Schematic Layout of Initial Sonic Rig: $\frac{1}{4}$inch copper pipe, simply supported in sucrose filled tank.

However, in some experiments another motion at a somewhat lower frequency was also observable; the pipe appeared to oscillate from side to side around the attachment of the T-connector at the force gauge. It appeared that as well as the desired "up and down" piston motion, some moment was acting on the pipe, as there was a rhythmical motion causing the pipe to move up and down at each end on top of the mode shape of the vibration. Some evidence of this was found in the Nyquist 4.2 plots derived from the experiments. The fit of the circle to this data was poor. This is particularly seen at the right hand side of the plot, i.e. near the resonant frequency; where the data falls a long way from the best fit circle. This may have been due to the relative stiffness of the brass T-connector to the copper pipe. Any slight misalignment could then cause a moment to be transferred to the system in addition to the desired piston motion. This made modelling more difficult as the motion being modelled (an idealised flexural mode) was dissimilar to the mode produced in the experiment.

– Damping was difficult to repeat when the rig was dismantled and reconstruc-
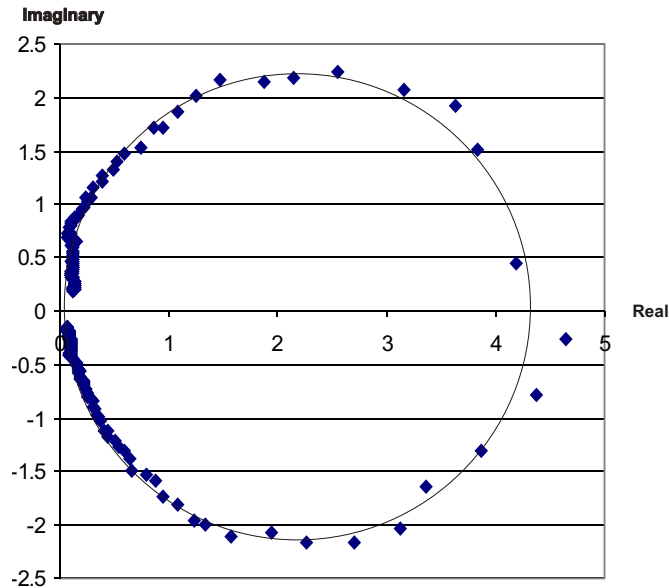
Figure 4.2: Nyquist plot of a $\frac{1}{4}''$ copper pipe supported at its mid-length for strain and force.

ted. This effect was particularly evident in this configuration as the silicon connecting tubes were very flexible when they were at room temperature. Therefore, early tests on the system (in air and in water at RTP) were encouraging. When the tubes were cooled, ice started to freeze onto the outside of the silicon pipes. When the system damping was recorded before and after ice formed on the silicon tubes there was a significant change in the system damping. This might be due either to an increase in the stiffness of the system, or to added mass acting on the ends of the pipe caused by ice formation. Ice could still be removed from the pipe but the dynamic properties of the system had changed from those measured while using the system at RTP. This would have led to serious problems when trying to successfully model the system using finite element analysis. Experiments would have to be conducted for each condition to be investigated - to feed a stiffness value and added mass value into the model to account for the changes in the silicon pipe, which was not modelled at all for the pipe in air or pipe in water cases. This of course is antagonistic to the aim of the finite element modelling, which was intended to predict whether ice would fail under given conditions after suitable verification

had been conducted.

– The laser vibrometer method for determining the amplitudes of vibration was successful on the rig when run in air or when run in liquid with no ice present. Useful data could be obtained for very thin ice layers, where exposed areas of metal still existed. For thicker ice layers, i.e. full coverage, the method broke down and useful data could not be obtained in these situations. Other methods of measuring the performance of the system online were therefore required.

– Alternatively, small accelerometers could be attached to the surface of the metal pipe in all conditions and repeatable results could be obtained in this way. But, there were still problems associated with this method. Even the smallest accelerometers available had a weight which was significant when compared to that of the copper pipe, i.e. the accelerometers were around $5 - 10\%$ of the mass of the pipe. Locally this constituted a large percentage of the mass of the pipe and ice, effectively an addition of a sizable point mass on the pipe. The accelerometer seemed to alter the mode shape of the pipe on the side it was mounted on, giving modes at two slightly shifted frequencies. One could not be sure that the results from the accelerometer accurately predicted the behaviour of the other side of the pipe, where the ice removal was being observed. The removal had to be observed at the other side of the pipe as the ice was firmly adhered to the pipe around and including the accelerometer. As the behaviour on each side of the pipe appeared to be slightly different, there would be less confidence in any results for pipe stresses derived from finite element models of the system. This is because it would be harder to verify the outputs from the finite element model against the actual behaviour of the rig where the ice was being removed.

– Physical attachment of the accelerometers was problematic. With smaller accelerometers, Bee's wax is typically used to attach the transducer to the test piece. This was fine when the accelerometer was tested in air, but when the experiments were conducted in water or sucrose solution the accelerometer would simply fall off after a short time. Gluing the accelerometers proved little

better as the area available for adhesion was small and the accelerometers would still fall off the pipe after a short time. A larger size of accelerometer would have been required in order to mount the accelerometers on the pipe using studding soldered onto the pipe, adding an even larger mass to the pipe.

– Mixing effects of the accelerometers and their attachment leads appeared to be reasonably significant. The effects were especially obvious in the sucrose solutions tested, where the mixing of the liquid from different parts of the tank was pronounced. The effect of drag on the mode shape near the accelerometer is not well understood under these conditions. All of the problems associated with using accelerometers made their use undesirable and other means of measurement were sought.

– The LDS V201 [118] shaker proved to be problematic. When the system was run near a resonant frequency the shaker would seize up after a short time and required resetting before experiments could continue. This led to significant increases in the times required to conduct a run of experiments, as the whole rig required dismantling and reassembling. This behaviour was probably due to a lack of support on the pipe, allowing excessive transverse motion. Due to the fragile nature of the teflon spiders used in this design of shaker, it was necessary to change the free-free pipe configuration to avoid damage to the shaker.

– Control over the temperature in the tank of sucrose or water was problematic using this setup. This was due to the large volume of water/sucrose to be chilled. To obtain stable temperatures was difficult if not impossible. Even in cases where the temperature appeared to remain stable near to the pipe, moving the thermocouple to another point in the tank at some distance from the pipe would often reveal that there was a temperature difference of around $8 - 9°$C.

4.2.4   Second Sonic Rig: $\frac{1}{4}''$ Copper Pipe, Ends Clamped

Despite the drawbacks, the first sonic flexural rig met some of the experimental requirements and was partially successful. The rig provided a solid base of un-
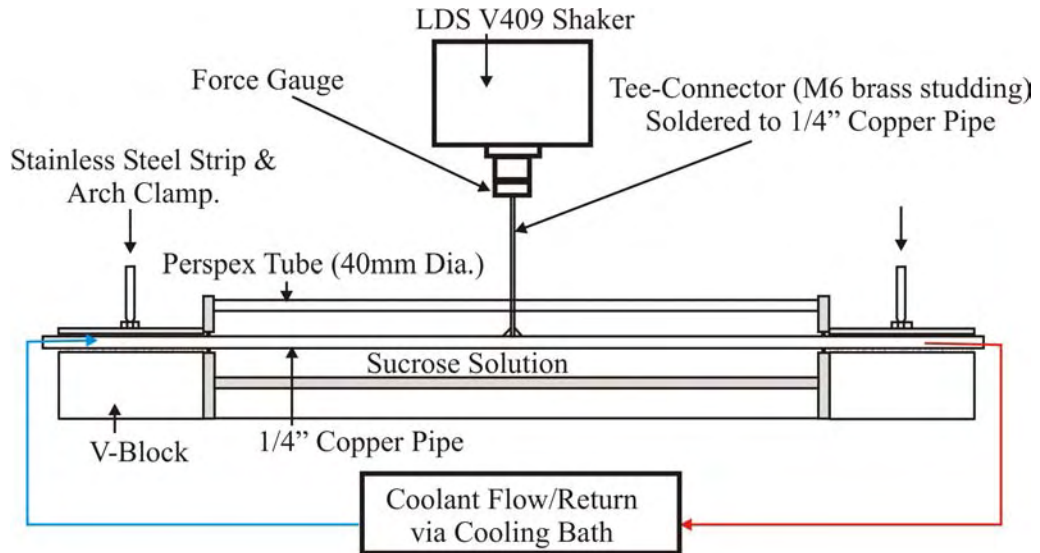
Figure 4.3: General Layout of Revised Sonic Flexural Rig

derstanding that allowed for improvements in the experimental setup. Using this understanding a revised experimental rig was designed and constructed to achieve improved repeatability and better data capture.

The principle of a slender pipe vibrating near a flexural resonance was retained, as ice removal had been successful over a range of frequencies ($\sim 0 - 1000\,\text{Hz}$). The setup of the pipe was changed slightly to achieve better stability in the system and also to make the system easier to model using finite element analysis. These improvements were achieved by clamping both ends of the $\frac{1}{4}''$ copper pipe in steel V-blocks, and by using a larger more robust shaker with an improved clamping arrangement.

4.2.5 Description of Rig

The copper pipe, T-connector and fastening method remain unchanged from the initial sonic rig detailed in section 4.2.1. The overall layout of the revised rig can be seen in the schematic diagram of Figure 4.3. The main changes to the rig are outlined in the following paragraphs.

New Smaller Tank

Figure 4.3 shows a cross-section of the revised tank design for the flexural tube experiments. The tank was constructed from acrylic tube and sheet. The tube was 404 mm in length and had an inner diameter of 40 mm, with a wall thickness of 10 mm. A slot was cut down the length of the tube to allow the T-connector to connect to the pipe and shaker.

Two 10 mm thick acrylic sheets made the ends of the tank. The sheets were glued in place using Tensol12 [120] cement. Holes were drilled through the sheets to allow the copper pipe to pass from the tank to rest in the V-blocks. O-rings were used to seal the tank at the junction of the tank and pipe. This arrangement restrains the motion of the pipe, but as the O-rings are very close to the end of the pipe this effect was considered to be minimal.

Altered Shaker Setup

Due to the problems with the previous design the shaker arrangement was changed for the improved experimental rig. A larger LDS V406 [121] shaker was used to actuate the system. Using this design led to fewer problems with overheating and jamming of the shaker. This shaker was significantly larger than the previous shaker, and more robust clamping was required. An angle iron frame was constructed for this purpose, and a square plywood platform was used to support the shaker. The frame was clamped to the table using large G-clamps.

V-block Arrangement

The free ends of the copper pipe were clamped in V-blocks. The details of the V-block arrangement are shown in Figure 4.4. The pipe was located in the base of the V, separated from the V-block by a thin layer of silicon rubber sheet. The top of the pipe was held in place by a strip of stainless steel $\frac{1}{4}$ inch deep. The clamping bolt of the V-block was located by a M6 nut welded on to the top centre of the stainless

steel strip. The V-blocks were clamped in place on the workbench.
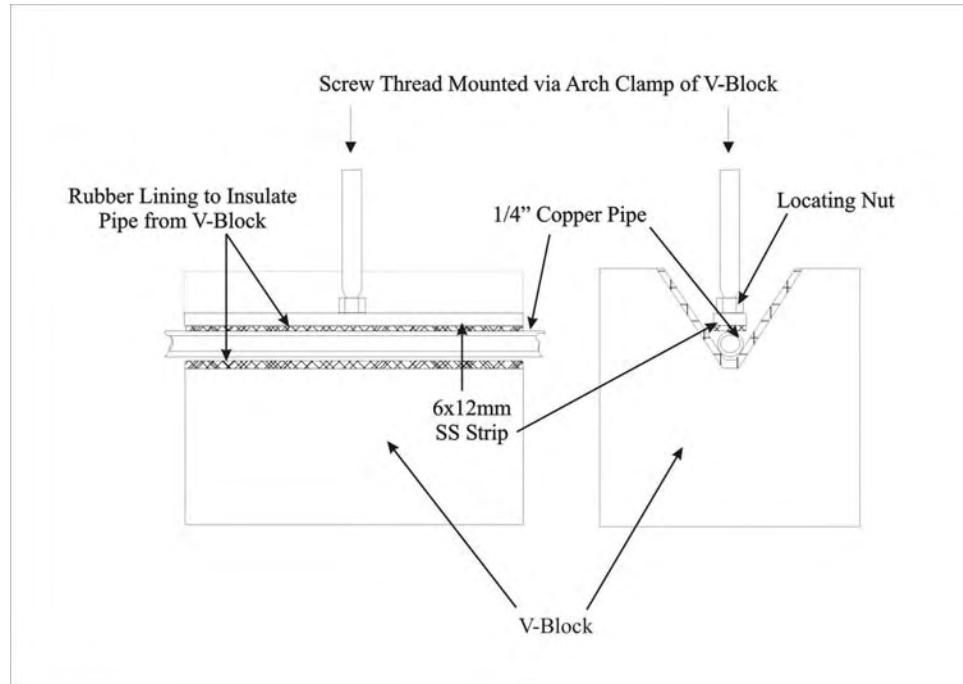
Figure 4.4: Schematic of V-block Clamping on First Revised Experimental Rig.

Cooling

The source of coolant to the system was the Grant LTS [122] cooling bath, as used in the previous setup. The ends of the pipe were free, projecting from the outer ends of the V-blocks. The lagged silicon tubing was attached to the pipe by jubilee clips.

4.2.6 System Performance

The revised rig proved to be more reliable than the first sonic rig. Sucrose/ice removal could be achieved over the first three flexural modes of vibration for the system (i.e. pipe flexural modes 1, 3 and 5). For modes 1 and 3, sucrose/ice could could be removed in layers of up to $\sim 2.0\,\mathrm{mm}$. For the mode 5 vibrations only thicknesses of approximately 0.5mm could be removed repeatably.

Problems

Several problems have been identified with this experimental setup.

- Clamping. The clamping utilised to constrain the ends of the pipe is an improvement over the previous rig. However, it was still far from satisfactory. The issues that arose from this were:

  - Repeatability. When the rig was disassembled and reassembled it was desirable to have consistent amplitudes of vibration for "the same" input vibration. Due to the imperfect clamping method employed, some significant vibration still occurred at the "fixed" portion of the pipe. As the clamping was dependent on the single bolt on the arch clamp attached to the V-block, slight variations in the torque in the bolt could lead to significant variations in the compliance of the system, as can be seen in table 4.1. These results were obtained from nominally the same setup, but were repeated after each reassembly.

  - Modelling of Boundary Conditions. There is a certain variability in the amount of structural damping induced in the system by the clamping of the pipe. The variation was approximately 20%, ranging from 0.050 to 0.059 (see table 4.1). Therefore, correct modelling of the system might prove difficult as the rig stands. The finite element model (section 5.3.5) assumes that the pipe is built in at both ends. However, as the clamping is imperfect there is some vibration at the "fixed" end of the pipe. The more vibration that is present at this end position, the less accurate will be the prediction of stresses in the pipe using the FE model.

- Relative movement between the V-block clamped firmly to the lab-bench and the water tank, which was not directly clamped to the lab-bench. In this rig iteration the tank was pressed in between the two V-blocks. When the setup was first used it appeared that the tank was firmly located between the two V-blocks, which were then clamped firmly in place. After some experimentation near the first flexural mode of the system the tank became loose between the two V-blocks. This freedom to move was allowing the tank to "rest" on the

Case	Damping	Vib. at End mm	Vib. at Cnt. mm	%Max.
1	0.055	0.11	0.77	14.3
2	0.059	0.09	0.77	11.7
3	0.053	0.10	0.77	13.0
4	0.050	0.14	0.77	18.2
5	0.056	0.11	0.77	14.3

Table 4.1: Table showing the variation of the measured properties of Mode 1 Damping and End Vibration with resetting of the experiment, measured in 20% Sucrose solutions.

pipe as it vibrated. The natural frequency and damping of the system changed as this happened, moving the physical behaviour of the rig away from the finite element predictions for the system.

– The T-connector attachment was also a problem. Although this is not strictly a modal testing problem, a number of the techniques normally applied in modal testing situations were employed to characterise the dynamic properties of the system. Therefore, anything that caused the results of this type of characterisation to become unclear or inaccurate should be resolved as far as possible, assuming that the correct function of the system, (ice removal), is not compromised. The T-connector was relatively stiff in bending compared to the copper pipe. Combined with slight misalignments to the normal contact desired in the experiments, some moments were created within the system. Nyquist plots of the resonances of the system were not circular and hence some error was introduced into the estimations of damping in the system.

– As seen in figure 4.5, fatigue in the copper pipe was also a problem. Although the experiment had run for some time before the pipe fractured fully, some experimental data was corrupted by the presence of ethylene-glycol solution in the sucrose.
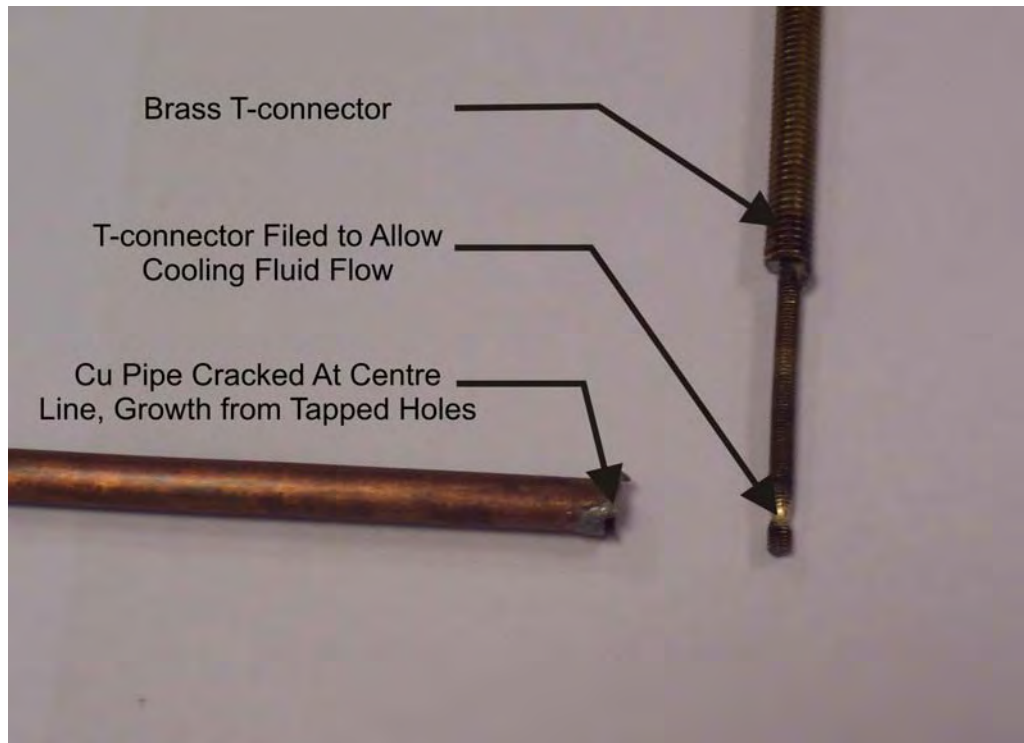
Figure 4.5: Photograph showing a fatigued copper pipe with a through thickness crack at the centre of the pipe, on left hand side shown.

4.3 Final Setup

Although the functionality of the second experimental rig had improved when compared to the initial setup, it was far from the ideal solution. It became apparent after some experimentation on the improved rig, that significant improvements could still be made, allowing the physical rig to mirror the assumptions of the finite element model more closely.

With this in mind some further improvements were made to the experimental setup. The aims were to improve the robustness of the rig, draw the finite element predictions closer to the data output from the experimental rig and to maintain the ability to remove ice from the cooled metal surface over a reasonable range of frequencies. The following paragraphs detail these attempts and describe the successes and shortcomings of these improvements.

4.3.1 Description of Rig

The setup of the final revision of the experimental rig can be seen in Figure 4.6 and Figure 4.7. The experimental rig is similar to that of the second rig in operation, (i.e. a centrally excited pipe, clamped at each end). However, some of the details of the rig have been changed to improve the quality of the data that can be collected.

The rig is constructed as follows: A steel base plate runs under the pipe, tank and v-blocks. Holes are drilled into the plate to locate the V-blocks and the redesigned tank (see section 4.2.5). The pipe is located within the new tank and is clamped at each end by the V-blocks, using the modified arch clamp setup (see section 4.3.1). The T-connector has been modified as described later in this section.
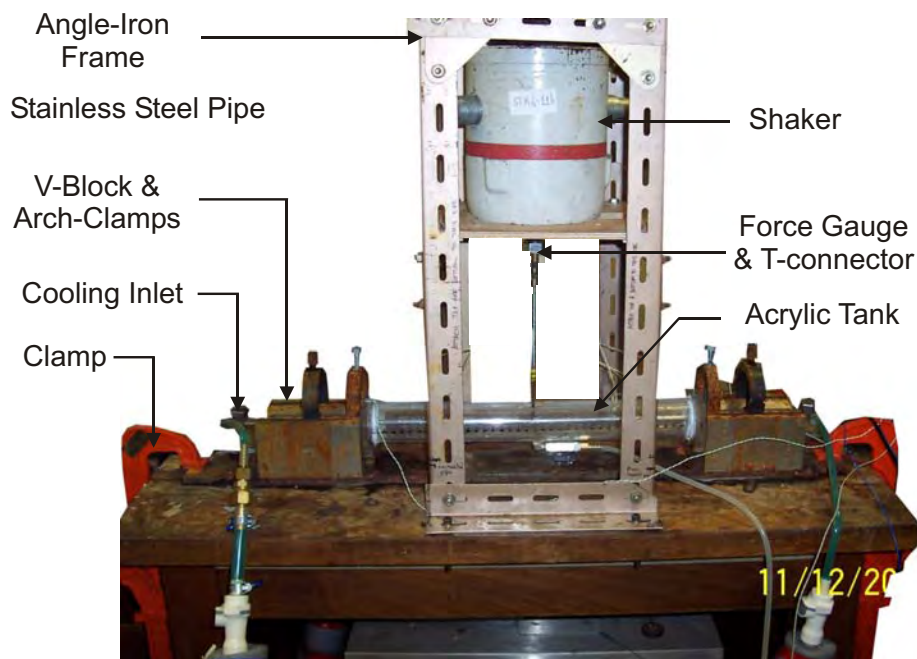
Figure 4.6: Photograph showing the setup of the final experimental rig

Modified Tank

The upright ends of the tank had to be altered to allow correct location and clamping of the tank to the steel base plate which was introduced to increase the rigidity of the system. A square section was cut from each corner of each upright at the base
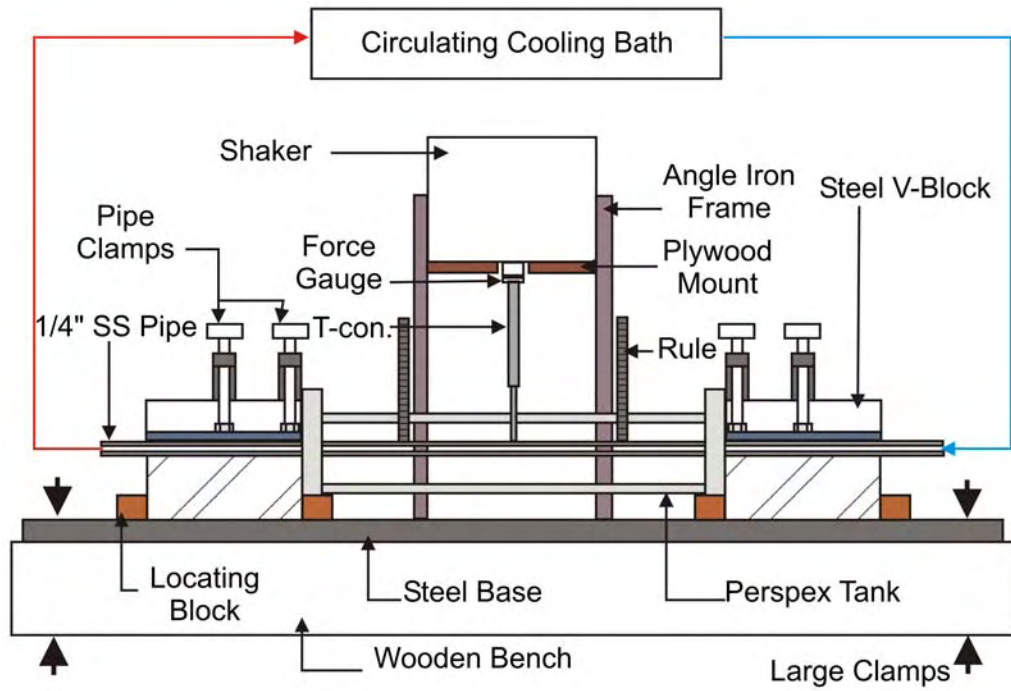
Figure 4.7: General layout of revised sonic flexural rig, showing final configuration
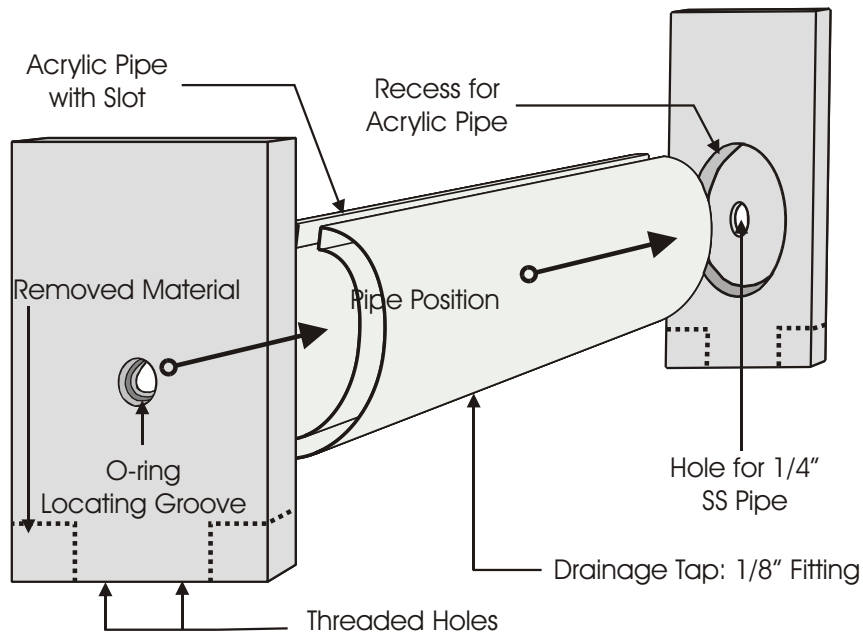
Figure 4.8: Diagram showing minor alterations to the construction of the revised tank for sucrose/water.

of the uprights. This allowed the "locating blocks" shown in Figure 4.7 to slide into place without moving the tank out of position. The section of the tank remaining at the bottom edge of the uprights had two M4 holes drilled and tapped at 10 mm either side of the centre line. Therefore the tank could also be bolted directly to the steel base between the V-blocks. An illustration of these changes can be seen in Figure 4.8.

New V-block and Clamp Arrangement

As there had been some problems with the previous V-block arrangement detailed in section 4.2.5, some redesign was required. The previous design had allowed some vibration at the inlet and outlet of the pipe near the V-block clamp. Several measures were employed to improve the vibration at the clamping position.

The first was to bolt the V-blocks on to an underpinning steel base plate. Locating blocks were made to achieve this. These blocks comprised a single piece of brass bar, with one end turned-down to a cylindrical peg shape. As the V-block had holes drilled lengthways through, them these pegs would fit in, one at each corner, at the base of the V-block. Holes were also drilled into the locating blocks at right angles to the pegs to allow the locating blocks to be bolted to the steel base. Using this method the V-blocks could be securely attached to the steel base, hence reducing the relative motion between the V-blocks and the tank.

To better approximate the clamped-clamped condition which was modelled (as shown in Section 5.3.5) some small alterations were made to the V-block design. Figure 4.9 shows the layout of the improved V-block arrangement. In the new design, the thin insulating layer of silicon sheeting has been removed from between the pipe and the V-block. The thermal performance of the system was slightly degraded, which could be compensated for by altering the temperature of the cooling bath by a few degrees Celsius. However, the structural capabilities of the system were improved by reducing the ability of the pipe to move relative to the clamping between the arch clamp and the V-block base.

Figure 4.9: Improved Clamping using New V-Block Design

Figure 4.9 also shows that the arch clamp arrangement was improved in comparison to that described in Figure 4.4 to reduce any moment that might have been introduced. In the previous configuration of the V-block and clamp, a single clamp positioned at the centre of the stainless steel strips was used to hold the pipe in place. In the revised design the single central clamp was augmented by a secondary clamp at the inside of the V-block, (i.e. at the built-in position). This second clamp was used to ensure that the motion of the pipe was constrained at the "end". In the previous design of Section 4.2.4, the clamping at the end of the tube was solely dependent on the rigidity of the $\frac{1}{4}''$ strip of stainless steel that was used to run down the section of the stainless steel pipe contained within the length of the V-block.

The new V-block arrangement was designed to reduce vibration at the ends of the nominally "clamped-clamped" pipe, and therefore bring the experimental rig closer to the assumptions used for the Finite Element model of the system of Section 5.3.5.

The relative movement at the clamps was reduced from the $0.11 \pm 3\,\mathrm{mm}$ at each end, (Mode 1), in the rig of Section 4.2.4, to $0.01\,\mathrm{mm}$ at the "clamped" end in the rig described in this section. This represents a reduction from $\sim 12\%$ of maximum displacement to $\sim 1.4\%$ of maximum displacement at the "built-in" end of the pipe. These readings were based on a peak displacement of $0.77\,\mathrm{mm}$ at the centre of the pipe. However, both percentages decrease with increased amplitudes as the quoted displacements appear to be the maximum possible displacements that could occur at the supposedly fixed end of the pipe.

New T-connector Method

Due to problems introduced by the original configuration of the T-connector used with the copper pipes, a different design was sought. The use of stainless steel (316L) meant a simpler and more robust design of T-connector was possible. Steel studding of two different diameters was chosen to provide a compromise between the stiffness required to correctly actuate the pipe and the desire to avoid undesirable

moments being formed within the system as described in the previous section.

A $140\,\mathrm{mm}$ length of $M6$ steel studding was attached to the clamp near the force gauge. At the other end a shorter $45\,\mathrm{mm}$ section of $M3$ steel studding was attached to the centre point of the stainless steel pipe by welding the two components together while clamped at $90°$. Further to this a $M3$ hole was drilled and tapped in the end of the $M6$ studding, allowing the $M3$ studding to be silver soldered into the larger diameter studding.

Strain Gauge Measurement

It was desirable to obtain online measurements from the system without adversely affecting the structural vibrations within the system. The laser interferometer [110] had originally been used to this effect but could not be used in the presence of ice layers over the whole pipe. Miniature accelerometers [119] attached to the pipe were also used with limited success, but tended to alter the mode shape of the system.

Strain gauges were a useful alternative - with little effect on the system but offering continuous operation even in the presence of ice or frozen sucrose, but initial trials with readily available strain gauges were less than promising.

Specialist strain gauges were ordered due to the particular demands of this application (e.g. small diameter pipe and low temperature operating conditions). The strain gauges were a single axis type, specially prepared for use in sub-zero temperatures. These strain gauges had a gauge length of $0.2\,\mathrm{mm}$ and could, with careful placement, be located on the centre line of the pipe with minimal curvature. Also they provided relatively stable gauge factors over the range of experimental temperatures, see Table 4.3. To prevent the same kind of mixing problems observed when using the accelerometer in Section 4.2.1, low diameter wire of $0.2\,\mathrm{mm}$ was used when connecting the strain gauges to the amplifier. Additionally the gauge connections were adhered to the pipe where possible using gauge terminals, to reduce erroneous strains from movements of the connecting wires.
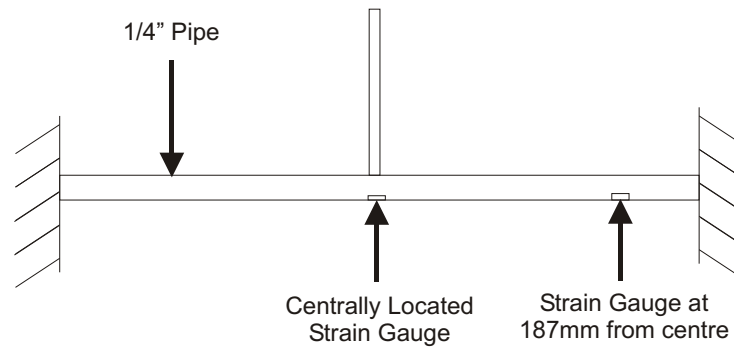
(a) Positioning of strain gauges on the stainless steel pipe
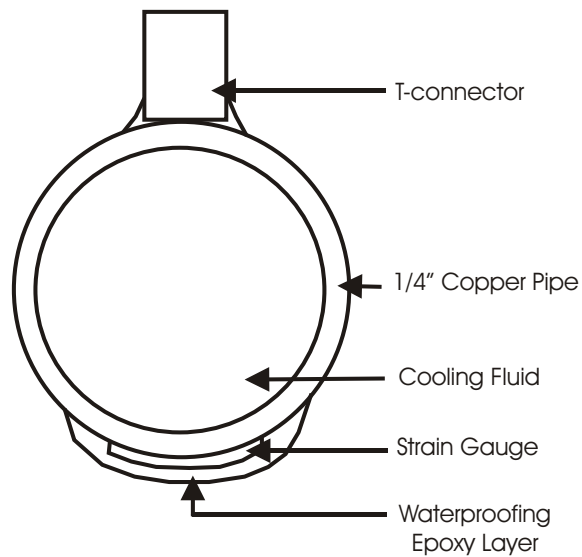
(b) Epoxy resin used to seal the strain gauges against the liquid in
the tank

Figure 4.10: Arrangement of the stainless steel pipe, detailing the positioning, attachment and waterproofing of the strain gauges

Figure 4.10 shows the positioning of the strain gauges on the stainless steel pipe and the nature of the waterproofing layer on the pipe and strain gauge. The method was still imperfect, as the ice layer would not be in contact with the pipe in the location where the strain gauge is attached, due to the intermediate epoxy layer. The strain gauges were attached in accordance with the guidelines supplied by the manufacturer [123]. After each gauge was installed and waterproofed the resistance was checked using a multimeter. Each was found to have a resistance of $119.8\,\Omega$, which was in accordance with the standard resistance of $120.0 \pm 0.5\,\Omega$ supplied by the manufacturer.

Some assumptions have to be made when modelling the pipe, based on the readings from the strain gauges. One must assume that the epoxy layer is thin enough that it will have little bearing on the dynamic performance of the pipe. Also that the pipe is behaving in a similar fashion at the other end relative to the end strain gauge, and any behaviour there is equivalent to that where the strain is actually measured. For the centre strain gauge it must be assumed that the ice behaviour a short distance from the gauge is unaffected by the presence of the gauge and surrounding epoxy and that the strains can be accurately predicted in this region via the finite element model of the system.

Thermocouple Array

A set of thermocouples was attached to the rig. This was to replace the one thermocouple that had previously been used and had been moved by hand to various locations in the tank during the experiments. The thermocouples were placed in various significant locations within the tank and the cooling bath. The locations of the thermocouples are shown in the following list:

1. Outside Rig (Air temperature)

2. Cooling Bath (Core Temperature)

3. On Surface of Stainless Steel Pipe at Inlet (At $Z = -207\,\text{mm}$)

4. On Surface of Stainless Steel Pipe at Outlet (At $Z = 207\,\text{mm}$)

5. In Liquid: Position One, tank wall drilled and thermocouple inserted into front side of tank at $Z = -90 \pm 2\,\text{mm}$ at $10 \pm 2\,\text{mm}$ from the pipe, and glued into position.

6. In Liquid: Position One, tank wall drilled and thermocouple inserted into rear side of tank at $Z = -90 \pm 2\,\text{mm}$ at $10 \pm 2\,\text{mm}$ from the pipe, and glued into position.

7. In Liquid: Position Two, tank wall drilled and thermocouple inserted into front side of tank at $Z = 100 \pm 2\,\text{mm}$ at $10 \pm 2\,\text{mm}$ from the pipe, and glued into position.

8. In Liquid: Position Two, tank wall drilled and thermocouple inserted into rear side of tank at $Z = 100 \pm 2\,\text{mm}$ at $10 \pm 2\,\text{mm}$ from the pipe, and glued into position.

The aim of these thermocouples was to measure the temperatures that were likely to be important in using the results from the rig. The temperatures recorded from these thermocouples were used to refine the modelling of the rig - in particular to determine the properties of the sucrose/ice in the finite element models and also to determine the predictions of sucrose/ice failure conditions. The temperatures were automatically recorded during experimentation through a Picolog eight channel digital thermocouple meter [124].

The thermocouples were located in a fixed position by drilling 1.5 mm holes in the acrylic tank and feeding the thermocouple leads through the holes. The thermocouple leads were then held in place using fast drying epoxy resin. Accurate positioning of the thermocouples was achieved by bending the thermocouple leads through a small angle, using curved tweezers: the leads were coated with a glass fibre sheath and were stiff enough to maintain their position to within a few millimeters during experimentation.

4.4   Experimental Method

The rig was set up as described in section 4.3.1. Different types of experiment were conducted on this rig and are outlined below.

4.4.1   Main Experiments - Ice Removal

1. The tank was cleaned with a weak solution of water and detergent, before a run of experiments was commenced.

2. Sucrose solution was mixed by adding sucrose (table sugar) to heated water. The amounts of sucrose and water were weighed using an electronic scale accurate to within 0.1 grammes. The mixture was thoroughly stirred until the sucrose was completely dissolved in the solution. Several litres of solution were mixed at one time. Concentrations of 10% and 20% by mass sucrose solution were used for these experiments.

3. The solution was placed in a refrigerator until it reached around 5°C, i.e. the equilibrium temperature of the refrigerator.

4. The cooling tank was turned on and was left to reach its equilibrium temperature. This was typically −20°C, but other temperatures were used in some experiments.

5. Some of the sucrose solution was poured into the tank using a funnel, and the tank was filled to within a few millimeters of the slot at the top of the tank, giving a volume of ~ 450 mL.

6. A test run was conducted.

   – The ice was allowed to grow to the required thickness on the outer surface of the pipe.

   – Then the output from the signal generator was increased gradually until the ice was removed from the pipe.

– The voltage required to remove the ice was noted on the oscilloscope. This value was not used as a valid data point. Instead it was used to calibrate the dynamic range for that ice thickness. This step was repeated for each ice thickness from 0.5 to 4.0 mm of ice.

7. The now cooled liquid was drained from the tank by opening the tap at the bottom of the tank. The liquid was returned to the bulk of the sucrose. Several minutes were allowed before the tank was refilled, to allow the chunks of ice at the bottom of the tank to melt and run into the sucrose container.

8. Now the "real" experiments were conducted at the given thickness. The thickness of the ice was measured using two steel rules, glued to the slot in the tank, normal to the pipe. Parallax error was minimised by marking the measurement position on the side of the angle iron frame.

9. The ice was removed by gradually increasing the amplitude of vibration. The increase in amplitude was carefully controlled and significant events, (i.e. ice removal, bubbles under surface, the nature of the ice at removal), were recorded along with the voltages from the strain gauges that coincided with these events.

10. The temperatures of the ice and solution in the tank at various positions were also noted.

11. The strains were calculated and used to produce inputs for the finite element models of Section 5.3.5.

12. The experiments were repeated a number of times for each thickness of ice and a number of ice thicknesses from 0.5 mm to 4.0 mm were investigated.

Results from these experiments are presented in full in Chapter 6 in conjunction with finite element modelling results from Chapter 5.

4.4.2 Ancillary Experiments

The main experiments were based on 20% sucrose solution frozen on to a stainless steel pipe. The aim was to produce data that could be combined with the Finite Element modelling of Chapter 5, to give an understanding of why the frozen sucrose

was removed by structural vibrations of the system.

However, these experiments were not able to reveal fully all of the aspects required to determine the failure of the sucrose. Therefore, some additional experiments were performed in order to investigate certain aspects of the ice (sucrose) removal. The experiments are outlined in the following paragraphs.

4.4.3 Determining Natural Frequencies and Ensuring Rig Still Operating as Expected

As the rig had changed slightly from the former revision, it was first necessary to check the natural frequencies of the flexural modes. In addition to this it was also desirable to separate the frequency response function into the two components, i.e. the velocity and the force. The reason behind this is simple. In terms of ice removal the resonance may not be the optimal operating condition. The resonant frequency (f_{res}) is determined as a function of the displacement (x) and the force (F) input to the system, i.e. where $f_{res}\left(\frac{x}{F}\right)$ is a maximum. It does not follow that the maximum displacement occurs at this frequency. The position of maximum displacement is required for these experiments, as the maximum strain/stress will occur at this position.

Table 4.2 shows a section of the findings from the experiments. The resonant frequencies of the system were recorded for comparison with the finite element modelling of section 5.3.6. Ideally, the experiments should have been conducted at the strain maximum, which occurs at a frequency just below the resonant frequency of the system. However, most of the experiments were not conducted at this optimal position.

The actual experimental conditions were recorded in Table 4.2, and some of the points occur at frequencies lower than the half-power points. This means that the system was not running at the best position and more power was required to the

shaker to drive the amplitudes necessary to remove the ice layers from the pipe. In modes 1 and 3 this seems to have had little effect on the ice removal capabilities of the systems as the strains remained relatively large even outside of the half-power point frequencies. To ensure that the finite element models were still valid it was important to check that the mode shapes of vibration were the same shape as those nearer to the resonant frequency. As the system damping was light, there was not a significant difference in the measured mode shape at the ice removal frequencies and the resonant frequencies.

At various points during the experimentation, which was conducted over several weeks, it was sensible to check that the rig was still operating as expected. Therefore, some experiments were conducted to ensure that some easily measurable parameters (e.g. system natural frequency and damping) stayed within a small range of variation.

4.4.4 Axial Crack Determination

The main experiments were used to determine the mechanisms behind the removal of frozen aqueous sucrose solution from the cooled stainless steel pipe. Other experiments were also conducted as a check for the modelling of this system.

For example it was desirable to determine the order of failure, (e.g. through axial stresses, hoop stresses or shear stresses). To achieve this some way of observing how the failures appear was necessary. Some experiments where the amplitudes of vibration were gradually increased with sucrose in solution were conducted. However, the frozen sucrose solution was a quasi-opaque white solid. Therefore, crack initiation and formation could not be observed.

Similar experiments were conducted with tap water ice in water, with similar results. The ice was clearly cracking, as the ice would be removed in chucks of $10 - 20\,\mathrm{mm}$ at high amplitudes of vibration. However, as cracks formed, the surrounding water flowed between the free surfaces. As the water was near to freezing point and the

Mode	NF (Hz)	SM (Hz)	Viscous Damping (Ns/m)
		Pipe in Air	
$Mode$	NF (Hz)	SM (Hz)	Viscous Damping (Ns/m)
1	79 ± 2	51 ± 5	0.027 ± 0.002
3	746 ± 8	687 ± 15	0.035 ± 0.003
5	1950 ± 12	1826 ± 30	0.049 ± 0.005
		Pipe in 20% Sucrose	
$Mode$	NF	SM	Damping.
1	73 ± 2	47 ± 5	0.055 ± 0.005
3	693 ± 8	646 ± 15	0.064 ± 0.006
5	1805 ± 12	1699 ± 30	0.069 ± 0.006
		Pipe in Water	
$Mode$	NF	SM	Damping
1	76 ± 2	49 ± 5	0.035 ± 0.003
3	681 ± 8	637 ± 15	0.041 ± 0.003
5	1825 ± 12	1707 ± 25	0.057 ± 0.006
		Pipe in 20% Sucrose: Frozen Sucrose 4 mm	
$Mode$	NF	SM	Damping
1	54 ± 2	43 ± 5	0.066 ± 0.006
3	501 ± 8	476 ± 15	0.073 ± 0.006
5	1741 ± 12	1639 ± 25	0.081 ± 0.007
		Pipe in Air: Frozen Sucrose 4 mm	
$Mode$	NF	SM	Damping
1	69 ± 6	51 ± 5	0.059 ± 0.006
3	630 ± 8	546 ± 15	0.067 ± 0.006
5	1658 ± 12	1592 ± 30	0.076 ± 0.007

Table 4.2: Variation of operating parameters with each flexural mode and environmental conditions, NF = Natural Frequency, SM = Frequency where maximum strain occurs, Damping = viscous damping ν based on half-power point readings.

surfaces of the cracks were close to each other, regelation may have occurred, and would have closed the cracks.

Instead the ice was formed in water as before and then the water was drained out of the tank when the ice had reached the desired thickness. Once the tank was drained then the amplitude of vibration was slowly increased until cracks formed. When the ice was in air the cracks could clearly be heard and seen by eye. This was due to the cracks forming as an opaque white line in the otherwise colourless transparent ice. A clear cracking sound could also be heard with the initiation of each crack, which would suddenly appear.

The amplitude at which each crack appears was noted, and a brief description of the ice at this point is also noted. Based on this information the modelling in Section 6.3 can be verified as shown in Section 6.3. The results from these experiments are also detailed in full in that Section.

These experiments were conducted for Modes 1, 3 and 5. Good results were found for Modes 1 and 3, however, the experiments were unable to produce useful results for Mode 5.

4.5   Prediction of Errors

Although the final revision had brought about many improvements in reliability and repeatability, some errors were bound to be present due to the experimental method and also due to the experimental equipment used. The following sections will outline errors that are expected and predictions of these errors, where possible.

4.5.1   Strain Gauge Errors

Due to Transverse Sensitivity

Errors associated with strain gauges should be estimated before the results from the gauge can be fully trusted. As the strain gauges are to be used in a triaxial stress field the errors due to transverse sensitivity should be calculated. (Although the stress field is strictly triaxial, the axial stress being measured by the strain gauges is significantly greater than the other stresses in the system.) The transverse errors have been measured using the formulae found in TN-509 by Measurements Group Incorporated [125]. The error, $\mathbf{n}_\epsilon$, can be estimated from the following equation.

$$
\mathbf{n}_\epsilon = \frac{\mathbf{K_t}(\frac{\epsilon_\mathbf{t}}{\epsilon_\mathbf{a}} + \nu_\mathbf{0})}{1 - \nu_\mathbf{0}\mathbf{K_t}} \times \mathbf{100}
\tag{4.1}
$$

Where, $\mathbf{K_t}$ is the transverse sensitivity of the strain gauge, $\epsilon_\mathbf{t}$ is the actual transverse strain measured by the gauge, $\epsilon_\mathbf{a}$ is the actual axial strain measured by the gauge and $\nu_\mathbf{0}$ is the poisson's ratio of the material on which the manufacturer calibrated the strain gauge.[1]

Using the data from the finite element model detailed in Chapter 5 and assuming a transverse sensitivity of $\sim 3\%$, it can be shown that the error due to transverse sensitivity of the strain gauge is in the range of $0.93 - 1.00\%$. Compared to other errors in the system this error is negligible.

Due to Misalignment

A further source of error that could arise systematically from the strain gauges is due to misalignment of the strain gauge. The above section determined that there is little error caused by the transverse sensitivity of the strain gauges, due to the dominant nature of the bending (axial) stresses within the pipe. However, if the strain gauges are misaligned significantly, errors can be introduced. The maximum misalignment is likely to be $5 - 10°$ from the axial - due to pre-marking the position of the strain gauge before adhering the gauge to the pipe. For such a range of

---

[1]The typical value of $\nu_\mathbf{0}$ is 0.285

misalignments the error would be in the range of $0.4 - 1.5\,\%$.

4.5.2 Errors From Oscilloscope

Two channels were used to capture the data from the experiment, one for the strain gauge at the centre of the stainless steel pipe and one at $187\,\mathrm{mm}$ from the centre of the stainless steel pipe. The strain gauges which were used were Kyowa type $\mathrm{KFL} - 02 - 120 - \mathrm{C1} - 11$. These strain gauges are suited to low temperature operation. The gauge factor is calibrated to give 2.02 at 20°C and in the temperature range of 0°C to -20°C there is a 2% variation in the gauge factor. The strain gauges have a small gauge length of $0.2\,\mathrm{mm}$ which was dictated by the need to position the gauges accurately on the small diameter pipe and to avoid errors due to transverse sensitivity [126].

Temperature (°C)	Gauge Factor	Strain Modifier
20	2.020	1.000
0	2.031	0.995
-20	2.064	0.979

Table 4.3: Variation of Gauge Factor with Temperature

As can be seen from Table 4.3 the variation in the strain predicted from the manufacturer's gauge factor is of the order of 2% maximum over the maximum temperature range of the experiments. Therefore, any error associated with this can simply be incorporated into the error bars of the data without any further investigation.

The oscilloscope which was used was a LeCroy Scopestation 140. The readings were often captured from the automatic measuring facility of the oscilloscope. To gain some understanding of the errors introduced by this method a reading was taken from the system with no input applied to the shaker. Theoretically this should give a zero output and when, say, 20 cycles were averaged, this was the case. However,

when a "live" reading was taken a non-zero reading was obtained.

A number of these readings were taken for different sensitivities of voltage per division over a range of times. For each sensitivity it was found that the error was relatively constant with the absolute peak to peak values varying by only a few percent. The measured averaged errors and variations can be found in Table 4.4. As these erroneous signals were sitting on top of the correct sinusoidal signal the value obtained experimentally was the peak to peak magnitude of the signal plus the peak to peak magnitude of the error. Therefore the real value of the signal due to the vibration was the recorded signal minus the error caused by electrical interference in the system. This should be represented in the signal as a correction bar below the measured value of strain from the strain gauge. For example if an experiment gave a reading of $1.80\,\text{V}$ at a sensitivity of $0.5\,\text{V/div}$ then the reading should be $1.80 - 0.112\,\text{mV}$.

Sensitivity[V/div]	NoLoadReading[mV]	Variation[mV]
0.1	26	± 12
0.2	51	± 10
0.5	104	± 8
1.0	116	± 6

Table 4.4: Averaged errors and variability added by dynamic measurements from Scopestation 140.

4.5.3 Repeatability

It was important to have a rig with which results could be produced reliably and repeatably. It was desirable to have some means of determining whether the rig would behave the same way time and again under a range of operating conditions. If this could be shown then a certain degree of confidence in the reliability and repeatability of the rig could be assumed.

Check No.	N.F. (HZ)	Damping [Ns/m]	% of Max. Vib. at End
1	79 ± 1	0.028 ± 0.002	1.5
2	80 ± 1	0.026 ± 0.002	1.3
3	79 ± 1	0.027 ± 0.002	1.4

Table 4.5: Parameters calculated for pipe run in air to determine reliability and repeatability of system.

To achieve this it was necessary to measure parameters that could be monitored as the experiments progressed. The parameters identified were the natural frequency of a flexural resonance, the damping of that mode and the vibration at the end of the pipe for that mode at a set amplitude of vibration to give the percentage of the maximum displacement at the built-in end.

Table 4.5 shows the variation of these values for Mode 1. It can be seen that there is little variation of these parameters during the course of experimentation. Therefore, some confidence in the reliability and repeatability of the rig can be assumed.

4.6 Rig Verification

To obtain useful results it was necessary to determine that the experimental data produced agreed with that of the Finite Element model of Section 5.3.5. To this end some means of comparing the physical output of the experiment to the data from the Finite Element model was required. The attempts to show the relationship between the finite element model and the results from the experimental rig will be shown in the relevant sections in Chapter 5 for each of the experimental rigs.

4.7 Discussion of Improvements

4.7.1 Clamping & O-ring Damping

Clamping

As described in Section 4.3.1 the clamping has been improved in this experiment to try to improve the approximation to a clamped end condition for the pipe. This has met with some success: if we compare the data from the first revision of the experimental rig to that of the final experimental rig we can see that the degree of vibration near the end clamp has been reduced significantly, falling from $\sim 0.11\,\mathrm{mm}$ in the first case to $\sim 0.01\,\mathrm{mm}$ in the final case for the same maximum peak displacement in the same mode.

O-Ring Damping

Some deviation from the finite element model described in Section 5.3.5 has been introduced in the final version of the experimental rig. Some of this is due to the O-ring sealing of the smaller tank described in Section 4.2.5. If any deviation is caused by this addition then it will have to be accepted as a small error compared to the significant advantages of control and repeatability introduced by the use of a small volume of liquid during the experiments.

4.8 Summary

Through this chapter a number of different rigs have been described and detailed. Each of the rigs was successful at ice removal to some extent. The first rig could remove ice under several modes of flexural vibration, but the setup of the rig could not be repeated satisfactorily if any adjustments were made to the experiment.

The system was prone to mechanical failure, meaning that it often had to be reconstructed. As the damping coefficients etc. tend to show a significant sign of variance with the experiment being altered, little confidence could be taken in the

experimental results produced by the experiments in this format.

The Finite Element model of the system models the pipe at room temperature quite well. However, when the temperature of the pipe is well below the freezing point of the liquid, say by $\geq 10°$C then the stiffness of the silicon connecting tubing appears to increase significantly. Thus the results from the model (which does not incorporate this effect) make a less realistic prediction of the stresses in the pipe and in the ice, as the mode shapes have deviated from those predicted by the Finite Element. The Finite Element model of the first sonic rig is not described in Chapter 5.

Several iterations based on the experimental rig described above have been reported. Each shows an improved agreement when compared to the model of the system. The rigs have been incrementally changed to bring the physical rig closer to the predictions of the finite element model. The final iteration of the rig was capable of producing repeatable and reliable data for comparison with the Finite Element model of the clamped-clamped pipe.

Through this Chapter the rigs have been constructed and tested to show repeatability and reliability. Although each of the rigs was capable of ice removal under several operating conditions improvements have been conducted in order to extract the most useful data for determining the failure mechanisms in ice when acted on by structural vibrations. The last iteration that was carried out has produced a rig capable of ice removal in at least the first three excited modes of vibration (Flexural modes 1, 3 and 5). Further modes were not tested, as these modes gave a range of $50 - 1800$ Hz, which was considered large enough for this investigation: as significant differences in inertial, bending, cohesive stresses and adhesive shear stress could be investigated over this frequency range.

Chapter 5

Modelling Process

5.1 Introduction

This chapter will demonstrate the important parts of the modelling process used to achieve this goal. Not all of the work done in this area during the course of the investigation will be presented here. Instead this Chapter will focus on those aspects the modelling which led to improved understanding of the mechanisms behind ice removal from cooled metal surfaces.

Several areas of modelling are detailed in this chapter; the primary form of modelling being finite element analysis based on the commercially available software Ansys 6.1 [127]. Basic analytical modelling will also be described where appropriate.

A description of the basic models used to predict the behaviour of the systems of Chapter 3 will be given, along with their preliminary results. More detail will be provided on the modelling of the built-in pipe experiments of Chapter 4. Processes used to verify the accuracy of the model will be explained and the outcomes of the verification will be demonstrated. Using the model, the relative stress fields predicted from the Eigenvalue solutions will be compared and scaled using the experimental data as a reference. The stresses produced by scaling will be presented in full in Chapter 6.

5.2   Models of Chapter 3: Ice Removal from Cooled Metal Plates

5.2.1   Introduction

The initial experiments (where ice is formed onto a thin metal plate and removal is attempted using ultrasonic vibrations) are included in the thesis for various reasons. Firstly the experiments present an obvious way of approaching the problem of ice removal from cooled metal surfaces, so it is convenient to show the successes and failures of these methods to the reader interested in this area. Secondly, the experiments show how the understanding of the ice removal has been increased through the processes of experimental development. Thirdly, the Branson probe experiments have shown that the use of ultrasound to remove ice from a cooled metal surface is feasible.

In this section the experiments will be briefly described and the models associated with the rigs will be outlined. The verification of the rigs will be briefly described and some results from the initial experiments will be shown.

5.2.2   Factors under Consideration

An understanding of the factors influencing the systems must be gained to model their behaviour successfully. This section aims to identify the major forces and resulting stresses acting on the systems under normal operation.

Figure 5.1 shows the general layout of the systems from Chapter 3. The major features are the same from each experiment: the cooled metal surface is a plate, out of plane excitation is provided through a transducer aligned normal to the plane of the plate and ice is formed onto the surface of the plate. Flexural modes are then excited in the plate; the transducer was positioned to cause flexure along the Y -axis, however, flexure of the plate is also predicted along the X-axis. The resulting forces act on the metal and ice and generate a stress field within the two components of

the system. If the system design is successful, then ice will be removed.
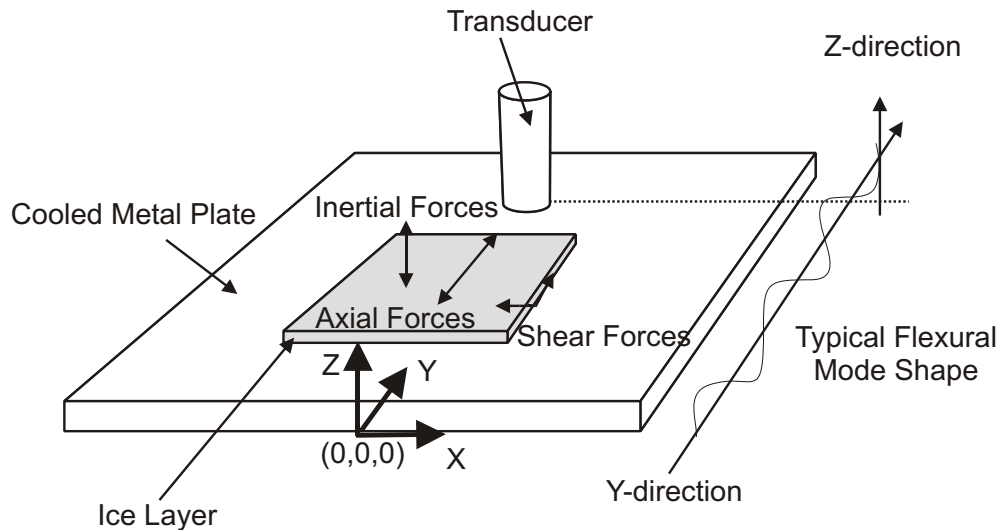
Figure 5.1: Generic layout of the systems described in Chapter 3

The system operating parameters, frequency and amplitude are predicted and measured using the finite element models described in this section and the experiments of Chapter 3. The mode shape of the finite element model can be compared to the mode shape measured from the experimental rig. If the results compare suitably well then the finite element model can be considered verified. Once this is achieved the stress field of the system can be predicted by scaling the output from Eigenvalue solutions to a physical parameter measured during experimentation.

Forces Acting on System

The flexural modes excited in the plates will cause a number of forces to act on the system. The cartesian co-ordinate system used for the finite element models is shown in Figure 5.1. The major forces that will be exerted on the system are as follows:

Axial Forces (F_{YY}) **and** (F_{XX})**:** As the excitation of the systems will cause flexural modes of vibration there will be axial forces acting on the system, due to the bending of the plate.

Shear Forces (F_{YZ})**:** Shear forces will also be created in the thickness of the plate and the ice due to the curvature of the system during the vibration in the flexural modes.

Normal Forces (F_{ZZ})**:** The major cause of forces normal to the plate will be due to the inertia of the system caused by the acceleration and deceleration of the plate in the Z-direction. These normal forces will vary with position on the plate due to the variations in acceleration with the mode shape of the flexural mode.

Stresses

The forces described above will create stress fields in the system of metal and ice. The stresses can be divided as follows:

Shear stress (σ_{YZ}, σ_{XZ} **and** σ_{XY})**:** The curvature of the plate caused by each mode of vibration, will produce shear stresses in the system. These shear stresses will act in the plate, ice and at the interface between them. Of particular interest are the shear stresses in the plane of the plate, acting at the interface. The stress component σ_{YZ} caused by the flexure of the plate in the Y-direction is likely to dominate the other shear stresses. If the sum of the shear stresses is greater than the adhesive strength of the interface then the ice will be cleanly removed. If the shear stresses are greater than the cohesive strength of the ice but less than the adhesive strength, then the bulk of the ice may be removed leaving a residue at the interface.

Shear stresses due to differentials in the thermal expansion coefficients in the two materials may be created. However, studies by Mantovani and Valeri [128] have shown the magnitude of these shear stresses to be small in comparison with the tensile and adhesive strengths of ice at comparable temperatures to those covered during these experiments, i.e. T $> -25°$C. Therefore, this shear stress is not considered during modelling of this system.

Normal stress (σ_{ZZ}): Similarly the vibration of the plate will cause normal stresses to act at the interface and in each material. This stress will be caused by inertia and Poisson's effect due to the stretching of the plate, with inertia likely to dominate. If the sum of the normal stresses is greater than the adhesive strength of the bond then the ice (or sucrose) layer will come free from the plate in areas where this imbalance occurs. Cohesive failure could also be caused, again leaving a residue on the plate.

Tensile stresses in ice (σ_{XX} and σ_{YY}): Bending stresses in the ice will be generated by the vibration of the plate. If this stress overcomes the cohesive strength of the ice then cracks may be nucleated normal to the direction of the stress (i.e. cracks in the XZ plane), which will be perpendicular to the main plane of the plate. As such these stresses will not lead to ice removal on their own. However, if a crack reaches the metal surface it may initiate cracks at the interface between the ice and the plate.

Other Factors

Of course a number of factors will play a part in determining where the forces will act, the nature of the stress field, and the relative importance of the different forces/stresses. Major factors in determining the dynamic behaviour of the system are the dimensions of the plate (determining stiffness, second moment of inertia), ice layer thickness, and transducer amplitude of vibration at various operating frequencies. The mechanical properties of the ice will also be affected by a number of factors; for example the grain size of the ice crystals, the temperature and the strain rate.

The importance of many of these factors can be assessed and modelled using a combination of an initial finite element model and complementary experimental investigations. This method will be used in each of the following sections on the experiments of Chapter 3 to determine optimal operating conditions for producing suitable flexural modes.

5.2.3 PZT Disc on Aluminium Plate

In the following sections various experiments of Chapter 3 will be briefly outlined, starting with the aluminium plate ($100 \times 100 \times 1.2$ mm) excited by a small PZT-disc.

Description of Model and Assumptions

An aluminium plate of 100 mm by 100 mm and 1.2 mm thick was used as the basis for this setup. These dimensions were chosen to coincide broadly with dimensions used by Unilever Research Group [22] for another experiment, so existing cooling equipment could be used. The first step in the process was to create a model of the plate to predict the natural frequencies of flexural modes in a frequency range that would be compatible with pre-existing transducers that were available in the laboratory.

One half of the plate was modelled, using the line of symmetry of the system (i.e. cutting the plate in the YZ plane at the X-axis). A symmetry condition was applied at the area of the 'cut' in the X-direction, to account for the central location of the transducer. As the plate in the experiment rested on a soft foam base no clamping constraints were required in the model and it was considered to be a free plate.

It was assumed that the transducer would act as a point source exciting the system at a given frequency. The ice layers formed on the top surface of the plate were very thin (≤ 0.5mm). They were not included in the finite element model, and only the natural frequencies of the plate itself were obtained. The mode shapes obtained from this model were used to estimate the mode shape of the ice layer, assuming that it had little effect on the shape of a given mode.

An eigenvalue solution was performed to determine the modes in the frequency range in which the transducer nominally operated. i.e. $100 - 300$ kHz. Many modes were found in this range, after some experimentation, using a standard 200 kHz transducer [129] coupled to the plate by treacle. A mode at ~ 150 kHz was found to be promising, giving peak amplitudes of displacement in the order of 53 nm. Other

modes investigated had somewhat smaller amplitudes of vibration in the order of 30 nm. The results presented are based on experiments and modelling of this mode.

Once the frequencies were predicted and the accuracy of the system had been checked, then a more robust rig was constructed on the basis of these findings. The aim was to produce a rig capable of removing a thin ice layer from the cooled metal plate, by vibrating the plate at this flexural mode.

Validation

The validation of the performance of the model was conducted in an approximate manner. As mentioned above, the ice layer was not included within the model. A laser vibrometer was focused on the plate. By scanning over a range of frequencies, the natural frequencies of the system could be obtained. For each resonance the mode shape could be determined by scanning the laser spatially.

Use of this data could be made to verify how well the finite element model predicted the behaviour of the system. For example the natural frequencies of flexural modes were predicted from the finite element model. By comparing these frequencies with the frequency response function of the rig some idea of the accuracy of the model could be obtained. For these frequencies a displacement mode shape could be extracted from the eigenvector part of the solution, which was also compared to the experimental data.

FEM Predictions kHz	Experimental Data kHz	Error %
149.3	149.1	0.1

Table 5.1: Comparison between finite element prediction of resonant frequency and real resonance

Table 5.1 shows the correlation between the frequency of the mode of interest as determined from the experiment and as predicted by the finite element model. Ad-
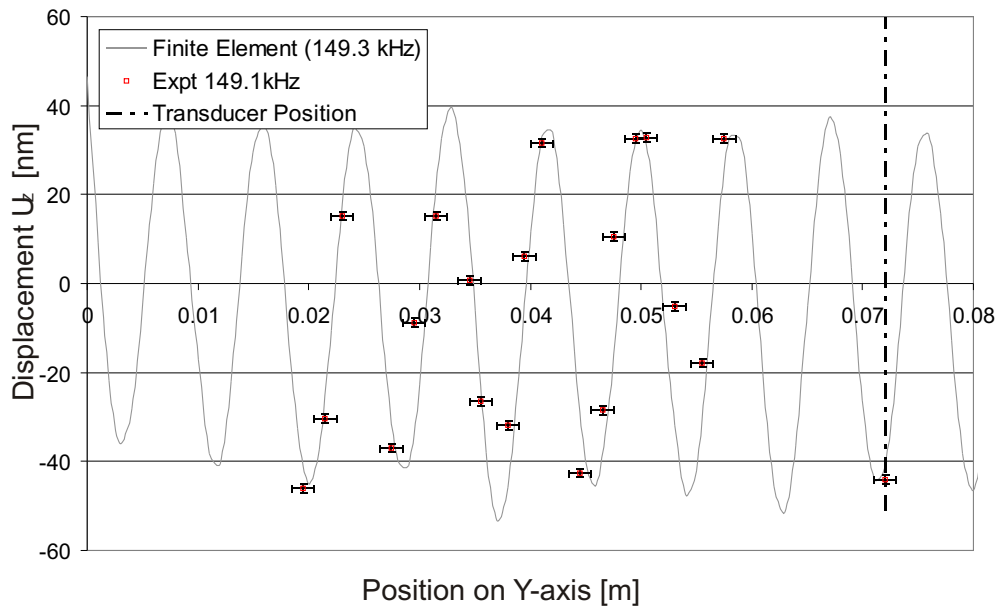
Figure 5.2: Graph showing the comparison between the finite element model predicted mode shape and the mode shape measured by experiment.

ditionally the mode shape at this frequency is shown in Figure 5.2. Good agreement is shown between the natural frequency predicted by Ansys and that which was determined experimentally. Reasonable agreement is shown between the mode shape from Ansys and the experiments. The agreement is good enough that the model can be used to determine an estimate of the axial stress in the plate, as shown in the next paragraphs. This measurement included a verification of the phase. Whereas, Figures 3.5(b) and 3.9(b) did not include a verification of the phase.

Findings

By using the same scaling factor that was used to "match" the plot of the displacement (U_Z) from Ansys to the data from the experiment, an estimate of the axial stress (σ_{YY}) in the plate can be determined.

At this mode and at the maximum displacement possible, the stress generated was in the order of 8×10^5 Pa in the axial direction. Assuming that a very thin layer of

ice was attached to the plate, and that it had little effect on the mode shape of the plate, an estimate of the stress in the ice (σ_{YY}^{Ice}) can be obtained.

The strain in the Z-direction remains constant in the ice and aluminium at either side of the interface between them. We know that $\sigma \simeq \varepsilon E$ for both the ice layer and the aluminium plate, and that the strain is constant at the interface between the two layers. It should be noted that temperature effects due to αT were not explicitly accounted for in this work. We have an estimate of the stress experienced in the aluminium plate (σ_{YY}^{Plate}) from the scaled Eigenvalue solution from the finite element model. Comparing the strain in the ice with the strain in the plate at the interface gives the following relationship:

$$\sigma_{YY}^{Ice} \simeq \frac{E_{Ice}}{E_{Aluminium}}\sigma_{YY}^{Plate} \tag{5.1}$$

Using equation 5.1 and the values: $E_{Aluminium} = 75\,\text{GPa}$ [116], $E_{Ice}|_{T=-6^\circ} = 9.32\,\text{GPa}$ [26] and the estimate of σ_{YY}^{Plate}, we can estimate the axial stress at the interface of a thin layer of ice. The value obtained is $0.1\,\text{MPa}$. This value is considerably less than the value of $0.48\,\text{MPa}$ predicted by Gold [115] for crack nucleation in undamaged ice with grain sizes in the order of the thickness of ice considered, i.e. $\leq 0.5\,\text{mm}$. Higher values of stress might be required to cause nucleated cracks to propagate, due to the increased energy required to grow the plastic deformation zone at the crack tips.

5.2.4 Mass Backed Transducer on Aluminium Plate

In an attempt to increase σ_{YY}, a narrow bandwidth transducer was constructed from a thin PZT-disc with a mass backing attached firmly via a superglue layer. The centre-frequency of the transducer, attached to the system, had reduced to $95.8\,\text{kHz}$. More detail can be seen in section 3.3.2. The mass backing should act to narrow the bandwidth of the transducer, with more energy at one frequency. This should lead to an increase in the amplitudes of displacement. However, as the mass of the transducer is increased, the resonant frequency should fall as the relationship $f = \sqrt{\frac{k}{m}}$, where f is the frequency, m is the mass and k is the stiffness of the

transducer. More detail can be seen in section 3.3.2.

Assumptions + Description of Model

The model used for the mass backed transducer was the same as that for the PZT-Disc on the aluminium plate described above. The only variation to the model was the frequency range over which the model would be evaluated. As the centre frequency of the transducer had changed, reducing from $\sim 215\,\mathrm{kHz}$ to $95.8\,\mathrm{kHz}$, a modal solution around the new frequency was required, i.e. $90 - 100\,\mathrm{kHz}$.

It should be noted in lightly damped structures that a small shift in the frequency of the system can mean that the frequency that the system is being excited at is no longer coincident with the of the natural frequency of the system. This could easily be the case during ice cracking on the system.

Verification

The basic verification was performed for this case in the same way as the case in section 5.2.3. The mode was predicted at $95.8\,\mathrm{kHz}$ by the finite element model and the experiment revealed the equivalent mode to be at $95.1\,\mathrm{kHz}$. Again this showed good agreement between the prediction of the finite element model and the experimental data in terms of the natural frequency. The agreement between the two mode shapes was reasonable - but not without some variation.

Findings

Using the same argument as described in section 5.2.3 the axial stress in the plate can be estimated. In this case, although the amplitude of vibration of the plate had increased to $120\,\mathrm{nm}$ from $48\,\mathrm{nm}$ in the previous case, the maximum axial stress fell to $2.8 \times 10^5\,\mathrm{Pa}$.

It is possible that the ice started to crack during the experiments, and that the cracks in the ice of a lightly damped system could cause the resonant frequency of the system to change enough that the forcing frequency did not lie in the half-power point frequency range. If this was the case the amplitude would decrease significantly and the ice would not be removed. This was not investigated further during the course of these experiments.

5.2.5 Branson and Etrema Probes on Steel Plate

Following the findings from the previous sections it was clear that the amplitudes achievable from the standard non-destructive testing type piezo-electric transducers would be unlikely to induce a stress field of great enough magnitude to remove the ice from the metal plates under investigation.

With this in mind some modifications to the system and hence the finite element models were required to try to produce stress fields with a significantly greater magnitude. An obvious first step was to increase the amplitude of vibration of the system *considerably*. A convenient way to achieve this was to use a commercially available probe that operated at a fixed frequency producing high amplitudes of vibration. A Branson probe was a good choice as amplitudes of $40 - 120\,\mu$m were claimed as free tip displacement amplitudes at $20.0 \pm 0.5\,$kHz.

Some limitation on the size of the plate was introduced by the use of an aluminium cooling plate supplied by Unilever [22] following from related experiments which they had conducted. A combination of finite element modelling and experimentation was used to find a suitable flexural mode of vibration. It was key that the mode should fall within the normal operating frequency range of the Branson probe. Figure 3.8 shows the typical experimental layout of the system investigated for Branson or Etrema probes.

Assumptions + Description of Model

The aim of this model was to produce a quick portrayal of a small steel plate with a transducer attached, producing flexural modes of vibration. The aim was to use the model in a short parametric study to determine the dimensions of a plate which would have a suitable flexural mode in the frequency range of $19.5 - 20.5\,\mathrm{kHz}$. Experiments would then be conducted to verify the predictions of the model.

The plate dimensions were limited to $40 - 60\,\mathrm{mm}$ in width and $70 - 150\,\mathrm{mm}$ in length. It was decided that the material used should be less than $1\,\mathrm{mm}$ thick, to allow high amplitudes of vibration through reduced stiffness. The minimum dimensions were required to locate the plate securely on M2 aluminium studs that were at each corner of the cooling system. The maximum dimensions were determined by an outer enclosure used by Unilever for atmospheric regulation.

Therefore, the finite element model represents a thin plate with dimensions varying as described above, however, holes in the plate were fixed relative to the M2 studding of the cooling plate (i.e. two holes at $10\,\mathrm{mm}$ from the front and side edges of the plate (one on each side), and two holes at $10\,\mathrm{mm}$ from the side, $60\,\mathrm{mm}$ from the front of the plate). A number of different lengths were used to change the expected frequencies of the flexural modes of the plate. The width of the plate was fixed to $50\,\mathrm{mm}$ to correspond to the width of the cooling plate.

A number of lengths, in the range of $70 - 150\,\mathrm{mm}$ were modelled using the finite element model. Eigenvalue solutions were obtained and the mode shapes extracted. Eventually a $0.5\,\mathrm{mm}$ thick plate with dimensions of 50 by $84\,\mathrm{mm}$ was chosen. Figure 5.3 shows the two modes that were predicted by Ansys [127] in, or around, the frequency range, of $19.5 - 20.5\,\mathrm{kHz}$, in which the Branson probe operates.

Verification: Branson Probe

Good agreement was found between the experiments and finite element model prediction in terms of natural frequencies and mode shape, shown in Figure 3.5(b).
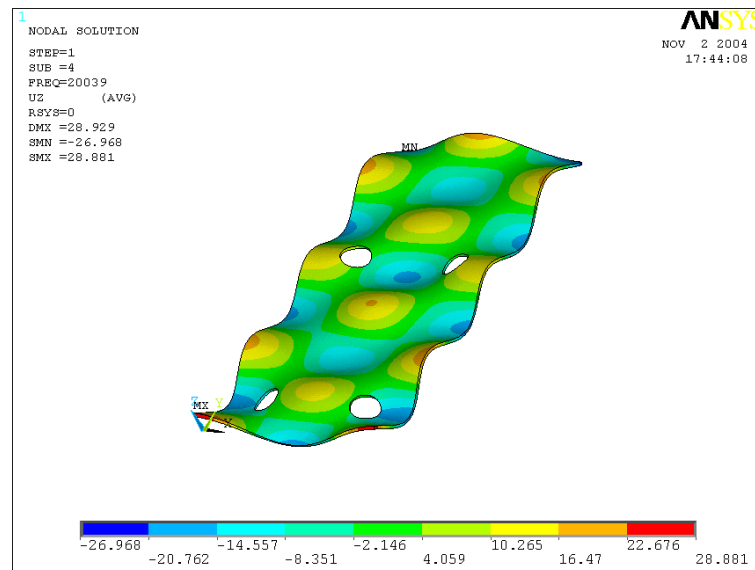
(a) Possible Mode of Vibration of Small Steel Plate under Branson Probe or Etrema Probe Excitation: @ ~ 20.0 kHz.
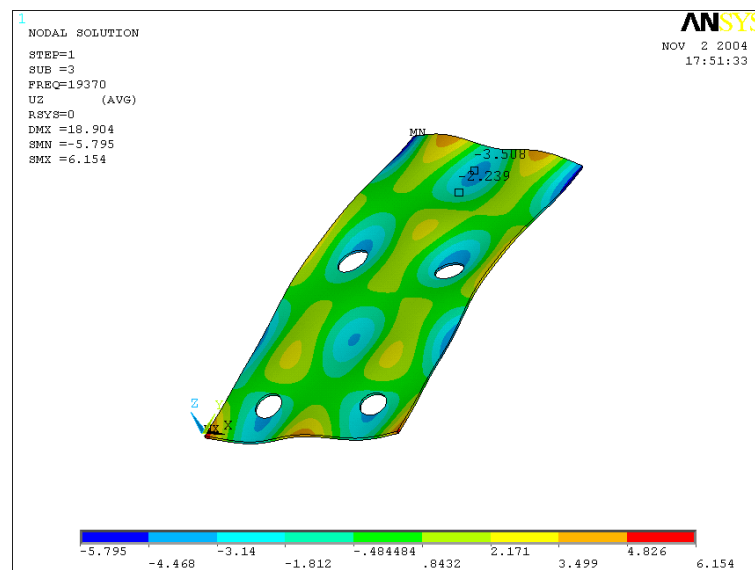
(b) Another Possible Mode of Vibration of the Small Plate under Excitation by the Branson or Etrema Probe: @ ~ 19.4 kHz.

Figure 5.3: Ansys predictions of the mode shapes of the small plate under perpendicular excitation. Mode shapes taken from Eigenvalue solutions.

It appears that the mode which was excited is the flexural mode at $20.0\,\mathrm{kHz}$, as depicted in Figure 5.3(a). This was determined by comparison of the data to the predicted mode shape. The frequency also ties in well with the operating range of the Branson probe - if the system moves out of this frequency range the probe will not work, due to an electronic limitation applied by the amplifier. The data was collected by scanning the laser vibrometer along the Y axis (refer to Figure 5.1), while the system was operating.

Findings: Branson Probe

Figure 3.6 shows the estimate of σ_{YY}^{Plate} along the Y-axis. The scaling ratio which was used was the same as that used to produce the finite element mode shape of Figure 3.5(b). By using equation 5.1 and substituting the Young's modulus of steel for that of aluminium, an estimate of the axial stress in a thin ice layer was obtained. A value of $12.2\,\mathrm{MPa}$ is obtained using this method [37, 35, 36]. This compares well with values for cohesive failure of ice in the literature in the temperature ranges over which the experiments were conducted, (i.e. down to $-18°\mathrm{C}$). Values for adhesion can be significantly lower than this, typically $\frac{1}{10}$ of the tensile strength [61, 73].

Verification: Etrema Probe

To determine the stress fields in the experiments using the Etrema probe and investigate the reasons why the ice could not be removed it was desirable to use the existing model of the Branson probe on the small plate. First the mode shape must be compared between the finite element model and the experimental results. With a suitable comparison some confidence can be drawn that the Eigenvalue stresses can be scaled to give the "actual" stresses.

Figure 3.9(b) shows that a good agreement can be reached. The finite element model was scaled to "match" the Z-displacement of the experiments using a single constant, thus maintaining the relative values from the model. The scaling factor which was obtained can then be used to scale the relative stresses from the Eigen-

value solution of the finite element model. The axial stress (σ_{YY}) obtained from this method is illustrated in Figure 3.10. Confidence in these values of stress was obtained by the good agreement between the experimental Z displacements and the scaled finite element model Z displacements.

Findings: Etrema Probe

We know that the ice remains attached to the plate during the experiments in most cases during the Etrema Probe experiments. Therefore, if we assume that a thin layer of ice has little effect on the amplitudes of the system under ultrasonic excitation, an estimate of the stress in the ice at the interface can be made.

Again making use of equation 5.1, we can estimate the axial stress in the ice. The value of Young's modulus for steel must be substituted for that of aluminium. The estimate of the axial stress in the ice is 0.38 MPa. This value is on the verge of crack nucleation as predicted by Gold [115] for ice crystals around 1 mm in diameter (0.48 MPa). The peak-peak amplitudes of vibration achieved were $\sim 1.5\,\mu$m. This is somewhat lower than the quoted $10.5\,\mu$m maximum peak-peak amplitude of vibration quoted by the probe manufacturer [114]. Therefore, with improved actuation these experiments might be worth revisiting.

5.2.6 Section Summary

This section has illustrated the different methods that were attempted to try to remove ice from a cooled metal plate. The Branson probe was the only successful method and this is reflected in the finite element modelling, which demonstrates that the axial stress in the ice is significantly greater than that required to cause cracks to form in the ice. Even if the other stresses in the system are an order of magnitude lower than the peak axial stress, they should still be great enough to overcome the adhesive strength between the plate and the ice, (as is indeed the case).

However, due to the practical limitations of the experiments, modelling was not

conducted beyond this basic level. Instead, the approach of experimentation on plate structures in the ultrasonic regime was abandoned in favour of pipes in the sonic frequency regime. The modelling of such systems is described in the following section.

5.3 Models of Chapter 4: $\frac{1}{4}''$ Pipes

5.3.1 Introduction

The prime aim of this thesis is to determine the failure mechanisms when ice is removed from a system comprising a cooled metal surface with an ice layer attached. To achieve this a suitable system must be devised, where the factors influencing the behaviour of the system can be monitored and the resulting stress fields can be predicted for a number of operating conditions.

As part of an iterative process, the rigs of Chapter 4 were produced in conjunction with an ongoing modelling process. As a result of basic analytical and finite element models of the systems, a refined experimental rig was produced. This rig was made from a $\frac{1}{4}''$ 316L stainless steel pipe. A steel T-connector was welded perpendicular to the axis of the pipe at the of centre it. The T-connector was attached to a modal testing type shaker, which provided the actuation to the system. The shaker was driven at a number of frequencies to excite flexural modes in the pipe.

The stainless steel pipe was held in a specially constructed cylindrical acrylic tank and was clamped securely at the exit to this tank at either end. The pipe was filled and the pipe could be immersed in a variety of liquids (water, 10% and 20% sucrose solutions). Ice was formed on the outer surface of the pipe. The ice was subsequently removed by exciting the system near to a flexural resonance of the system. The response of the system to the excitation leading up to and including the removal of the ice was monitored by two strain gauges, reading the axial strain at various points along the bottom of the pipe, at $Z = 0$ and $187\,\text{mm}$ (see Figure 5.1). A finite element model of the system was created using Ansys 6.1 [127].

A number of physical and finite element models were created during the development of the experimental rig. The first configuration involved a copper pipe with a T-connector rod attached to its centre at right angles to the pipe, with the ends of the pipe free in the liquid. This method was rejected because of problems in correctly modelling the boundary conditions for the free ends. When the liquid was at room temperature the model behaved as predicted by the finite element model, but, when the liquid began to freeze, an ice layer formed on the silicon tubes connecting the pipe to the cooling bath. This added an extra mass to the end of the pipe and hence changed the natural frequency and mode shape of the system. This made running experiments and verifying the finite element model more complicated. Instead a built-in pipe system was developed, which removed this problem.

The following section will describe the modelling of two pipe systems, based upon a clamped-clamped configuration. The model for the two systems was in essence the same, differences being material properties for the sucrose, ice, copper and stainless steel, and minor geometric changes.

5.3.2 Factors Under Consideration

Co-ordinate System

The basic co-ordinate system and rig layout is shown in Figure 5.4. As can be seen, the pipe system (fully described in Chapter 4) consists of a pipe fixed at each end. The stress field components as calculated by finite element modelling are shown in Figure 5.5, and will be referred to during this section. The pipe is excited at its centre perpendicular to the Z-direction. Cooling fluid flows through the centre of the pipe, below the freezing point of the liquid; causing ice to form on the outer surface of the pipe. The ice layer is removed by structural vibrations of the pipe at or near to a flexural mode of vibration.
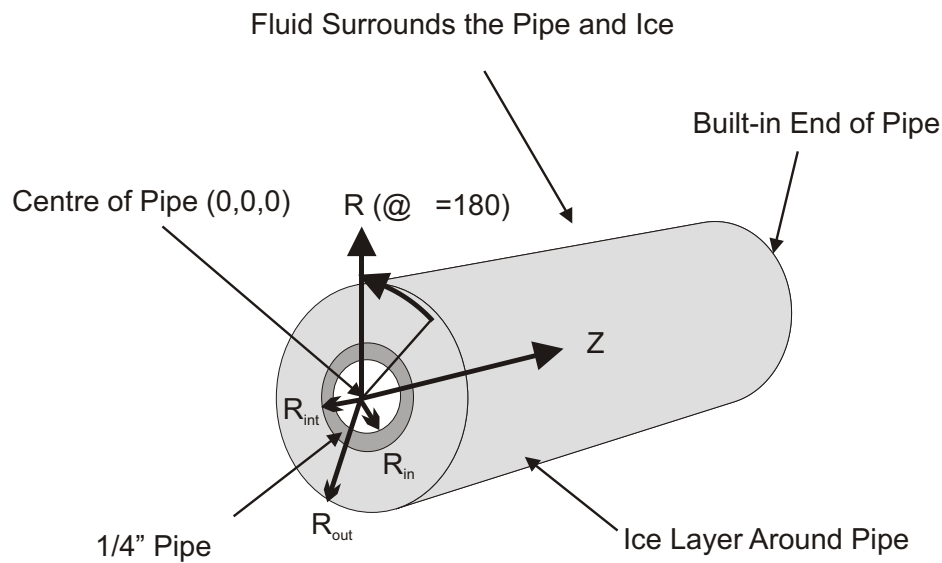
Figure 5.4: Cylindrical co-ordinate system of the built-in pipe described in Chp. 4.

Forces Acting on System

A number of forces acting on the system have been identified. The forces that are to be considered while modelling the system are shown below:

Axial Force Due to Bending Axial forces are caused in the pipe and in the ice due to the bending of the pipe. These forces act both in the pipe and the ice layer and will be predominantly in the Z-direction. As the pipe is slender and low order modes of vibration were excited, it is expected that these forces will be large compared with the other forces acting on the system.

Shear Forces Due to Bending: The flexural modes excited in the pipe will also cause shear forces to be generated in the pipe. However, as the pipe is long and slender the shear forces should be small compared with the axial forces caused by the bending. This does not mean that the shear forces can be neglected. Shear forces will be described by the forces acting at the interface between the pipe wall and the ice in the $r\theta$, rZ and θZ planes.

Drag Forces (Normal and Shear): As the pipe and ice system will be submerged
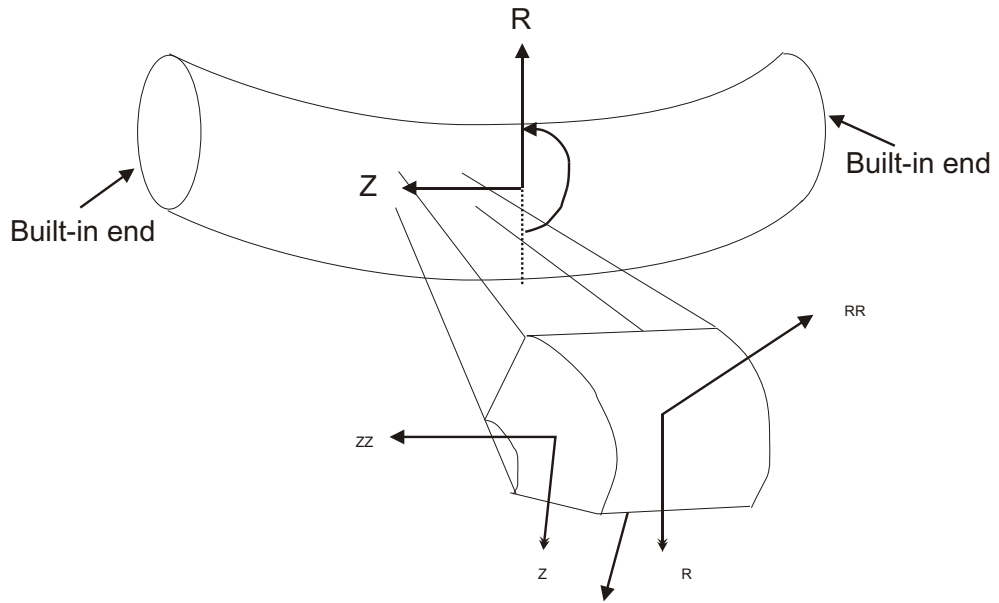
Figure 5.5: Components of the stress field expected within the system
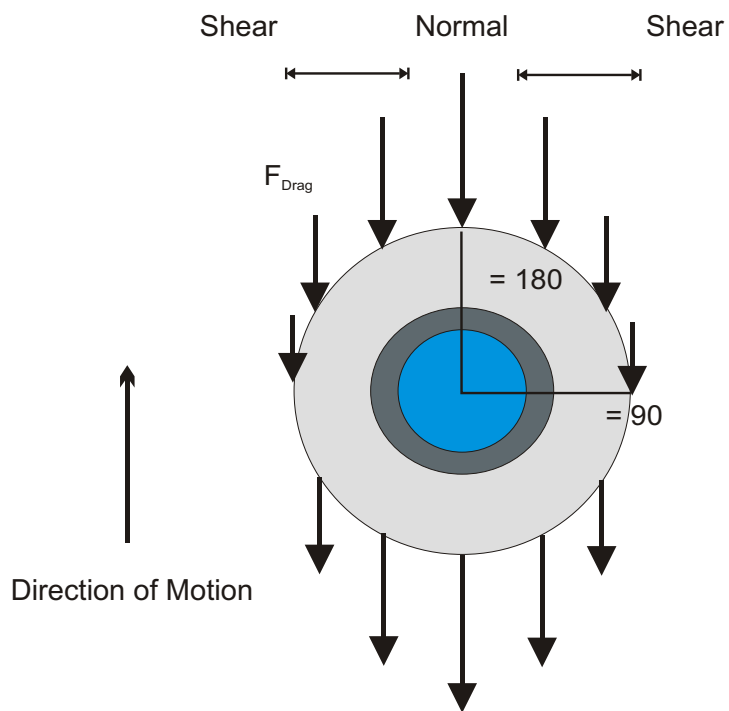
Figure 5.6: Illustration of approximately how and where drag forces will act.
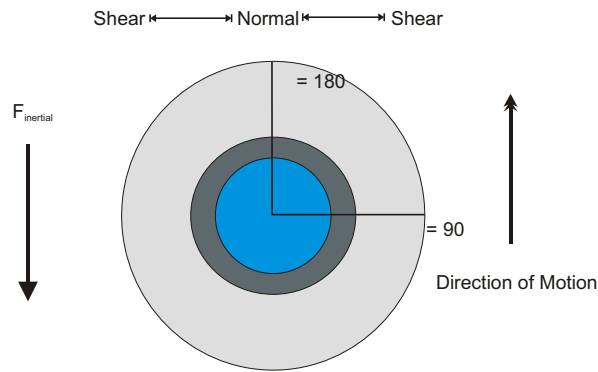
Figure 5.7: Illustration of how and where inertial forces will act, resisting the motion of the system.

in a liquid, there will be drag forces acting in the opposite direction to the fluid motion, retarding the motion of the pipe. These forces will largely act in the direction of R at $\theta = 180°$, when the pipe is moving in the direction of R at $\theta = 0°$ as shown in Figure 5.6. The drag forces will vary with the velocity profile as it varies in the Z-direction: which will depend on the mode shape of the vibration. The drag forces act parallel to the R-direction at $\theta = 180°$ & $0°$ over the length of the pipe and ice, wherever the pipe is moving in that direction. These forces can produce normal and shear forces on the system. For example normal forces will be created at the centre of the pipe but shear forces will act at R_{out} at $\theta = \pm 90°$ due to the viscous drag from the pipe moving in the surrounding liquid. This variation between normal and shear forces is illustrated in Figure 5.6.

Inertial Forces (Normal and Shear): The acceleration of the pipe as it vibrates at a resonance will induce inertial forces in the ice normal to the axis of the pipe at the top and bottom surfaces ($\theta = 0°$ & $180°$), whereas the same forces acting away from the centre of the pipe will tend to induce shear stresses, as can be seen in Figure 5.7. These forces will cause a force at the interface between the ice and the metal at their interface. As the frequency of each mode increases the importance of these effects grow as the relative accelerations

of the pipe will increase. Again the mode shape of the pipe will affect the accelerations in the pipe. Hence, the inertial forces acting on the ice will vary with position in the Z-direction.

Stresses Expected in System

Figure 5.5 shows the expected locations of the stresses in the system. For a full prediction of the stress field see Section 5.3.5.

Shear Stresses ($\sigma_{r\theta}$, σ_{rZ} and $\sigma_{\theta Z}$): Shear stresses at the ice metal interface will be caused by a combination of the forces acting on the pipe and ice due to the vibrations. Shear stresses will arise from the forces acting due to drag, inertial forces and the shear stresses generated by the flexure of the pipe. If the shear stresses are greater than the shear adhesive strength then the ice may be freed from the surface of the pipe. Shear stresses will also act in the body of the ice and may cause cohesive failure away from the interface.

Normal Stresses at Interface (σ_{rr}): The normal forces acting at the top and bottom of the pipe due to drag and inertia cause normal stresses at these locations. If the stresses generated at these locations are greater than the normal adhesive strength of the bond between the metal and the ice then bond will fail and the ice will come free from the metal surface.

Tensile Stresses in Ice Layer (σ_{ZZ}, $\sigma_{\theta\theta}$ and σ_{rr}): Due to the bending of the pipe, there will be an axial stress created in the Z-direction. The magnitude of this stress will vary in the Z-direction with nodes and anti-nodes along the top and bottom surfaces of the pipe. Additionally there will be a variation in the θ-direction, with an absolute maximum at $\theta = 0°$ and $180°$ and a minimum at $\theta = \pm 90°$. The axial stress in the pipe cannot directly remove the ice from the pipe. Instead the ice may be broken into collars that will remain on the pipe. The stress in the R-direction could cause layers of ice to come off by cohesive failure, but the main consideration is described in the above paragraph on shear stresses.

5.3.3 Failure Mechanisms

Using suitable modelling the stress field described in the above section was determined. Having an understanding of stress variations in the ice allows for some estimation of the mechanisms of failure in the ice and also the order in which such failure is likely to occur.

Method and Order of Failure

For the ice to be removed cleanly from the pipe several events must occur. The ice must fail in the hoop (θ) *and* axial (Z) directions. For example *both* conditions: $\sigma_{\theta\theta} > \sigma_{Critical}^{cohesive}$ and $\sigma_{ZZ} > \sigma_{Critical}^{cohesive}$ must be achieved. In addition to this the interfacial shear ($\sigma_{r\theta}$, σ_{rZ} or $\sigma_{\theta Z}$) or normal σ_{rr} stress must overcome the shear or normal adhesive strength of the bond between the ice and metal at the interface.

The net effect of this is to say that the ice must be removed in "chunks". Of course ice could be removed without all of the above conditions being met. For example the ice could fail cohesively in three directions Z, θ and R or Z, θ and a shear failure in the body of the ice. However, such a failure mechanism would not represent success in this investigation, as the aim is to prevent ice build-up on the pipe surface.

To be able to predict when ice will be removed cleanly it is paramount to determine the adhesive and cohesive properties of the ice and sucrose solutions under investigation under the conditions experienced during the experiments. The yield and tensile strengths of both ice and sucrose have shown temperature and strain rate sensitivities [35, 36, 37]. To accurately predict the likely response of a system, a map of these failure criteria i.e ductile-brittle failure transition, must be constructed. An attempt to create this information is shown in section 6.2.

By careful comparison of the stress data generated using a combination of experimental results and finite element modelling to the failure stresses predicted in the literature the hypothesis of the failure mechanism above can be tested.

5.3.4 Basic Analytical Model

Using the formulas for a built-in beam from Blevins [130] a first estimate of the natural frequencies of the flexural modes of a built in pipe can be obtained. Equation 5.2 is used for this purpose.

$$f_i = \frac{\lambda_i^2}{2\pi L^2} \left(\frac{EI}{m}\right)^{\frac{1}{2}} ; \, i = 1, 2, 3. \tag{5.2}$$

f_i is the natural frequency of the i_{th} flexural mode of vibration; λ_i is the root of the frequency equation; E is the Young's modulus of the pipe; I is the second moment of inertia in the bending direction and m is the mass of the pipe.

The values for λ_i in the range $i = 1 - 5$ were required to assess the frequencies of the modes that would be encountered during experimentation. Only symmetrical modes are expected due to the centrally attached T-connector. Therefore, the values for λ_1, λ_3, and λ_5 are required.

The values of the natural frequency were calculated in this way to determine the dimensions of the pipe to produce flexural modes over a range of frequencies which could be successfully generated in the frequency range of the shaker (i.e. $0 - 3\,\text{kHz}$). This was important as some factors to be investigated might be strongly affected by changes in the frequency of the system (operating in different modes), due to changes in the relative velocity and acceleration in the system. Therefore a significant variation in the natural frequencies of the modes would be advantageous in determining the changes in these effects. A frequency range of $\geq$ one order of magnitude would be ideal. (To determine frequency effects such as $\dot{x} = 2\pi f |x|$ and $\ddot{x} = -(2\pi f)^2 |x|$).

Another reason for this modelling was to try to produce a mode at or around $50 - 60\,\text{Hz}$ to compare with data from another experiment conducted at the same frequency but using a rigid body motion (the experiment is not included in this Thesis). The pipe has a central mass [M], effectively the T-connector rod. The effect of the central mass was incorporated using a modified model [131]. Using equation 5.3 and numerically determining the roots, improved values of λ_i can be

obtained. This is the frequency equation for a built-in beam of mass, m, and with a central mass, M, attached, for symmetrical modes of vibration.

$$\left(\frac{M}{m}\right)\left(\frac{\lambda_i}{2}\right)\left[1 - \cos\left(\frac{\lambda_i}{2}\right)\right] = \cos\left(\frac{\lambda_i}{2}\right)\sinh\left(\frac{\lambda_i}{2}\right) + \sin\left(\frac{\lambda_i}{2}\right)\cosh\left(\frac{\lambda_i}{2}\right) \quad (5.3)$$

Tables 5.2 and 5.3 show the experimental results from the copper and steel pipes respectively. Taking the values calculated from Equation 5.3 an estimate of the natural frequency of the system is obtained - giving an error which overestimates by $\leq 10\%$ the experimental figure obtained, (except for Mode 1 for the stainless steel pipe shown in Table 5.3, where the analytical figure is 11.5% less than the recorded figure).

Further modelling was possible [132], however, as reasonable agreement had already been obtained (using the clamped pipe with central mass model) this approach was not required. An accuracy of 10% was seen as an adequate level of modelling for this investigation.

	Built-In Pipe		Pipe with central mass [M]		Experimental	Error
Mode i	λ_i*	f_i (Hz)	$\lambda_i(\frac{M}{m})$	f_i (Hz)	f_i (Hz)	%
Mode 1	4.7300	141.9	2.90 ± 0.01	53.3 ± 0.5	52 ± 0.1	2.7
Mode 3	10.9956	766.7	9.65 ± 0.01	590.5 ± 2.1	558 ± 4	5.8
Mode 5	17.2786	1893.2	15.831 ± 0.0005	1589.1 ± 0.1	1499 ± 13	6.0

Table 5.2: Analytical estimate of flexural natural frequencies and comparison with experimental data for the copper pipe. (∗ Taken from Blevins)

5.3.5   Finite Element Model

The analytical model described above was useful for gaining a preliminary understanding of the physical behaviour of the rig. It was used to plan experiments, by predicting suitable frequencies of operation. However, little or no information was available regarding the strain and stress fields that would be produced in the pipe and ice under experimental conditions. The finite element modelling performed to

Mode i	Built-In Pipe		Pipe with central mass [m]		Experimental	Error
	λ_i	f_i (Hz)	λ_i	f_i (Hz)	f_i (Hz)	%
Mode 1	4.7300	194.4	2.88 ± 0.01	69.9 ± 0.5	79 ± 1	-11.5
Mode 3	10.9956	1050.5	9.61 ± 0.01	777.9 ± 2.4	746 ± 8	4.3
Mode 5	17.2786	2594.1	15.806 ± 0.001	2104.8 ± 0.2	1950 ± 12	7.9

Table 5.3: Analytical estimate of flexural natural frequencies and comparison with experimental data for the stainless steel pipe

obtain an improved understanding of the failure mechanisms is described in the following section.

Factors Covered by Modelling

A finite element model was created to give more insight into the mechanisms that were acting on the system. The aim was to create a model that would suitably represent the significant aspects of the physical rig, whilst allowing short enough computation times that a parametric study could be conducted for a number of variables, such as thickness of ice formed and the mechanical properties of the ice with concentration of sucrose from $0-20\%$ (by mass).

The pipe is fully represented in the finite element model. The T-connector is represented as a point mass at the mid-length of the pipe on the upper surface and is not modelled exactly as it appears on the physical rig. The ice layer is modelled as a complete covering on the surface of the pipe with a uniform thickness. In the experiments, some variation in thickness of the ice layer was observed, particularly at the mid-length of the pipe, where the T-connector attached to the stainless steel pipe. The clamps at the end of the pipe were modelled using a zero displacement boundary condition.

In the finite element model the fluid surrounding the pipe is not modelled. This was omitted for two reasons: i) to produce an acceptable computation time, and

ii) because effects of the drag forces acting on the system were found to be small compared to the other forces acting on the ice layer. Therefore, the drag forces are not included in the finite element model of the pipe.

Assumptions

A model of the built-in pipe system for both copper and steel pipes was created.

The following assumptions were made:

- The pipes were perfectly clamped at each end. Experimentation had already shown this was not the case, but any errors were thought to be acceptable as the amplitudes of displacement at the end of the pipe were small compared with those at displacement anti-nodes. This can be seen in Figure 5.9.

- The T-connector rod attaching the pipe to the shaker acts as a rigid central mass. This was checked by modelling the T-connector in Ansys. One flexural mode of the rod was found in the measured frequency range of the experiments (at 1040 Hz), but no longitudinal modes were predicted. The excitation for the flexural mode was minimal due to the layout of the system. During experiments to determine the natural frequencies of the system a *very* small strain peak (ε_Z) was noted at 1119 ± 10 Hz which may be due to flexural vibration in the T-connector. However, it was very small compared to the flexural modes of the pipe and not close to the frequency of these modes and so it was concluded that it was unlikely to interfere with them.

- 100% adhesion is achieved between the metal of the pipe and the external ice layer. This assumption will require further discussion in chapter 6.

- When experiments are conducted near, but not at, the natural frequency of the system, the stresses predicted from the finite element model can still be considered valid. This is important as the experiments were conducted at the strain maximum near each mode, rather than at the system resonance, i.e. the operating frequency was just below the natural frequency of the resonance. A

system resonance occurs when $\frac{F}{\varepsilon}(f)$ is at a minimum. Such a minimum occurs when the strain (ε) is a maximum and the Force (F) is a minimum. The frequencies at which the strain maximum and the force minimum occur do not exactly coincide. The strain maximum is at a frequency slightly lower than that of the resonant frequency.

– Even when cracks have formed in the ice layer (some part of the ice has passed the yield stress), the predictions of stress in other locations can still be used. This was checked using a finite element model of the system with cracks modelled as through thickness in the ice layer, normal to the axis of the pipe. The cracks were placed at the positions of maximum axial stress (σ_{ZZ}), as predicted by the finite element model, in the axial direction (Z). Away from the cracks the other stresses were of similar magnitude to those in the un-cracked model.

Description

The Ansys [127] model is depicted in Figure 5.8, which shows a bi-layer pipe. Only $\frac{1}{4}$ of the pipe is modelled, taking advantage of two planes of symmetry to reduce the number of nodes and elements required and thus reducing computation times for solution of the model.

The centre of the pipe is at the origin, and the built-in end of the pipe is at 207 mm from the centre of the pipe. The pipe dimensions are shown in Table 5.4. It should be noted that the T-connector was made up of 50 mm of M3 studding and 130 mm of M6 studding. The pipes were nominally $\frac{1}{4}''$ (or 6.35 mm) in diameter, however, the final measured diameter was somewhat smaller at 6.28 mm. The decrease in diameter was due to careful polishing of the pipe, using $P320$ emery paper, to obtain a consistent surface roughness at all positions on the outer surface of the pipe. Additionally, several pipes were used during the course of the investigation and each pipe received the same amount of polishing so that the surface roughness would be similar on each pipe.

The pipe was created from solid eight noded brick elements ("Solid45" [133]) with
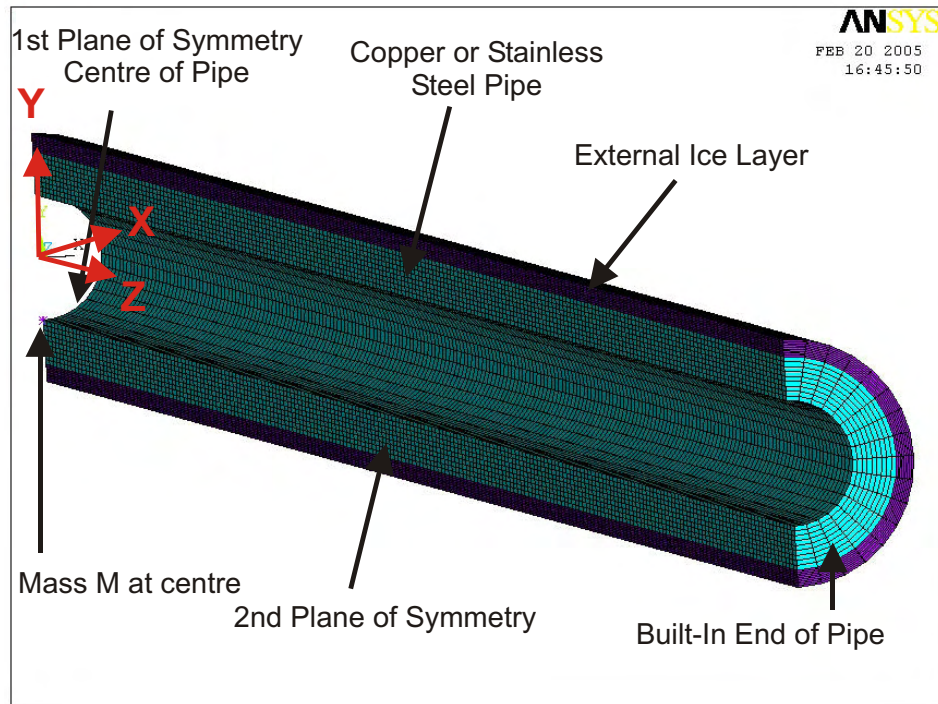
Figure 5.8: Ansys printout of the built-in pipe model: 0.5 mm ice layer shown.

Physical Property	Steel Pipe	Copper Pipe
Length (L)	414 mm	414 mm
$r_{pipe\,inner}$	1.84 mm	2.28 mm
$r_{pipe\,outer}$	3.14 mm	3.14 mm
t_{ice}	$0.0 - 4.0$ mm	$0.0 - 4.0$ mm
T − connector	174 mm	180 mm
Mass T − conn.	0.136 kg	0.129 kg
E	210GPa	110GPa
ν	0.285	0.328
ρ	8000kg/m³	8900kg/m³

Table 5.4: Dimensions of the system for copper and steel pipes

nine elements through the thickness of the pipe and sixteen elements around the half circumference modelled. Each slice of such elements was one millimeter thick, and 207 slices were created in the length of the pipe. The material properties of the copper pipe [116] and the stainless steel pipe ($316L$) [134] are shown in Table 5.4.

Gold [135] shows that the static Young's modulus for polycrystalline ice is given by the expression:

$$E = 5.69 - 0.0648 * T \,[GPa], \tag{5.4}$$

where T is the ice temperature in °C; and that the Poisson's ratio varies from ~ 0.5 at -6°C to ~ 0.38 at -40°C. A value of 0.5 is assumed for the models described in this chapter. Daniel et al. [105] provide a method for predicting the Young's modulus for frozen sucrose solutions (see Chapter 2). For 20% (by mass) sucrose solution a value of $E_{suc20\%} = 0.5\,$GPa is obtained, and for sucrose solutions of 10% a value of $E_{suc10\%} = 2.5\,$GPa is calculated.

Condition	Position
Symmetry	$Z-$ direction (On nodes, Z $= 0\,$mm)
Symmetry	$X-$ direction (On nodes, X $= 0\,$mm)
UX $= 0$	On nodes, Z $= 207\,$mm
UY $= 0$	On nodes, Z $= 207\,$mm
UZ $= 0$	On nodes, Z $= 207\,$mm

Table 5.5: Constraints applied to the pipe and ice layers to represent the physical conditions in the experimental rig

Tables 5.2 and 5.3 showed that a simple model of a pipe which was built-in at each end produced significant errors in terms of natural frequency, and that marked improvements were achieved by modelling a rigid central mass with no rotational inertia (Using Ansys element Mass21 [133]). Therefore, the T-connector was modelled as a point mass at the centre of the pipe. A mass of $0.033\,$kg was used to represent the T-connector rod (steel case), which was $\frac{1}{4}$ of the total mass of the connector

effective from the front face of the force gauge attached to the shaker, i.e. where the force for the frequency response function was measured. One quarter of the total mass was used, as the element was placed coincident with both planes of symmetry.

5.3.6 Validation of Model

Validation of the finite element model was important to establish that the model behaved satisfactorily and that the stress field described by the model was accurate. To achieve a satisfactory level of validation the measured physical properties of the rig must be compared to an equivalent output from the finite element model. If the difference between the two properties is small then it is concluded that the finite element model should give a good prediction of the stress field experienced within the rig.

For each finite element model (i.e. steel or copper pipe, with each ice thickness considered) an Eigenvalue solution was calculated. The stress, strain and displacement fields for the system were extracted for each solution. These fields in the correct proportions, relative to each other, but were at an arbitrary scale.

Information on the strain field was recorded during all of the experiments (with or without ice/sucrose), and some measurements were taken of the displacement fields during the earliest experiments, where no ice was formed onto the pipe surface. By comparing the measured strain and displacement data to the strain and displacement fields predicted by the finite element model, a scaling factor was predicted for each case. All of the data from the finite element model was multiplied by the scaling factor. This gave estimates of the actual strain, displacement and stress fields from the finite element model outputs.

Several physical properties can be measured directly from the system. These are:

The out of plane velocity and its variation with position. The laser vibrometer could be used to obtain the out of plane velocity of the pipe at a number
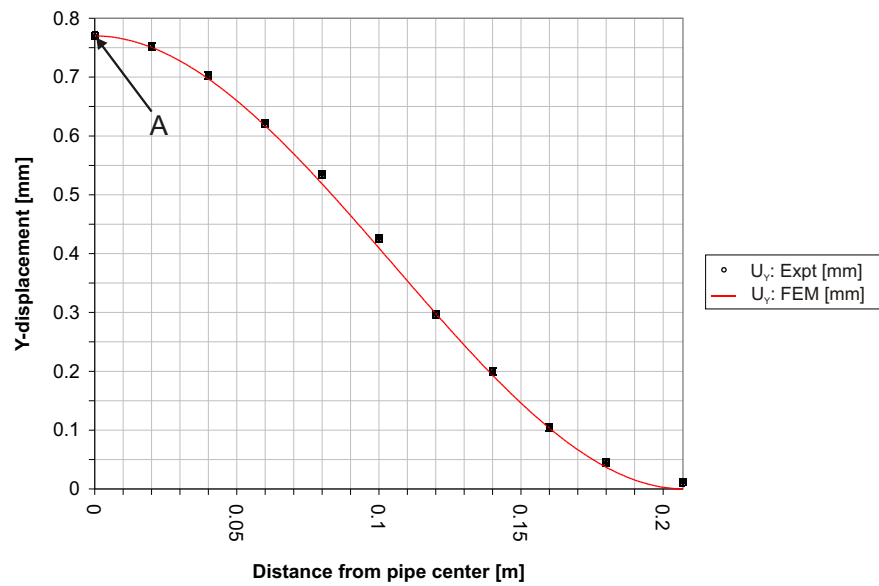
Figure 5.9: Comparison between Finite Element predicted mode shape and experimentally determined mode shape for 414 mm stainless steel pipe. Finite Element results are normalised to measured displacement at the mid-length of the pipe (Point "A").

of positions on the top centre-line of the pipe. As the motion of the pipe was sinusoidal in time these velocities could be integrated to give displacements. The finite element mode shape only gives a shape and has to be normalised to an actual displacement. By using the maximum displacement of the pipe (at the centre for flexural mode 1), the Y-displacement from the finite element model can be scaled to compare it with the experimental data. Figure 5.9 shows the comparison between the two mode shapes. There is excellent agreement between the measured and predicted mode shapes, except at the very end of the pipe. Some vibration was experienced at the positions where the ends of the pipe were clamped in v-blocks. The vibration was minimised as described in Chapter 4. It does mean that the finite element model does not completely model the physical behaviour of the rig, as the clamped boundary conditions do not exist in the rig. However, the amplitude of vibration at the ends of the pipe is small compared to that at the displacement maxima for each mode. The finite element model predictions were used, and any effects

due to the end vibration were ignored.

The strain at two locations on the pipe. The system is monitored by two strain gauges located on the underside of the pipe, at $\theta = 0°$, $Z = 0$ and $Z = 187 \, \text{mm}$ (see Figure 4.10(a)). Taking ratios of the strain output from the two positions allows another comparison to be made between the rig and the finite element predictions. A comparison can be made for each mode of vibration; Table 5.6 shows the comparison between the predicted and measured values of the strain ratio. It can be seen that the values for each mode are within the error bounds, however, there is some disagreement between the measured values and the values predicted by the finite element model, as shown in Table 5.6. The values show a fifteen percent error.

This variation is included in the finite element model by using both experimental values of strain to scale predicted strain field. Therefore, two scaling factors are produced to describe each experiment, and two sets of data for strain, stress and displacement are produced from the finite element model. (This effect can be seen in Figures 5.13, 5.14 and 5.15).

Mode	Expt. $\left(\frac{\varepsilon_{Z}|_{Z=0}}{\varepsilon_{Z}|_{Z=0.187}} \right)$	Ansys $\left(\frac{\varepsilon_{Z}|_{Z=0}}{\varepsilon_{Z}|_{Z=0.187}} \right)$	Error (%)
1	1.185 ± 0.128	1.141 ± 0.014	-3.7
3	2.023 ± 0.202	1.760 ± 0.077	-13.0
5	2.933 ± 0.568	3.282 ± 0.381	11.9

Table 5.6: Ratio of strain at Z = 0 and Z = 0.187, as determined i). experimentally and ii). from finite element analysis

Comparison Between Scaling Factors. A scaling factor is obtained from each of the methods mentioned above, i.e. the strain and displacement from the experiment can be used to scale the strain and displacement predicted by the finite element model. In an ideal situation the two scaling factors obtained would be identical. An experiment was conducted, where the pipe vibrated at just below the resonant frequency in air. The displacement at the mid-length

of the pipe and the strain at that displacement were recorded, by laser vibrometer and strain gauge respectively. Similarly, the strain and displacement data were extracted from the finite element model.

The scaling factors from the two data sets were calculated and the values compared. For the first mode of vibration the ratio based upon displacements readings was 3.491×10^{-4}, and the ratio based on strains (at the mid-length) was 3.358×10^{-4}. This gave a difference of 0.133×10^{-4} with an error of just under 4.0%; based on the strain ratio, as this would be the value taken during the experiments with an ice layer formed on the surface of the pipe. The scaling ratios used to normalise the data extracted from the finite element model, vary, depending on the amplitudes of vibration. However, the error in the ratios calculated was found to remain within $4 - 5\%$ for the range of displacements and strains used during the experimental investigation. A similar error level was found for modes one and five. Errors of this magnitude were evident from the readings taken from the strain gauges due to noise on the recorded signal, so it appears that there is good agreement between the scaling factors obtained by both methods.

The natural frequency of the system. The finite element model calculates the natural frequency of each mode for each ice thickness modelled. The frequency response function for each mode can also be determined experimentally. This was achieved by forming ice on to the pipe in 20% sucrose solution. The sucrose was drained from the tank when the ice had reached the desired thickness. The frequency response function was then obtained by running the Solartron FRA [136] with a low generator output voltage. An estimate of the natural frequencies of the system was obtained by noting the peaks of the frequency response curves. These experiments were conducted for a number of modes and ice thicknesses. The finite element predictions and the experimental data, where taken, are shown in Table 5.7. Good agreement is seen for modes 3 and 5, with agreements in the value of frequency typically $\leq 10\%$. Larger errors are seen in the prediction of natural frequency for tests in mode 1, often being

$\geq 10\%$.

Case	Mode 1			Mode 3			Mode 5		
	F.E.	Expt.	Error (%)	F.E.	Expt.	Error (%)	F.E.	Expt.	Error(%)
Pipe No Ice	78.0	79 ± 1	1.3	795.5	746 ± 8	6.6	2113.0	1950 ± 12	8.4
0.5mm ice	77.7	$68 \pm 6*$	14.3	774.1	$776 \pm 8*$	-0.2	2053.6	$2009 \pm 12*$	2.2
1.0mm ice	77.4	74 ± 6	4.6	752.1	731 ± 8	2.9	1992.3	1886 ± 12	5.6
1.5mm ice	77.1	73 ± 6	5.6	730.1	712 ± 8	2.5	1930.8	1849 ± 12	4.4
2.0mm ice	76.8	72 ± 6	6.7	708.6	671 ± 8	5.5	1870.3	1803 ± 12	3.7
2.5mm ice	76.5	$62 \pm 6*$	23.3	687.9	666 ± 8	3.2	1812.0	1763 ± 12	2.7
3.0mm ice	76.3	70 ± 6	9.0	668.4	652 ± 8	-2.5	1756.5	1731 ± 12	1.47
3.5mm ice	76.2	69 ± 6	10.4	650.3	640 ± 8	-1.6	1704.6	1696 ± 12	0.5
4.0mm ice	76.1	69 ± 6	10.3	633.8	630 ± 8	0.6	1656.7	1658 ± 12	-0.1

Table 5.7: Predictions of natural frequencies of system; i). Finite Element Model, ii). comparison with Experimental Data.($*$ Slight variation in T-connector setup compared with FE model. In configuration 1 the T-connector was 210 mm long for ease of measurement. In later experiments, configuration 2 ,the length was reduced to 174 mm to reduce the chance of unwanted flexural modes in the T-connector.)

Comparison with Mode Shapes from Disperse. Disperse is a computer program designed to calculate dispersion curves for elastic waves in flat or cylindrical multi-layered structures [137]. Disperse also calculates the through thickness mode shapes for such structures. Disperse gives solutions for waves propagating along is in infinitely long waveguide. However, it matches the solution for finite length when the finite length matches a multiple of λ. For instance, σ_{rr}, $\sigma_{\theta\theta}$, σ_{ZZ}, $\sigma_{r\theta}$, σ_{rZ} and $\sigma_{\theta Z}$ can be obtained for a multilayered pipe system. Disperse provides the maximum values of these stresses at some position in the pipe and ice. The position of these mode shapes is not displayed with the mode shapes. By locating the maxima of these stresses in Ansys [127] and extracting the through thickness data a check into the stresses predicted by the Ansys model can be obtained.

The Disperse solution did not take account of the central mass attached to the pipe, so its representation is not strictly correct. The model in Disperse is set up in two dimensions, with an inner radius, outer radius equivalent to that of the pipe in the Ansys model. A third radius for the ice layer is added,
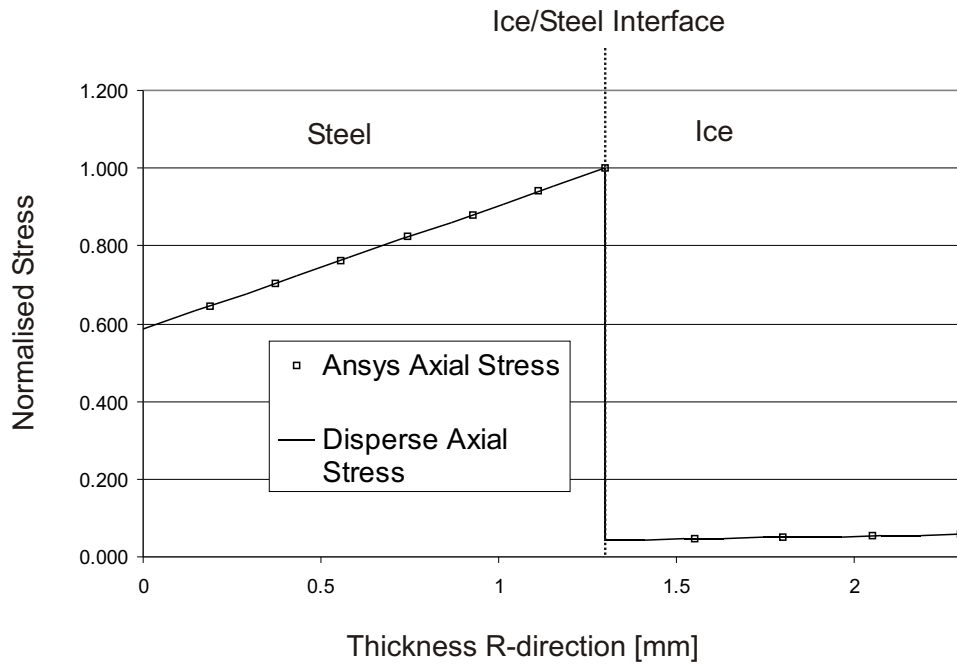
Figure 5.10: Comparison of σ_{ZZ} for Disperse and Ansys (Mode 1, 1 mm ice): normalised to peak σ_{ZZ} in steel pipe at interface.
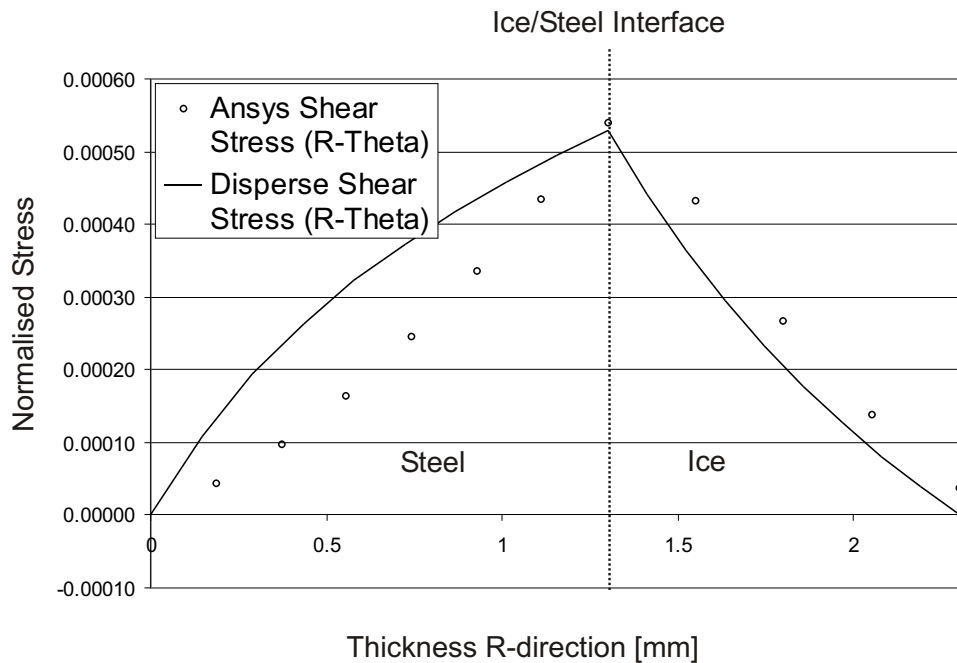
Figure 5.11: Comparison of $\sigma_{R\theta}$ for Disperse and Ansys (Mode 1, 1 mm ice): normalised to peak σ_{ZZ} in steel pipe at interface.
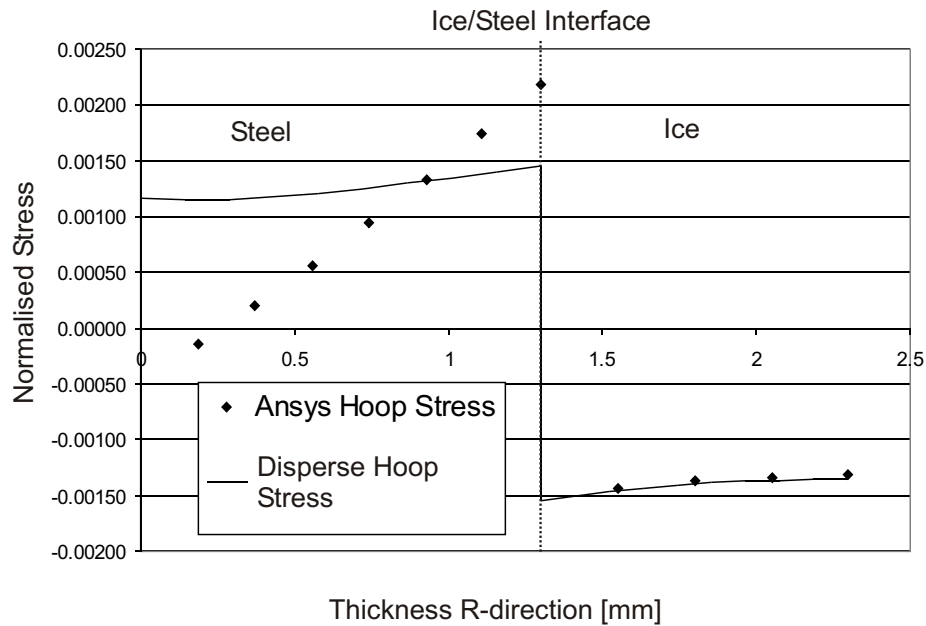
Figure 5.12: Comparison of $\sigma_{\theta\theta}$ for Disperse and Ansys (Mode 1, 1 mm ice): normalised to peak σ_{ZZ} in steel pipe at interface.

and depends on the thickness of ice to be investigated. By choosing the mode shape at a suitable frequency, a comparison between the Disperse and Ansys mode shapes can be obtained. The frequency in Disperse must be chosen to give the correct number of wavelengths in a pipe of 414 mm for each mode. Figures 5.10, 5.11 and 5.12 show the comparison between the different Ansys and Disperse mode shapes for σ_{ZZ}, $\sigma_{r\theta}$ and $\sigma_{\theta\theta}$.

The prediction of the behaviour in the ice layer is good, but, there is some divergence in the behaviour of the prediction of the stress variation in the thickness of the pipe. However, the normalised stresses agree reasonably well in terms of magnitude. A significant difference in the shape of the stress distribution curves can be seen between the Ansys and Disperse models in Figure 5.12. This is probably due to the mass attached to the pipe to represent the T-connector in the Ansys model. The flexural mode shapes are also slightly different, the Disperse mode shape is sinusoidal, whereas the Ansys flexural mode shape is close to sinusoidal, with a short flattened length at the mid-length of the pipe. It is in this short flattened area where the maximum value

of the hoop stress $\sigma_{\theta\theta}$ occurs. This seems to account for the difference between the Ansys and Disperse models, with the divergence being greatest at the point near to the attachment of the point mass and becoming less pronounced near to the ice layer/liquid interface.

5.3.7 Results Extracted from Model

The stress field information is key to understanding the behaviour of the ice removal in the experiments. A sample of the results obtained by this method and the calculation of the stress field is outlined in the following paragraphs.
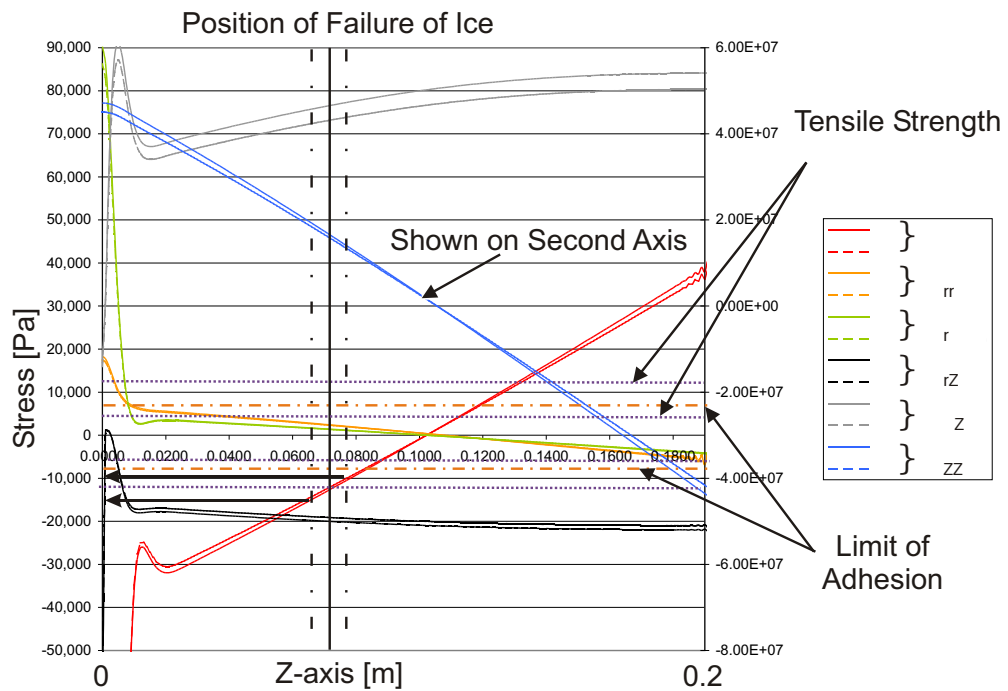
Figure 5.13: Mode 1: 1.5 mm ice/sucrose. Stress variations with distance from midlength of pipe. Vertical lines show locations where ice removal ended.

Examples of the results from the finite element model of 1.5 mm frozen sucrose solution (20%) are shown in Figures 5.13, 5.14 and 5.15, which show the stress variations predicted for flexural modes 1, 3 and 5 respectively. The distance from the midlength of the pipe is shown in the ordinate direction and the stress is shown in the abscissa direction. The axial stress (σ_{ZZ}), is shown on a second ordinate as it is
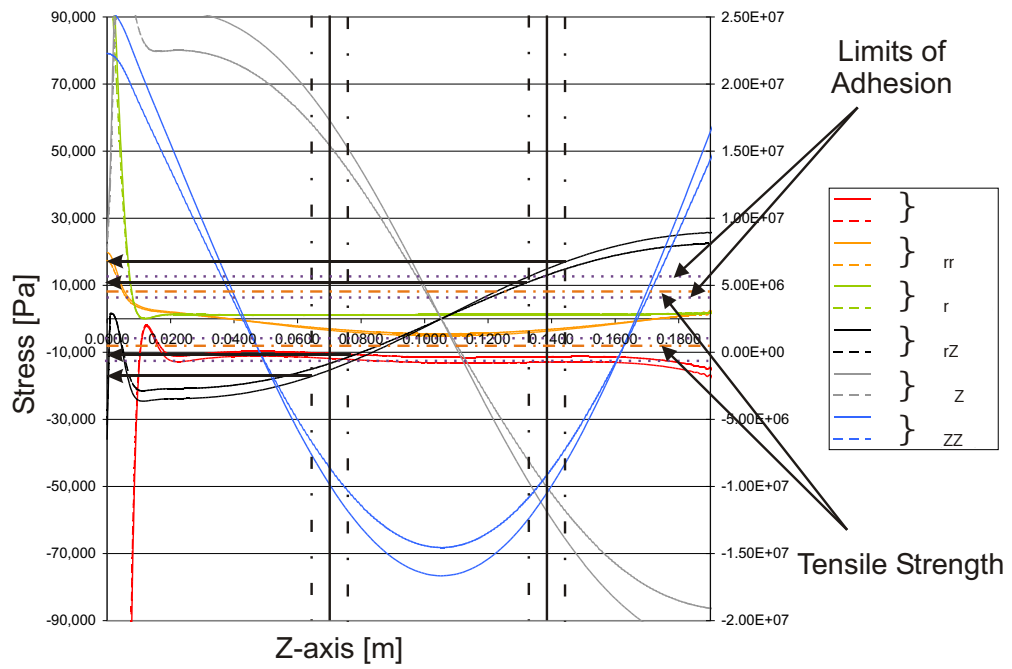
Figure 5.14: Mode 3: 1.5 mm ice/sucrose. Stress variations with distance from mid-length of pipe. Vertical lines show locations where ice removal ended.
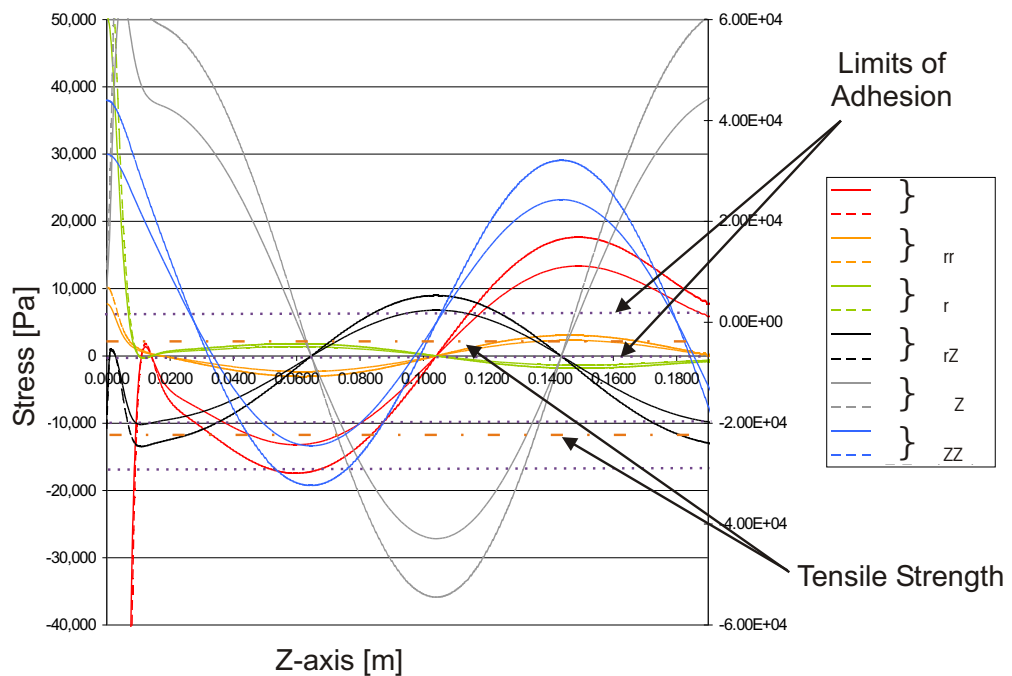
Figure 5.15: Mode 5: 1.5 mm ice/sucrose. Stress variations with distance from mid-length of pipe.

several orders of magnitude larger than the other stresses. The stress field shown is the maximum of each stress at either $\theta = 90$ or $180°$ at some position in the thickness of the ice.

In each case the strain at 0 and 187 mm from the centre of the pipe were obtained from the experiment. The experimental value of strain ($\varepsilon_{ZZ}|_{Expt}$), was divided by the corresponding value from the finite element model ($\varepsilon_{ZZ}|_{FEM}$). This ratio was used to scale the relative stress field in the system. For example, the strain at the centre of the pipe for one experiment for Mode 1 vibration was $\varepsilon_{ZZ}|_{EXPT:Z=0} = 0.89$ [mstrains] and the equivalent value in the finite element model was $\varepsilon_{ZZ}|_{FEM:Z=0} = 2.0285$ [strains]. The scaling ratio was thus $\varepsilon_{Ratio} = 2.19e - 4$, bearing in mind that the strain from the experiment was measured peak to peak and the strain in the finite element model is measured by amplitude. The value of axial stress in the system was $\sigma_{ZZ}|_{FEM:Z=0} = 2.13 \times 10^{11}$ Pa, according to the finite element model. After scaling of the model using ε_{Ratio} as a multiplier, a value of $\sigma_{ZZ}|_{Predcited:Z=0} = 0.26$ MPa was obtained. The other stresses could also be scaled in the same manner. If we assume that $\sigma \approx \varepsilon E$ then the stress can be estimated from E = 0.5 [GPa] and $\varepsilon = 0.45$ [ms], giving $\sigma \approx 0.23$ MPa. This provides a reasonable check that the model was behaving as expected.

There appears to be some distortion of the stress field near the centre of the pipe (Z = 0). This is also the location of the central mass. Mode shapes for the same system, but with the central mass set to 0, showed a smoother curve without the kink near the location of the mass. The values of stress obtained far from the mass location were of similar magnitude in both cases - but the displacement mode shapes, with no central mass, showed some divergence from the measured mode shapes from the experiments. Therefore, the mode shapes from the model with the mass included were used, but data from the first 10 mm was not considered.

Further information on the stress field was available from the experiments. During the experiments the ice was not always fully removed. The interface between ice/sucrose removal and continued adhesion to the pipe was noted as a distance from
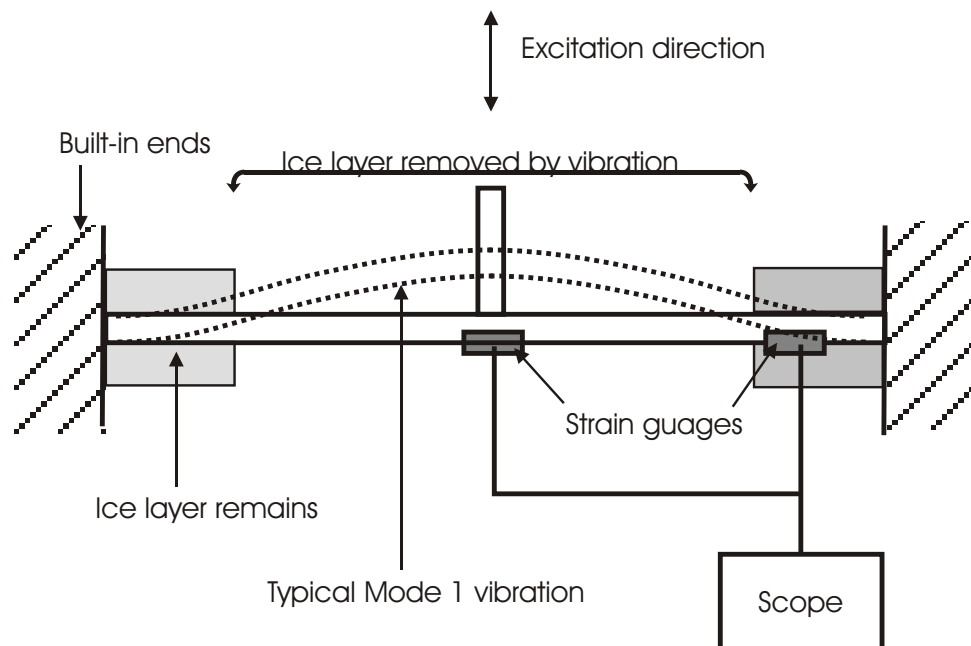
Figure 5.16: Representation of positions on pipe where ice may typically be removed during Mode 1 excitation.

the centre of the pipe. The broken vertical black lines on Figures 5.13 and 5.14 show how this data was used to gain further information on the stress levels at the failure condition.

By plotting the vertical lines, which represent the line of removal/adhesion where the ice failed to be removed from the surface of the pipe (which was sometimes a range of positions, due to parallax errors in reading the position during ongoing experiments), the value of each stress was obtained at this/these locations. Figure 5.16 shows how the positions on the Z-axis were obtained by experimental observation. An estimate of the adhesive and cohesive strength of the sucrose was also plotted on the graphs (adhesive strength: purple —, and cohesive strength: orange -.-). From Figures 5.13 and 5.14 it appears, tentatively, that the critical stress in the system was σ_θ, as it is very similar to the cohesive failure stress at the position noted for failure. The ice/sucrose was removed over the entire length of the pipe for Mode 5 experiments. Therefore, no vertical lines are plotted in Figure 5.15.

5.3.8   Section Summary

The clamped pipe experiments described in Chapter 4 have been modelled using both analytical and finite element approaches, using suitable assumptions about the behaviour of the rig. The finite element model has been verified by comparison with the physical outputs measured during experiments on the rig.

It has been shown that the stress field in the clamped-clamped pipe system can be modelled satisfactorily using a finite element model. The stress field can be predicted successfully over most of the length of the pipe and compared to predictions of the failure conditions in both adhesive and cohesive failure modes.

Full results from the combination of experimental data and this finite element modelling can be seen in Chapter 6.

5.4   Modelling Drag Forces Acting on System

5.4.1   Introduction

The finite element model represents the copper/stainless steel pipe, the ice layer formed on the outer surface of the pipe, and the T-connector rod attachment. In the physical rig, the pipe is immersed in the fluid to be examined (either sucrose solution or water). This fluid part of the system is not represented by the finite element model. As the system vibrates, the fluid will have some effect on the system and vice versa, i.e. drag forces will act on the surface of the pipe. No estimate of the drag forces was produced by the finite element model, and another method was required to assess their significance. The attempts to predict the magnitude of the drag forces acting on the ice are shown in the following section. Once an estimate of the drag forces was obtained the magnitude of the stress field produced was estimated. If the stress generated by the drag forces acting on the pipe is small compared with the other stresses in the pipe, then the drag induced stress can be ignored.

5.4.2   Methods for Estimation Drag Forces

Basis for Model

Classical fluid mechanics describes the drag forces acting on a smooth, rigid infinite cylinder moving sinusoidally through a fluid. Empirical solutions to this particular problem can easily be found in fluid dynamics textbooks [138].

The problem being investigated in this investigation is of a cylinder moving through a fluid with a varying velocity, while the cylinder is undergoing flexure. Therefore, the classical method for determining the drag forces acting on the pipe/ice cannot be used directly, as the velocity of the pipe will vary with distance from the mid-length of the pipe. Instead a modified method was planned, where the pipe was divided into a number of shorter sections. Each short section was assumed to be rigid and smooth.

The displacement mode shape was extracted from the finite element model for each mode. This was converted into a velocity distribution by taking the frequency of vibration into account and using the relationship $|\dot{x}| = 2\pi f.|x|$. Each short section was considered as a smooth rigid pipe moving with a uniform velocity in the fluid. For the sake of this calculation the mean velocity of each section of the pipe, at the mid-length of each section, was considered for the drag calculation.

Using this approach an estimate of the drag force acting on each section of pipe could be calculated [138]. To ensure good results, it was necessary to check the validity of the estimate. A second method, which quantifies the viscous damping force on the pipe due to motion in the fluid was used for comparison. As this second method produced a single value for each mode and fluid, the individual results obtained by the first method were summed to represent the total viscous drag force acting on the pipe. If the comparison between the two methods gives a similar value for the drag force acting on the system then the results from the first method can be used to predict the magnitude of the stress acting on the pipe and ice due to the drag forces.

The method devised to compare with the fluid mechanics method, relies upon data collected from the system as though modal testing had being carried out. Assuming that the system behaves as a single degree of freedom system, at or near each resonant frequency, the viscous damping force ($F_C = c.\dot{x}$) can be estimated. Through the use of suitable experiments, an approximation of the drag force acting on the pipe and ice can be produced. Once this estimate has been obtained, then the value calculated from the second method can be compared with the sum of each estimate from the first method.

The two methods and the results arising from each method will be discussed in more detail in the following paragraphs. Additionally, estimates of the stress induced in the ice layer of the system will be calculated; based on the results from the first method and their significance evaluated.

Method 1: Estimation of Drag Forces using Empirical Fluid Mechanics Method

The following equation was taken from Batchelor [138], and represents the damping force for a rigid circular cylinder moving sinusoidally in a fluid medium:

$$\frac{F}{2a\frac{1}{2}\rho U_0^2} = 2\pi\sqrt{2}\left(\frac{\mu}{U_0\epsilon}\right)^{\frac{1}{2}}, \tag{5.5}$$

Where a is the radius of the cylinder, U_0 is the maximum velocity of the pipe, μ is the dynamic viscosity of the fluid, ρ is the density of the pipe, f is the frequency of oscillation and $\epsilon = \left(\frac{U_0}{f}\right)$. (The best relationship with experimental data is reported for data up to $\epsilon = 0.1a$). This represents a cylinder moving in a viscid fluid with laminar flow at the liquid cylinder interface. For $\epsilon > 0.1a$, the implication is that the fluid will enter the turbulent regime.

As the "cylinder" was in this case a bi-material pipe (formed from ice/sucrose adhered to a stainless steel pipe) , some minor adjustments to this standard case were made. An equivalent density for the pipe was calculated using the following

relationship:

$$\rho_{equivalent} = \frac{(a^2 - r_o^2)\,\rho_{Ice} + (r_o^2 - r_i^2)\,\rho_{ss}}{a^2}; \tag{5.6}$$

where a = total outer radius, r_o = the outer radius of the stainless steel pipe, and r_i = the inner radius of the steel pipe.

Additionally, this method requires the pipe to remain rigid during the oscillation. Obviously this is not the case for a pipe vibrating near a flexural resonance. However, by dividing the pipe as shown in Figure 5.17 an improvement in the estimate of the drag force can be obtained. The drag force acting on each short section of pipe can be obtained, by treating each section as a rigid cylinder. The velocity of each short pipe section is taken as the mean of the velocity profile predicted over that length of pipe. A broadly similar method was applied by Manners [139], although accelerations were used. The total drag force can be obtained by summing the drag forces for each cylinder and can then be compared to the estimate obtained from the method based on the use of modal parameters.

Frequecny Hz	Liquid	$\Sigma F_D\,[N]$	$\hat{F}_D\,[N]$	$F_D\,[N/m]$
65	Water	0.161 ± 0.009	0.012 ± 0.001	0.608
65	Sucrose (20%)	0.239 ± 0.010	0.019 ± 0.001	0.903
630	Sucrose (20%)	0.542 ± 0.009	0.021 ± 0.002	2.042

Table 5.8: Table showing damping values obtained using method 1: ΣF_D is sum of damping forces, $\hat{F}_D$ is peak damping force acting on a pipe section, and F_D is the force per unit length.

U_0 of equation 5.5 was taken as the velocity of each short section of pipe, i.e. V_1, V_2, $V_3...V_n$ (see Figure 5.17). a was taken as the outer radius of the pipe plus the ice thickness, and for mode 1 vibrations the pipe was divided into 20 sections of 0.0207 mm in length. Again the peak displacement was taken as 1.2 mm at the centre of the pipe. This gives values slightly outside of the range $\epsilon = 0.1a$ for the pipe sections near the peak amplitudes of velocity (the calculation was executed
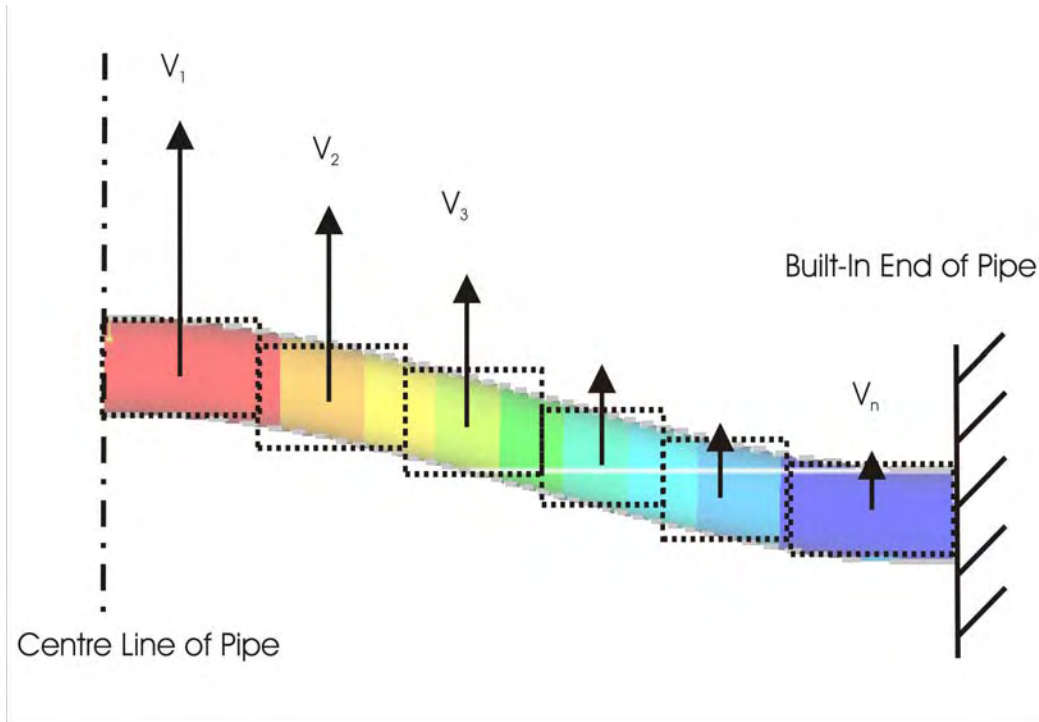
Figure 5.17: Illustration of pipe and ice separated into short sections for the drag estimation model.

regardless, as only an order of magnitude estimate is required for these purposes). However, for water at 0°C ($\mu = 1.787e-3\,[Pa.s]$ [140]) the sum of the damping force is calculated as $F_{Damping} = 0.161 \pm 0.009\,[N]$, which agrees well with the result obtained from the second method ($F_{Viscous\,Damping} = 0.181 \pm 0.009\,[N]$). For estimations of the drag force of the third flexural mode 40 equal divisions were required to obtain an estimate of the damping force accurate to three significant figures. Values obtained from the method outlined above are shown in Table 5.8. For the purposes of estimating the stress induced by the drag forces, the value of drag obtained at the point of maximum velocity (i.e. V_1 on Figure 5.17 for Mode 1 vibrations) on the pipe was used. This drag was converted into a force per unit length that could be used in later finite element modelling of the stress caused by drag forces.

Method 2: Estimation of Viscous Drag by Use of Modal Parameters

The second method uses the modal parameters recorded during the experiments conducted on the system during ice removal. The modal parameters for each mode

are used to determine the damping force acting on the pipe. By careful experiment-
ation the total damping force can be separated into a structural damping force and
a viscous damping force.

The equation of motion for a body undergoing forced vibration takes the form:

$$m\ddot{x} + c\dot{x} + kx = F(x) \tag{5.7}$$

To determine the magnitude of the forces due to viscous drag then we are interested
in the velocity component of the equation, i.e. $F_{Damping} = c\dot{x}$. The value of c can
be estimated using a modal testing type analysis. The loss factor ,ζ; stiffness, k; and
effective mass m for each mode can be determined from the mobility and Nyquist
plots obtained by taking the frequency response function of each mode of vibration.
The relationship between ζ, c, k and m is shown in Equation 5.8. More detail on
the calculations is shown by Ewins [141] and the Solartron manual [142].

$$\zeta = \frac{c}{2\sqrt{km}} \tag{5.8}$$

The velocity of the system can be obtained by differentiating the sinusoidally vary-
ing displacement of the system, which has already been determined for the system
(as in Equation 5.9). The finite element approximation of displacement was used for
the purposes of calculation and scaled to the strain values obtained experimentally
at ice failure.

$$x = A\sin(\omega t) \tag{5.9}$$

$$F_{Damping} = c\frac{dx}{dt} \tag{5.10}$$

$$|F_{Damping}| = c\omega|x| \tag{5.11}$$

This value $F_{Damping}$, obtained from Equation 5.11, can be used to give an estimate of
the total viscous force acting to retard the system during vibration. By calculating

this force for the system in air and the system in a liquid and by subtracting the former from the latter, an estimate of the drag force on the system can be produced as shown in Equation 5.12. No separation of the viscous and inertial (or wake) drag forces will be possible, and a single value will be obtained.

$$F_{Viscous\,Damping} \approx F_{Damping}^{In\,Liquid} - F_{Damping}^{In\,Air} \tag{5.12}$$

For a 1.5 mm thick layer of ice in water with the system resonating at 65 Hz; with an amplitude of 1.2 mm at the centre of the pipe, the following results were obtained. $c_{Water} = 0.431 \pm 0.018\,[ks/s]$, $c_{Air} = 0.062 \pm 0.002\,[kg/s]$ and $\dot{x}_{Max} = 0.49\,[m/s]$. Therefore, using the relationship shown in equations 5.11 and 5.12, we can see that the damping force can be estimated as $F_{Viscous\,Damping} = 0.181 \pm 0.009\,[N]$. This value was used to compare with the estimate of viscous drag as calculated by method 1, as shown in the previous subsection. The values obtained are shown in Table 5.9.

Case	ΣF_D : Method 1	ΣF_D : Method 2	Error (%)
Mode 1 : Water	0.161 ± 0.009	0.181 ± 0.020	11.0
Mode 1 : 20% Sucrose	0.239 ± 0.010	0.247 ± 0.020	3.2
Mode 3 : 20% Sucrose	0.542 ± 0.009	0.553 ± 0.025	1.6

Table 5.9: Comparison between the damping estimates obtained from method 1 and method 2.

This estimate of the damping force is useful for purposes of comparison only as only a single value of the force is obtained. It can be seen from Table 5.9 that the comparison between the two method is good. The agreement between the values obtained from the two methods is within 11.0%. This agreement is good enough for the purposes of this investigation, as an estimate of the stress caused by the drag forces is only required to within an order of magnitude to compare with the other stresses acting on the ice and the pipe/ice interface.

5.4.3 Estimation of Stress Induced by Drag Forces

The good agreement between the two methods, allows an estimation of the drag forces acting on the pipe at various locations. By using the maximum drag force acting on the pipe at the velocity anti-node, an estimate of the stresses due to drag was attempted. The values used for the estimates of drag/damping stresses are shown in table 5.8.

A $2D$ model of the pipe was created, using the same mechanical properties for stainless steel and frozen 20% sucrose as used in the $3D$ structural finite element described previously. The ice thickness investigated was 1.5 mm. The force was distributed as shown by the black arrows at the edge of the ice layer of Figure 5.18, in accordance with distributions predicted from a more rigorous finite element modelling approach [143]. In some finite element programmes such as Abaqus "Gap" elements might be used to create the same effect.
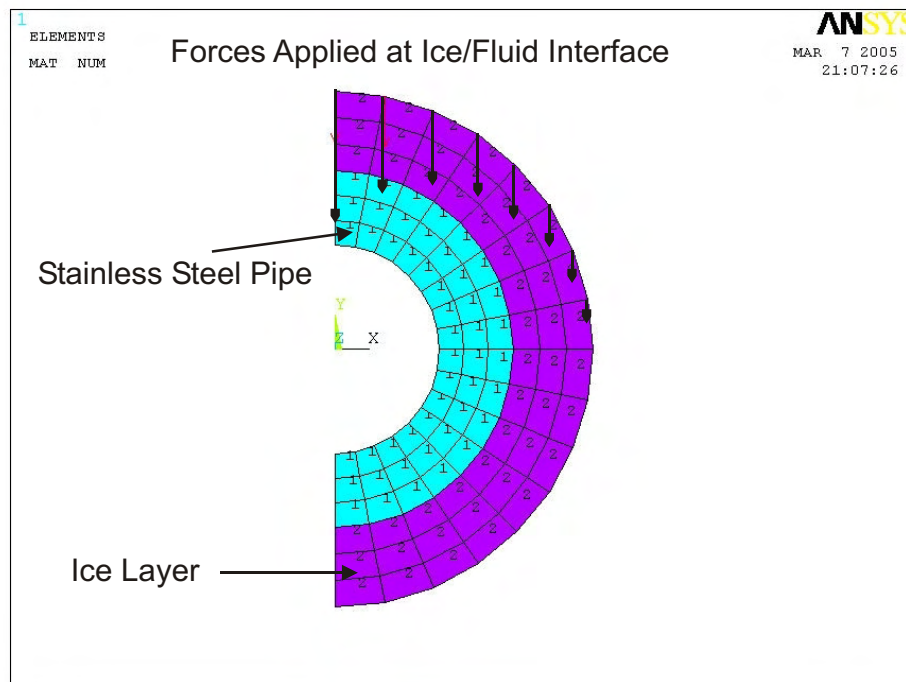
Figure 5.18: 2D Ansys model of drag force applied to the pipe and ice system

Results and Conclusions
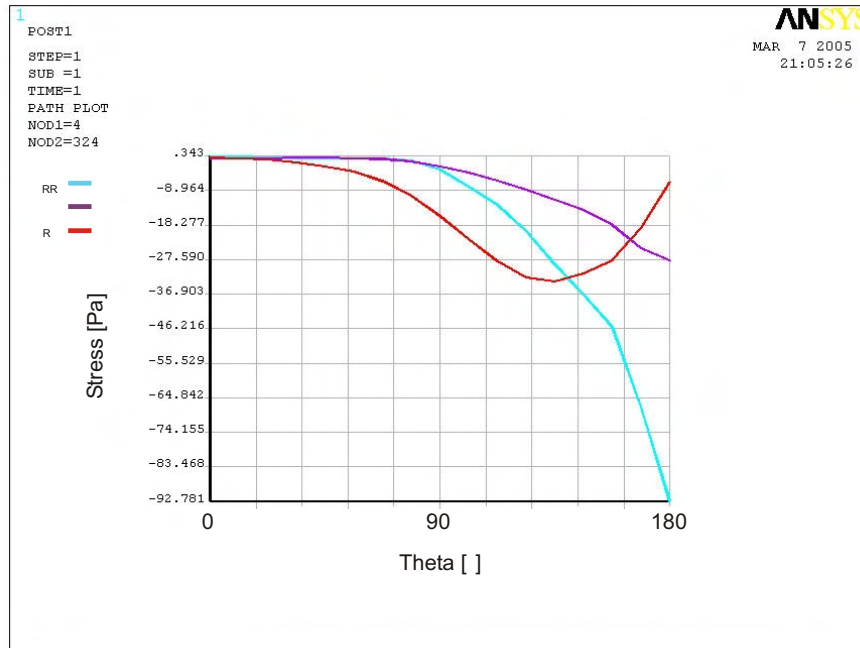
Figure 5.19: Variation of stresses due to drag with θ for mode 1 vibration

Figures 5.19 and 5.20 show the prediction of the stress levels caused by the drag on the cylinder. In both cases the stresses induced are in the order of $10^2 \, Pa$, which is considerably less than the general level of stress in the ice layer, as shown in Figures 5.13 and 5.14, which is in the order of 10^4 to $10^5 \, Pa$ under the same conditions.

The above results indicates that the drag forces experienced by the system in the first mode are an order of magnitude or more less than the other forces and can thus be left out of the FE model.

5.4.4 Section Summary

The above section has shown that a suitable estimate of the drag forces acting on the system has been obtained. The estimated drag forces were then applied to a simplified finite element model of the system (pipe and ice layer only, ignoring flexural effects). The model was then used to estimate the stresses acting on the pipe due to
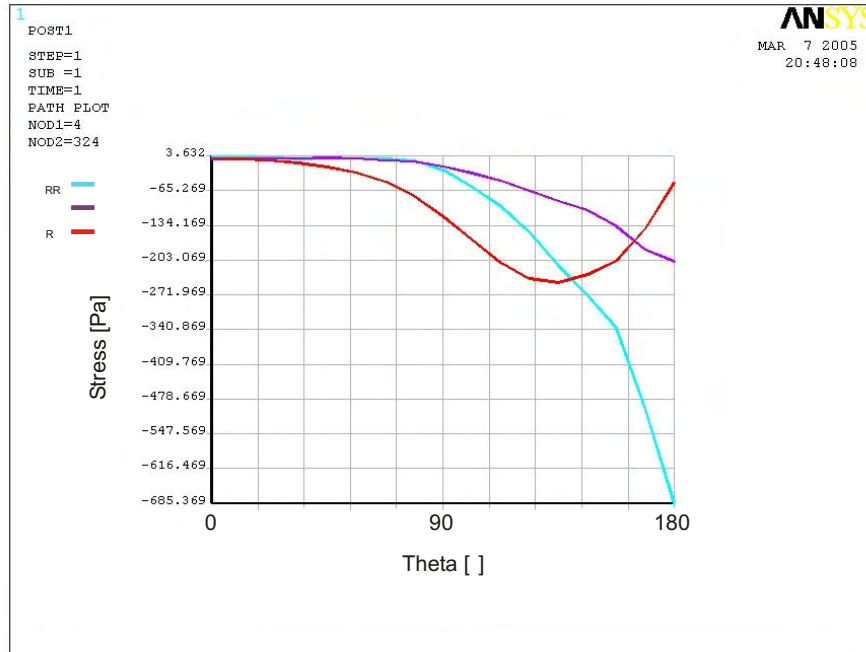
Figure 5.20: Variation of stresses due to drag with θ for mode 3 vibration

the drag forces induced by the motion of the system in the surrounding cooling fluid.

The values produced probably only give an estimate of the forces acting to within an order of magnitude. However, even if this is assumed to be the case, the estimate of the stress caused by the drag forces is small compared with the stress required to remove ice from the pipe. Modes 1 and 3 were investigated, and this seems to be the case for both modes. Therefore the drag forces are ignored for this investigation, although for a full investigation of ultrasonic modes (at much higher frequencies) a further investigation of the drag forces would be required.

5.5   Summary

This chapter has shown the modelling used for the full range of experiments described in this thesis. The first models show the experiments of Chapter 3, where the ice was formed on to the surface of a plate and ultrasonic transducers were used

to try to remove the ice layer from the plate. Basic finite element modelling was used to predict the axial stress produced by bending in the plate with only a thin ice layer present. This modelling confirmed that the stress levels produced were lower than the expected cohesive and adhesive strengths of the ice and ice/aluminium/steel bonds, except for the Branson probe experiments, where the axial stress predicted was significantly greater than the tensile strength of ice.

The sonic pipe experiments were represented using a combination of analytical and finite element models. The finite element model of the system provides an estimate of the major factors influencing the ice removal from the cooled metal pipe. Verification of the model has shown that the results are reliable. The drag forces were estimated using an analytical fluid mechanics approach, and were seen to be small compared with the other stresses acting on the ice and pipe system.

The finite element model predictions can be used in combination with the data recorded from the experiments of Chapter 4. The results are shown in Chapter 6.

Chapter 6

Results

6.1 Introduction

This Chapter will detail the findings from the main experiments. This data will be used to determine as far as possible the mechanisms behind the removal of ice from cooled metal surfaces by structural vibration. The results presented in this Chapter represent experiments on 20% (by mass) frozen sucrose solution. The frozen sucrose solution was formed onto a $\frac{1}{4}''$ stainless steel pipe using the method described in Chapter 4.

The built-in pipe was excited centrally using harmonic forcing in the sonic frequency range. The three main frequencies used were $\sim 60\,\text{Hz}$, $\sim 730\,\text{Hz}$ and $\sim 1730\,\text{Hz}$; which are at or near the first, third and fifth flexural natural modes of the pipe. For each frequency a number of experiments were conducted for different thicknesses of frozen sucrose. Values of the dynamic strain from each experiment were collected and the limiting positions of ice removal in the axial direction were also noted. In mode 1 and mode 3 experiments a clear demarcation between ice removal and ice adhesion from/to the pipe could clearly be observed during the experiments.

It had been predicted in Chapter 2 that the structure of the ice forming on the metal surfaces would be dendritic ice. A knowledge of the structure of the ice crystals formed during the experiments was important to correctly predict the behaviour of the ice/sucrose matrix under loading, as the structure will affect the behaviour
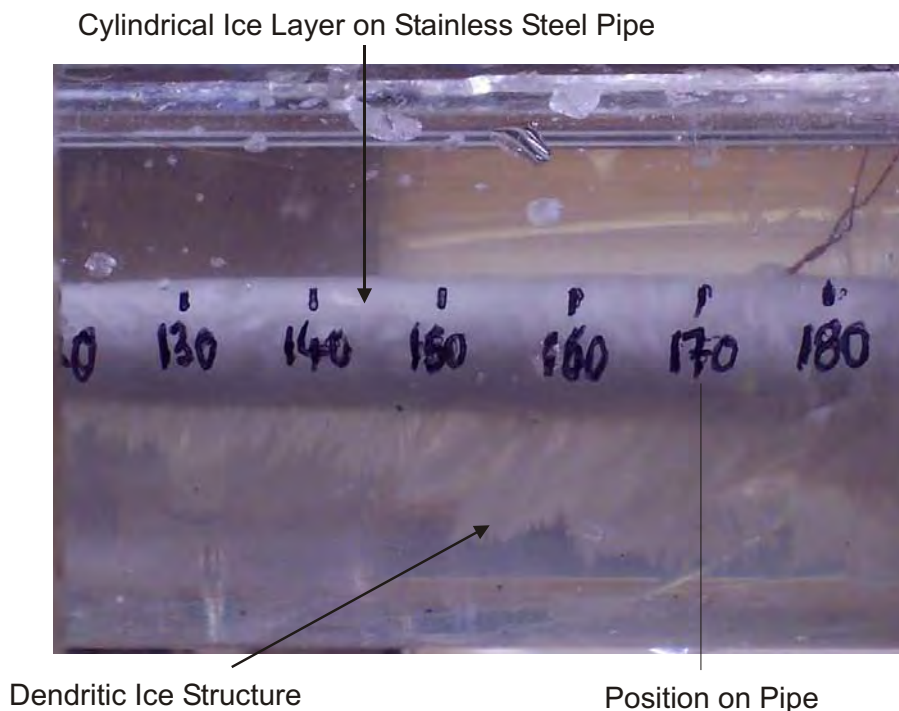
Figure 6.1: Photograph showing the formation of dendritic ice on the stainless steel pipe

of the material.

In most of the experiments, an even layer of frozen sucrose formed on the pipe, thus making a cylinder, and it was difficult to determine whether dendritic structures were forming or not. However, after experiments were conducted where some of the frozen sucrose was removed and some remained, a striking effect could be seen when the shaker was deactivated. Small cylinders of frozen sucrose solution remained attached at some positions on the pipe, mainly near each end at $180 - 207$mm from the centre of the pipe. Dendrites grew out from the existing cylinders of ice. This can be seen on the underside of the pipe, shown in Figure 6.1. As the ice is probably replicating existing structures it appears that the ice structure is likely to be dendritic, as predicted.

Assuming that the structure is dendritic and behaves accordingly as a polycrystalline ice/sucrose matrix, the modelling of frozen sucrose behaviour detailed in Chapter 5 can be used to compare the experimentally derived data to that of the predicted

adhesive and cohesive failure strengths. The data from the experiments is combined with the finite element modelling described in Chapter 5 to describe the stress field experienced by the system during the vibration of the pipe.

6.2 Estimating Adhesive and Cohesive Strengths of Frozen Sucrose and Ice

Chapter 5 described the development of a finite element model which can be used to predict the stresses induced in an ice layer (formed on a pipe) when flexural vibrations are excited in the pipe. To determine when the ice will fail and also the likely order of such failures, information on the adhesive and cohesive strength of the ice must be known. This section aims to derive the cohesive and adhesive strengths that were experienced during the experiments to remove ice from the cooled metal pipe which were described in Chapter 4.

6.2.1 Estimating UTS of Frozen Sucrose

As little literature was available on the dynamic failure stress of frozen sucrose, most of the comparisons for this thesis will be based on works carried out by Xu et al. [37, 71, 66]. Where applicable further trends will be estimated from similar trends in pure ice under similar conditions. This will be necessary particularly in the case of the highest strain rates, where a small amount of data is available for pure water ice, but none appears to be available for frozen sucrose solution.

The strain rates experienced by the ice are of vital importance to obtaining the estimates of the Ultimate Tensile Strength of the ice under structural vibrations. The strain rates are estimated from the maximum axial strain experienced during the cycle of vibration in the ice component of the vibrating system, the axial being the largest strain component. This was obtained from the scaled Eigenvalue solution from the Finite Element model of the clamped-clamped pipe. As the frequency of

vibration of the system is known, an estimate of the strain rate can be achieved for each experiment. Assuming that the maximum strain occurs at the centre of the pipe, a direct measurement can also be obtained from the strain gauge output of the system, by differentiating the signal from the system to obtain the strain rate. For sinusoidal signals this is relatively simple.

Obtaining such a value does not tell the whole story about the strain rate of the system under structural loading. Due to the flexural mode shape of the system, the strain rate will vary along the length of the pipe. Strain nodes and anti-nodes (and hence strain rates) will also be produced around the circumference of the pipe.

Therefore, a range of strain rates will be induced at any given time within the ice. The maximum value as predicted in the above method will only be present in the system for short periods of time. However, the data presented in materials testing information is usually in terms of a constant axial strain rate. So an averaged value was chosen to represent the axial strain rate in the system: the average strain rate was calculated as the root mean square of the sinusoidally varying strain rate.

Xu [66, 37] shows that the following formula can be used to predict the yield stress of frozen sucrose or water ice up to and including a critical strain rate. Up to this strain rate the ice/frozen sucrose follows a ductile behaviour. Past this point the ice/frozen sucrose follows a brittle behaviour. Values for the constants are shown in Table 6.1.

$$\sigma_{YS} = \mathbf{A} \cdot \dot{\varepsilon}^{\frac{1}{m}} \cdot e^{\frac{\mathbf{Q}}{m\mathbf{R}\mathbf{T}}} \tag{6.1}$$

The critical strain rate appears to be at $\dot{\varepsilon}_{crit} = 10^{-2} \left[\frac{1}{s}\right]$. There is a small variation with temperature and material composition, i.e. percentage sucrose by mass. The data from the experiments of Chapter 4 were mainly above the critical strain rate $\dot{\varepsilon}_{crit}$. Therefore, we can assume that the Yield Strength of the ice will be the Ultimate Tensile Strength of the ice, or very close, as the tests are conducted above the brittle transition of the ice and sucrose. Some estimate of the failure strength of the ice is therefore attempted by extending the data Xu produced to encompass the strain rates and ice temperatures that are encountered in the experiments described

by this thesis. For example, Xu's data finishes at $-20°\,\mathrm{C}$, but the experiments conducted on the cooled metal pipes were in the range of $(-2.1) - (-12)°\,\mathrm{C}$. Additionally, some of the strain rates in this work were higher than those recorded by Xu in his work on sucrose [71, 66].

Substance	A $[\mathrm{MPa\,s}^{1/m}]$	m	Q $[\mathrm{kJ/mol}]$
ice	$2.40e-1$	5.25	54
20% Sucrose	$3.10e-13$	2.4	138

Table 6.1: Parameters for equation 6.1, as determined by Xu.
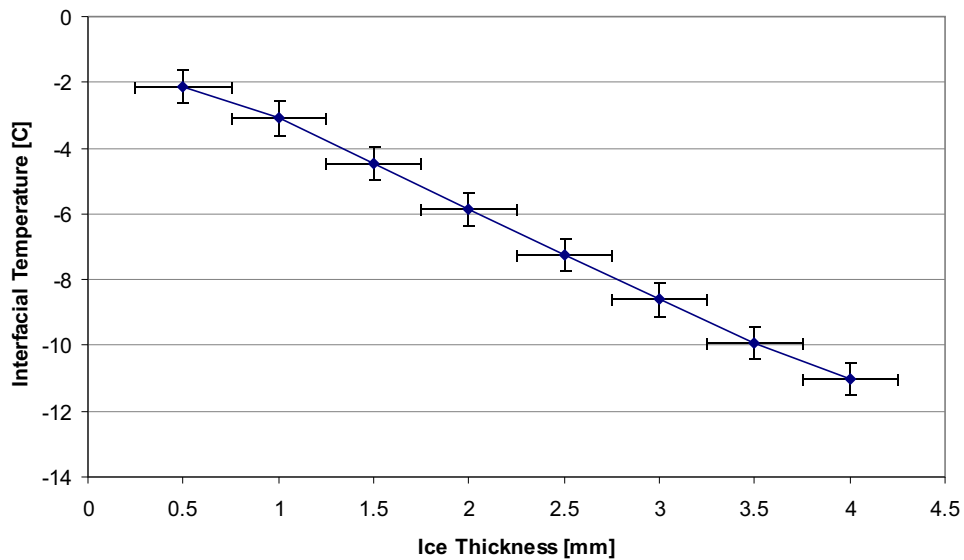
Figure 6.2: Variation of temperature with frozen sucrose thickness, measured at interface of ice with pipe, determined by experiment.

By using the temperature of an experiment with Equation 6.1, and the values of Table 6.1 for $\dot{\varepsilon}_{crit}$, an estimate of the maximum Yield Strength at each temperature can be obtained. This value of Yield Strength can be assumed as the Ultimate Tensile Strength at values of $\dot{\varepsilon} \; > \; \dot{\varepsilon}_{crit}$. Figure 6.2 shows the variation of temperature with frozen sucrose thickness. This data can be used to produce Figure 6.3,
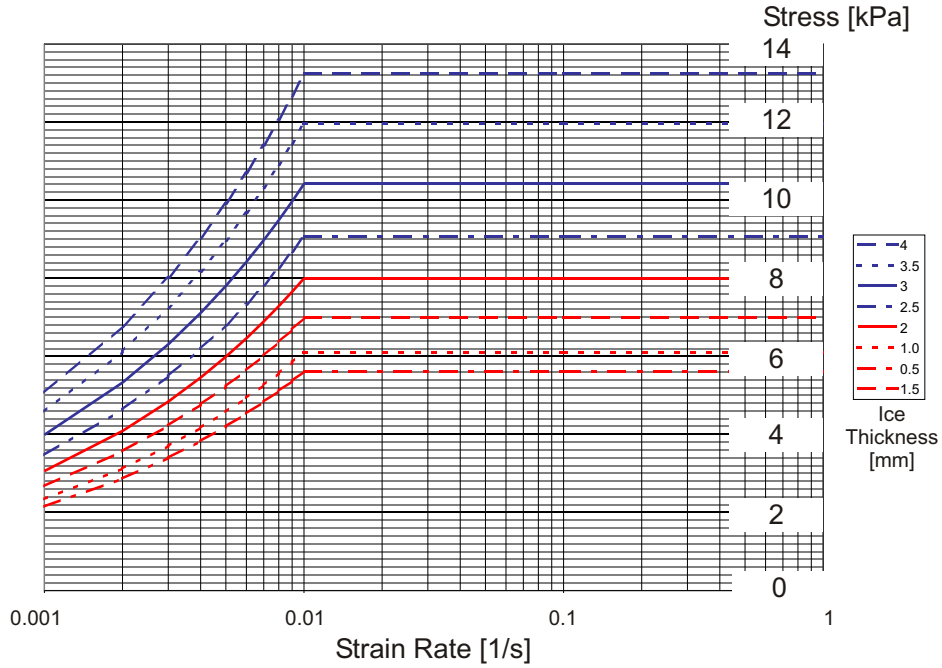
Figure 6.3: Variation of yield strength with strain rate for frozen 19% sucrose solution; after $\dot{\varepsilon} \simeq 0.01$ yield strength $\approx$ ultimate tensile strength due to ductile brittle transition. The Legend shows the thickness of ice formed on the pipe in mm.

which is based on Xu's data up to $\dot{\varepsilon} = 10^{-2}$ and assumes that YS/UTS $\neq f(\dot{\varepsilon})$; for $\dot{\varepsilon} > \dot{\varepsilon}_{crit}$.

In the subject of investigation of frozen sucrose solutions very little or no data is available at strain rates greater $0.01 \frac{1}{s}$. This investigation gives some information on the effects of these higher strain rates at levels between $0.08 - 1.13 \frac{1}{s}$. As this is apparently a novel exploration of the tensile and adhesive strength of ice at these strain rates no data is available for direct comparison across this range of strain rates.

The last good data for comparison is given by Xu *et al.* [66] with peak reported strain rates at just above $0.01 \frac{1}{s}$. This datum point is represented by the horizontal line in Figure 6.3, which is set as a constant, as no further information on the strain rate sensitivity was known above $0.01 \frac{1}{s}$.

To have confidence in any comparison a calibration point was desirable. An exper-

iment was conducted using pure water ice at -20°C with Mode 1 vibrations. A strain rate of $0.07\frac{1}{s}$ was obtained at the first signs of cracking normal to the Z direction. The stress component σ_{ZZ} gave a peak value in the ice of 6.2 MPa calculated from the finite element model. Xu's data for pure water ice gave tensile strengths between 7 and 5 MPa for strain rates between 0.6 and $0.7\frac{1}{s}$. This result showed that the data from Xu compared well with the data obtained from the experiments of this investigation, where comparisons could be made.

A similar comparison could not be made with frozen sucrose solutions as cracks in the frozen sucrose solution were impossible to see, due to the opaque nature of the frozen sucrose solution. However, the good correlation between the ice experiments gave some confidence that good agreement could be achieved.

6.2.2 Shear and Normal Adhesion in Frozen Sucrose Solution

The shear adhesion of different concentrations of sucrose and different temperatures has been calculated from unpublished data produced by Unilever Research Group [22]. The data for 20% sucrose solution in the temperature range of the experiments is shown in Figure 6.4.

The experimentally determined variation of interfacial temperature (from the built-in pipe experiments), where the temperature was related to the thickness of ice formed on the pipe, is depicted in Figure 6.2. A range of shear adhesion strengths can be estimated for each thickness of ice by combining these two pieces of information. The result of this approach can be seen in Figure 6.5.

No data was available on the normal adhesive strength for 20% sucrose solution. It was reported by Unilever Research Group [22] that attempts to directly measure the normal adhesive strength were largely unsuccessful, as cohesive failure often resulted in the body of the frozen sucrose, rather than at the interface between the steel and
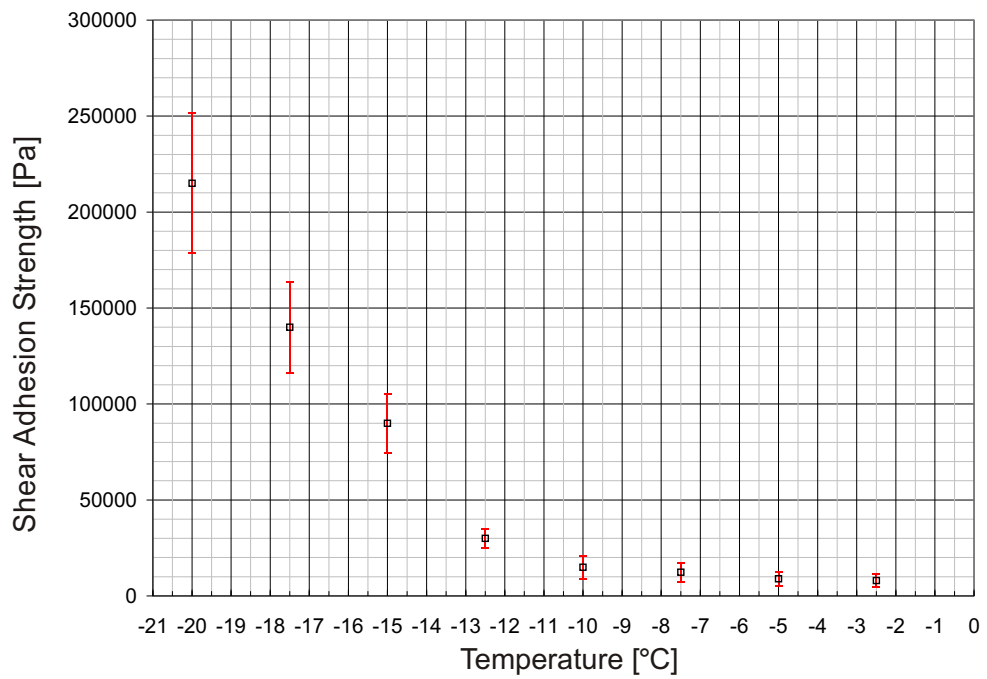
Figure 6.4: Variation of shear adhesion of 20% sucrose/ice matrix with temperature (Unilever [22]): ice/sucrose on stainless steel.
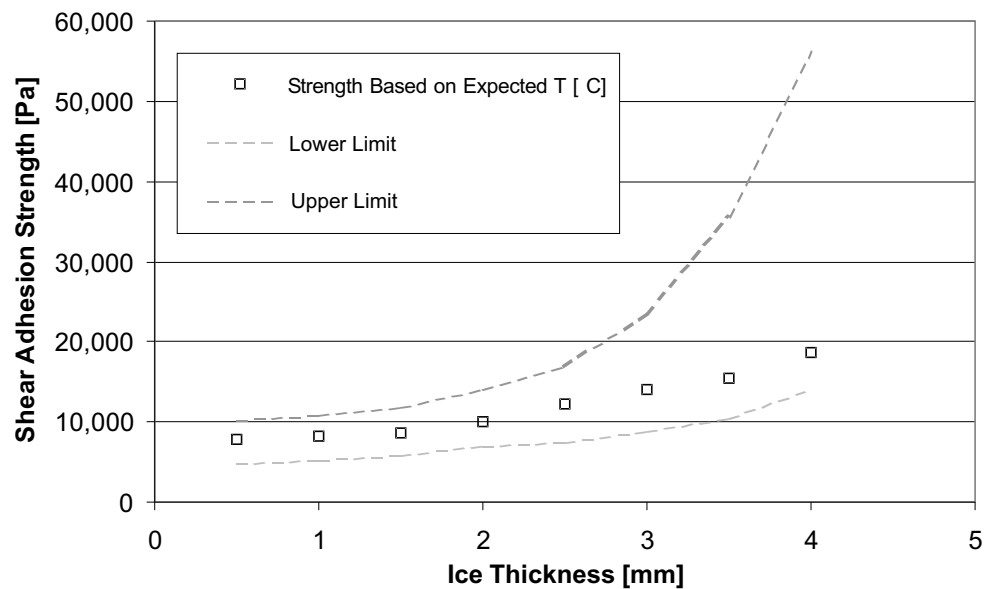
Figure 6.5: Variation of shear adhesion of 20% sucrose with ice thickness

the ice/sucrose matrix. This indicates that the normal adhesion strength may be larger than the shear adhesion strength, as is the case reported by Jellinek [61] for pure polycrystalline ice.

6.2.3 Shear and Normal Adhesion in Ice and Stainless Steel Bonds

Thickness mm	Temperature °C	Shear Adhesion Strength MPa
0.5	-1.2 ± 0.5	0.128 ± 0.061
1.0	-3.1 ± 0.5	0.360 ± 0.061
1.5	-4.5 ± 0.5	0.530 ± 0.067
2.0	-5.9 ± 0.5	0.700 ± 0.089
2.5	-7.2 ± 0.5	0.858 ± 0.109
3.0	$\sim -8.6 \pm 0.5$	1.028 ± 0.131
3.5	$\sim -10.2 \pm 0.5$	1.223 ± 0.155
4.0	-11.1 ± 0.5	1.333 ± 0.169

Table 6.2: Variation of shear adhesion strength in polycrystalline ice

Jellinek [61] describes the shear adhesion strength varying as:

$$S_A = (-1.24t - 0.18) \times \frac{9.81}{0.01^2} \,[\text{MPa}], \tag{6.2}$$

where t is the temperature in °C. For tensile adhesive failure, Jellinek reports adhesive failure strengths of circa $15.5 \, \text{kg/cm}^2$ at temperatures around -4.5°C, which equates to $1.52 \, \text{MPa}$. Below -13°C ice tends to fail cohesively, rather than at the adhesive bonds. Slightly lower values for normal adhesive strength are reported by Nelson and Young [81] at $\sim 0.91 - 1.20 \, \text{MPa}$ for -19°C for pure polycrystalline ice bonded to 316L stainless steel. This data broadly agrees with that of Nelson and Phukan [144] and Sackinger and Sackinger [145].

The temperature at the interface between the stainless steel pipe and the ice was recorded using a permanently attached thermocouple. The data is shown in Fig-
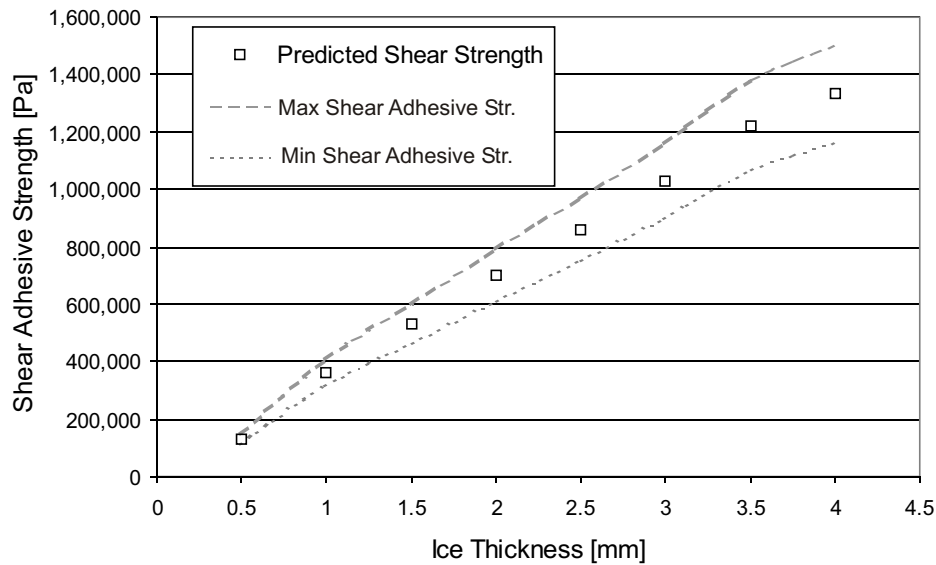
Figure 6.6: Variation of predicted shear adhesion strength with the thickness of the ice layer formed.

ure 6.7. Data in Table 6.2 and Figure 6.6 show the predicted range of shear failure conditions for each thickness of ice, based on equation 6.2.

6.2.4 Prediction of Cohesive Failure in Ice

Xu [37] presents some data for the cohesive failure of ice in the range of $(-20) - (-40)°$C. His data compare well with other studies in the field [36, 63, 35]. Again the data from most of these studies are in a temperature range that is too low to encompass the experiments conducted during this investigation. However, from Barnes [75] we can see that ice maintains a significant portion of its mechanical strength up to the melting point of $0°$ C, due to low dislocation mobility of vacancies and other defects such as OH^- and H_3O^+. Additionally Schulson [38] shows the tensile strength of ice varies by less than 25% with temperatures decreasing from $-5°$C to $-20°$C. Therefore, the data can be extrapolated with some confidence some distance from the temperature ranges reported by the various work.
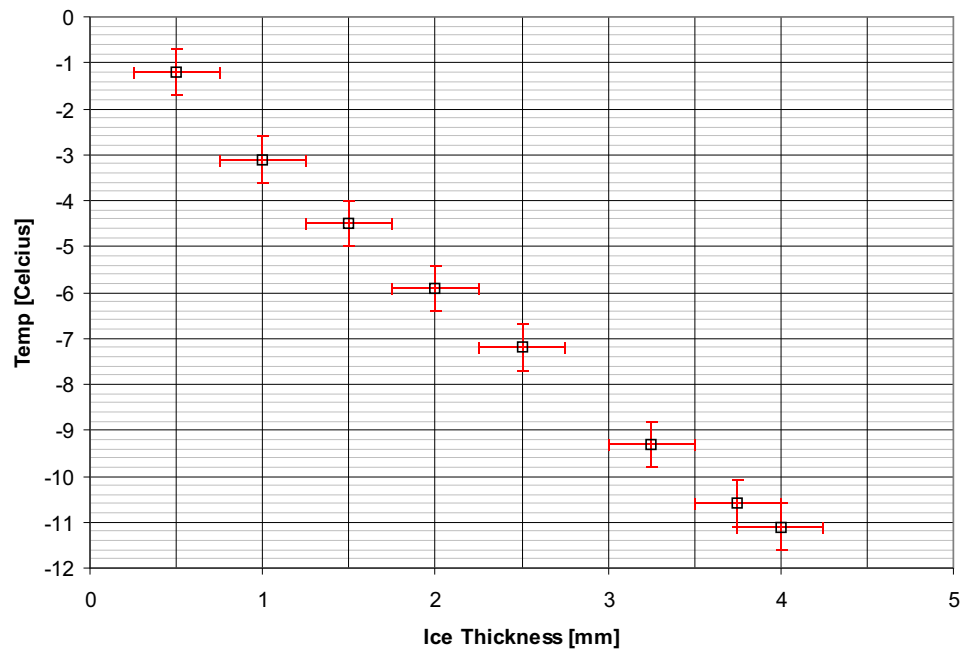
Figure 6.7: Variation of temperature with ice thickness, measured at interface of pipe and ice

A prediction of the tensile strength with increasing strain rate can be made using the data shown in Figure 6.8 . Brittle fracture occurs after the strain rate passes a critical value of $\dot{\varepsilon} = 10^{-2} \frac{1}{s}$. The dotted black line shows the predicted UTS extension in the brittle region, however, no data is presented for this temperature in the literature. This prediction is based upon the gradients of the line linking the data points in this region for data from $-15°$C and $-20°$C which is reported by Xu [66]. It can be seen from the data from the built-in pipe experiments at $-10°$C that the predicted trend agrees well with the experimental data gathered.

6.2.5   Section Summary

Estimates of the adhesive and cohesive strengths of both ice and frozen sucrose solution (20% by mass) have been shown in this section. The values and trends obtained will be used in section 6.4 to compare with data obtained by experiment and used
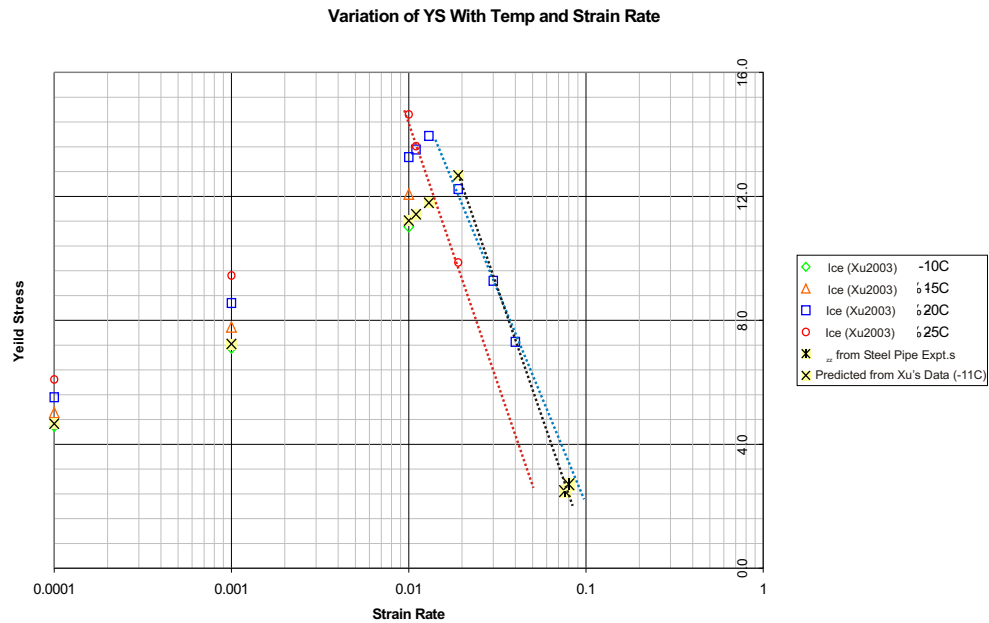
Figure 6.8: Yield strength versus strain rate for pure polycrystalline ice. Published data compared with experimental data from built-in pipe experiments at $-11°C$.

as inputs to the finite element models of Chapter 5.

6.3   Modelling Order of Failure In Water Ice

It was predicted that the ice would fracture first in the axial direction as the axial stresses (σ_{ZZ}) produced from the Ansys model were one to two orders of magnitude larger than the stresses in the other directions. It would be of interest to show that the failure predicted by the Ansys model was mirrored by the behaviour of the experiments. To show this some extra modelling was required. The first case to be examined was ice in air with the system vibrating near mode 1.

6.3.1 Cracks in Mode 1 Vibration

A crack was introduced into the finite element model at the σ_{ZZ} anti-node, by removing one complete slice of the ice elements at the mid-length of the pipe, see Figure 6.9. The model was run again to find the new axial stress distribution, accounting for the stress relaxation at the crack interface. The new peak value of σ_{ZZ} will be at some distance from the initial crack. By taking the difference in the two axial positions the length of the ice collar that will be formed can be determined. This process is shown in Figure 6.9, where a crack is shown at the mid-length of the pipe (C1) and a second crack (C2) is shown at the location where the finite element model predicts the next maximum of the axial stress (σ_{ZZ}). This maximum σ_{ZZ} is due to the stress relief caused by the first crack in the ice. With cracks C1 and C2 included in the finite element model the position of the next crack could then be predicted using the position(s) of maximum axial stress from the updated finite element model, and so on.
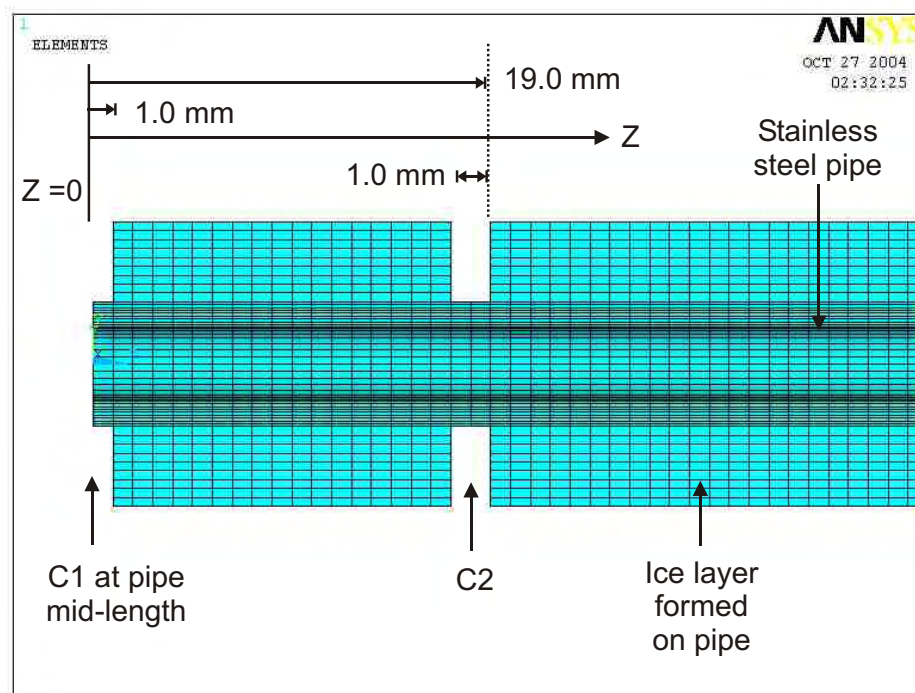
Figure 6.9: Axial failure positions as predicted by Ansys: Mode 1, 4.0 mm ice in air.

Although some evidence of collar-like failure was shown during preliminary experi-

	FEM Predictions		Experiment	
	Position mm	Collar Lng. mm	Position mm	Collar Lng. mm
InitialCrack	0.0 ± 0.0		0.0 ± 1.0	
1stCollar	19 ± 1.0	19.0 ± 1.0	22.5 ± 2.5	22.5 ± 3.5
2ndCollar	32.5 ± 1.0	13.5 ± 2.0	42.5 ± 2.5	20.0 ± 6.0

Table 6.3: Values of predicted collar length versus experimentally observed collar length in axial direction: Mode 1, 4.0mm ice, (distances measured from mid-length of pipe).

ments based on sucrose/ice immersed in sucrose solution, no quantifiable dimensions were shown, i.e. the ice was removed in collar like segments, but the formation of cracks could not be observed prior to the removal of the collar. Problems with estimating the crack positions were caused by the semi-opaque nature of the sucrose/ice, which obscured the location of any cracks formed. Therefore, another experimental strategy was required to obtain a better understanding of what happened during the increase of axial loading.

A separate experiment was conducted on the rig, involving water ice frozen around the pipe, but exposed to the air. The pipe was initially actuated from a very small amplitude of vibration. The amplitude of vibration was slowly increased until the first cracks appeared axially at the centre of the pipe. The amplitude of vibration was then increased further until the second set of axial cracks appeared in the ice. The cracks could be readily identified by their opaque white appearance as opposed to the colourless transparent appearance of the rest of the body of "undamaged" ice. The values of strain in the system were recorded for each crack position.

Table 6.3 shows the lengths of collars of ice that were formed due to the ice failing in tension axially, as estimated by finite element prediction and also as seen experimentally. The operating condition was Mode 1 vibration with an ice thickness of $4.0 \pm 0.5\,\text{mm}$. Although there is some difference between the finite element predictions and the experimental findings, the comparison between the two data sets demonstrates that the nature of the behaviour is understood.
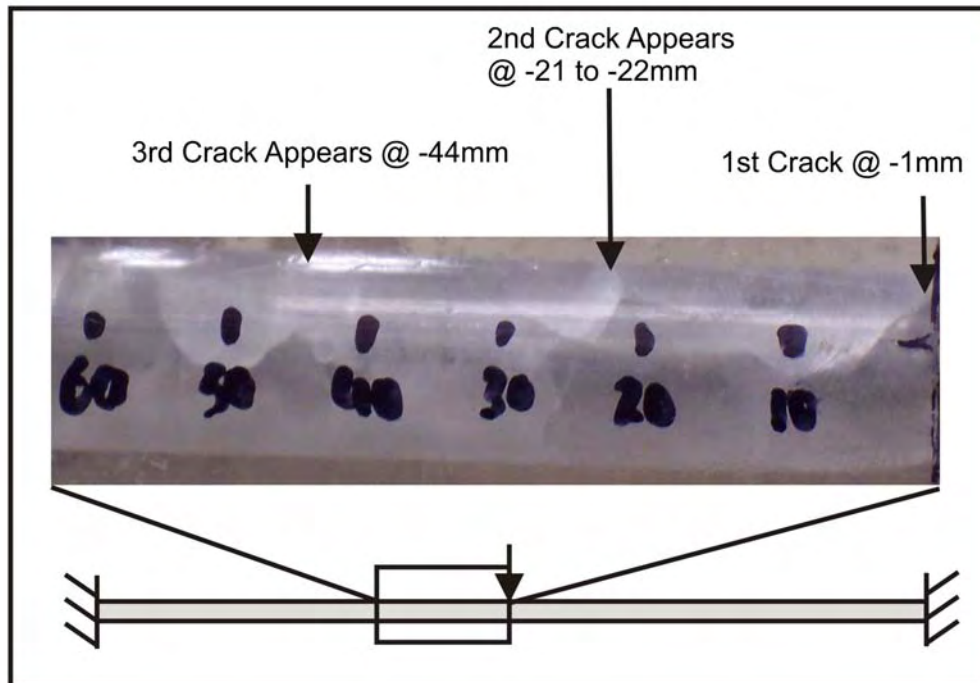
Figure 6.10: Photograph showing the location and alignment of cracks in water ice due to bending stresses under mode 1 excitation.
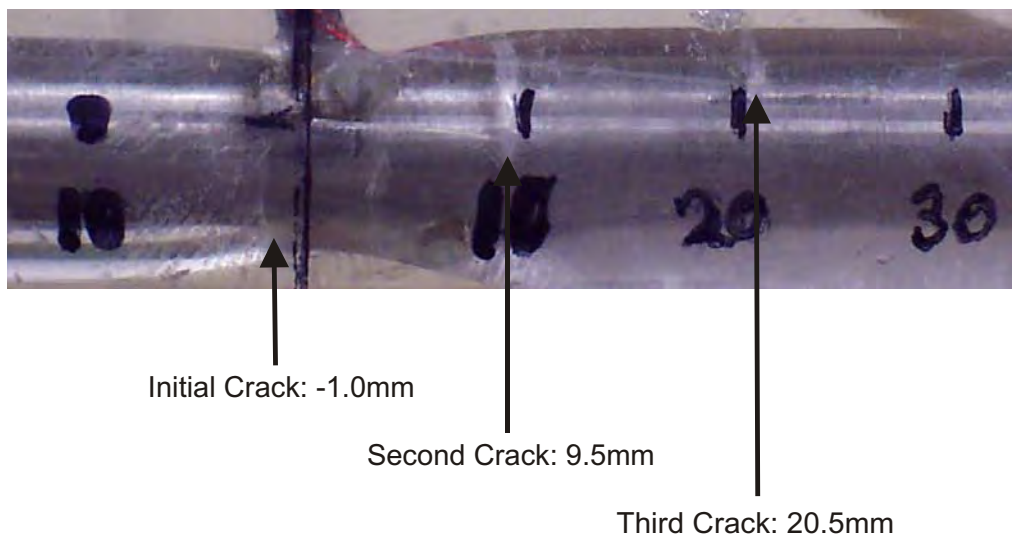
Figure 6.11: Photograph showing the location and alignment of cracks in water ice due to bending stresses under mode 3 excitation towards the centre of the pipe.

Figure 6.10 shows a typical example of the axial cracks forming in the cylinder of ice during excitation close to the first mode at around 65 Hz. Although the cracks initiate in similar positions to those predicted by the finite element model they tend to veer off as though caused by stresses acting in the θ-direction. This is probably due to the axial stresses becoming small along the neutral axis of the pipe and other stresses, in particular $\sigma_{\theta\theta}$, becoming more dominant.

Another interesting feature clearly shown in Figure 6.10 is the non symmetrical nature of the cracks formed in the ice. The stresses induced from the vibration will be broadly symmetrical, and the cracks might be expected to be symmetrical. It seems that the anomaly could be caused by gravitational effects. For instance, while the sucrose solution is freezing the part at the bottom of the ice sheath would become more dense than that formed at the top part of the sheath. The amount of material available to resist the stress induced by the vibrations of the system would be greatest at the bottom of the ice/sucrose sheath. This is consistent with the evidence, where cracks are seen at the top surface at just above the predicted failure strength, but none are seen at the bottom of the sheath.

These experiments were conducted to confirm that σ_{ZZ} overcame the cohesive strength of the ice before the other stress components overcame the adhesive or cohesive strength of the ice. Once this had been shown (evidence by the first appearance of hoop cracks), some other interesting observations could be made from these experiments. If the amplitude of vibration is increased above that required to just form axial cracks in the ice, then more cracks form at roughly regular intervals along the length of the cylinder of ice. At some higher amplitude the cracks induced by hoop stress ($\sigma_{\theta\theta}$) grow until the ice is removed completely.

However, before the ice is removed, bubbles can be seen near to the T-connector, through the ice, at the interface between the pipe and ice. The bubbles appear to be gas trapped within a liquid medium although the cracked nature of the ice makes viewing of the bubbles difficult at best. Even though the exact time of formation

of these bubbles (and therefore the amplitude of vibration) is hard to pin down, it is before the hoop stress derived cracks meet and cause separation of the ice. The appearance of bubbles at this point implies that the adhesion between the ice and the steel has been overcome before the hoop stress ($\sigma_{\theta\theta}$) has become greater than the cohesive strength of the ice. Therefore, qualitatively at least, it appears that an order of failure in the system might be:

1. $\sigma_{ZZ} > \sigma_{Crit.}^{Cohesive}$

2. $\sigma_{shear} > \sigma_{Crit.}^{Adhesive}$

3. $\sigma_{\Theta\Theta} > \sigma_{Crit.}^{Cohesive}$

6.3.2 Cracks in Mode 3 Vibration

The finite element model was altered to include cracks in the ice for mode 3 vibrations, in a similar way to that described in the above section. Cracks $C1$ and $C2$ were placed at the absolute maxima of axial stress predicted by the unmodified finite element model for mode 3 harmonic vibrations. Figure 6.12 shows the plot of axial stress (σ_{ZZ}) against Z from the finite element model in which cracks $C1$ and $C2$ had been introduced. The absolute maxima on the plot of the axial stress (σ_{ZZ}), shown in Figure 6.12, were used to determine where cracks $C3$, $C4$ and $C5$ would appear. The new system of cracks in the finite element model is shown below the plot of the axial stress. The process would be repeated to obtain the positions of the next cracks, and so on.

Table 6.4 shows the positions of the cracks and calculated collar lengths for the rig operating in Mode 3. The ice thickness observed in this experiment is $2.5 \pm 0.5\,\text{mm}$ There is very good agreement between the data obtained from the experiment and the predicted data from the finite element model. It should be noted that the observed cracks did not form around the entire circumference of the pipe in Mode 3 experiments on water ice in air. The cracks were observed at the top and bottom of the ice layer, i.e. at 0 and $180°$ relative to the finite element model. This effect can be seen, although not very clearly, in Figure 6.11; the cracks were more visible to
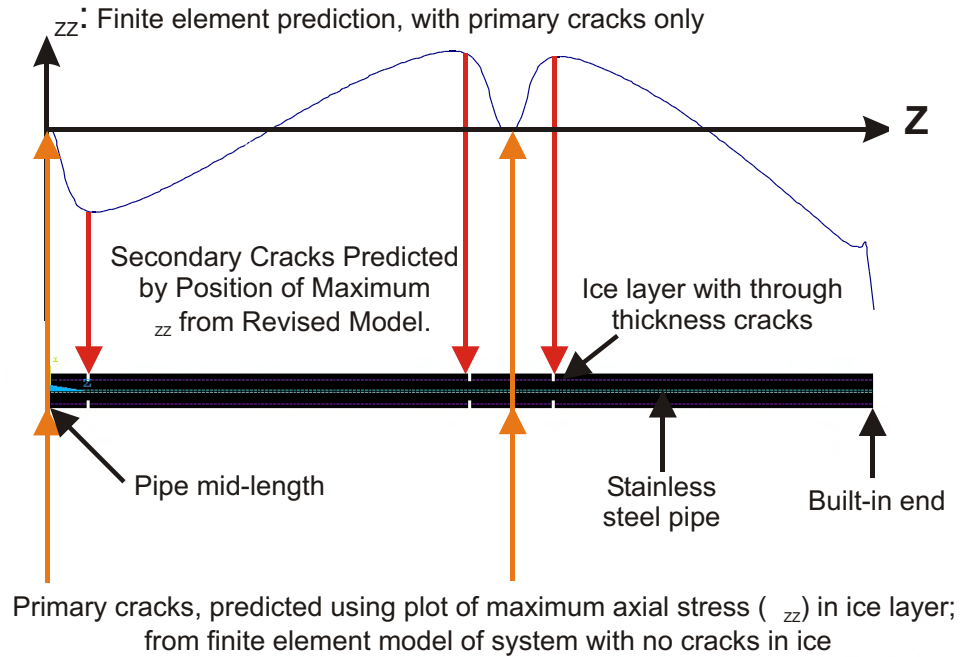
Figure 6.12: Mode 3, 2.5mm Ice: Modelling of Cracks in Ice. Primary cracks $C1$ and $C2$, predicted using plot of maximum axial stress (σ_{ZZ}) in ice layer; from finite element model of system with no cracks in ice.

the naked eye.

Even at the maximum amplitudes of vibration, of Mode 3, the ice could not be removed. In fact, the cracks that formed remained in the hoop direction. No "turning" to the axial direction was observed. Also no bubbles were seen at the interface during these experiments. Therefore, we can say that the order of failure appears to be first axial σ_{ZZ}, but after this no experimental data could be captured from these experiments based on ice formed from tap water.

6.3.3 Mode 5 Experiments

No experimental data could be gathered from the same type of experiment based on Mode 5 vibrations, as cracks were not observed, even in thin layers of ice $\leq 0.5\,\text{mm}$. In the experiments, where sucrose/ice was removed from the outer surface of the pipe, there was little evidence of the ice being removed in cylinders, as was the case
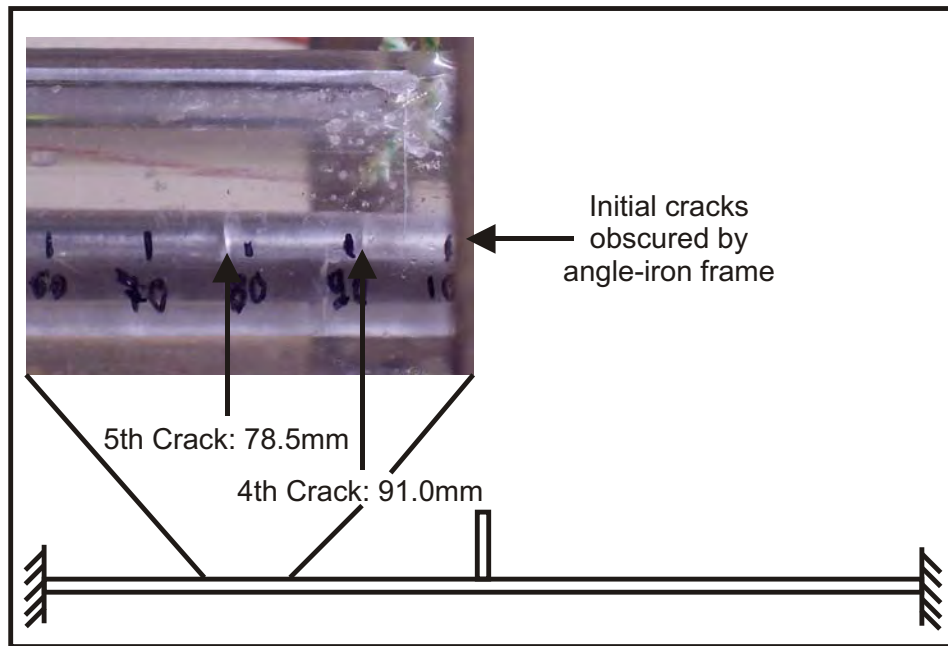
Figure 6.13: Photograph showing the location and alignment of cracks in water ice due to bending stresses under mode 3 excitation near 120 mm from the centre of the pipe.

	FEM Predictions		Experiment	
	Position mm	Collar Lng mm	Position mm	Collar Lng mm
InitialCrack	0.0 ± 0.5		0.0 ± 1.0	
1stCollar	9.5 ± 0.5	9.5 ± 1.0	10.0 ± 1.0	10.0 ± 2.0
2ndCollar	18.5 ± 0.5	9.0 ± 1.5	19.0 ± 1.0	9.0 ± 3.0
InitialCrack	116.0 ± 0.5		120 ± 1.0	
1stCollar	105.5 ± 0.5	10.5 ± 1.0	110.0 ± 1.0	10.0 ± 2.0
2ndCollar	94.5 ± 0.5	11.0 ± 1.5	100.0 ± 1.0	10.0 ± 3.0
InitialCrack	116.0 ± 0.5		120 ± 1.0	
1stCollar	126.5 ± 0.5	10.5 ± 1.0	130.0 ± 1.0	10.0 ± 2.0
2ndCollar	135.5 ± 0.5	9.0 ± 1.5	140.0 ± 1.0	10.0 ± 3.0

Table 6.4: Values of predicted collar length versus experimentally observed collar length in axial direction: Mode 3, 4.0 mm ice in air (distances measured from mid-length of pipe).

in Mode 1 and 3 experiments. Instead, the ice appeared to be removed in a cloud of small flakes, of approximately $0.5 - 2.0\,\text{mm}$ in diameter.

6.3.4   Discussion of Experiments and Modelling

The finite element model did not directly account for the temperature of the system. However, the material properties of ice (E, ν and ρ) do vary slightly with temperature as shown in Chapter 5, Equation 5.4. The values used in the finite element model are taken as those corresponding to the temperature at the interface between the ice and the stainless steel pipe. The material properties (E, ν and ρ) are assumed to be constant through the thickness of the ice.

In the experiments this was not true. Some temperature variation was observed through the thickness of the ice and also along the axis of the pipe. The temperature variation in the case for Mode 1, $4.0\,\text{mm}$ of ice was from $\sim -10°\,\text{C}$ at the interface between the pipe and the ice to $\sim -1.6°\text{C}$ where the ice contacts the surrounding fluid. As the ice thickness investigated in these experiments for Mode 3 was less than that of the first mode the temperature variation was also less.

The mechanical properties used in the finite element model are unlikely to fully represent the actual mechanical behaviour of the experimental rig, as they varied with temperature through the thickness of the ice. Also the cracks observed during experimentation had small crack mouth openings of $< 1\,\text{mm}$ (see Figures 6.10, 6.11 and 6.13) and the cracks in the finite element model are really notches with width of $1\,\text{mm}$. This may have been significant in producing the errors in the prediction of collar length, as the areas where stress relaxation were predicted were significantly larger than the areas where stress relaxation occurred on the physical rig. However, as the aim was only to determine the behaviour of the system, this effect has small overall significance.

In addition figure 6.10 shows another discrepancy between the model of the ice and the cylinder of ice itself. At the mid-length of the cylinder, (i.e. in the region of

the T-connector), there is a dip in the thickness of the ice layer around this position. This is probably due to less effective heat transfer in this region - as the T-connector also has to be cooled and there is a thin layer of epoxy (waterproofing for the strain gauge) effectively acting as insulation on the pipe at this position. Whatever the reason for this change in thickness of the ice compared with the rest of the pipe, it does represent a deviation from the FE model and is therefore likely to represent a reduction in the accuracy of the prediction of the collar lengths in the ice.

These effects might be more accurately represented by enhanced finite element modelling of the system. For instance, the ice layer could be considered as several annular layers; each with a separate value for E, ν and ρ. However, this level of modelling was not practical in the time available. Also, the effects of such modelling are unlikely to produce a significant improvement in the results obtained from the finite element model.

There is much more uncertainty associated with the fracture properties of the ice (which is well known to be variable) than with the inaccuracies and errors mentioned above. Thus, these errors and inaccuracies are considered to be unimportant.

6.4 Results for 20% Sucrose Solution

This section will present the results from the built-in pipe experiments described in Chapter 4. The basic results were augmented by finite element models produced using Ansys 6.1 [127]. The failure stress for the ice and sucrose was predicted using a combination of the finite element model output and experimental data.

Each data point presented in the following sub-sections on modes 1, 3 and 5 experiments to remove frozen sucrose is taken from a minimum of eighteen data points, typically $50-60$ data points were obtained for each thickness. The experimentally determined stress components at failure were taken as the average of these data points.

6.4.1 Mode 1

In the experiments that produced the data to be discussed in this section, the pipe was excited in the frequency range of $56 - 80\,\text{Hz}$, producing mode 1 vibrations. The amplitude of vibration was raised by increasing the gain of the amplifier [146]; the gain was increased slowly until the ice was just removed from the pipe. Frozen sucrose was removed near to the centre of the pipe as shown in Figure 6.14. In some of the experiments the amplitude was increased still further and the ice could be removed from almost the whole length of the pipe over the range of thicknesses examined, i.e. $0.5 - 4.0\,\text{mm}$.
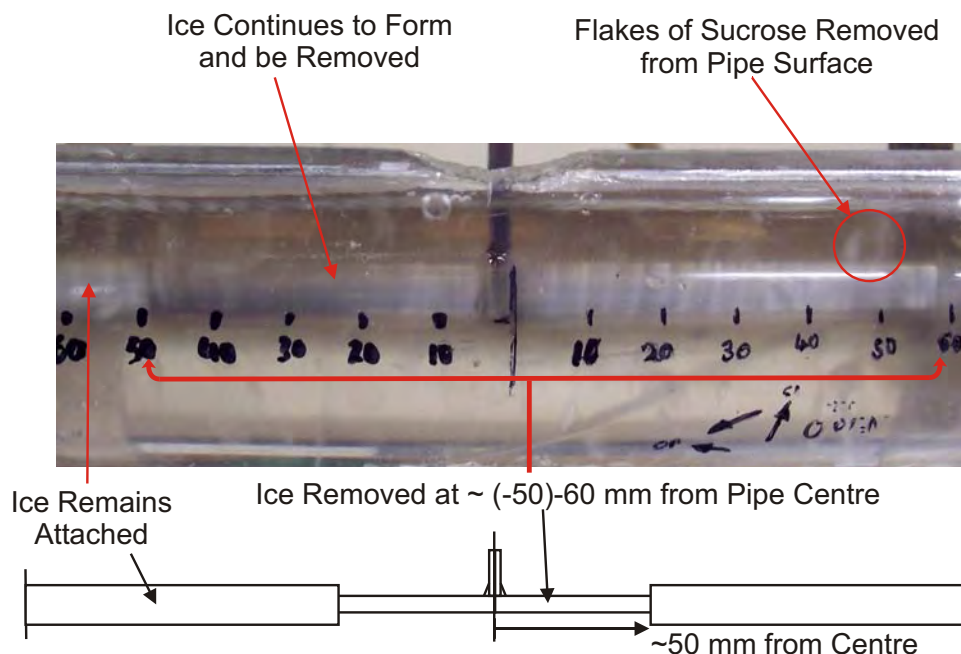
Figure 6.14: Photograph showing position of sucrose/ice removal from an experiment on the stainless steel pipe for Mode 1 vibrations.

For each experiment the dynamic strain was noted at the final failure condition of the ice. A reading was taken from a strain gauge at the centre of the pipe and another at $187\,\text{mm}$ from the centre of the pipe, with both strain gauges on the un-

derside of the pipe. The axial position on the pipe where ice removal finished and the two associated strain values were recorded for each experiment. Each value of strain was used to scale the relative values of strain and stress obtained from the finite element model of the pipe. The stress components were recorded at the position where ice removal had finished.

The absolute values of each stress output (σ_{ZZ}, $\sigma_{\theta\theta}$, σ_{rr}, $\sigma_{r\theta}$, σ_{rZ}, and $\sigma_{\theta Z}$) from the finite element model of the system vibrating at mode 1 were plotted against the thickness of frozen sucrose used in the experiment. The value of each stress parameter varied with the position on the pipe and was determined by using the stress variations shown in Figure 6.15. This figure was produced from the finite element model of a pipe with 1.5 mm frozen sucrose solution (20%) formed on the surface, and was scaled to the experimental data for a pipe with 1.5±0.25 mm frozen sucrose solution (20%) attached to the surface, see section 5.3.7 for explanation of scaling methodology.

The axial position of the failure was noted from the experiment, but even with this information some work had to be conducted to obtain suitable values for each component of stress, as each stress component varies in position in the R and θ-directions at the noted axial position. The values of stress plotted from each experimental condition are the values predicted by the finite element model at the appropriate location (R, θ) for the noted Z value. For example the shear stresses $\sigma_{r\theta}$, $\sigma_{\theta Z}$, σ_{rr}, and σ_{rZ} are the predictions of the relevant stresses in the frozen sucrose at the interface between the pipe and frozen sucrose layer that are likely to cause failure of adhesion between the two materials.

Therefore, due to the sinusoidal variation of the stress in the theta direction, the maximum of each stress component was at either $90 + n \times 180°$ or $0 + n \times 180°$; where n is an integer. The value of each stress was calculated at both $\theta = 90°$ and $\theta = 180°$ at the interface, and the maximum of the two values was plotted against the thickness of the frozen sucrose layer. Similarly the values of $\sigma_{\theta\theta}$ and σ_{ZZ} were taken as the maximum values calculated within the thickness of the frozen sucrose
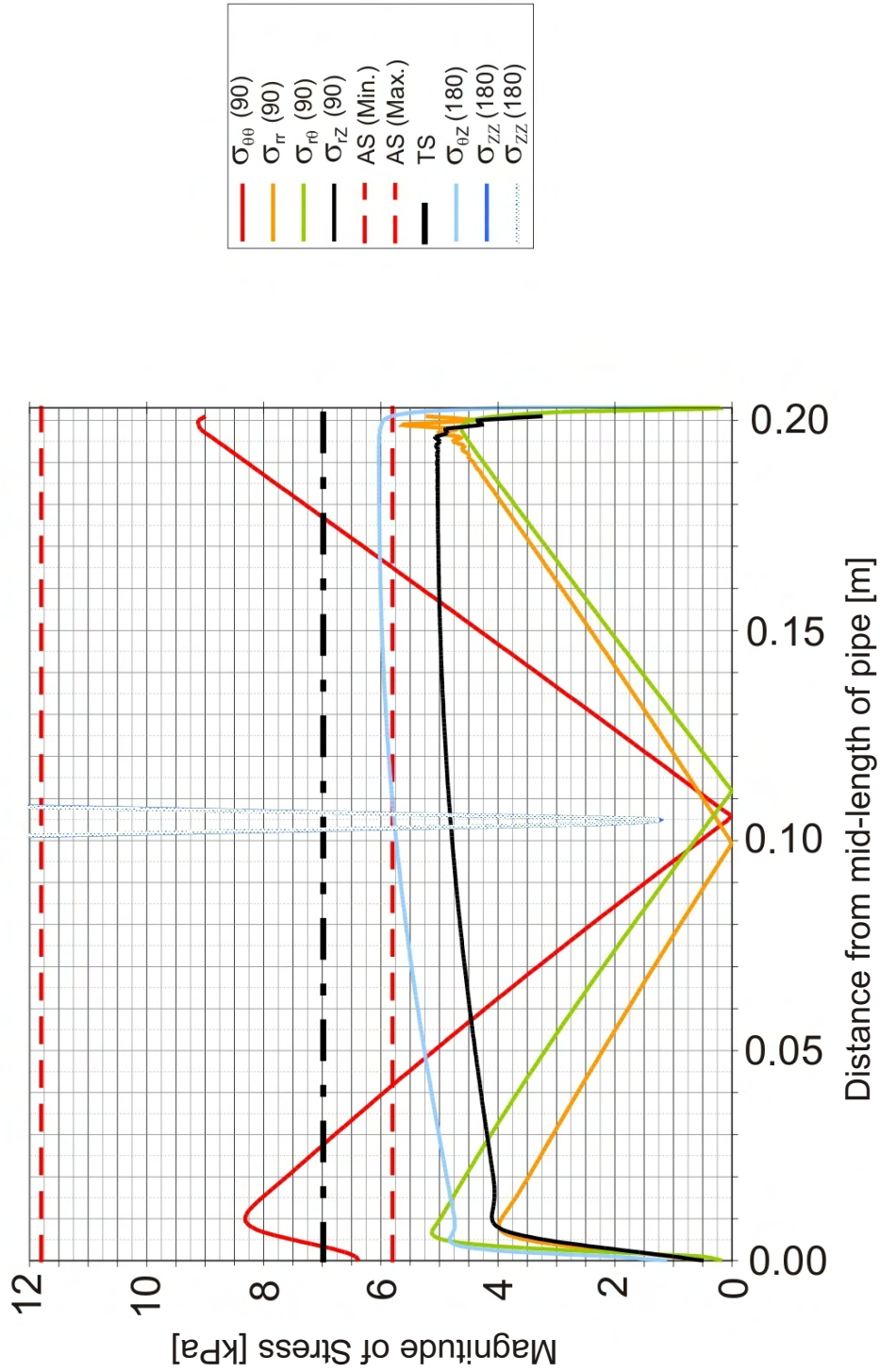
Figure 6.15: Variation of stress with position on the pipe: Mode 1, 1.5 mm ice. The Z-axis corresponds to the central axis of the pipe, with $Z = 0$ being the mid length of the pipe. Experimental data was used to scale the finite element model data as described in Section 5.3.7. The stress parameter σ_{ZZ} is not fully shown on this graph, see Chapter 5 for further information on this stress parameter.

layer, and both stress components were found to be greatest at $\theta = 180°$.
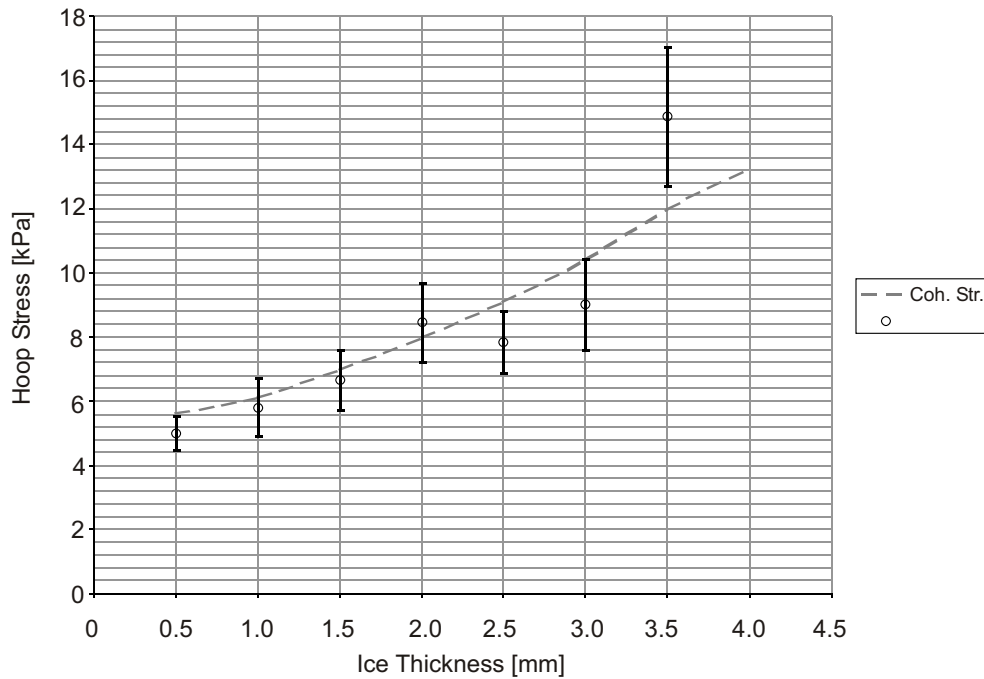
Figure 6.16: Variation of stresses predicted by experiments and Ansys modelling, with thickness, Mode 1: $\sigma_{\theta\theta}$

Figure 6.16 shows the values of the theta stress plotted against the prediction of the cohesive failure strength as calculated in Chapter 5. The data used to obtain these results were taken from the built-in stainless steel pipe operating below the first flexural mode of vibration at $56 - 72\,\text{Hz}$. This was the position of maximum recorded strain. It can be seen that there is a good agreement between the stresses calculated from the experiments and the cohesive failure strength predicted from other works, as shown in section 6.2.1. The experiments were performed in the strain rate range of $\dot{\varepsilon}_\theta = 0.08 - 0.195\,\frac{1}{\text{s}}$. These strain rates are relatively close to the strain rate at which the predicted value of ultimate tensile strength was calculated $(\dot{\varepsilon}_{\theta,crit} = 0.01\,\frac{1}{\text{s}})$, compared to the experiments for the higher order modes, which were in the range of $\dot{\varepsilon}_\theta = 0.38 - 1.13\,\frac{1}{\text{s}}$.[1]

---

[1] $\dot{\varepsilon}_{\theta,\text{crit}}$ is the critical strain rate at which the ductile-brittle transition occurs [66, 71].

The point at 3.5 mm of ice thickness is well above the line of cohesive strength predicted from the literature. Additionally, the ice could not be removed from the rig at thicknesses of 4.0 mm consistently. At 3.5 mm of ice thickness the adhesive strength of the ice/sucrose layer starts to increase. This effect was noted by Jellinek, where adhesion becomes dominant as the temperature decreases below $-13°$C [61]. This implies that the final removal of ice from the pipe is controlled by the adhesive failure at thicknesses of 3.5 mm. At lower thicknesses (i.e. higher temperatures) the effects are difficult to separate.
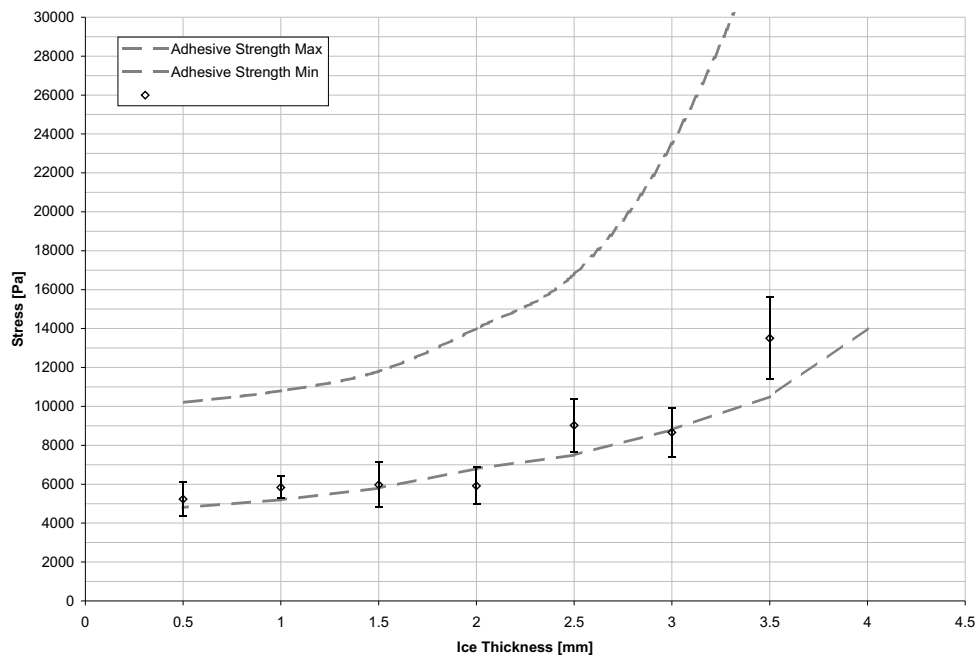
Figure 6.17: Variation of stresses predicted by experiments and Ansys modelling, with thickness, Mode 1: $\sigma_{\theta Z}$. ($\dot{\varepsilon}_\theta = 0.08 - 0.19\frac{1}{s}$)

Figure 6.17 shows the predicted shear stress at failure against the thickness of ice for the experiments of mode 1 flexural vibrations. The two broken grey lines are the predictions of the minimum and maximum shear adhesion strengths for 20% sucrose solution frozen onto a stainless steel plate suitable for food preparation. Derivation of these limits is shown in Chapter 5.

The large variation in the values predicted is due to the possible temperature vari-

ations within each experiment, and the significant scatter in the experimental data for shear adhesion strength. The strain rate at which the experiments were conducted was not included with the data used [22] to make the estimations of the shear adhesion strength, as it is likely that the experiments were quasi-static in nature. If the shear strength follows a similar pattern to that of the cohesive strength, with strain rate as shown later in this Chapter in Figure 6.18, then the data would fall towards the left-hand (ductile) side of the graph. The data obtained from the experiments using the built-in pipe rig would be towards the right hand (brittle) side of the graph of Figure 6.18.

It appears from Figure 6.18 that the data for $-35°$C and $-40°$C do not follow the same trend as the rest of the data, as the $-40°$C data crosses the $-35°$C data. However, Xu shows that the data gives a consistent trend [66], it is that the ductile-brittle strain rate which changes with temperature. From the graph it can be seen that the peak yield strength for the data recorded at $-40°$C occurs at a lower strain rate than that of the data recorded at $-35°$C. The effect of temperature on critical strain rate is less apparent at higher temperatures.

The graph in figure 6.17 appears to show a good agreement between the adhesive strength of the sucrose and the maximum interfacial shear stress ($\sigma_{\theta Z}$) that is predicted by the finite element model of the system. The experimental results follow the lower prediction of the shear adhesion strength of 20% sucrose solution adhered to stainless steel. This agreement suggests that the frozen sucrose may have been released from the surface of the pipe by the peak shear stress produced at these locations along the length of the pipe (e.g. at 45 mm from the end of the pipe, where ice remained at 46 mm and was removed at 45 mm).

It is interesting to note that the shear stress $\sigma_{\theta Z}$ at the failure condition is similar (or greater) in magnitude to the hoop stress at the failure condition at 180°. Jellinek [61] shows that when a crack in pure ice is not constrained to propagate in a given direction it will tend to shear, and similar values for shear and tensile failures in pure ice are often recorded due to this effect. A similar effect was noted by Uni-
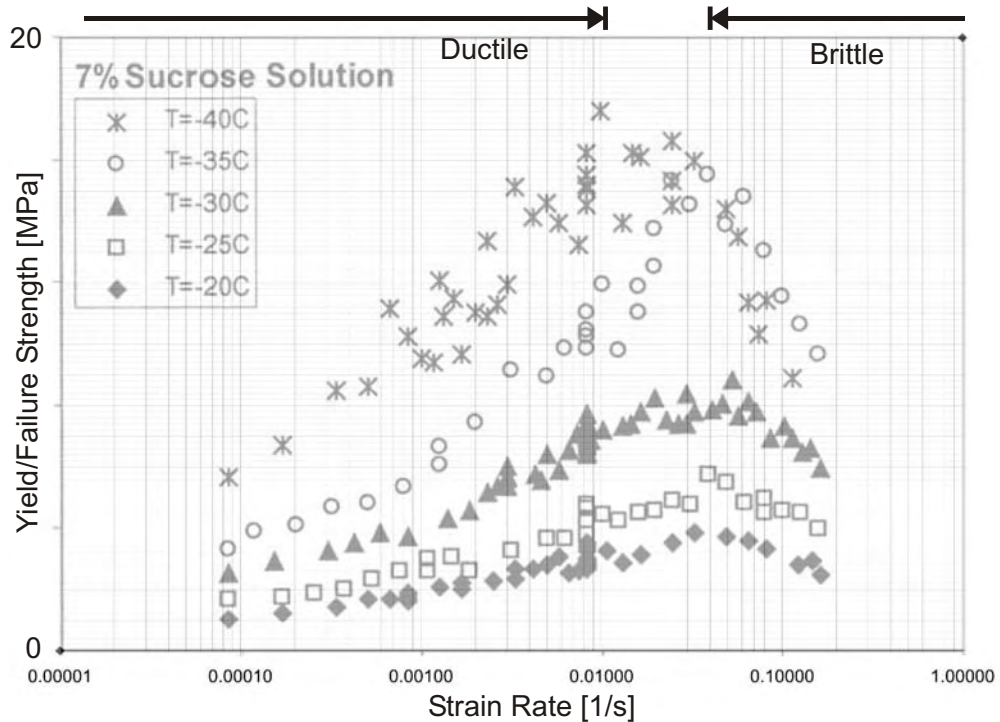
Figure 6.18: Graph showing the relationship between yield strength and strain rate of 7% frozen sucrose solution. Adapted from Xu *et al.* [66].

lever Research Group [22] when attempting the measurement of normal adhesive strength. The failure would occur at very similar values to that of the measured shear adhesion, and shear surfaces were observed in subsequent inspection of the failed frozen sucrose. Assuming that the shear and tensile strengths were similar in 20% frozen sucrose solution, this could account for the apparent failure of the ice in cracks normal to the circumference of the frozen sucrose layer at 90°. This failure was suggested by several sources:

1. The frozen sucrose is removed in flakes, which appear to have roughly the same lengths as the collars predicted by the modelling of Chapter 5, i.e. $\sim$ $15 - 20$ mm in mode 1 and $\sim 5 - 10$ mm in mode 3 experiments. These flakes also appear to be removed in a complete section around a radius of approximately 90° in mode 1 and mode 3 experiments and can be seen clearly in experiments on the thicker layers of sucrose. (The effect cannot be seen in mode 5 experiments as the sucrose appears to come away in a cloud of particles).

After Amplitude of Vibration Increased
Cracks Steer Parallel to Z-Axis at θ=90

Ice Removed when Cracks at θ=180
form Parallel to Z-Axis

Initial Cracks Perpendicular to Z-Direction
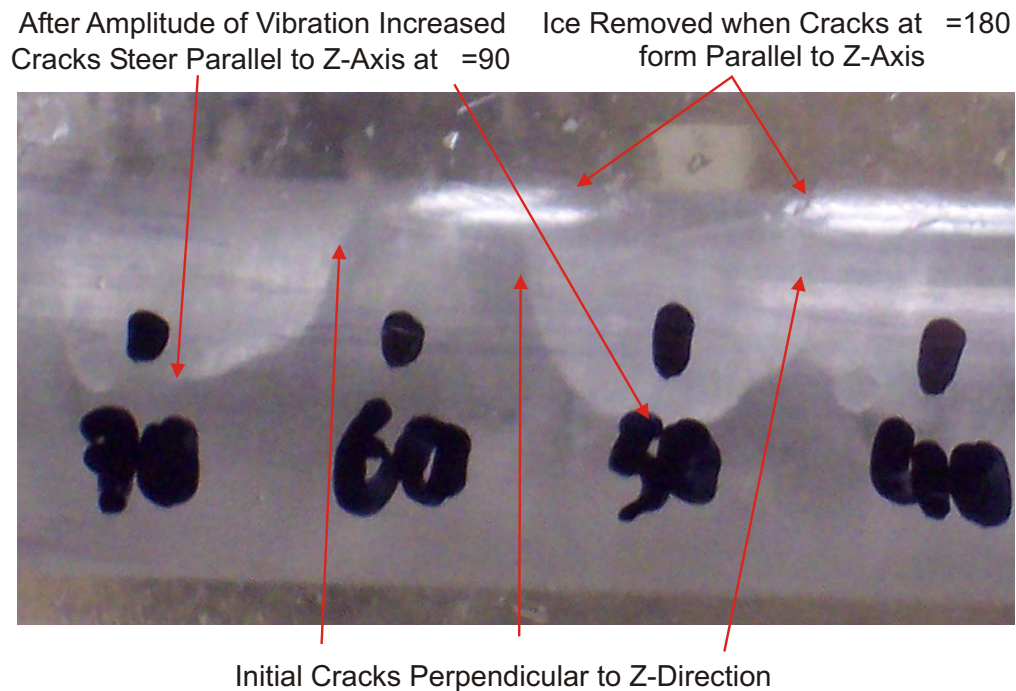
Figure 6.19: Photograph showing location of cracks during experiments on pure ice in air for mode 1 vibrations

2. In the experiments on pure ice in mode 1 the first cracks appear normal to the Z-axis, apparently being caused by the bending stress in the ice. After these initial cracks form the cracks seem to "bend" through 90° towards the Z-axis at a position $\theta \simeq 90°$, as greater amplitudes of vibration are excited. Failure of the ice finally occurs when similar cracks appear at $\theta = 180°$ in the direction of the Z-axis at even higher amplitudes of vibration. These cracks are illustrated in Figure 6.19.

Assuming that shear and tensile loading conditions produce a similar failure strength, it is possible to infer that the observed failure at $\theta = 90°$ in the rZ plane is caused by cohesive shear failure. Further experimentation would be required to show this more rigorously.

6.4.2   Mode 3

Figure 6.20 shows the variation of stress with axial position; the maximum at either 90 or 180° is quoted. Like the results from mode 1 experiments, the position of the limit of ice removal was noted along with the magnitude of the strain for each experiment.

Similarly to the results from mode 1 experiments, the values of the different stresses were obtained at the failure position noted (there was again some error in the prediction of the failure position, $\pm 5\,$mm, as shown in Figure 6.14 for mode 1 vibrations - similar errors were exhibited for mode 3 vibrations). The stress values at failure were plotted against the ice thickness. The results for each of the stresses were plotted and the relevant values are shown in this section.

Figure 6.21 shows that the ice was first removed at or around the stress anti-node (for σ_{ZZ}, $\sigma_{\theta\theta}$ and $\sigma_{r\theta}$), between the centre and built-in end of the pipe, at a position between $\sim 70 \pm 5$ to $140 \pm 5\,$mm. This positioning cannot be seen clearly due to parallax effects in the photograph, which was taken at an oblique angle to the pipe. This was necessary because of the positioning of the angle-iron frame supporting the shaker which obscured the perpendicular view of the pipe at this distance from the centre. The position of limiting ice failure was typical of the other experiments conducted for the range of ice thicknesses investigated in the mode 3 experiments. The values of the stresses were taken at $Z = 65$ and 75 and at $Z = 135$ and $145\,$mm from the centre of the pipe. The thickness of the ice layer was $2.5\,$mm and the values of stress obtained from this experiment were as follows: $\sigma_{\theta\theta} = 4750 \pm 880$Pa, $\sigma_{r\theta} = 8120 \pm 790$Pa, and $\sigma_{\theta Z} = 5050 \pm 850$Pa. The axial stress ($\sigma_{ZZ}$) was significantly larger than the cohesive failure strength of the ice over most of the length of the pipe. This was clearly shown in section 5.3.7 of Chapter5.

Figure 6.22 shows the hoop stress ($\sigma_{\theta\theta}$) versus ice thickness, with the prediction of the maximum tensile strength of 19% frozen sucrose solution, taken from work by Xu [66] on the yield strength of ice and sucrose solutions. The values obtained from the experiments appear to be lower than the maximum possible tensile strength
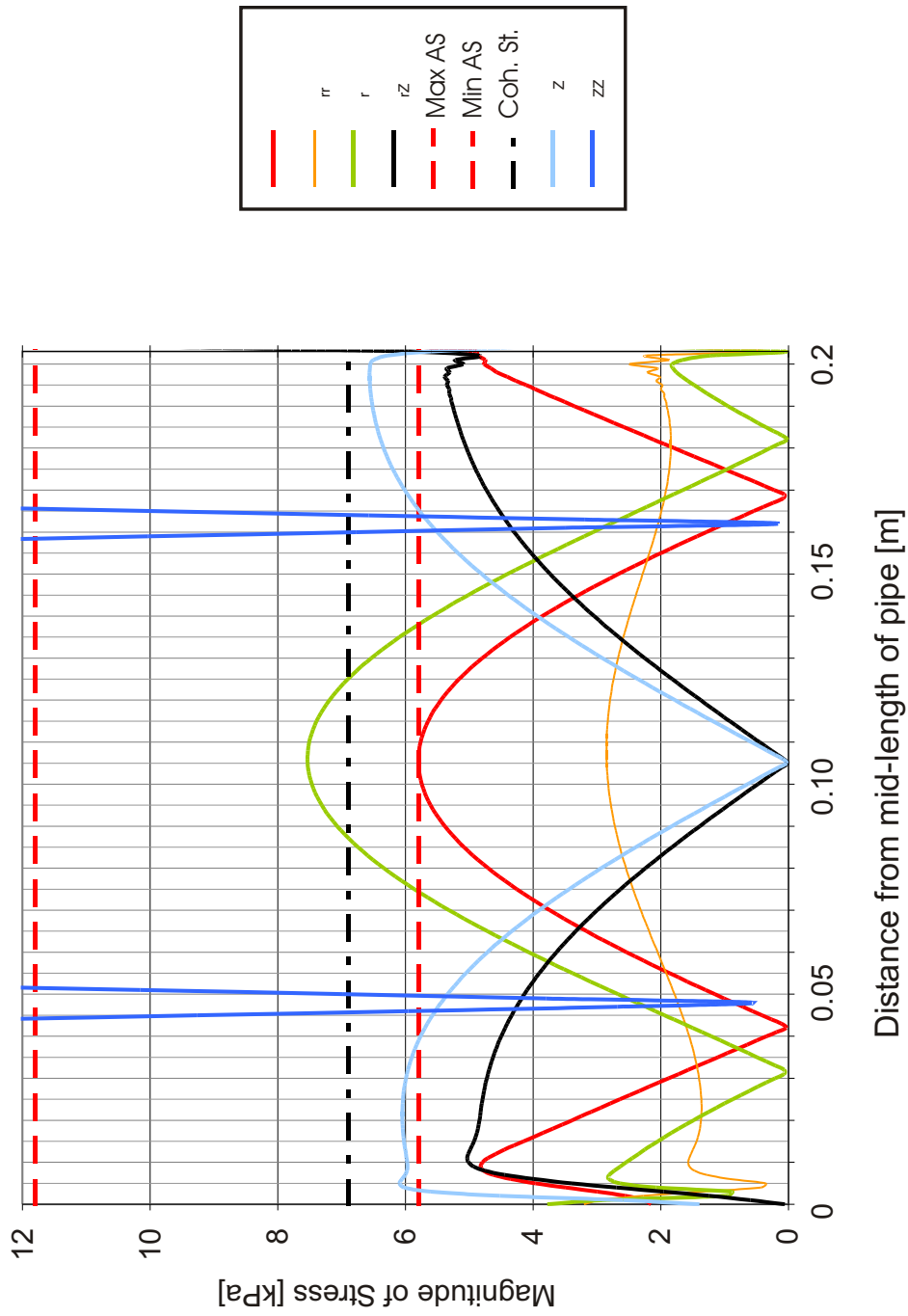
Figure 6.20: Variation of stress with position on the pipe. Mode 3, 1.5 mm ice. Experimental data was used to scale the finite element model data as described in Section 5.3.7.
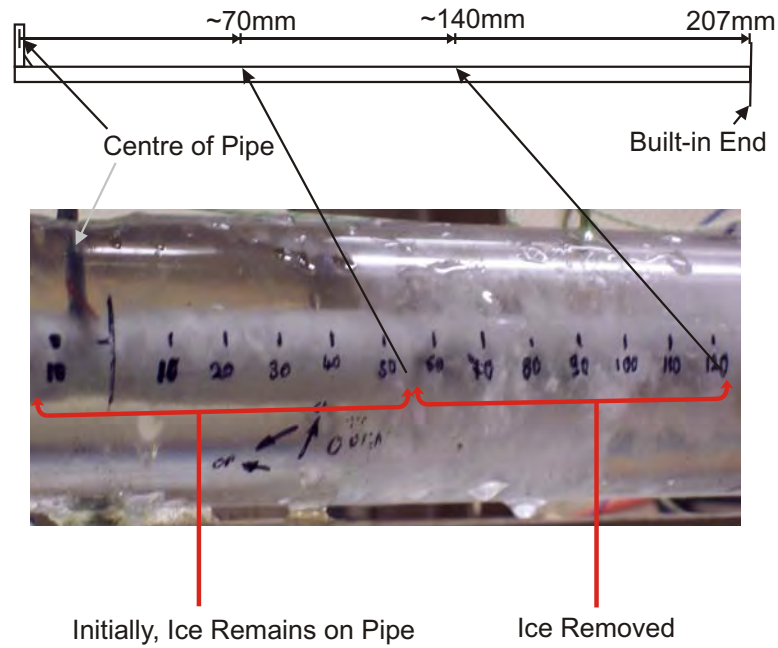
Figure 6.21: Typical position of ice removal from an experiment on the stainless steel pipe for the fifth flexural mode of vibration.
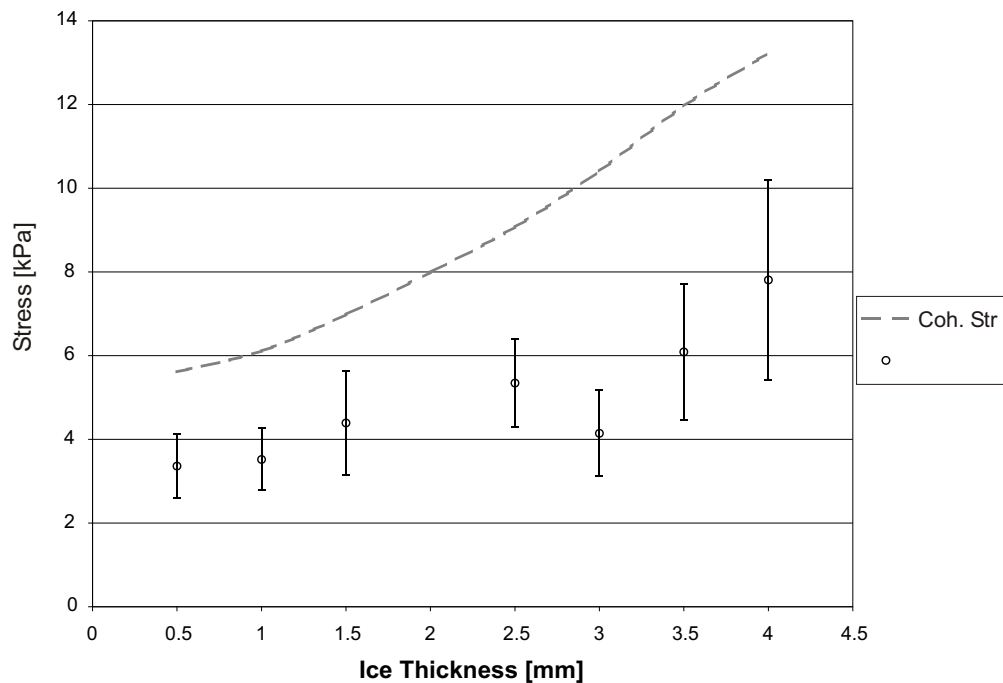
Figure 6.22: Variation of stresses predicted by experiments and Ansys modelling, with thickness, Mode 3: $\sigma_{\theta\theta}$, ($\dot{\varepsilon}_\theta = 0.38 - 0.76\,\frac{1}{\text{s}}$.)

based on the ductile-brittle transition strain rate ($\dot{\varepsilon}_{crit} = 0.01 \frac{1}{s}$). It should be noted that no data is shown in the literature for experiments of such elevated strain rates i.e. greater than $0.09 - 0.10 \frac{1}{s}$. It is probable that these new results represent the true value of the limit of cohesive strength, but this cannot be shown conclusively from these experimental results. Some further comment will be made in Section 6.4.4 regarding this hypothesis.
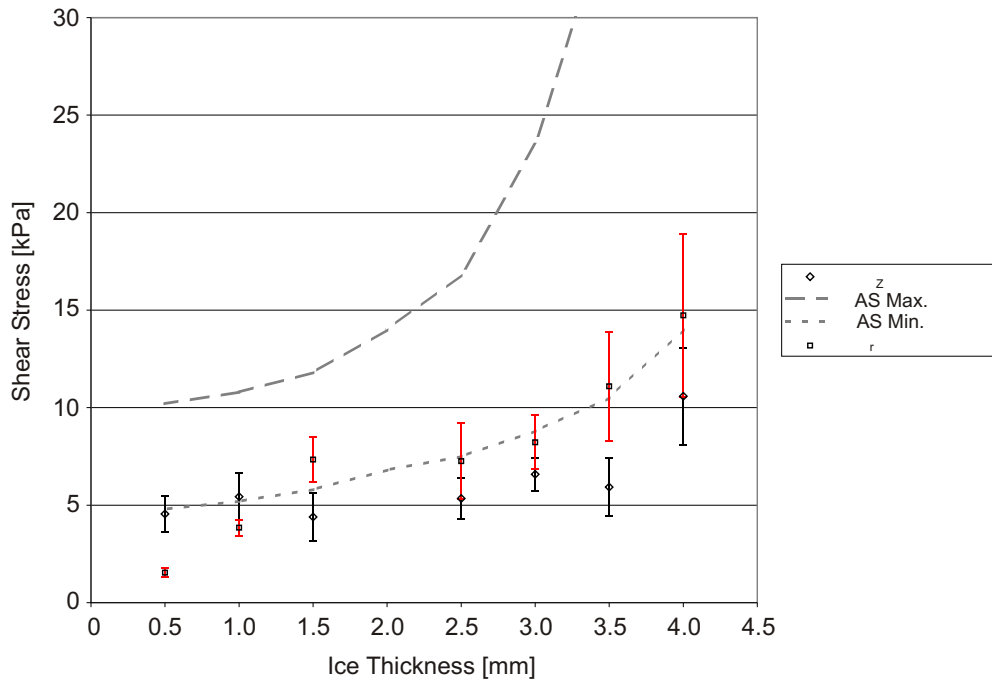
Figure 6.23: Variation of stresses predicted by experiments and Ansys modelling, with thickness, Mode 3: $\sigma_{r\theta}$ and $\sigma_{\theta Z}$, ($\dot{\varepsilon}_{\theta\theta} = 0.38 - 0.76 \frac{1}{s}$.) Compared with strength data from Section 6.2.1.

There appears to be good agreement between the experimentally determined data for interfacial shear stress and the limits predicted for the shear adhesion strength of the frozen sucrose. This tends to strengthen the argument that the shear adhesion strength does not exhibit strain rate sensitivity. This can be shown as the magnitudes of the values predicted at failure were again very similar to those seen in the mode one experiments shown in Figure 6.17.

Again the shear stress $\sigma_{\theta Z}$ at $\theta = 90°$ is similar in magnitude to the cohesive stress

$\sigma_{\theta\theta}$ acting at $\theta = 180°$ and may be responsible for failure in the rZ plane at $\theta = 90°$ (see Figure 6.23). This corresponds well with the same data in the mode 1 experiments, and failure at $\theta = 90°$ was visible in both of these experiments.

6.4.3 Mode 5

Figure 6.24 shows how the stress field varies with the axial position in the fifth mode of vibration. The previous sets of experiments for modes 1 and 3 had allowed some estimation of the stress at failure using the following method. The position of failure in the axial direction was noted and then each of the stress components at that position were compared. These components were calculated as the maximum value in the θ-direction and at the relevant radial position, i.e. at the interface for shear stresses and at the position of maximum stress for the cohesive stresses under consideration.

However, in mode 5 the frozen sucrose solution appeared to be removed along the entire length of the stainless steel pipe. Visibility of ice removal was poor as the frozen sucrose was removed in what appeared to be a cloud of small particles, rather than the more substantial "flakes" that were removed during the ice removal in modes 1 and 3. To gain an idea of the stress required in the different directions to remove the ice the maximum stress predicted from each experiment was taken. The actual value of stress required to remove the ice may therefore be lower than the value quoted for these mode 5 experiments, as this maximum calculated value acts at only a few positions along the length of the pipe, i.e. at $\sim \pm 60\,\text{mm}$ and $\sim \pm 145\,\text{mm}$ for σ_{ZZ}, $\sigma_{\theta\theta}$, $\sigma_{r\theta}$ and σ_{rr} and at $\sim 0\,\text{mm}$, $\sim \pm 105\,\text{mm}$ and $\sim 207\,\text{mm}$ for the other stresses. This can be seen in Figure 6.24.

Figure 6.25 shows the relationship between the thickness of frozen sucrose formed onto the pipe, and the hoop stress ($\sigma_{\theta\theta}$) predicted by the finite element model at the failure of ice. As with the mode 3 experiments it seems that the stress at failure is somewhat lower than the prediction of the cohesive strength of the frozen sucrose estimated at a strain rate of $\dot{\varepsilon}_{critical} = 0.01\,\frac{1}{\text{s}}$.
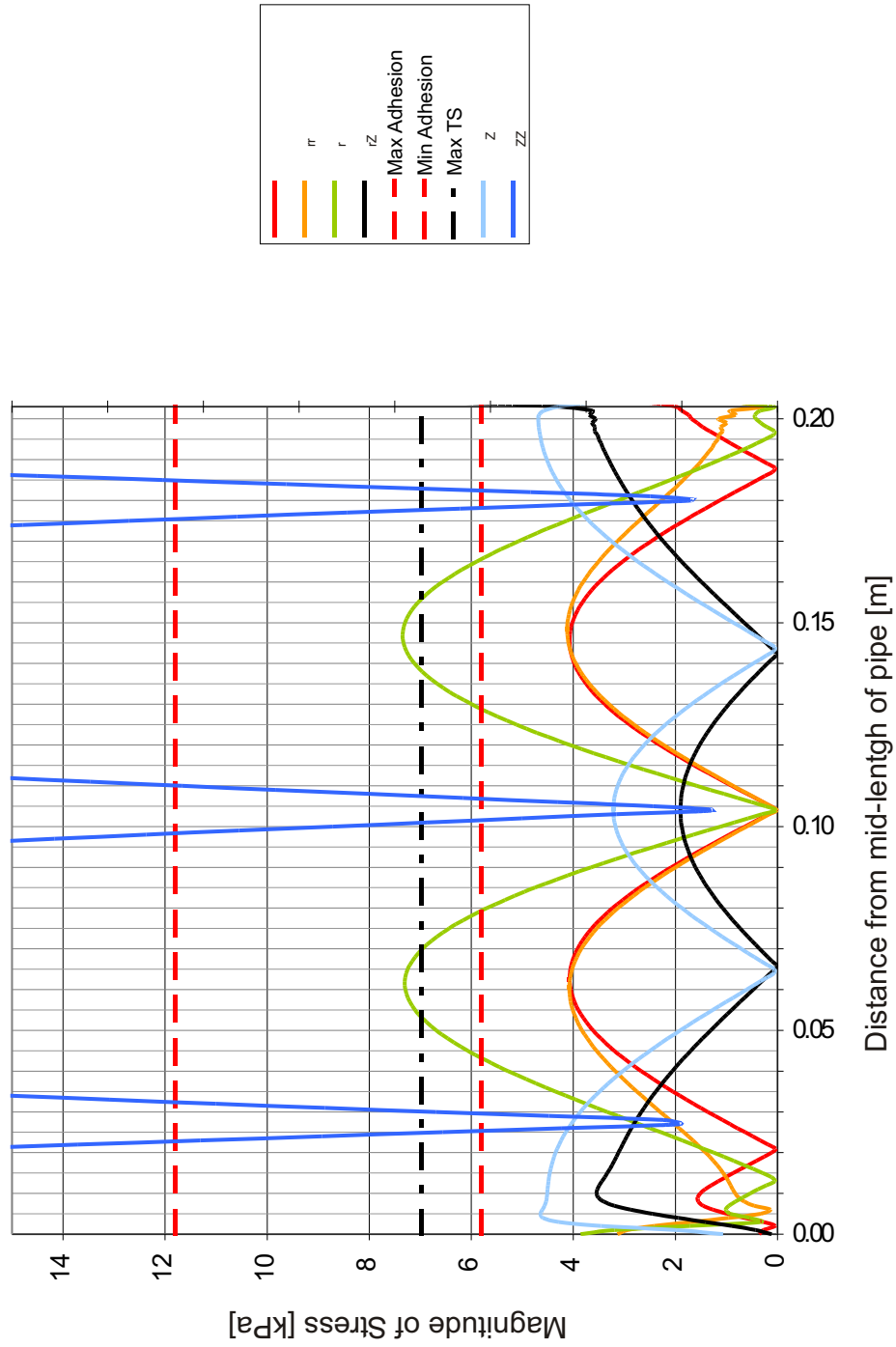
Figure 6.24: Variation of stress with position on the pipe. Mode 5, 1.5 mm ice. Experimental data was used to scale the finite element model data as described in Section5.3.7.
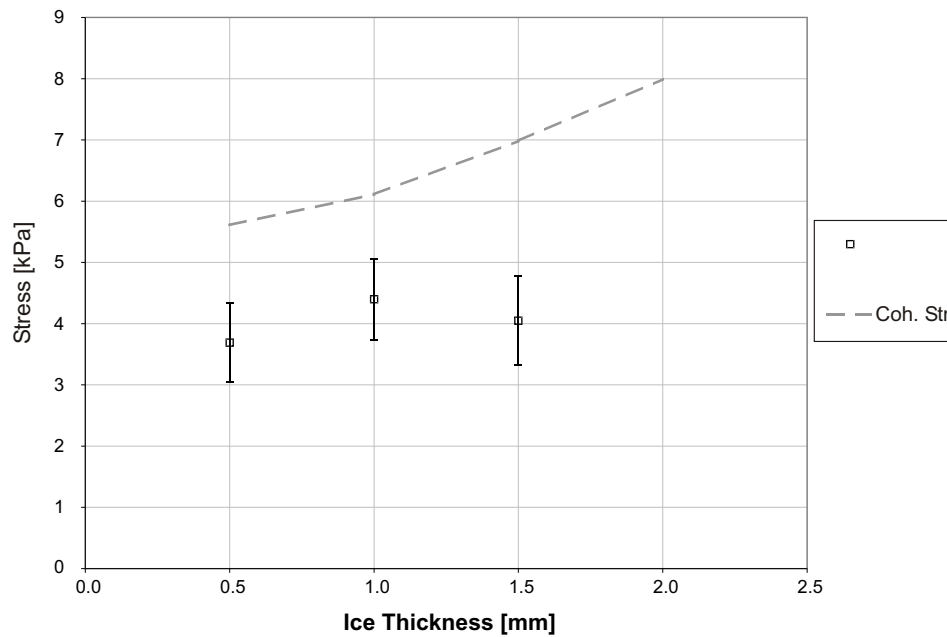
Figure 6.25: Variation of stresses predicted by experiments and Ansys modelling, with thickness, Mode 5: $\sigma_{\theta\theta}$, $(\dot{\varepsilon}_\theta = 0.76 - 1.13 \frac{1}{s})$.

Figure 6.26 shows the relationship between the shear adhesive strength of the frozen sucrose solution compared with the values for shear stress, obtained by finite element model predictions based on the experiments conducted for mode 5 vibrations, at the various thicknesses of frozen sucrose solution investigated. These values appear to lie in the range predicted for the adhesive strength of 20% frozen sucrose solution adhered to stainless steel. The magnitudes of the shear stress are similar to those predicted by finite element modelling for experiments in mode 1 and mode 3 vibrations.

It is unclear whether this is a genuine effect, i.e. there is no strain rate sensitivity in shear adhesion of frozen sucrose solution, or if the adhesive strength happens to rise and then fall with increasing strain rate, in a similar fashion to that shown in Figure 6.18. As the values of shear strength for modes 3 and 5 remain near this predicted value, but at significantly increased strain rates, $0.58 - 1.13 \frac{1}{s}$, it appears that the shear adhesion strength does not exhibit a strain rate sensitivity - see Fig-
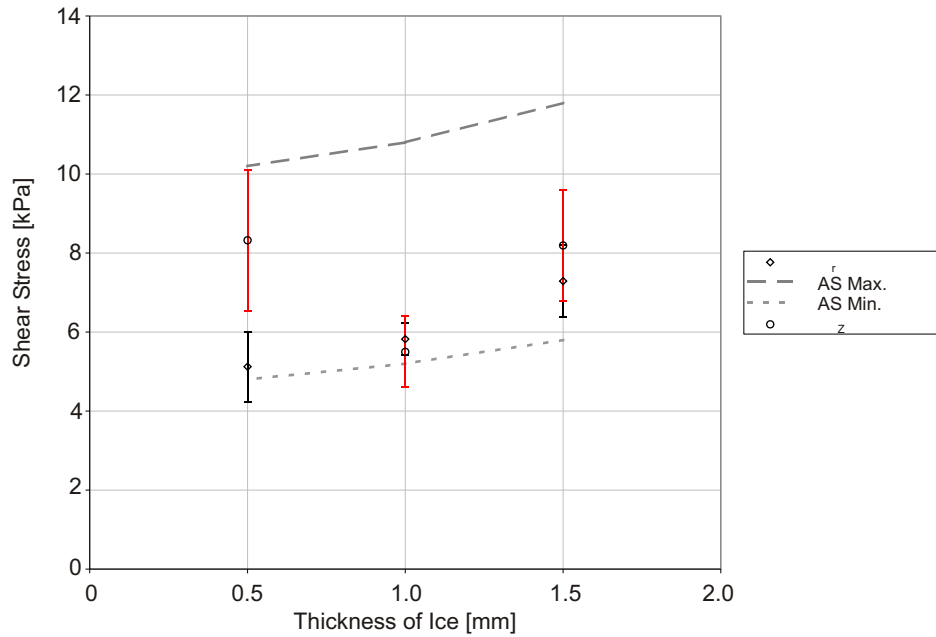
Figure 6.26: Variation of stresses predicted by experiments and Ansys modelling, with thickness, Mode 5: Shear stresses, ($\dot{\varepsilon}_\theta = \sim 0.76 \frac{1}{s}$.).

ures 6.23 and 6.26. However, this assertion is not proven by this data, and further investigation would be required to determine the true nature of the relationship between the adhesive strength and the strain rate. As this data is currently unavailable the quasi-static results will be used for comparison at this stage, assuming that the shear adhesion strength does not vary significantly with strain rate in the range examined, based tentatively on the similar shear stresses at failure across the three modes (and thus strain rates) investigated.

6.4.4 Strain Rate Comparison of Data

The data produced from the three experiments from flexural modes, 1, 3 and 5 provided some interesting findings. Figures 6.16, 6.22 and 6.25 show that the hoop stress is less than or equal to the tensile/yield strength at the critical strain rate ($\dot{\varepsilon}_{\theta, crit} = 0.01 \frac{1}{s}$). This was not entirely unexpected, as can be seen in Figure 6.18, where, after the critical strain rate, the tensile strength of the frozen sucrose solution (7% by mass) tends to decrease with increasing strain rate. The strain rate

at the failure of frozen sucrose (20% by mass), $\dot{\varepsilon}_\theta$, increases with increasing mode number; from $0.08 - .19$ in mode one vibrations to $0.75 - 1.13\,\frac{1}{\mathrm{s}}$ in mode 5 vibrations.

The data for hoop stress at the failure position for each mode was plotted against the strain rate at which the failure occurred. The resulting graph can be seen in Figure 6.27. The data for each thickness of frozen sucrose is plotted with increasing strain rate. The critical strain rate ($\dot{\varepsilon}_{crit} = 0.01\,\frac{1}{\mathrm{s}}$) is the dividing line between data obtained from expressions derived by Atkins et al. [147, 148] relating the hardness and yield strength of a material, and the data obtained from the experiments using the stainless steel built in pipe rig. The constants A and m, necessary to solve equation 6.1 were determined experimentally by Xu et al. [71, 66], using an indentation plunger method. It should be noted that Xu's data did not include strain rates above circa $0.08\,\frac{1}{\mathrm{s}}$. The data plotted above this strain rate on Figure 6.27 is data for a strain rate range which has not been reported before for frozen sucrose solutions. As such no direct comparison to this data was available.
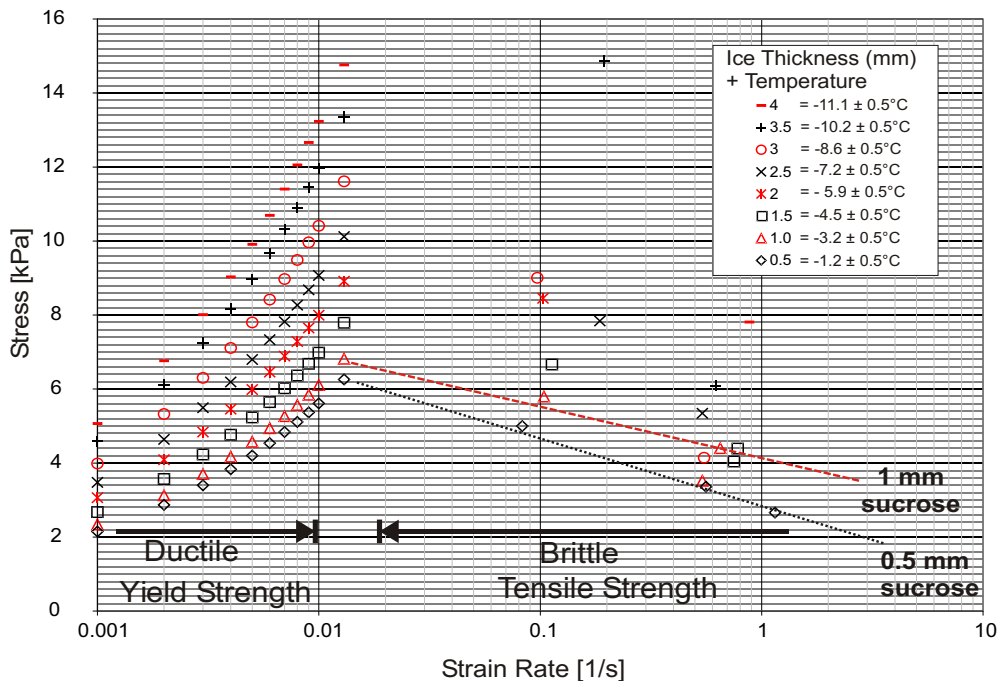
Figure 6.27: Variation of tensile and yield strength of 20% sucrose solution with strain rate.

The data shown in Figure 6.27 for 20% frozen sucrose at greater than -12°C exhibits the same general trend as that of pure ice and 7% frozen sucrose solutions above the critical strain rate for each material. The relationship for thicknesses of ice of 0.5, 1.0 and 1.5 mm appears to give close agreement with a linear trend in the semi-log scale plotted.

Although the thickness of ice formed is of particular interest for this investigation a more generally useful parameter is that of temperature. Therefore, the temperature of the interface between the frozen sucrose and the stainless steel pipe is also displayed. This information could be used to obtain a general feeling for the way frozen sucrose solution (at 20% by mass) fails with strain rate and temperature. If doing so, some care should be taken, as the temperature did vary across the thickness of the ice layer from the temperature noted on Figure 6.27 to the freezing point temperature of the sucrose solution at the interface with the liquid sucrose solution; which means some variation in the material properties will occur through the thickness.

Some means of predicting whether ice will be removed or remain adhered to a cooled system is desirable to enable a suitable design of a higher frequency vibrating device for ice removal purposes. As such the experimental data produced from these experiments has led to an improved understanding of the failure properties of 20% frozen sucrose solution over a range of strain and frequency rates and for various thicknesses of frozen sucrose.

The trends shown here are: (i) the strain rate dependent tensile strength of the frozen sucrose in cohesive failure; where tensile strength decreases with increasing strain rate ($\dot{\varepsilon} > \dot{\varepsilon}_{crit}$) and, (ii) the apparently strain rate independent behaviour of the shear adhesive strength of the frozen sucrose. In Chapter 7 this data and the observed trends will be used to model a system to operate in the ultrasonic frequency range that should be able to remove a thin ice layer - say of 0.5 mm.

6.5   Summary

This Chapter has shown the results of the ice removal experiments from the stainless steel built-in pipe experiments (shown in Chapter 4). Experimental results for flexural modes of vibration for the first, third and fifth modes were shown. In each case the shear stresses at the interface of the pipe and ice layer were near to the prediction of the shear adhesive failure strength of the frozen sucrose solution.

For mode 1 vibrations the stress in the theta direction was also very close to the predicted maximum value of the cohesive failure strength. The first flexural mode of vibration produced strain rates in the theta direction ($\dot{\varepsilon}_\theta$) in the range of $0.08 - 0.19\,\frac{1}{\mathrm{s}}$. The value of maximum tensile strength was calculated at a strain rate of $0.01\,\frac{1}{\mathrm{s}}$. The third mode of vibration of the pipe produced strain rates of $0.38 - 0.75\,\frac{1}{\mathrm{s}}$ and the fifth mode of vibration produced strain rates at failure in the order of $0.76 - 1.13\,\frac{1}{\mathrm{s}}$.

It can be seen from experiments on pure ice and for frozen sucrose solutions of 7% concentration that there is a change in the strain rate sensitivity curve, above a strain rate of a value of around $0.01\,\frac{1}{\mathrm{s}}$ (i.e. the strain rate at which a ductile to brittle transition occurs), where the tensile strength decreases with increasing strain rate. Some experiments on 19% sucrose solution have been carried out by Xu [66] at $-20°C$, but due to the scale used to plot the results it was not possible to gain an estimate of the relationship between the strain rate and the tensile strength above the transition strain rate. However, it is likely that the frozen sucrose solution will still have a similar strain rate sensitivity in this range of strain rate.

The hoop stress at failure for modes three and five are lower than the predicted maximum tensile strength (calculated at $\dot{\varepsilon}_\theta = 0.01\,\frac{1}{\mathrm{s}}$). This would be as expected if the tensile strength falls with increasing strain rate as with pure polycrystalline ice, and for frozen sucrose solutions of lower concentrations, after the ductile/brittle transition at $\dot{\varepsilon}_\theta \geq 0.01\,\frac{1}{\mathrm{s}}$.

The results obtained from the experiments do not make a clear case for determining the order in which the stresses will cause failure in the ice, other than that the ice

will fail first due to the axial stress caused by bending of the pipe. This effect is shown in Section 6.3, where collars of ice form in bands along the Z-direction, with the delimitation clearly visible in both modes 1 and 3 for pure ice.

It appears that the hoop and shear stresses approach the cohesive and adhesive failure strengths at similar amplitudes of vibration for each mode investigated. Observations of the experiments conducted to complement the modelling of axial cracks in Section 6.3 lead to an impression that the order of failure in the ice is:

1. $\sigma_{ZZ} > \sigma_{crit,\,cohesive}$, leading to collar like divisions along the length of the ice, beginning near the stress anti-node and moving outwards in both directions from the failure position ($Z_{failure}$).

2. $\sigma_{shear} > \sigma_{crit,\,adhesive}$, leading to the separation of the ice layer from the stainless steel pipe where the adhesive strength is overcome.

3. $\sigma_{shear} > \sigma_{crit,\,cohesive}$, this occurs at $\theta = 90°$.

4. $\sigma_{\theta\theta} > \sigma_{crit,\,cohesive}$, finally the cohesive strength is overcome by the hoop stress at $\theta = 180°$ causing the ice to come away in a flake.

Thus the ice is removed because the cohesive strength is overcome at 90 and 180° and at two positions in the Z-direction, and the shear stresses have overcome the adhesive strength at the interface between the pipe and the ice.

The evidence from the experiments does not conclusively show this order of failure to be correct. However, enough evidence has been gathered to provide an estimate of when frozen sucrose is likely to be removed from a cooled stainless steel pipe operating at a higher frequency. If the bending stress and hoop stress overcome the cohesive stress shown in Figure 6.27 at the appropriate strain rate and thickness of frozen sucrose, and a shear stress (probably $\sigma_{\theta Z}$ or $\sigma_{R\theta}$) overcomes the shear adhesion strength (which appears to be relatively constant with strain rate for a given thickness of frozen sucrose), then the ice will be removed.

The data gathered from the experiments on the stainless steel pipe will be used in Chapter 7 to design a system capable of ice removal at ultrasonic frequencies.

Of course, care should be taken where higher strain rate are encountered as no ice strength data has been found for strain rates greater than $\dot{\varepsilon} \simeq 1\,\frac{1}{\mathrm{s}}$.

Chapter 7

Discussion and Application Optimisation

7.1 Introduction

This Chapter will aim to address certain issues arising from the investigation of ice removal from cooled metal surfaces. This will involve discussions of the experimental and modelling limitations of the rig and finite element models that have been developed and described in Chapters 4 and 5. Additionally, a discussion of the implications of developing more useful applications of this technique for ice removal will be presented in section 7.3 on system optimisation for ultrasonic operation. This will involve a discussion of basic modelling that has been conducted for higher frequency vibrations, and work that would need to be conducted to validate this modelling.

7.2 Discussions

7.2.1 Introduction

This section outlines the key discussion points that arose during the investigation, and actions taken to address these areas as required. Both experimental and finite element modelling areas are covered. Issues arising from Chapters 3, 4, 5 and 6

are addressed. Works that might be carried out to address such issues for future investigations are outlined.

7.2.2 Discussion of Errors and Unknowns from Experiments and Modelling

Lack of data for strain rate sensitivity of UTS and Adhesive Strength

This meant that some data has to be extrapolated outside of the range of data available, hence reducing certainty in the extrapolated range (see section 6.2). In the range of data at greater than the brittle transition strain rate there was no data available to predict the tensile strength of the sucrose. To make an estimate of the tensile strength at increased strain rates, the value of tensile strength at the brittle transition strain rate was used, assuming that the tensile strength was not strain rate sensitive.

The data obtained from the experiments across different frequencies, and hence strain rates, showed that there was a variation in the tensile strength with varying strain rate. This was highly significant when considering the order of failure of the frozen sucrose in terms of the different stress components. It appeared for example that the ice should not be removed as the limiting component, $\sigma_{\theta\theta}$, had not equalled the estimated tensile strength.

To overcome this limitation of the modelling the data produced from the experiments were plotted against the strain rate. A trend was predicted that was in keeping with data for 7% sucrose as shown by Xu [71, 66].

Extrapolating this trend shown by the data was necessary for the comparison of the tensile strengths for increased frequency operations, as presented later in this Chapter. The errors in the extrapolation are unknown as no data appears to exist in the literature in the strain rate range $\dot{\varepsilon} > 1$. If this trend did not continue after the measured points, but tended towards an asymptotic value, then an error of

20% could arise. This appears to be insignificant for vibrations of up to 33 kHz, see section 7.6.2. However, for even higher frequency vibrations, where achievable amplitudes of vibration are smaller and drag effects are potentially larger, differences in the tensile strength at higher strain rates could be the deciding factor between ice removal success or failure.

Determining order of failure of ice

It is clear that the axial stress (σ_{ZZ}) will be the first uniaxial stress component to cause fracture in the ice layer attached to the pipe, see Section 5.3.7: Figures 5.13, 5.14 and 5.15. In each case the axial stress is significantly greater than the other stress components. Visible evidence is also seen in Figures 6.12 and 6.13, where the ice cracks into collars, with the cracks in a plane perpendicular to the Z-axis.

Figures 6.16 and 6.17, 6.22 and 6.23, and 6.25 and 6.26 show that the shear adhesive stresses and the hoop stress for each mode appear to approach their respective failure strengths (shear adhesive and cohesive) concurrently. It is difficult to accurately assess the order of failure from this data.

It appears, tentatively, that the order of failure is as follows:

1. The axial stress component (σ_{ZZ}) overcomes the cohesive strength of the ice/sucrose, as evidenced by cracks in the plane perpendicular to the Z axis.

2. The shear stress overcomes the shear adhesive strength.

3. The shear stress overcomes the cohesive strength at a position of around $\theta = 90°$.

4. The hoop stress ($\sigma_{\theta\theta}$ finally overcomes the cohesive strength of the ice/sucrose.)

When these conditions are in place the ice is removed, either as a chuck or a flake. In mode 1 experiments, large chunks were observed; in mode 3 experiments smaller flakes were observed and in the mode 5 experiments very small flakes were seen to

be removed in clouds.

The evidence from the experiments does not conclusively show this order of failure to be correct. However, enough evidence has been gathered to provide an estimate of when frozen sucrose is likely to be removed from a cooled stainless steel pipe operating at a higher frequency. If the bending stress and hoop stress overcome the cohesive stress shown in Figure 6.27 at the appropriate strain rate and thickness of frozen sucrose, and a shear stress (probably $\sigma_{\theta Z}$ or $\sigma_{R\theta}$) overcomes the shear adhesion strength (which appears to be relatively constant with strain rate for a given thickness of frozen sucrose), then the ice will be removed.

Differences Between Finite Element Model and Rig

It has been assumed, for modelling purposes, that the pipe is rigidly clamped at each end and that there is no movement at the fixed end of the pipe. In the physical rig this is not the case and measurable vibration has been recorded. For practical reasons the pipe must be contained within a tank to hold the sucrose solution. To achieve reasonable experimental times and temperature control the volume of sucrose to be cooled was limited to around 400 ml. Therefore the tank was closed around the pipe and sealed with O-rings at $1 - 2$ mm from each end of the pipe.

The method of clamping was not perfect and some compliance remained in the system due to this. This compliance was not modelled in the finite element model. Zero displacement boundary conditions were applied at the ends of the pipe, which does not fully represent the physical behaviour of the system. Some structural vibration in the system is not accounted for in the finite element model. Suitable modification of the end clamping arrangement led to a significant reduction in the vibration at the clamping position to a maximum $\sim 1.5\%$ of the peak vibration at the mid-length of the pipe (see section 4.3.1).

No further account was made for the difference in the finite element model and the rig as the modelled and measured mode shapes were very similar (see Figure 5.9).

Errors arising from this discrepancy were probably small compared with other errors due to recording of the signal etc..

Temperature Variations in the Ice/Frozen Sucrose Layer

The temperature for each experiment was recorded at the cooling bath and at the external surface of the stainless steel pipe (at each end of the pipe i.e. $Z = \pm 207\,\text{mm}$). This information was used to calculate an average temperature at the interface between the surface of the pipe and the ice layer. Separate readings were taken in the body of the liquid surrounding the ice layer. There was a significant difference in the average reading of the temperature at the interface and in the liquid near to the outside of the ice layer. For example for a 4.0 mm layer of frozen sucrose the average interfacial temperature was $-10°\text{C}$ and the average temperature in the surrounding fluid at $5 - 6\,\text{mm}$ from the frozen sucrose layer was $-1.2°\,\text{C}$.

The temperature in the liquid was close to the freezing point of the sucrose solution which is $\sim -1.6°\text{C}$; which implies as expected that a temperature gradient exists in the thickness of the frozen sucrose layer ranging from the temperature at the interface to the freezing point temperature at the outer edge of the frozen sucrose layer. There will be some variation in the mechanical properties of the frozen sucrose layer (E, ν and ρ) in the ice layer due to this temperature gradient. This is not accounted for in the finite element model described in Chapter 5. The values for the mechanical properties of the frozen sucrose in the finite element model are those for the temperature at the interface between the frozen sucrose and the pipe surface.

The significance of this in terms of the finite element model representation is low, as the properties of the ice and frozen sucrose (E, ν and ρ) do not vary widely in the temperature range in question ($(-10) - 0°\text{C}$). However the temperature used could have a large effect on the tensile strength of the material. The temperature at the interface was used, as this was the lowest temperature - hence giving the largest value of tensile strength. This should make the modelling of the ice failure conservative, although it may lead to an overestimate of the strength of the frozen

sucrose. The full consequences of this are unknown.

Errors Due to Strain Gauge Measurements

The signal from the strain gauges was measured as described in Section 4.3.1. The total errors predicted from the readings of strain due to:

1. noise on the signal $(5.0 - 8.0\%)$

2. misalignment of the gauge $(0.4 - 1.5\%)$

3. variations of gauge factor with temperature $(0.0 - 2.0\%)$

4. variations due to transverse sensitivity $(0.9 - 1.0\%)$

were estimated to be in the range of $6.3 - 12.5\%$. Where possible, measures to reduce the magnitude of these errors were undertaken. For example strain gauges were adhered to the pipe with great care, following the supplier's instructions to the letter. Similarly dynamic calibration for each thickness of ice and frequency combination was performed prior to the main experimentation, to give the best signal to noise ratio possible.

The most significant of these errors was the noise on the signal obtained from the strain gauges during experimentation. This error was consistently large, i.e. $\geq 5\%$, and the other errors were probably in the lower regions of the estimates shown above. Therefore, the majority of the error arising from the strain gauge measurements was probably due to the noise on the signal.

Parallax Errors During Experimentation

There are two main sources of parallax error in the experimental setup. These are:

- Ice Thickness Reading: The ice thickness that was grown on the stainless steel pipe had to be measured and recorded. As explained in the experimental methodology, in section 4.4, this was achieved using a steel ruler as near to the

ice as possible without interrupting the motion of the system during experimentation. However, the reading of ice thickness could not be taken directly at the metal ruler. Instead it was taken remotely by positioning the eye at a position of equal height from the ground as the end of the metal ruler. Due to this the thickness of the ice layer could only be measured to an accuracy of $\pm 0.25\,\mathrm{mm}$. This error was not considered during the finite element modelling. The effects of this in terms of the finite element modelling were deemed to be small compared to other errors and unknowns existing in the system.

– Ice Removal Point Reading: During many of the experiments the ice was not removed over the entire length of the stainless steel pipe. When this occurred the location(s), on the pipe, where the ice was removed were noted during the course of the experiment. The tank containing the sucrose solution was marked at $10\,\mathrm{mm}$ intervals, both at the front and rear faces. Where possible the readings of failure position were taken during the experiment. By aligning the appropriate measuring line at the front and rear a reading to within $5\,\mathrm{mm}$ could be obtained. Errors recorded due to this, i.e. difference in readings obtained from the finite element model, were in the range of $5 - 9\%$. Therefore, these errors were significant compared to errors in reading the thickness of the ice layer and had a similar magnitude to those caused by noise on the strain gauge signal.

Significance of Factors

The most significant unknowns and errors are the noise on the strain gauge signals, and the ice removal point reading error, which give combined error of $10 - 17\%$. The effect of temperature on the tensile strength of the ice and frozen sucrose may also be significant, but the magnitude of the error is not well understood. Having said this, the standard deviation of each of the stress components fell within the error bounds determined for the system as a whole. Therefore, it appears that the results obtained for the system give a true representation of the behaviour of the system.

The standard deviation in the stresses predicted using the experimental values for

the different modes and ice thicknesses etc. was in the region of $\pm 10 - 18\%$, with a maximum recorded deviation of $\pm 23\%$.

The error bounds estimated from all of the known errors had a range of $\pm 14.3 - \pm 26.5\%$. The fact that the standard deviation was mostly smaller than the error bounds for a given experiment indicates that the experiments were correctly reporting the data.

The magnitude of these errors is judged to be acceptable as variations in the data reported in the literature for ice failure tend to be in the order of $\pm 25\%$ of the tensile strength or fracture toughness reported [149].

Ansys/Disperse Comparisons

In Chapter 5 outputs from Ansys and Disperse models were used to show that the predictions of the stresses generated in the ice layer were of the correct magnitude. Section 5.3.6 shows that there was good agreement for the two models, when the ice layer was considered. There was some disagreement between the two methods when the stresses in the stainless steel pipe were considered.

The disagreement is probably due to the differences in the way the two models were representing the system. On one hand Ansys was used in an attempt to model the rig and on the other hand Disperse modelled a bilayer pipe with a sinusoidal mode shape - not considering the effects of the T-connector at the mid-length etc.. When this was considered, the correlation between the two models seems satisfactory for the purposes of this investigation.

The predictions from the Disperse modelling were used to confirm that the Ansys model was behaving as expected. Therefore any discrepancies between the two models were not significant in terms of the final results, as the Ansys modelling was used to predict the stresses from the experimental data.

Drag Forces at Higher Frequencies

Simple modelling of the drag forces was used for the purposes of this study, and the effects subsequently discounted for the modes currently under consideration. The drag forces produced stress levels at least 2 orders of magnitude less than the stress levels predicted for the other components of stress. Therefore the significance of the drag forces for the sonic rig was small compared to other factors in the experiments.

If modes at significantly higher frequencies of vibration were to be investigated a more rigorous approach to the modelling of the drag forces would be required. See section 7.6.1 for more details. In these higher frequency modes the drag forces may induce significant stresses.

Summary of Significance of Errors and Unknowns

Typical errors quoted from experiments to determine the strength or fracture toughness of ice tend to be in the range of $\pm 7.5 - \pm 25$ of the magnitude of the value quoted. This is due to the variation of crack lengths that can exist in ice.

The errors associated with the experiments detailing ice removal were typically within this range. The most significant parts of the estimated errors were those associated with noise on the signal from the strain gauge and errors due to parallax on readings of the failure positions. Each of these errors had a magnitude of $\sim 5 - 9\%$ of the stress recorded. Another potentially significant unknown was the effect of temperature variations in the ice layer on the tensile strength of the ice during experimentation. Other errors have been noted and estimated, but their significance was generally small.

7.3 System Optimisation

7.3.1 Introduction

It was proposed in Chapter 1 that a low amplitude of vibration, inaudible system might be produced to remove ice from cooled metal surfaces. This section will use the findings of Chapters 5 and 6, to propose a system to remove ice from a cooled metal pipe using vibrations at ultrasonic frequencies of greater than 30 kHz. Frequencies in this range will be investigated, as they are outside of the frequency range in which damage to hearing has been observed (i.e. $10 - 20$ kHz) [150].

A number of factors must be considered when trying to model the behaviour of the system at increased frequencies. As mentioned in Chapter 1 there are a number of frequency dependent mechanisms that must be accounted for. The key factors are the bending stress acting on the pipe, the normal stress caused by inertia acting on the ice, viscous drag forces acting on the outer surface of the ice, and the variation of the tensile strength of the ice/frozen sucrose with temperature and strain rate. During the sonic experiments the bending stress and the strain rate sensitivity dominated the behaviour of the system.

At higher frequencies of vibration it is expected that some of the other mechanisms will become more significant. For example the inertial forces will increase with frequency squared and may increase rapidly in the order of importance. Similarly, the effects of viscous drag will increase linearly with velocity and hence also with frequency. Additionally, the strain rate should increase with increasing frequency and hence the tensile strength may decrease when compared to that exhibited in the sonic experiments.

Therefore the behaviour of the system at increased frequencies presents a complicated problem with many variables. The variation of the stresses will be accounted for by the finite element model, and estimations of the strain rate sensitivity of the tensile strength of the sucrose can be made from the data of Chapter 6. The possible effects of changes in viscous drag will be considered, but not comprehensively

modelled in this Chapter.

The finite element model used to calculate the operating conditions of the sonic rig will be used to predict the frequency of the ultrasonic flexural modes of vibration. The corresponding values for the stress in the pipe at various positions will also be calculated, by assuming a value for the displacement required to remove ice and scaling the stress field to this value. Additionally the strain rate in the θ-direction will be estimated by the finite element representation. By careful comparison between the predicted values of strain rate and predicted stress with the cohesive and adhesive strengths at the same strain rate, it can be determined whether the frozen sucrose is likely to be removed under these operating conditions.

7.4 Finite Element Model Predictions

The previous modelling of the sonic systems (see Chapter 5) was conducted on a stainless steel pipe of length 414 mm and diameter 6.28 mm. So that a minimum number of changes were made, the same system geometry was retained for this modelling as had been used in the sonic rigs of Chapter 4.

The stress field in the system has to be calculated in order to predict when the ice layer will be removed from the surface of the pipe during excitation of the pipe. However, the failure stress is strain rate dependent. Therefore, once the frequency of operation has been chosen, the strain rate for an expected stress will have to be calculated. The lower limit for operation will have been reached when the predicted stress and failure strength have the same magnitude .

7.4.1 Selection of Frequency Range

To achieve the "no noise" requirement, as stated in Chapter 1, either the ice must be removed by ultrasonic means or the system should be enclosed. For the purposes of this investigation the high frequency alternative is of interest. To avoid damage

to the hearing, in the high frequency range $(10-20\,\mathrm{kHz})$, of operators of ice removal equipment, a frequency in excess of $\sim 30\,\mathrm{kHz}$ would be preferable [150].

To investigate this the finite element model of the system was run for ultrasonic frequencies of greater than $30\,\mathrm{kHz}$ to obtain Eigenvalue solutions. However, other considerations require that the frequency of operation should not be too high, i.e. the higher the frequency, the lower the amplitudes of displacement that can be achieved by typical transducers. Another concern was that the strain rate experienced at much higher frequencies would be significantly higher than the strain rates from the existing experiments. Confidence in the yieled/failure strength is decreased the further away from the known good data points. As this data is to be extrapolated (from data obtained from the sonic rig) for comparison with the scaled strain rates predicted by the finite element models of the $> 30\,\mathrm{kHz}$ mode, it is desirable that the predicted strain rates should be as close to the known strain rates as possible, thus avoiding undue errors in extrapolating the data. With this in mind only one mode at just above $30\,\mathrm{kHz}$ was considered for further investigation. The reasons being that the frequency used should be high enough to be safe for human use and as low as possible to remain as near to the good data points as possible.

7.4.2   Iteration of Stress and Strain Rate

In Chapter 6, results from physical experiments (where ice was removed from cooled pipes), were combined with Eigenvalue solutions from a finite element model, which represented the rig. (For further information see Chapters 4 and 5). Now the aim is to use the data collected and interpreted from the existing experiments and finite element models, to predict operating conditions for the same rig where ice will be removed at ultrasonic frequencies.

One of the aims stated at the beginning of this thesis, in Chapter 1, was to use ultrasonic vibrations to remove ice from a cooled metal surface. Although this potential was demonstrated for a flat plate in Chapter 3, by the Branson probe experiments, the system was not particularly useful. This section will attempt to predict a system where ice can be formed and removed from a cooled metal pipe, offering a more

practical solution.

In this modelling there will be no direct experimental results to which the finite element model data can be scaled. The frequency range of interest must first be selected. Then the Eigenvalue solutions for the modes in this range should be calculated. Only the 23rd flexural mode was selected for this investigation, as this was the first flexural mode above $30\,\text{kHz}$ predicted by the finite element model. To begin the solution an amplitude of vibration should be chosen that will be used to scale the stress, strain and displacement data from the Eigenvalue solution. This amplitude of vibration should be within a range that is sensible for typical transducers that operate around the frequency of the mode of vibration that has been chosen. The stress field can then be predicted.

Initially, however, the strain rate in the frozen sucrose solution will be unknown and therefore the failure stress of the frozen sucrose solution will also be unknown. The strain rate can then be calculated from the scaled finite element strain data and the frequency of the vibration. Therefore, an iterative process is required to determine whether the ice layer can be removed under a given amplitude and frequency of operation. For example the data from Figure 6.27, taken from Chapter 6, can be extrapolated to predict the tensile strength versus strain rate. When the solution predicted by the finite element model lies on the predicted line of tensile cohesive strength for the lower of σ_{ZZ} or $\sigma_{\theta\theta}$ then it can be predicted that the ice will be removed, as long as one or more of the predicted shear stresses is greater than the shear adhesion strength. An estimate of the operating conditions likely to remove the ice from the vibrating pipe can be made purely from the finite element model of the system.

7.4.3 Results of Stress and Strain Rate Iteration

A system with only $0.5\,\text{mm}$ of frozen sucrose (20% by mass) formed on the pipe surface was considered. This thickness was selected as the strain rate from the experiments was the greatest for $0.5\,\text{mm}$ of ice. Figure 7.1 shows the stresses as the
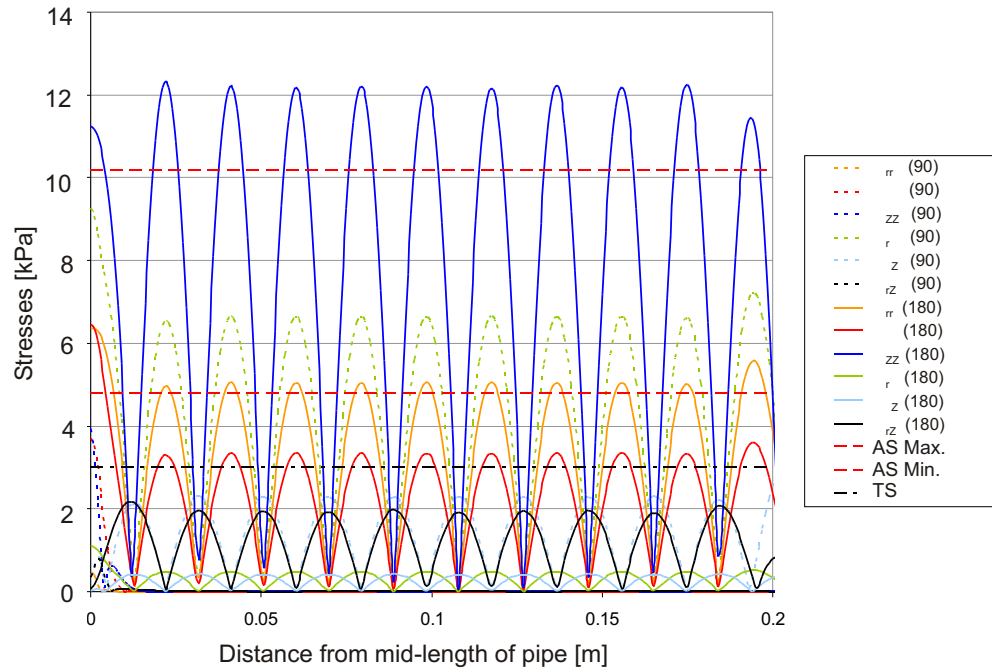
Figure 7.1: Variation of stress levels with angle θ and Z-position for the $23rd$ flexural mode of vibration

final stage of the iteration. The criteria for ice removal as observed in Chapter 6 have been met, i.e. both σ_{ZZ} and $\sigma_{\theta\theta}$ have surpassed the cohesive strength of the sucrose and a shear stress ($\sigma_{r\theta}$) has exceeded the shear adhesion strength of the sucrose under the vibration conditions predicted from the data shown in Figures 6.27 and 6.5.

The displacements predicted for the system to produce the stresses of Figure 7.1 are shown in Figure 7.2. The peak to peak displacement predicted as necessary to cause removal of the frozen sucrose is $0.8\,\mu$m at the mid-length of the pipe in the Y-direction. The general peak to peak displacement of the mode along the length of the pipe is $0.6\,\mu$m.

A 15% over estimate of the stress required to cause ice removal is added to the value of the hoop stress $\sigma_{\theta\theta}$ to account for expected variations in the predictions of ultimate tensile strength of the ice. The effects of this are included in the predictions of transducer amplitudes required to remove ice from the pipe vibrating at $32.5\,$kHz.
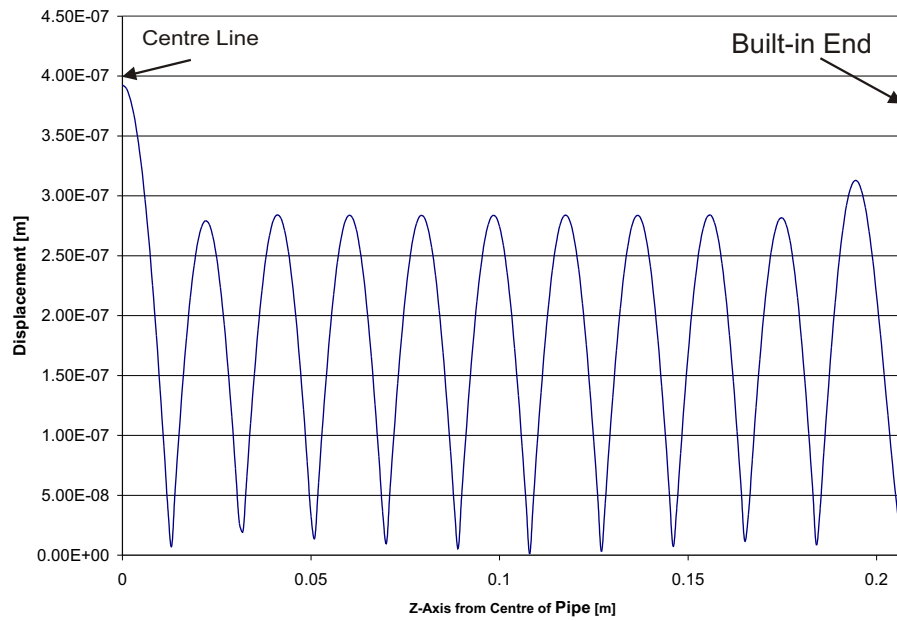
Figure 7.2: Graph showing the scaled displacement mode shape in the Y-direction, with position on the Z-axis.

7.5 Discussion of Actuation

Once an "ideal" theoretical operating state has been reached it is then necessary to discover if the system can be made viably using affordable means. i.e. Does a transducer exist that can meet the criteria for cold operation and also produce the amplitudes required to remove the ice from the system that is proposed? If yes, then an engineering solution may be achieved.

Amplitudes of $7.5\,\mu$m peak to peak are achievable at frequencies of $\sim 500\,$kHz [154]. Amplitudes of $10.6\,\mu$m at $125\,$kHz have been reported in ultrasonic welding transducers [153]. Peak amplitudes of vibration of the order of $35\,\mu$m have been reported for horn type piezo-electric transducers operating at a single frequency of $40\,$kHz [152]. For similar transducers peak amplitudes of $65\,\mu$m have been presented at frequencies of $20\,$kHz [151].
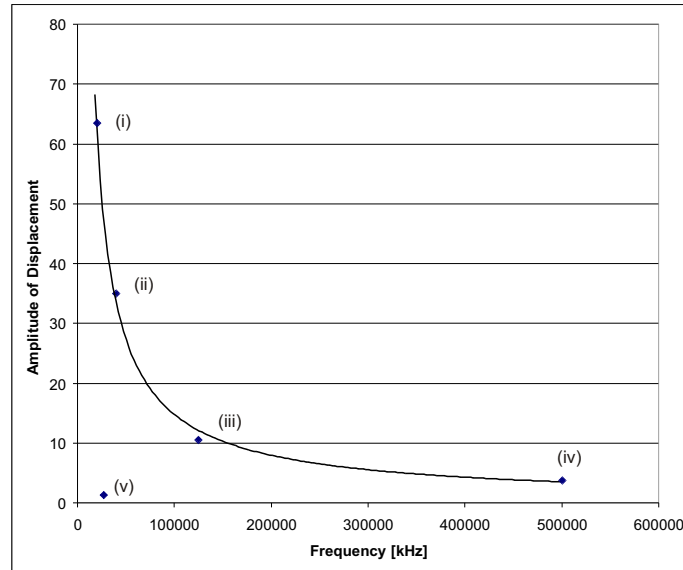
Figure 7.3: Graph showing typical amplitudes of displacement for horn-type transducers over a frequency range of 20 kHz to 500 kHz: (i) single frequency horn-type transducer [151], (ii) single-frequency horn-type transducer [152], (iii) ultrasonic welder [153], (iv) stacked horn-type transducer [154], and (v) prediction of amplitude necessary for ice removal from section 7.4.3.

Figure 7.3 shows the amplitudes of vibration that have been noted for various horn-type piezo-electric transducers over a wide frequency range. At the lower end of the frequency range at around 20 kHz the largest amplitudes at around $60 - 70\,\mu$m are seen. As the frequency of operation increases the amplitude of vibration achievable seems to fall away quickly, reaching a level of $10 - 15\,\mu$m by a frequency of 100 kHz.

The prediction of the amplitude necessary to cause ice removal from the $\frac{1}{4}''$ stainless steel pipe has been plotted as point (v) on the graph of Figure 7.3. It is clear that the amplitudes required fall well within the range of amplitudes that can currently be produced by "high" amplitude horn-type piezo-electric stack transducers. Therefore, it seems that ice can be removed from the pipe at ultrasonic frequencies. The amplitudes of vibration predicted are significantly lower than the maximum amplitudes achievable, and there is plenty of scope for higher amplitudes of vibration if required.

Direct experience from experiments in Chapter 3, has shown that magnetostrictive transducers become hot after even a short period of continuous operation. Based on this it appears that magnetostrictive transducers are not attractive for this purpose, therefore it would be better to use piezo-electric stack transducers. This confirms the successful experimentation with the Branson probe of Chapter 3. It appears that with different actuation, with finer control and by selecting a suitable frequency range for operation a probe of similar design to the Branson probe might be used to remove thin layers of ice from the stainless steel pipe described in Chapter 4.

7.5.1 Estimation of Fatigue Life of Pipe

It was noted in Chapter 1 that consideration of the fatigue life of the pipe would be important in a system where high frequency vibrations are occurring at amplitudes of significant magnitude. This subsection will aim to address the lifespan of a system operating at ultrasonic frequencies.

Paris Law calculations for a pipe with an internal elliptical flaw are relatively well understood and are covered in both the literature and the standards [155, 156]. This type of defect is introduced as an example for illustrative purposes. A similar type of calculation would be required to identify fatigue problems in any chosen specific design. At this stage fatigue effects at the weld of the T-connector and the pipe or at the clamped ends of the pipe are ignored, although they may both be significant. Figure 7.4 shows the geometry of the crack to be investigated. The equations for Paris Law and for evaluation of the pipe geometry are described in the following section.

$$log\left(\frac{da}{dN}\right) = mlog(\Delta K) + logC \tag{7.1}$$

$$\frac{da}{dN} = C\Delta K^m \tag{7.2}$$

Where:

$$K = \sigma \sqrt{\frac{\pi a}{Q}} F_t \tag{7.3}$$

The geometric factor for a pipe with an internal semi-elliptical crack, as shown in Figure 7.4, is described in Equation 7.4 [155].
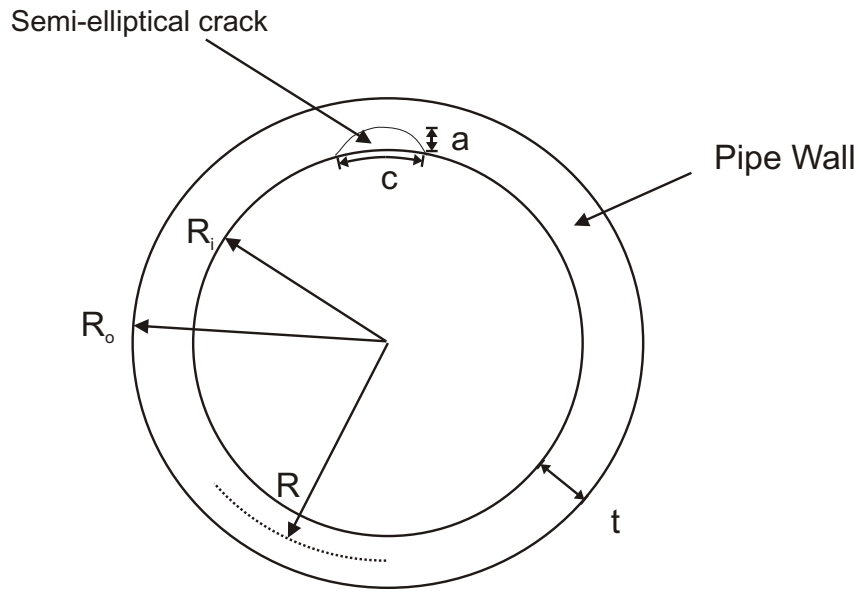
Figure 7.4: Diagram showing the cross-section of a pipe with a semi-elliptical crack on the inner surface.

$$F_t = 1 + \left[0.02 + \zeta(0.0103 + 0.00617\zeta) + 0.0035(1 + 0.7\zeta)(\frac{R}{t} - 5) \right] Q^2 \tag{7.4}$$

Where:

$$\zeta = \left(\frac{a}{t}\right)\left(\frac{a}{2c}\right) \quad and \quad Q = 1 + 1.464\left(\frac{a}{c}\right)^{1.65} \tag{7.5}$$

Substituting the stress intensity factor (K) of Equation 7.3 into the Paris law Equation 7.2, the following relationship is obtained.

$$\frac{da}{dN} = C(\Delta\sigma\sqrt{\frac{\pi a}{Q}}F_t)^m \tag{7.6}$$

Rearranging and integrating Equation 7.6, gives Equation 7.7:

$$\int_0^{N_f} dN = \int_{a_i}^{a_f} \frac{da}{CF_t^m \Delta\sigma^m(\frac{\pi a}{Q})^{\frac{m}{2}}} \tag{7.7}$$

Where a_i is the initial crack length; a_f is the final crack length, either at fast fracture or at the through thickness value (t); and N_f is the final number of cycles.

Substituting Equation 7.4 into Equation 7.7 yields Equation 7.8, as shown below.

$$\int_0^{N_f} dN = \dots \tag{7.8}$$
$$\int_{a_i}^{a_f} \frac{Q^{\frac{m}{2}} da}{C\left(\Delta\sigma_{ZZ}\sqrt{\pi a}\left(1+\left[0.02+\zeta(0.0103+0.00617\zeta)+0.0035(1+0.7\zeta)\left(\frac{R}{t}-5\right)^{0.7}\right]Q^2\right)\right)^m}$$

The constants C and m for stainless steel $316L$ are 3.0×10^{-10} and 3.25 respectively [157]. Substitution of these values into Equations 7.8 and 7.5 along with the relevant value for the axial stress in the pipe due to the vibration allows an estimate of N_f to be calculated. A numerical solution for the integral is required.

An initial crack size is required for the integration of equation 7.7. It is assumed that the pipe begins as a virgin material, with no known defects. The external surface roughness of the steel is approximately $0.3\,\mu$m when the metal is polished using 320 grit emery paper [158]. The internal surface roughness of the pipe is approximately $1.0\,\mu$m after production [159]. The typical grain size of Stainless Steel $316L$ is approximately $60\,\mu$m [160]. It would appear that the grain size of the stainless steel provides a suitable initial condition ($a_i = 60\,\mu$m) for the calculation of the integral. Similarly, choosing $a_f = t$ would provide an estimate of the total life span of the system, where the component would have to be replaced significantly before this period of operation had elapsed. For this case to be acceptable the critical fatigue strength of the material must not be exceeded by the value of K as calculated by Equation 7.3 at the operational stress and with $a = t$. If this is not the case, then

the critical crack length, where the pipe would fail by fast fracture should be found.

The fracture toughness (K) of 316 stainless steels has been found to fall between the values of $K_C = 220 - 250 \, \text{MPa.m}^{\frac{1}{2}}$ for samples of $\sim 2 \, \text{mm}$ thickness [161], which compares with the value of $K_{1C} = \sim 360 \, \text{MPa.m}^{\frac{1}{2}}$ for larger test specimen sizes [162]. To produce a conservative results the lower values of K should be used, as the pipe thickness under investigation is $\sim 1.2 \, \text{mm}$.

The initial crack length was $60 \, \mu\text{m}$. The axial stress in the sucrose was taken to be $14 \, \text{kPa}$, as shown in Figure 7.1 for the 23rd mode which occurs at approximately $32.4 \, \text{kHz}$. This gives an axial stress in the stainless steel pipe of approximately $5.9 \, \text{MPa}$. As the integration of Equation 7.8 had to be solved numerically it was necessary to find a value for δa which would provide a stable solution. The solution was calculated based on the crack increasing in length by $\delta a = x\% \times a_{initial}$; where x is a percentage. It was found that a step length of $2.0\% \times a_{initial}$ gave 7401 operating hours, based on continuous running at $32.4 \, \text{kHz}$ and $1.5\% \times a_{initial}$ gave 7406 operating hours under the same conditions. This gave a good enough agreement considering the preliminary nature of the study and the value of ~ 7000 operating hours could be used. A component life of this order of magnitude would be suitable for replacement of equipment at an annual maintenance.

It must be noted that there may be other areas that are equally likely or more likely to fail than the pipe itself. These might include the welded area at the T-connector, or the built-in ends of the pipe. Additionally, the stresses required to cause sucrose-ice removal might be significantly higher than expected due to drag effects etc..

7.6 Limits of Modelling

7.6.1 Drag Effects

The effects of drag forces acting on the system should be carefully considered, to determine whether the stresses resulting are of a similar magnitude to the stresses

caused by the vibration and therefore might prevent the removal of the ice/frozen sucrose layer.

Using the model of drag described in method 1 of section 5.4.2 an estimate of the drag force acting on the pipe was obtained using the displacement data from the estimate of amplitude required to remove ice, i.e. $0.3\,\mu$m peak displacement. The pipe was assumed to have a layer of ice of 0.5 mm thick attached to it. The estimate of the total drag force obtained on this pipe was $\sim 40\times$ greater than the estimate of the total drag force acting on the pipe under mode 3 vibrations, for the same geometry. The stress induced by the drag forces should still be smaller than the stresses induced by bending. However, the drag forces have become large enough that they cannot be completely ignored.

The simple modelling of drag described in Chapter 5 is probably insufficient to explain the behaviour of the drag forces acting on the pipe, and more detailed finite element modelling of the system would be required. However, as the transducer seems to be well within the bounds of amplitudes that have previously been achieved; it seems that using a design with a greater maximum amplitude than that predicted would allow the required stresses to be produced, even with the drag acting on the pipe.

7.6.2 Ultimate Tensile Strength at High Strain Rates

The values of UTS used for this case lay slightly outside those obtained during experiments on the sonic rigs at $\dot{\varepsilon} \cong 1.5\,\frac{1}{\text{s}}$. Therefore, care should be taken when using the data obtained by extrapolation.

The last data point from Chapter 6 was at approximately $\dot{\varepsilon} = 1.17\,\frac{1}{\text{s}}$. The tensile strength at this strain rate was 3.7 ± 0.6 kPa. This is not significantly greater than the value of 3.0 kPa used to determine the failure conditions for the pipe vibrating at 32.5 kHz. Even if the value of 3.7 kPa itself is used the typical amplitude of displacement required in the pipe only rises to $0.35\,\mu$m from $0.30\,\mu$m. There-

fore, it is assumed that any variation in the prediction of this tensile strength would not be great enough to affect the viability of ice removal using this mode of vibration.

7.7   Summary

The model described in Chapter 5 has been used in conjunction with the experimental data from Chapter 6 to predict operating conditions for the rig described in Chapter 4 to remove frozen sucrose (20% by mass) from the pipe when vibrating at the 23rd flexural mode of the pipe. Effects of flexural and longitudinal vibrations in the T-connector have been ignored at this stage. A suitable combination of strain rate and displacement in the pipe has been found where the amplitude of vibration will cause stresses in the pipe just large enough to remove the frozen sucrose from the pipe.

The modelling of the system has not included the effects of drag on the pipe. Also the true values of adhesive and tensile strengths at strain rates equivalent to those predicted for this mode of vibration are not fully understood. Therefore, to check that this operating condition is capable of removing frozen sucrose from the pipe a transducer should be attached that can produce amplitudes of vibration as predicted.

The Branson probe described in Chapter 3 would probably be able to provide suitable amplitudes of vibration if run from a tunable signal generator. Such experiments were beyond the scope of this investigation, but would provide a valuable insight into the effectiveness of this model to predict ice removal from the cooled metal pipe.

The design case presented in this Chapter indicates that the ice removal should be easily achievable with the selection of a correctly designed transducer, as the amplitudes predicted for ice removal are well within the boundaries of existing transducers. It should be remembered that the results presented are for a single geometry, as described in Chapter 4.

If higher frequency modes were to be investigated it should be noted that the fatigue life of the components may be significantly reduced, and the damping effects of drag forces may become more severe, hence limiting amplitudes of vibration that can be achieved. Therefore, removing ice at significantly increased frequencies may prove problematic.

Chapter 8

Conclusions

8.1 Introduction

This chapter will outline the findings from the investigation, showing what has been achieved and conclusions that have been drawn from the results.

8.2 Conclusions by Chapter

8.2.1 Chapter 3: Initial Experiments

A number of experiments were conducted using ultrasonic rigs which are described in Chapter 3. The aim of these rigs was to remove ice from cooled metal surfaces, which were metal plates in the case of the experiments of Chapter 3. Mixed results were obtained from these experiments, i.e. in most of the experiments thin layers of ice and frozen sucrose solutions could not be removed from the chilled metal plates they were formed onto.

There was one exception to the general failure to remove ice layers from the metal plates. The Branson probe experiments (see Section 3.4) were very successful at removing ice from the thin steel plate which the probe excited perpendicularly. Ice or frozen sucrose layers could be built up and then removed, or if the probe ran ice build-up could be prevented.

Unfortunately the Branson probe had a low tunability, and as ice was removed at every setting of its integrated amplifier, no threshold of the adhesive or cohesive strengths of either of the materials could be mapped. Additionally, the integrated system meant that only a narrow bandwidth was available. Any systems to be investigated had to have a natural frequency of vibration in the range of 19.5–20.0 kHz, or the transducer would not function.

The Etrema probe experiments were set up in a virtually identical fashion to the Branson probe experiments and a very similar mode shape was produced experimentally. The same finite element model was used to represent the two plates and predict the axial stress in a thin ice layer formed on the plate.

The two systems operated at nominally the same frequency, with the same mode shape. The amplitudes of vibration in the Etrema probe setup were smaller than those when the Branson probes were used. It can be concluded that the increased amplitudes of vibration contribute in some way to the ice removal. However, no firm understanding could be obtained from the data recorded during the experiments.

The conclusions that could be drawn from the experiments of Chapter 3 were somewhat limited. It can be concluded that:

- Ice can be removed from chilled metal plates using structural vibrations in the ultrasonic frequency range.

- Frozen sucrose solutions can also be removed from chilled metal plates using structural vibrations in the ultrasonic frequency range.

- Increasing the amplitude of vibration while other factors remain the same led to the ice layer being removed. No conclusion as to the mechanism behind this (e.g. increasing inertia or bending stress) could be drawn from these experiments.

No further conclusions of any significance can be drawn from the experiments of Chapter 3.

8.2.2 Chapter 4: Rig Development

The aim was to develop an experimental rig (for ice removal) that could produce reliable repeatable data. A number of rigs were constructed with varying success. The initial rig was able to remove ice but there was a problem with repeatability. A second rig was designed, constructed, and refined. The final version of this rig showed vastly improved reliability and repeatability compared with the earlier rigs.

It is possible to conclude that a rig which meets the criteria of reliability and repeatability has been developed and tested. The rig was capable of removing differing thicknesses of frozen sucrose solution under varying operating conditions.

8.2.3 Chapter 5: Modelling

In this chapter a number of finite element models relating to the experimental rigs of Chapters 3 and 4 were presented. The aim of the models was to determine and predict the stress field present in the various systems during experimentation.

To achieve this aim, the finite element models of Chapter 5 had to be experimentally verified by comparison with measurable parameters from the experiments of Chapters 3 and 4, and where appropriate, by comparison to other modelling approaches (analytical and Disperse comparisons were made with the finite element models of the pipe based systems).

Basic models of the plate based systems of Chapter 3 were created, and basic verification of the models was performed. An order of magnitude estimate of the principal bending stress in the ice layers was obtained. No further work was performed, due to the lack of promise shown by the experimental methods.

The pipe based models of Chapter 5 were verified in terms of measurable parameters

from the experimental rigs of Chapter 4, e.g. natural frequencies of vibration and relative mode shapes of vibration of unloaded pipe systems. Reasonable agreement (typically within 10% error) was obtained by this approach.

As a further check on the accuracy of the stress fields predicted by the finite element model under loaded conditions, the stress fields were carefully selected and normalised to allow comparison with the polar stress component outputs from the Disperse model of a comparable system. The stress components showed a similar mode shape through the thickness of the ice - although some differences were seen in the metal pipe part of the system. Good agreement was seen in the normalised stress magnitudes obtained from the finite element model and the Disperse model.

It was concluded that the finite element model of the $\frac{1}{4}''$ stainless steel pipe system produced an acceptable representation of the stress field formed in the pipe and ice (or frozen sucrose solution) system under experimental conditions. The effects of drag (although not directly included in the finite element model) were discounted using additional modelling.

Based on this conclusion, the experimental strain data was used to scale the Eigenvalue solutions from the finite element model. The data produced were compared to the cohesive and adhesive properties of ice and frozen sucrose solution obtained from the literature, and the results presented in Chapter 6.

8.2.4   Chapter 6: Results

Data obtained using the experimental rig of Chapter 4 and the finite element model of Chapter 5 was presented in Chapter 6. The data was presented in conjunction with the adhesive and cohesive strengths for ice and 20% frozen sucrose solution as found in the literature. Particular care was taken with the handling of strain rate data.

The aim of the comparison was to determine the the mechanisms of failure respons-

ible for removing the ice from the cooled metal pipe. The main findings can be summarised as follows.

In all the experimental cases investigated (modes 1, 3 and 5) the axial stress component (σ_{ZZ}) was considerably larger than the other stress components. Finite element modelling (shown in Section 6.3) demonstrated that the frozen sucrose solution first fails in collar-like structures along the length of the pipe. The effect is clearly demonstrated for experiments involving modes 1 and 3 flexural vibrations. It is expected that a similar mechanism occurs under mode 5 vibrations, but the effect could not be clearly observed. This is consistent with the findings, where the collar length decreased with increasing frequency. In mode 5 vibrations the collars may have become very short and therefore difficult to properly observe.

For 20% sucrose solutions it was found that the peak interfacial shear stresses observed at the conditions where ice was removed from the pipe were of a very similar magnitude to the shear adhesive strength found in the literature. This held true for failures during experiments using flexural modes 1, 3 and 5.

For mode 1 vibration the predicted peak hoop stress ($\sigma_{\theta\theta}$) was similar in magnitude to the value of cohesive strength stated in the literature. For modes 3 and 5 the hoop stress was lower than the last known point found in the literature. This is consistent with most findings in the literature for polycrystalline ice and 7% frozen sucrose solutions, where the cohesive strength decreases with increasing strain rate at strain rates greater than the ductile-brittle transition rate.

Based on this information it appears that no firm conclusions can be drawn on the specific order of failure within the frozen sucrose layer and at the pipe interface, other than as previously mentioned that cohesive brittle failure occurs first. This takes place in the ice layer normal to the axial direction, due to the action of the axial stress component (σ_{ZZ}). It is apparent, however, that certain criteria must be observed in a number of directions for the ice to be removed "cleanly" from the surface of the pipe described as follows.

It appears that the hoop and shear stresses approach the cohesive and adhesive failure strengths at similar amplitudes of vibration for each mode investigated. Observations of the experiments conducted to complement the modelling of axial cracks in Section 6.3 lead to an impression that the order of failure in the ice is:

1. $\sigma_{ZZ} > \sigma_{crit,\,cohesive}$, which is shown by the formation of cracks perpendicular to the axial stress direction. The cracks initially form near the stress anti-node and then move outwards in both directions from the failure position ($Z_{failure}$).

2. $\sigma_{shear} > \sigma_{crit,\,adhesive}$, leading to the separation of the ice layer from the stainless steel pipe where the adhesive strength is overcome.

3. $\sigma_{shear} > \sigma_{crit,\,cohesive}$, this occurs at $\theta = 90°$.

4. $\sigma_{\theta\theta} > \sigma_{crit,\,cohesive}$, finally the cohesive strength is overcome by the hoop stress at $\theta = 0$ and $180°$ causing the ice to come away in a flake or chunk.

Thus the ice was removed because the cohesive strength is overcome at 90 and 180° and at two positions in the Z-direction, and the shear stresses have overcome the adhesive strength at the interface between the pipe and the ice. The criteria mentioned in this paragraph must be met for ice to be removed cleanly from the pipe.

The evidence from the experiments does not conclusively show this order of failure to be correct. However, enough evidence has been gathered to provide an estimate of the conditions required for frozen sucrose to be removed from a cooled stainless steel pipe operating at a higher frequency. If the bending stress and hoop stress overcome the cohesive stress shown in Figure 6.27 at the appropriate strain rate and thickness of frozen sucrose, and a shear stress (probably $\sigma_{\theta Z}$ or $\sigma_{R\theta}$) overcomes the shear adhesion strength (which appears to be relatively constant with strain rate for a given thickness of frozen sucrose), then the ice will be removed.

This Chapter showed a general trend for the failure characteristics of frozen sucrose solutions at strain rates that had not previously been investigated. Results showed that at strain rates greater than $0.01\frac{1}{s}$ there was a continued decrease in the

yield/fracture strength of the frozen sucrose solution. This decrease appears to continue to the range of the experimental data at around $1.00 \frac{1}{s}$. A further investigation would be required to determine whether this trend continues at further elevated strain rates.

The data gathered from the experiments on the stainless steel pipe was used in Chapter 7 to design a system capable of ice removal at ultrasonic frequencies.

8.2.5   Chapter 7: Optimisation

It appears from the results of Chapter 6 that a basic grasp of the mechanisms responsible for ice removal from chilled stainless steel pipes has been obtained. In addition to this, a finite element model has been created which is suitable for predicting the stress field within the $\frac{1}{4}''$ stainless steel pipe and ice system under various conditions.

One of the original aims was to use ultrasonic vibrations to remove ice from cooled metal surfaces (see Chapter 1). Using the above mentioned information on ice removal mechanisms and the finite element modelling capabilities described in Chapter 5, an attempt to predict operating conditions where ice might be removed under ultrasonic frequencies of operation was attempted.

The results obtained show that the amplitudes of vibration predicted fall well within the limits of vibration amplitudes currently achievable through existing transducer technology. Both magnetostrictive or PZT stack transducers are technically capable of producing the amplitudes of vibration predicted by the finite element model of the ultrasonic system. PZT stack transducers would be favoured at this time due to the large heating effects caused by hysteretic heating commonly observed in magnetostrictive transducers.

Some significant uncertainties as to the actual amplitudes of vibration required to cause ice removal at ultrasonic frequencies remain. However, the amplitudes of vi-

bration that have been reported in the literature are significantly greater than those estimated to cause ice removal, and thus it is the judgment of the author that ice removal should be possible using the $\frac{1}{4}''$ stainless steel pipe systems investigated during this thesis. This judgement is supported by the Branson probe experiments of Chapter 3, where ice was removed violently using ultrasonic vibrations.

8.2.6 Future Works

Ice removal has been demonstrated on a sonic rig, which was based on a long slender pipe. Based on the findings from this rig a condition where ultrasonic vibrations might be used to remove ice from a very similar rig has been conjectured. The first obvious step for any further investigation would be to demonstrate this condition and verify if ice could be removed successfully.

Following on from this more sophisticated methods might be used to attempt ice removal. For example, longitudinal or torsional modes might be employed to remove ice from cooled metal pipes. Such methods might be achieved by careful selection and location of suitable transducers.

Also some effort might be spent on determining the general applicability of the results of this investigation. For example an attempt to conduct similar experiments on plates or tubes of varying diameters and thicknesses would give a better understanding of the mechanics of the ice removal. In addition to this a wider investigation of the temperature effects, especially below $-13°\,\mathrm{C}$ might be beneficial to investigate the relationship between adhesive and cohesive failure and the apparent change in dominance of the modes of failure below this temperature. This affect may have been observed in the 3.5 and 4.0 mm ice layer experiments.

References

[1] T. Theodorsen and W.C. Clay. The prevention of ice formation on gasoline vents. Technical Report 394, National Advisory Committee for Aeronautics, October 1931.

[2] F.C. Brown. The frequent bursting of hot water pipes in household plumbing systems. *Physics Review*, pages 500–503, 1916.

[3] Hideo Inaba, Dong Won Lee, and Akihio Horibe. Study on the critical conditions of ice formation for a continuous ice making system in a cooling pipe. *Heat Transfer-Japanese Research*, 27(1):74–83, 1998.

[4] T.J. Sheer, M.D. Butterworth, and R. Ramsden. Ice as a coolant for deep mines. In *Proceedings of the 7th International Mine Ventilation Congress*, pages 355–361, 1997.

[5] T. Shelly. A sound way to strengthen steel. *Eureka*, pages 28–29, 2002.

[6] Ying Xie, Wei Xie, Wei-Ping Pan, A. Riga, and K. Anderson. A study of ash deposits on heat exchange tubes using the sdt/ms and xrd techniques. *Thermochimica Acta*, 324:123–133, 1998.

[7] F. De Gregorio, A. Ragni, M. Airoldi, and G.P. Romano. Piv investigation on airfoil with ice accretations and resultant performance degradation. In *19th international congress on instrumentation in aerospace simulation*, pages 94–105, 22800 Cedar Point Rd, Cleveland, Ohio, August 2001. IEEE.

[8] T. Cebeci and K. Fassi. Aircraft icing. *Annual Review of Fluid Mechanics*, 35:11–21, 2003.

[9] Damian R. Ludwiczak. Aircraft anti-icing and deicing protection using ultrasound technology. Research and Technology TM107350, NASA: Lewis Research Centre, 1996.

[10] V.F. Petrenko. Reduction of ice adhesion to stainless steel by ice electrolysis. *Journal of Applied Physics*, 86:5450–5454, 1999.

[11] V.F. Petrenko. Effect of electric fields on adhesion of ice to mercury. *Journal of Applied Physics*, 84:261–267, 1998.

[12] V.F. Petrenko. http://www.iceengineering.com. Company Web Page for: Ice Engineering.

[13] A. Szkatula, M. Balanda, and M. Kopec. Magnetic treatment of industrial water. silica activation. *The European Physical Journal: Applied Physics*, 18:41–49, 2002.

[14] A. el Boher, M.Z. Pechatnikov, and B.M. Menin. Method and installation for continuous production of liquid ice, 1996. Patent Number: EP 0 708 300 A1.

[15] UTINLAB North West Centre of Ultrasonic Technologies. www.utinlab.ru/eng, 2001.

[16] Pil Woo Heo, Jang Lae Lee, Eui Su Lim, and Kwang Sik Koh. An experimental study for scale prevention in boiler by use of ultrasonic waves. *Journal of the Acoustical Society of America*, 12:2441, 2002.

[17] H.G. Schwartzberg and M.A. Rao. Food freeze concentration. *Food Process Engineering*, pages 127–202, 1990.

[18] E. Acton and G.J. Morris. Method and apparatus for the control of solidification of solids in liquids. World Patent, November 1992. WO9220420.

[19] P. Avan, M. Elbez, and P. Bonfils. Click-evoked otoacoustic emissions and the influence of high-frequency hearing losses in humans. *Journal of the Acoustical Society of America*, 101(5(1)):2771–2777, 1997.

[20] H.O. Ahmed, J.H. Dennis, O. Badran, M. Ismail, S.G. Ballal, A. Ashoor, and D. Jerwood. High-frequency $(10 - 18\,\mathrm{kHz})$ hearing thresholds: reliability and effects of age and occupational noise exposure. *Occupational Medicine*, 51(4):245–258, 2001.

[21] G. von Bekesy. *Experiments in Hearing*. McGraw-Hill (New York), 1960.

[22] Colworth House MK44 1LQ Unilever Research Group. Personal Communication, 2001-2003.

[23] C. Liddell and R. Weir. *Ices: The Definitive Guide*. Hodder and Stoughton, 1993.

[24] International Association of Ice Cream Manufacturers (IAICM), editor. *The History of Ice Cream*. IAICM, Washington DC, 1978.

[25] R. De-Goede and E.J. De Jong. Heat transfer properties of a scraped surface heat exchanger in the turbulent flow regime. *Chem Eng. Sci.*, 48:1393–1404, 1993.

[26] P.V. Hobbs. *Ice Physics*. Clarendon Press, Oxford, 1974.

[27] S. Sodawala and J. Garside. Ice nucleation on a cold surface. In *The 1997 Jubilee Research Event*, pages 477–480. Institute of Chemical Engineers, 1997.

[28] V.F. Petrenko. Systems and methods for modifying ice adhesion strength. World Patent, December 1998. Dartmouth College, US.

[29] J.P. Miller and C.M. Monroe. Methods and apparatus for freezing aqueous liquid. US Patent, November 1994.

[30] S.T. Jones. 3D lollies. *Dairy Industries International*, 62:31, 1997.

[31] R.L. Rauckhorst III and D.B Sweet. Pneumatic deicing system with protection for super cooled large droplet ice. European Patent, EP0806342, December 1997.

[32] http://www.idiny.com/deicing.html. Innovative Dynamics Ltd.

[33] P.B. Zieve, J.L. Hartmann, and J.K. Ng. High force density eddy current driven actuator. In *IEEE 1988*, Vancouver, BC, Canada, 1988. Electroimpact, Inc. Seattle, WA 98105. http://www.electroimpact.com/research/HFDECDASAE.asp.

[34] M Yamada, S. Fukusako, and H. Kawabe. A quantitative evaluation of the production performance of ice slurry by the oscillatory moving cooled wall method. *International Journal of Refrigeration*, 25:199–207, 2002.

[35] S.J. Jones. High strain-rate compression tests on ice. *J. Phys. Chem B*, 101:6099–6101, 1997.

[36] E.M. Schulson. The brittle failure of ice under compression. *J. Phys. Chem. B*, 101:6254–6258, 1997.

[37] X. Xu, G. Jeronimidis, A.G. Atkins, and P.A. Trusty. Rate-dependent fracture toughness of pure polycrystalline ice. *Journal of Materials Science*, 39:225–233, 2004.

[38] E.M Schulson. The structure and mechanical properties of ice. *Journal of Materials*, 5(2):21–27, 1999.

[39] K.G. Berger, B.K. Bullimore, G.W. White, and W.B. Wright. The structure of ice cream. *Dairy Industries*, pages 419–425 and 493–497, 1972.

[40] W.F Shipe and L.F. Blanton. Effect of ice cream stabilizers on the freezing characteristics of various aqueous systems. *Journal of Dairy Science*, 46:169–175, 1963.

[41] K. Kotte, P. Cornillon, and D. Reid. Effect of solutes and freezing velocity on the dendritic spacing of ice crystals. In 20th *International Congress of Refrigeration*, Sydney, 1999.

[42] R.W. Hartel. Ice crystallization during the manufacture of ice cream. *Trends in Food Science and Technology*, 7:315–322, 1996.

[43] E. Faydi, J. Andrieu, and P. Laurent. Experimental study and modelling of the ice crystal morphology of model standard ice cream. part i: Direct

characterization method and experimental data. *Journal of Food Engineering*, 48:283–291, 2001.

[44] A.B. Russell, P.E. Cheney, and S.D. Wantling. Influence of freezing conditions on ice crystallisation in ice cream. *Journal of Food Engineering*, 39:179–191, 1999.

[45] E. Faydi, J. Andrieu, P. Laurent, and R. Peczalski. Experimental study and modelling of the ice crystal morphology of model standard ice cream. part ii: Heat transfer data and texture modelling. *Journal of Food Engineering*, 48:293–300, 2001.

[46] C. Cogné, J. Andrieu, P. Laurent, A. Besson, and J. Nocquet. Experimental data and modelling of thermal properties of ice creams. *Journal of Food Engineering*, 58:331–341, 2003.

[47] N.F. Fletcher. *The Chemical Physics of Ice.* Cambridge University Press, 1970.

[48] D.M. Cole. The microstructure of ice and its influence on mechanical properties. *Engineering Fracture Mechanics*, 68:1797–1822, 2001.

[49] L.W. Gold. Deformation mechanisms in ice. In D. Kingery, editor, *Ice and Snow*, pages 8–27. The MIT Press, 1963.

[50] K. Arakawa. The growth of ice crystals in water. *Journal of Glaciology*, 2(17):463–468, 1955.

[51] C.M. Neils, K.R. Diller, and L.J. Hayes. An optical-axis directional solidification stage for topographical imaging of ice growth. The University of Texas at Austin, Texas 78712.

[52] Wei Bingbo. Unidirectional dendritic solidification under longitudinal resonant vibration. *Acta Metall. Mater.*, 40 (10):2739–2751, 1992.

[53] D.R Kelly, S.J. Harrison, S. Jones, M. Abid Masood, and J.J. Gwynfor-Morgan. Rapid crystallisation using ultrasonic irradiation - sonocrystallisation. *Tetrahedron Letters*, 34(16):2689–2690, 1993.

[54] N. Enomoto, T.-H. Sung, Z.-E Nakagawa, and S.-C. Lee. Effect of ultrasonic waves on crystallization from a supersaturated solution of alum. *Journal of Materials Science*, 27:5239–5243, 1992.

[55] C.P. Lee and Wang T.G. The effects of pressure on the nucleation of an under-cooled liquid. *Journal of Applied Physics*, 71, 1992.

[56] R.-Y. Botsaris, G.D. anf Qian. Process and system for freeze concentration using ultrasonic nucleation useful in effluent processing. Technical report, United States Patent Office, May 1999. Number: 5,966,966.

[57] S.J. Czysak. *Adhesion and Adhesives, Fundamentals and Practice, Society of Chemical Industry*. Wiley, New York, 1954.

[58] P.H. Gammon, H. Kiefte, and M.J. Clouter. Elastic constants of ice samples by brillouin spectroscopy. *J. Phys. Chem.*, 87:4025–4029, 1983.

[59] E.H. Andrews, H.A. Majid, and N.A. Lockington. Adhesion of ice to a flexible substrate. *Journal of Materials Science*, 19:73–81, 1984.

[60] T. Kärnä and E. Järvinen. Symmertic and asymmetric flaking processes. In *Proceedings of the 15th International Conference on Port and Ocean Engineering under Arctic Conditions*, volume 3, pages 988–1000, Helsinki, Finland, August 1999.

[61] H.H.G. Jellinek. Adhesive properties of ice. *Journal of Colloid Science*, 14:268–280, 1959.

[62] Andrews E.H. and N.A. Lockington. The cohesive and adhesive strength of ice. *Journal of Materials Science*, 18:1455–1465, 1983.

[63] M.A. Rist. High-stress ice fracture and friction. *Journal of Physical Chemistry B*, 101:6263–6266, 1997.

[64] E.M. Schulson. The brittle compressive fracture of ice. *Acta Metallica Materia*, 38:1963–76, 1990.

[65] P.K. Dutta. Compressive failure of polycrystalline ice under impact. In *Proceedings of the 3rd international offshore polar engineering conference*, volume 2, page 573, 1993.

[66] X. Xu, G. Jeronimidis, and A.G. Atkins. On the yield stress of frozen sucrose solutions. *Journal of Materials Science*, 38:245–253, 2003.

[67] A.M. Fish and Y.K. Zaretsky. Ice strength as a funtion of hydrostatic pressure and temperature. Technical Report 97-6, CRREL, October 1997.

[68] E.M. Schulson. Brittle failure of ice. *Engineering Fracture Mechanics*, 68:1839–1887, 2001.

[69] P. Duval, M.F. Ashby, and I. Anderman. Rate-controlling processes in the creep of polycrystalline ice. *J. Phys. Chem.*, 87:4066–4074, 1983.

[70] J.W. Glen. The creep of polycrystalline ice. *Proceedings of the Royal Society*, 228:519–538, 1955.

[71] X. Xu. *A study of the mechanical and fracture properties of water ice.* PhD thesis, University of Reading, UK., 2000. Fracture of Ice.

[72] I.A. Ryzhkin and V.F. Petrenko. Physical mechanisms responsible for ice adhesion. *J. Phys. Chem B*, 101:6267–6270, 1997.

[73] L.E. Raraty and D. Tabor. The adhesion and strength properties of ice. In *Proceedings of the Royal Society of London*, 1958.

[74] J.S. McFarlane and D. Tabor. Adhesion of solids and the effect of surface films. In *Proceedings of the Royal Society of London*, 1950.

[75] P. Barnes, D. Tabor, and J.C.F. Walker. The friction and creep of polycrystalline ice. *Proceedings of the Royal Society London: A*, 324:127–155, 1971.

[76] Norikazu Maeno and Masahiko Arakawa. Adhesion shear theory of ice friction at low sliding velocities, combined with ice sintering. *Journal of Applied Physics*, 95:134–139, 2004.

[77] D.A. Lynch III and D.A. Ludwiczak. Shear strength analysis of the aluminium/ice adhesive bond. Technical Report TM107162, NASA, 1996.

[78] Bowden. The mechansim of sliding on ice and snow. *Proceedings of the Royal Society of London: Series A*, 172:280–298, 1939.

[79] P.V. Hobbs and B.J. Mason. The sintering and ahesion of ice. *The Philosophical Magazine*, pages 181–197, 1963.

[80] M. Landy and A. Freiberger. Studies of ice adhesion: i. adhesion of ice to plastics. *Journal of Colloid and Interface Science*, 25:231–244, 1967.

[81] W.G. Nelson and E.J. Young. Adhesion of fresh and saline ice to bare and coated steel surfaces. In *OMAE - Volume IV, Arctic/Polar Technology*, pages 63–66. ASME, 1994, 1994.

[82] C. Blackburn, C. Laforte, and Laforte J.L. Apparatus for measuring the adhesion force of a thin ice sheet on a substrate. In *Ninth International Workshop of Atmospheric Icing of Structures*, 2000.

[83] V.F. Petrenko and R.W. Whitworth. *Physics of Ice*. Oxford University Press, 2002.

[84] L.W. Gold. Statistical behaviour of the deformation for first loading of polycrystalline ice. *Journal of Glaciology*, 49:37–49, 2003.

[85] C. Laforte, Laforte J.-L., and J.-C. Carrière. How a solid coating can reduce the adhesion of ice on a structure. In *IWIAS 2002: Session 9*, pages 1–6, 2002.

[86] H. Saito, K. Takai, and G. Yamauchi. Water and ice-repellent coatings. *Surface Coatings International*, 80:168–171, 1997.

[87] H.R. Baker, W.D. Bascom, and C.R. Singleterry. The adhesion of ice to lubricated surfaces. *The Journal of Colloid Science*, 17:477–491, 1962.

[88] W.D. Bascom, R.L. Cottington, and C.R. Singleterry. Ice adhesion to hydrophilic and hydrophobic surfaces. *J. Adhesion*, 1:246–263, 1969.

[89] J.M. Sayward. Seeking low ice adhesion. Technical Report 79-11, pages 1-31, U.S. Army Cold Regions research and Engineering Laboratory, Hanover, New Hampshire, 1979.

[90] V.K. Croutch and R.A. Hartley. Adhesion of ice to coatings and the performance of ice release coatings. *Journal of Coatings Technology*, 64:41–53, 1992.

[91] H. Saito, K.-I. Takai, and G. Yamauchi. A study of ice adhesiveness to water-repellent coating. *Materials Science Research International*, 3:185–189, 1997.

[92] V.A. Igoshin, V.I. Postol, and P. Paasivuori. Surface influence on adhesion of ice (translated from russian). *Trenie i Iznos*, 10:333–337, 1989.

[93] J.R. Jones and M.N. Gardos. Adhesive shear strength of ice to bonded solid lubricants. *Lubrication Engineering*, 28:464–471, 1972.

[94] H.F. Holtzclaw, W.R. Robinson, and W.H. Nebergall. *College chemistry with qualitative analysis.* D.C. Heath and Co., 1984.

[95] R.J. Williams and D.L. Carhan. Association between ice nuclei and fracture interfaces in sucrose:water glasses. *Thermochimica Acta*, 155:103–107, 1989.

[96] R.W. Hartel and A.V. Shastry. Sugar crystallization in food products. *Critical Reviews in Food Science*, 1, 1991.

[97] http://www.doitpoms.ac.uk/tlplib/biocrystal/water-sucrose.php.

[98] P. Chen, X.D. Chen, and K.W. Free. Solute inclusion in ice formed from sucrose solutions on a sub-cooled surface - an experimental study. *Journal of Food Engineering*, 38:1–13, 1998.

[99] A. van Hook and F. Frulla. Nucleation in sucrose solutions. *Industrial and Engineering Technology*, 44:1305–1308, 1952.

[100] B.M. Liang and R.W. Hartel. Contact nucleation in sucrose crystallization. *Chemical Engineering Science*, 42:2723–2727, 1987.

REFERENCES

[101] R. Chow, R. Blindt, R. Chivers, and M. Povey. A study on the primary and secondary nucleation of ice by power ultrasound. *Ultrasonics*, 43:227–230, 2005.

[102] C.A. Miles, M.J. Morley, and M. Rendell. High power ultrasonic thawing of frozen foods. *Jounral of Food Engineering*, 39:151–159, 1999.

[103] A. Martin and G. Jeronomidis. A study of the mechanical and fracture properties of ice cream. Technical report, Unilever Research Group, 1994.

[104] Martin A. and G. Jeronomidis. A study of the mechanical and fracture properties of ice cream ii. Technical report, Unilever Research Group, 1995.

[105] A. Daniel, D. Chamberlain, and J. Watts. Mechanical properties and microstructure of water ice. In *Ice Cream Symposium II*. Unilever Research Group, Colworth, 1997.

[106] P. Reiser, G. Birch, and M. Mathlouthi. *Physical Properties*. Blackie Academic and Professional, London, 1995.

[107] Y. Roos and M. Karel. Amorphous state and delayed ice formation in sucrose solutions. *International Journal of Food Science and Technology*, 26:553–566, 1991.

[108] X. Xu, G. Jeronomidis, and A.G. Atkins. Stress relaxation behaviour of frozen sucrose solutions. *Journal of Texture Studies*, 35:11–32, 2004.

[109] Macro Design Limited, 16 Palewell Park, East Sheen, London, SW14 8JG. *Wavemaker-Duet, High voltage wave packet and pulse generator/receiver unit: Hardware Manual*, June 1997.

[110] Polytec GmbH, Lambda Photometrics Ltd., Lambda House, Harpenden, Herts., AL5 5BZ. *User Manual: Laser Doppler Vibrometer*, December 2000. Sensor OFV-511, Controller OFV-3001.

[111] Branson Ultrasonics Corporation. *Digital Sonifer Models 250 and 450 User's Manual*.

[112] HAAKE, Gebruder Haake GmbH, Dieselstrasse 4, D-76227 Karlsruhe, Germany. *Instruction Manual: Circulator DC10, Including all Baths.* Bath Vessel K15.

[113] B. Chu and G. Machin. A low-temperature black body reference source to $-40°$C. *Measurements Science Technology*, 10:1–6, 1999.

[114] Etrema Products Inc., 2500 North Loop Drive, Ames, IA 50010 U.S.A. *Performance Results AU010N300-MS1 (No.3039)*, January 2002.

[115] L.W. Gold. The process of failure of columnar grained ice. *Philosophical Magazine, A*, 26:311–328, 1972.

[116] G.W.C. Kaye and T.H. Laby. *Tables of Physical and Chemical Constants.* Longman, Essex, 16 edition, 1995.

[117] D.L. Hall and A.B. Flatau. Nonlinearities, harmonics and trends in dynamic applications of terfenol-d. Iowa State University.

[118] Ling Dynamic Systems. *Installation and Operating Manual: $V200$ Series Vibrators*, 2nd edition. Manual Number 892071.

[119] Entran Limited, 4 Thames Park, Wallington, OX10 9TA. *User manuals for miniature accelerometers and force gauges.*

[120] Evo-Plas, Evode Speciality Adhesives Ltd., Leicester, LE3 1UQ, England. *Tensol 12.*

[121] Ling Dynamic Systems. *Installation and Operating Manual: $V400$ Series Vibrators*, 2_{nd} edition. Manual Number 892301.

[122] Grant. *Grant LTC cooling bath user's manual.*

[123] Sensors UK. Waterproof strain gauges. $www.sensors-uk-transducers-instruments.com$.

[124] Pico Technology Ltd., The Mill House, St. Neots, PE19 1QB. *User Manual: TC08 eight channel thermocouple.*

[125] MGI. Errors due to misalignment of strain gauges. Technical Report TN-138-4, Measurements Group Incorporated, 1980.

[126] MGI. Errors due to transverse sensitivity in strain gauges. Technical Report TN-509, Measurements Group Incorporated, 1982.

[127] Ansys Corporation. www.Ansys.com.

[128] S. Mantovani and S. Valeri. Mechanical bheaviour at ice-metal interfaces. *Philosophical Magazine A*, 37:17–26, 1978.

[129] http://www.panametrics-ndt.com.

[130] A. D. Blevins. *Formulas for Natural Frequency and Mode Shape.* Van Nostrand Reinhold Company, 1st edition, 1979.

[131] W.E. Baker. Vibration frequencies for uniform beams with central masses. *Journal of Applied Mechanics*, pages 335–337, 1964.

[132] M.S. Hess. Vibration frequencies for a uniform beam with central mass and elastic supports. *Journal of Applied Mechanics*, pages 556–558, 1964.

[133] Ansys Corp. *Ansys Element Reference.*

[134] $http://www.efunda.com$. Mechanical Properties of Stainless Steel 316L.

[135] L.W. Gold. The static and dynamic elastic constants. *British Journal of Applied Physics*, 11:522–523, 1960.

[136] Schlumberger. *User Manual Solartron FRA 1255.*

[137] B.N. Pavlakovic, M.J.S. Lowe, D.N. Alleyne, and P. Cawley. Disperse: A general purpose program for creating dispersion curves. In D.O. Thompson and D.E. Chimenti, editors, *Review of Progress in Quantitative NDE*, volume 16, pages 185–192. Plenum Press, New York, 1997.

[138] Batchelor. G.K. *An Introduction to Fluid Dynamics.* Cambridge University Press, The Edinburgh Building, Cambridge, 3 edition, 2000.

[139] W. Manners. Hydrodynamic force on a moving circular cylinder submerged in a general fluid flow. *Proceedings of the Royal Society: Mathematical and Physical Sciences*, 1992.

[140] http://www.engineeringtoolbox.com/.

[141] D.J. Ewins. *Modal Testing : Theory and Practice.* Research Studies Press Ltd, 1986.

[142] D.J. Ewins. *Measurement and application of mechanical mobility data.* Solartron Instrumentation Group.

[143] H. Dutsch, F. Durst, S. Becker, and H Lienhart. Low-reynolds-number flow around an oscillating circular cylinder at low keulegan-carpenter numbers. *Journal of Fluid Mechanics*, 360:249–271, 1998.

[144] W.G. Nelson and A. Phukan. Adfreeze strength of fresh and sea ice bonded to steel pipes. In *Proceedings of the 7th OAME, Volume 4*, pages 165–169, Houston, Texas, 1988. ASME.

[145] W.M. Sackinger and P.A. Sackinger. Shear strength of the adfreeze bond of sea ice to structures. In *Proceedings of the 4th International Conference on Port and Ocean Engineering Under Arctic Conditions, Volume 2*, pages 607–614, 1977.

[146] Ling Dynamic Systems. *Installation and Operating Manual: PA100E Power Amplifier*, 2nd edition. Manual Number 880501.

[147] A.G. Atkins. *The science of hardness testing and its research applications.* American Society for Metals, 1971.

[148] D. Tabor. *The Hardness of Metals.* Clarendon Press, 1951.

[149] W.A. Nixon and E.M. Schulson. Fracture toughness of freshwater ice as a function of loading rate. In *Ice Technology, proceedings of the first international conference*, pages 287–295. Springer-Verlag, Berlin, 1986.

[150] J. Grzesik and E. Fluta. High-frequency hearing risk of operators of industrial ultrasonic devices. *International Archive of Occupational and Environmental Health (Historic Archive)*, 53:77–88, 1983.

[151] http://www.amtechultrasonics.com/articles/.

[152] Personal Communication with Guillermo Coto, Director International Sales, American Technology, Inc. (AmTech).

[153] L. Parrini. Design of advanced ultrasonic transducers for welding devices. *IEEE Transactions on Ultrasonics, ferroelectrics, and frequency Control*, 48:1632–1639, 2001.

[154] S.C. Tsai, Yu L. Song, T.K. Tseng, Yuan F. Chou, Wei J. Chan, and Chen S. Tsai. High-frequency, silicon-based ultrasonic nozzles using multiple fourier horns. *IEEE Transactions on Ultrasonics, Ferroelectrics, and Frequency Control*, 53:277–285, 2004.

[155] T.L. Anderson. *Fracture mechanics: Fundamentals and applications, 2nd Ed.* CRC Press, London, 1995.

[156] RCC-MR. *Design and construction rules for mechanical components of FBR nuclear islands and high temperature applications, Appendix 16: Guide for leak before break analysis and defect assessment.*, 2002.

[157] Barson and Rolfe. *Fatigue Control in Structures.* Prentice-Hall, 2 edition, 1987.

[158] Meltzer. Bulletin on material welds and finishes. Technical report, DCI Inc., 1993.

[159] http://www.cardinaluhp.com. Pre-treated SS316L.

[160] N. Célard. *Determination of a unified defect assessment procedure for high temperature applications.* PhD thesis, Imperial College, 2000.

[161] M.A. Sokolov, J.P. Robertson, L.L. Snead, D.J. Alexander, P. Ferguson, M.R. James, S.A. Maloy, W.F. Sommer, Willcut¡ G., and M.R. Loutan. Fracture

toughness characterization of 304l and 316l austenitic stainless steels and alloy 718 after irradiation in high-energy, mixed proton/neutron spectrum. In *Effects of radiation on materials: 20th international symposium, ASTM STP1405.* American Society for Testing and Materials, 2002.

[162] W.J. Mills. Fracture toughness of types 304 and 316 stainless steels. *International Materials Reviews*, pages 45–82, 1997.